Nanostructure Science and Technology
Series Editor: David J. Lockwood

Tetsuya Osaka
Zempachi Ogumi *Editors*

Nanoscale Technology for Advanced Lithium Batteries

Springer

Nanostructure Science and Technology

Series Editor:
David J. Lockwood, FRSC
National Research Council of Canada
Ottawa, Ontario, Canada

For further volumes:
http://www.springer.com/series/6331

Tetsuya Osaka • Zempachi Ogumi
Editors

Nanoscale Technology for Advanced Lithium Batteries

Springer

Editors
Tetsuya Osaka
Waseda University Faculty of Science
and Engineering Shinjuku-ku
Tokyo 169-8555, Japan

Zempachi Ogumi
Society-Academia
Collaboration for Innovation,
Kyoto University, Gokasho,
Uji 611-0011, Japan

ISSN 1571-5744
ISBN 978-1-4614-8674-9 ISBN 978-1-4614-8675-6 (eBook)
DOI 10.1007/978-1-4614-8675-6
Springer New York Heidelberg Dordrecht London

Library of Congress Control Number: 2013951658

© Springer Science+Business Media New York 2014
This work is subject to copyright. All rights are reserved by the Publisher, whether the whole or part of the material is concerned, specifically the rights of translation, reprinting, reuse of illustrations, recitation, broadcasting, reproduction on microfilms or in any other physical way, and transmission or information storage and retrieval, electronic adaptation, computer software, or by similar or dissimilar methodology now known or hereafter developed. Exempted from this legal reservation are brief excerpts in connection with reviews or scholarly analysis or material supplied specifically for the purpose of being entered and executed on a computer system, for exclusive use by the purchaser of the work. Duplication of this publication or parts thereof is permitted only under the provisions of the Copyright Law of the Publisher's location, in its current version, and permission for use must always be obtained from Springer. Permissions for use may be obtained through RightsLink at the Copyright Clearance Center. Violations are liable to prosecution under the respective Copyright Law.
The use of general descriptive names, registered names, trademarks, service marks, etc. in this publication does not imply, even in the absence of a specific statement, that such names are exempt from the relevant protective laws and regulations and therefore free for general use.
While the advice and information in this book are believed to be true and accurate at the date of publication, neither the authors nor the editors nor the publisher can accept any legal responsibility for any errors or omissions that may be made. The publisher makes no warranty, express or implied, with respect to the material contained herein.

Printed on acid-free paper

Springer is part of Springer Science+Business Media (www.springer.com)

Preface

Today, economic growth in developing countries such as China and India has led to the rapid expansion of motorization in these countries. Motorization has, in turn, accelerated environmental problems and shortages of fossil fuels. Therefore, the widespread use of green vehicles in the future will be essential. In addition, renewable energy sources, such as solar power and wind power, whose energy generation depends on local weather have been introduced to reduce CO_2 emissions. The unfortunate and tragic accident at the nuclear power plant in Fukushima, Japan, caused by the earthquake and tsunami of March 11, 2011, dealt Japanese industry a serious blow by depriving it of electric power. This has further accelerated the introduction of renewable energy sources.

Under these circumstances, energy storage has become extremely important because green vehicles, such as hybrid electric vehicles (HEVs), plug-in hybrid vehicles (PHEVs), battery electric vehicles (BEVs), and even fuel cell electric vehicles (FCEVs), use batteries. Furthermore, the fluctuating energy generation of solar power and wind power plants necessitates a means of power leveling to stabilize electric power systems. Thus, batteries are being used in an ever-expanding field of applications. Different applications require different battery performances, that is, batteries should be customized for each application. For example, batteries with high power are required in particular for HEVs, PHEVs, and FCEVs, whereas batteries with a high energy density are required for BEVs. In addition, safety, reliability, and cost-effectiveness are essential features of batteries.

Nanotechnology has been the foundation of advances in many fields of science and technology. The term electrochemical nanotechnology (ECNT) is defined as *nanoprocessing by means of electrochemical techniques*. The use of ECNT has been increasing in various electronics applications, and in some cases it has been extended to applications in other fields. Understanding processes for the fabrication of nanoscale films and structures is essential for the development of new precision nanofabrication techniques.

The content of this book focuses mainly on nanotechnological research on lithium batteries (LIBs) in Japan. The active materials of LIBs are designed at the nano level in primary particles, and the surface of secondary particles is treated at the nano level. Battery reactions proceed on nano or subnanoscales.

Most of the contributors to this volume were selected from institutions that are at the forefront of research on LIBs in Japan, although experts from other organizations also contributed chapters on specific subjects in their area of expertise. This volume provides an overview of nanotechnology for LIBs from basic to applied research in selected high-technology areas with particular emphasis on the near-term and future advances in these fields.

We express our thanks to all authors, referees, and advisors for their help and support in making the publication of this book possible.

Waseda University, Tokyo, Japan Tetsuya Osaka
Gokasho, Uji, Japan Zempachi Ogumi

Contents

Chapter 1
Energy Systems for a Green Community: The Role of Energy Conversion and Storage

Zempachi Ogumi

1.1 Introduction

Society desires progress. Scientific and technological advances confer great benefits on people in developed countries using fossil fuels – coal, oil, and natural gas. Energy is essential for enjoying the benefits of advanced technology. Energy consumption is not the end but the means of enjoying life using advanced technology. There exist feasible approaches to suppressing carbon dioxide emissions.

The first method is to suppress energy consumption while retaining the benefits of our life styles brought about by the use of devices that depend on advanced technology.

The second approach is to develop new sources of energy that emits less or no carbon dioxide. Renewable energy resources including photovoltaic (PV) power, photothermal power, and wind power, which are based on solar energy, and geothermal and tidal power. Nuclear energy has also attracted much attention as a clean energy source, but the situation seems to be changing following the terrible accident at the Fukushima Daiichi nuclear power station in Japan in March 2011.

The third method is to enhance energy conversion. Fossil fuel is converted into heat and then electric energy. The higher the conversion efficiency, the lower the carbon dioxide emission to obtain energy. Among energy conversion systems, electrochemical energy conversion systems like fuel cells do not involve a thermal process, the conversion efficiency is not governed by Carnot's rule, and a high efficiency is expected theoretically for electrochemical energy conversion.

Fuel cells convert energy from chemical to electric energy. Batteries can store the electric energy in the form of chemical energy through electrochemical reactions based on redox reactions of active materials, that is, batteries are designed to convert

---

Z. Ogumi (✉)
Society-Academia Collaboration for Innovation,
Kyoto University, Gokasho, Uji 611-0011, Japan
e-mail: ogumi@scl.kyoto-u.ac.jp

T. Osaka and Z. Ogumi (eds.), *Nanoscale Technology for Advanced Lithium Batteries*,
Nanostructure Science and Technology 182, DOI 10.1007/978-1-4614-8675-6_1,

energy as is done in fuel cells. In principle, batteries contain materials for producing energy inside them, while active materials, oxidants and reductants, are supplied from outside to the fuel cells.

1.2 Batteries Open New Transportation

Batteries can play a major role in the first two categories by storing electric energy. Hybrid electric vehicles (HEVs) and plug-in hybrid electric vehicles (PHEVs) are attracting considerable attention from various sectors of society due to their high fuel efficiency. The high efficiency is a result of a leveling of the energy demand and supply using energy storage. Drivers drive their cars as they wish and the traction system must supply energy as needed by the drivers; likewise, drivers slow down as needed. Thus, the energy demand fluctuates widely and frequently. These fluctuations in the output power of the main traction lowers the well-to-wheel efficiency to as low as 15–18 %.

On the other hand, as shown in Fig. 1.1, batteries in HEVs supply insufficient power from the main traction upon ignition and acceleration and store excess energy during deceleration and normal cruising. In the case of ideal HEVs, the main traction operates in optimized conditions. The optimized efficiency of a gasoline engine has been estimated at 30–35 %. Energy recovery during deceleration may reach at least 2 % in busy, large urban traffic. HEVs with gasoline engines as the main traction source the reach over 30 %, which is twice the value for conventional gasoline engine vehicles.

The point is that batteries supply the required power and store the excess power from the main traction over demanded power. For this, rechargeable batteries are required in electric vehicles with high input and output power.

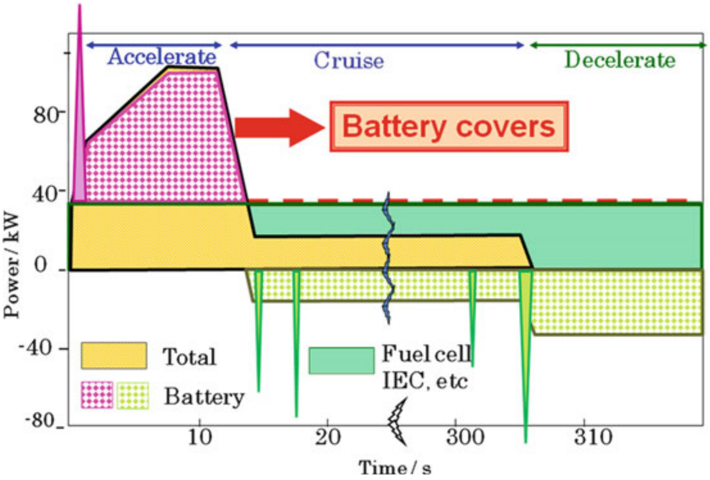

Fig. 1.1 Power generation and consumption in hybrid electric vehicles

1.3 Role of Batteries in Introduction of Renewable Energy

We mostly rely for our energy on the Sun, except for tidal power, geothermal power, and nuclear energy. Plants fix about 0.02 % of solar energy arriving at the Earth through their photosynthesis. Only a small fraction of the energy captured by plants is stored as fossil sources over a huge expanse of time, on the order of hundreds of millions of years. We use fossil energy sources and return carbon dioxide to the atmosphere, the amount of that reaches up to 5–10 % of the carbon dioxide captured by plants through their photosynthesis. This amount of energy is sufficient to disturb the carbon dioxide cycle on Earth.

Most renewable energy also originates from solar energy, including PV, photothermal, and wind power. PV is a typical renewable energy that has attracted much attention around the world. Solar energy is available during the day, and the weather determines the available PV power. Therefore, PV power is very unstable. The large-scale introduction of PV power to current power grids causes the grids to become unstable. The fluctuations in PV output power must be absorbed by storing the excess power. Further, peaks in PV output power do not correspond to peaks in power consumption. In Japan, a 1 kW household PV system requires a 3 kWh battery system to fill in the time-gap between consumption and production. These issues might be resolved if grids were connected globally, but such a situation is still far off into the future.

Different kinds of technology are used to store electric energy. Storage by pumped hydro is a well-known method. Others include compressed air in the form of pressure, high-temperature rocks in the form of thermal energy, flywheels in the form of mechanical energy, superconducting magnetic energy storage (SMES) in the form of electromagnetic energy, and batteries. Most of these systems are large and require specific sites that are adequate for the construction of facilities.

Among the alternatives, battery systems have features that make them unlike other systems. Such systems can entail large systems combined with large power plants, medium-sized systems with transformer stations, small systems with household PV systems, and miniature systems connected directly to electric appliances like air-conditioners and refrigerators. Siting problems for facility of energy storage system is remarkably decreased for battery energy systems, as shown in Fig. 1.2.

Currently, smart communities are attracting much attention. Smart energy systems represent the main part of a smart community. The energy system is considered to be based on green energy and future transportation systems with high energy efficiency in conjunction with advanced information technology. An energy storage system, especially one whose size can be customized, is essential to realize a smart energy system.

1.4 Battery Performances for Future Energy Systems

Batteries can play an important role in our future energy system. The following performances are required for batteries: high energy density in weight and volume, high input and output power density in weight and volume, long cycle life, long

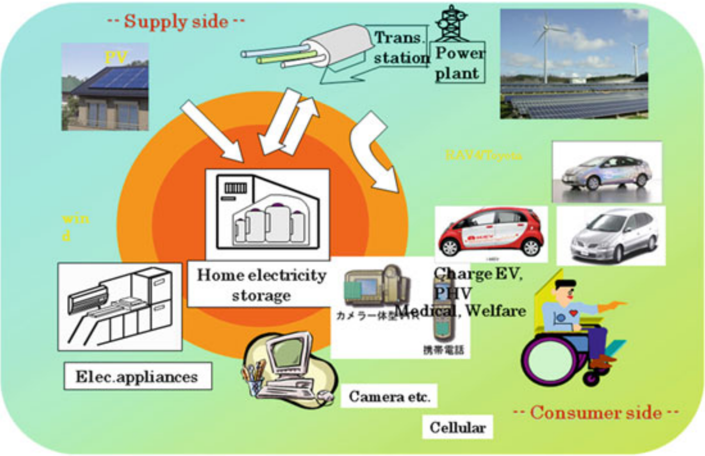

Fig. 1.2 Battery energy storage systems are installed at different stages of energy systems

calendar life, high energy efficiency in charging and discharging, low cost, high safety, high reliability, and so on. Present rechargeable batteries do not satisfy these requirements.

Safety is a prerequisite for all products, but batteries represent stored energy. It is reasonable to consider that the higher the energy density, the more the safety of the battery decreases. Therefore, maintaining the safety of batteries is of utmost importance.

In energy systems, the efficiency of the energy input (battery charge) and the output (battery discharge) must be high, whereas batteries for mobile IT devices do not require high energy efficiency.

Small batteries for mobile IT devices do not require significant cost reductions, but larger battery systems, such as vehicle batteries and stationary batteries for energy storage, require low initial cost and low lifetime cost. High energy density is important in all applications. Mobile IT devices require light batteries, electric vehicles and PHEVs require light and small batteries. A high energy density leads to cost reductions as well.

For stationary batteries, the initial cost of storing electric energy and lifetime costs, including maintenance, are more important than energy and power density. Batteries for electric vehicles require low costs because the battery system is large.

Lithium-ion batteries (LIBs) have the highest performance in many respects among commercially available batteries. Such batteries are widely used as a power source of mobile IT devices, and they are currently starting to be used in HEVs, PHEVs, and electric vehicles. Lithium-ion batteries have superior features compared with other commercial batteries, but their performance cannot meet the growing requirements from the ever-expanding application of rechargeable batteries. Further, the various performance aspects of lithium-ion batteries are interrelated. As shown in Fig. 1.3, enhancements to energy density enhance safety concerns and costs and

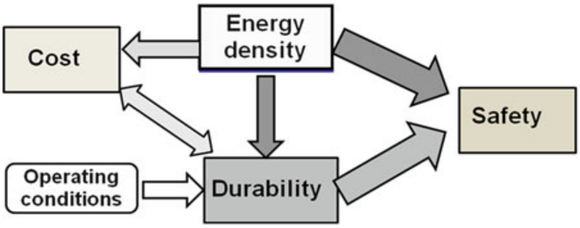

Fig. 1.3 Interrelated performance aspects of a lithium-ion battery

decreases battery life. Enhancements of energy density increase safety concerns and cost of battery systems and decrease battery life.

Inventing and producing batteries that satisfy all performance requirements represents a formidable challenge, and therefore batteries that fit their performances with the performances required for various applications are produced. For example, HEVs require a high power performance; thus, LIBs for HEVs are designed to enhance their power performance by making the composite active materials layer of negative and positive electrodes thinner using high-conductance electrolytes and separators.

New materials must enhance energy density, and much effort is devoted to developing new materials with high energy. There are two ways to enhance energy density: enhance the battery voltage or enhance capacity. Currently, the negative carbon electrode shows the extremely low potential and new negative electrode materials are directing to high-capacity materials, for example, lithium alloys, intermetallic materials, and conversion-type negative electrodes. There is a variety of positive electrode materials. Various kinds of high-voltage materials have been investigated, and sulfur and oxygen in air are attracting much attention as large-capacity positive materials.

Sodium-ion batteries are attractive from the viewpoints of cost and safety, though their energy density may be low. For example, the $Na_{0.44}MnO_2$/aq. Na_2SO_4/$NaTi_2(PO_4)_3$ system of Okada et al. uses no expensive elements then the cost is expected to be reduced [1].

What is a LIB? That depends on one's definition and what criteria one uses to define them. It is generally accepted that the first lithium-ion battery was commercialized by Sony in 1991. The concept of a rechargeable battery based on the shuttle reaction of lithium ions between negative and positive electrodes can be traced back at least to a paper by Scrosati et al. in 1980 [2]. They reported the charge–discharge performance of a Li_xWO_2/$LiClO_4$-PC/TiS_2 battery system. This system operates in the same manner as a C/$LiPF_6$-EC-DEC/$LiCoO_2$ system. There is a big difference between the two systems. The former can discharge first, but the latter requires charging before discharge. That is, the latter is produced in a stable discharged state, but the former is made in an active charged state. Thus, a lithium-ion battery may be defined as a rechargeable battery based on lithium-ion shuttle reactions prepared in a discharged state.

Historically, all practical rechargeable batteries were produced in an inactive state. The batteries became active through a first charging process (called formation). Present commercially available lithium batteries also fall into this category. This fact clearly shows the difficulty of processing rechargeable batteries, even a compared with primary batteries.

Insertion reactions have a long history in batteries; NiOOH is the typical insertion-extraction material of alkaline rechargeable batteries, and manganese oxide has been used as the positive electrode of primary lithium batteries.

Innovation in materials is, nevertheless, essential for making breakthroughs in LIBs. Further, post-lithium-ion batteries will be created using novel concepts in combination with innovations in their materials.

Rechargeable batteries are a hot topic in various sectors of society. Although lithium-ion batteries provide the highest performance among commercially available batteries, post-lithium-ion batteries may emerge in the next decade. Lithium-ion batteries, however, have superior features compared with other rechargeable batteries and will keep progress and be used long time like that lead-acid battery invented about 150 years ago is till widely used.

References

1. S.I. Park, I. Gocheva, S. Okada, J. Yamaki, J. Electrochem. Soc. **158**, A1067–1070 (2011)
2. M. Lazzari, B. Scrosati, J. Electrochem. Soc. **127**, 773–774 (1980)

Chapter 2

Positive Electrodes of Nano-Scale for Lithium-Ion Batteries (Focusing on Nano-Size Effects)

Jun-ichi Yamaki

Lithium-ion batteries are used as a power source for portable electric devices all over the world for their high power density and high discharge voltage, and they have begun to be used as a power source with high power for large electric equipment.

One of the most effective methods to improve power density is by the use of very fine cathode particles. We investigated a new excess-lithium method of preparing nano-sized $LiCoO_2$ powders. To begin with, lithium acetate and cobalt acetate are uniformly mixed by a molar ratio of 9, 13, or 21 to 1. The mixture is then calcined at 600 °C for 6 h. Finally, the obtained powders are washed with a large amount of water to remove impurities and then dried. Using this method, we obtained nano-sized spherical $LiCoO_2$ particles with a diameter of approximately 25 nm or needlelike $LiCoO_2$ particles with a diameter of approximately 5 nm and a length of approximately 60 nm. The discharge capacity of a Li/5 μm $LiCoO_2$ cell is 51 mAh g^{-1}, but when the nano-sized $LiCoO_2$ was used, the capacity increased to approximately 100 mAh g^{-1} in the same cycling conditions.

Cell performance was influenced not only by the size of the particles of the active materials, but also by other geometric factors such as the thickness of the electrode. Such inherent complications should be mainly due to the porous structure of the electrodes; the ohmic potential drop and mass transfer were very intricate, and there was no way to separate them. Some powerful methods are needed to review the experimental results methodically, which should contribute to the design of high-power batteries. It may be useful to simulate cell performance by calculation. Based on the program proposed by Newman's group, the discharge performance was investigated using $LiCoO_2$ particles of various sizes, ranging from 10 nm to 1 μm. The porosity that gave the largest capacity was different depending on the particle size of the active materials.

J. Yamaki (✉)
Dr. Engineering Office of Society-Academia Collaboration for Innovation, Kyoto University
Center for Advanced Science and Innovation, Gokasho, Uji, 611-0011 Japan
e-mail: yamaki@saci.kyoto-u.ac.jp

T. Osaka and Z. Ogumi (eds.), *Nanoscale Technology for Advanced Lithium Batteries*,
Nanostructure Science and Technology 182, DOI 10.1007/978-1-4614-8675-6_2,

The effect of cathode particle size on cell potential was investigated using a voltage prediction method based on the Coulomb potential created by the atoms of a cathode active material. $LiNiO_2$ was selected as a typical cathode of an ordered rock salt structure. From the calculation it was found that the voltage changed when the size became less than approximately 10 nm. The voltage increased with decreasing in-plane size and decreased when the number of layers was decreased.

2.1 Introduction

The technology for making materials into nano-sized particles has been used to improve remarkably the performance of nano-sized materials or allowed the discovery of new characteristics of materials. Therefore, the nanotechnology has been studied intensely in recent years. Nanotechnology can be applied to lithium-ion batteries, too. The performance of Li-alloy anodes can be improved using nano-sized particles of the alloys. For example, Li et al. [1] reported that nanostructured Sn-based electrodes showed improved rate capabilities relative to thin-film control electrodes prepared from the same material. Similarly, Larcher et al. [2] produced nano-sized α-Fe_2O_3 and reported that the discharge potential of the nanostructured α-Fe_2O_3 became higher than that of microstructured α-Fe_2O_3.

The reason for making the cathode materials of lithium-ion batteries from fine particles is to achieve high-powered output. Lithium-ion batteries are used as a power source for portable electric devices all over the world for their high power density and high discharge voltage, and they have begun to be used as a power source for large electric equipment, for instance, electric tools, hybrid electric vehicles (HEVs), and electric vehicles (EVs). However, of course, the batteries' safety issues must be considered carefully. The power output of lithium batteries is smaller than that of lead-acid batteries and nickel–hydrogen batteries, which are used as a high power source. One method to make high-power lithium-ion batteries is by the use of thin electrodes. Using a thin electrode, the surface area of the electrode becomes larger in a fixed volume of the battery. Therefore, the power of the battery increases. The other method is by the use of finer particles of cathode active materials. The finer the active materials are, the greater the diffusion of lithium in the cathode of the electrode if the electrodes weigh the same.

This chapter will explore the following four topics, which have been studied in my group:

1. Experimental study of the discharge performance of nano-sized $LiCoO_2$ cathode particles [3],
2. Theoretical study of the discharge performance of nano-sized $LiCoO_2$ cathode particles [4, 5],
3. The possibility of open circuit potential (OCP) change in nano-sized $LiNiO_2$ cathode particles [6],

2.2 Preparation of Nano-Sized $LiCoO_2$ Cathode Particles

Researchers have investigated some of the techniques used to make $LiCoO_2$ that are generally used for the cathode material of lithium-ion batteries for making nano-sized particles. Kumta et al. [7] mixed equimolar amounts of $LiCH_3COO \cdot 2H_2O$ and $Co(CH_3COO)_2 \cdot 4H_2O$ in water, and, following heat treatment at 400 °C, they obtained fine $LiCoO_2$ particles in a range of approximately 70 nm. However, this $LiCoO_2$ was the low-temperature polymorph of $LiCoO_2$ that is known to exhibit poor electrochemical behavior [8]. Sol–gel methods have also been tried. Peng et al. [9] mixed $LiCH_3COO$ and $Co(CH_3COO)_2$ (Co/Li = 1:1 atom ratio) with citric acid in ethylene glycol solution and heated the mixture at 140 °C to form a gel. They obtained approximately 30 nm of $LiCoO_2$ particles by calcining the gel at 750 °C. Yoon et al. [10] dissolved a stoichiometric amount of Li and Co acetate salts in distilled water and mixed them with an aqueous solution of acrylic acid; they obtained a clear viscous gel by heating the mixture at 70–80 °C for several hours. The precursor was calcined at 600–700 °C. Finally, they obtained approximately 300 nm of $LiCoO_2$ particles. Other techniques, for example, a spray drying method [11], a coprecipitation method [12], and a hydrothermal method [13], have resulted in $LiCoO_2$ particles of 200–700 nm, 20–100 nm, and 70–200 nm, respectively.

We focused on the report of Arai et al. [14], who used an excess-lithium method to synthesize $LiNiO_2$. However, their purpose was to obtain pure $LiNiO_2$, and they paid no attention to the rate capability of the fine $LiNiO_2$. In this section, we report a new method of synthesizing nano-sized $LiCoO_2$ particles using a method similar to that of Arai et al.

2.2.1 Experimental Setup

$LiCH_3COO \cdot 2H_2O$ (Wako Pure Chemical Industries, Osaka, Japan) and $Co(CH_3COO)_2 \cdot 4H_2O$ (Wako Pure Chemical Industries, Osaka, Japan), with molar ratios of 5:1, 9:1, 13:1, and 21:1, were dissolved in deionized water, and the solution was heated at 230 °C under stirring and then dried to form a mixed precursor in atmosphere. The dried product obtained was then heat treated in a furnace using an alumina crucible at 600 °C for 6 h. After heat treatment, a gray lump with a sponge-like structure was obtained. This product was washed with a large amount of water using a centrifugal separator (5200, KUBOTA) to separate Li_2CO_3 and $LiCoO_2$ after grinding the gray product in an agate mortar. After washing, the black powder obtained was dried in an incubator at 80 °C for 12 h in atmosphere. Then the product was ground again, and fine powders were obtained. The gray products and the black powders were analyzed for their structure using X-ray diffraction (RINT2100HLR/PC, Rigaku, Tokyo, Japan). The morphology and microstructure of the powders were examined using a scanning electron microscope (JSM-6340 F, JEOL, Tokyo, Japan).

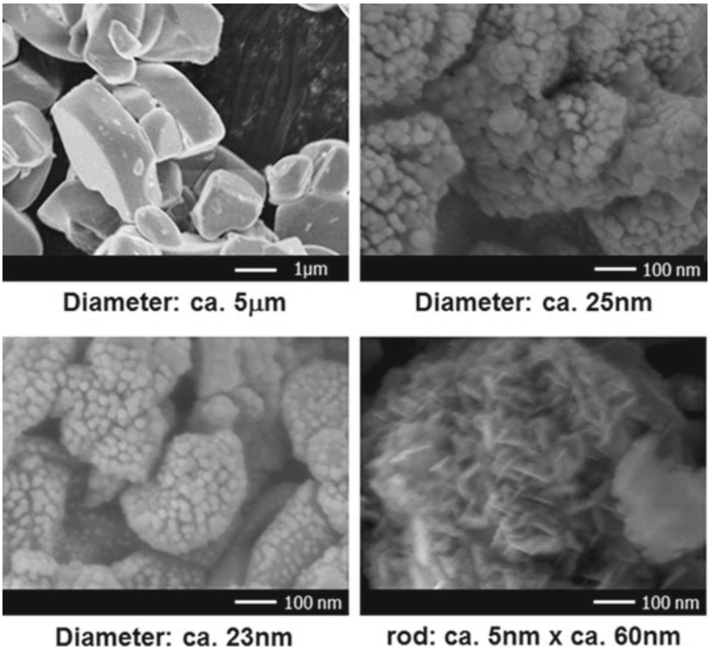

Fig. 2.1 SEM images of $LiCoO_2$ powders obtained by conventional solid synthesis (5 μm) and made by calcining mixtures of lithium acetate and cobalt acetate with molar ratios of 9:1(25 nm), 13:1 (23 nm), and 21:1 (5 × 60 nm), respectively

2.2.2 *Results and Discussion*

Figure 2.1 shows SEM images of $LiCoO_2$ powders obtained by conventional solid synthesis (5 μm) and made by calcining mixtures of lithium acetate and cobalt acetate with molar ratios of 9:1(25 nm), 13:1 (23 nm), and 21:1 (5 × 60 nm), respectively, which were washed with a large amount of water. $LiCoO_2$ particles obtained by mixing lithium acetate and cobalt acetate at a molar ratio of 13 to 1 are very small, approximately 23 nm, and uniform. The primary particles formed a larger secondary particle approximately 500 nm in size. From these results we concluded that nano-sized $LiCoO_2$ powders can be obtained when $LiCH_3COO \cdot 2H_2O$ is added nine to $Co(CH_3COO)_2 \cdot 4H_2O$ in molar ratio. Unlike the $LiCoO_2$ particles obtained by mixing a Li compound and a Co compound at a molar ratio of 9 to 1 or 13 to 1, needlelike particles approximately 5 nm in diameter and 60 nm long appeared in the micrograph when lithium acetate and cobalt acetate were at a molar ratio of 21:1. Needlelike $LiCoO_2$ particles have more surface area than do spherical particles, so the former are more suitable than the latter for a cathode material of lithium batteries for a HEV and an EV. We do not yet know why the particles became needlelike. It is likely that a lot of lithium carbonate affected the grain growth of the nano-sized $LiCoO_2$.

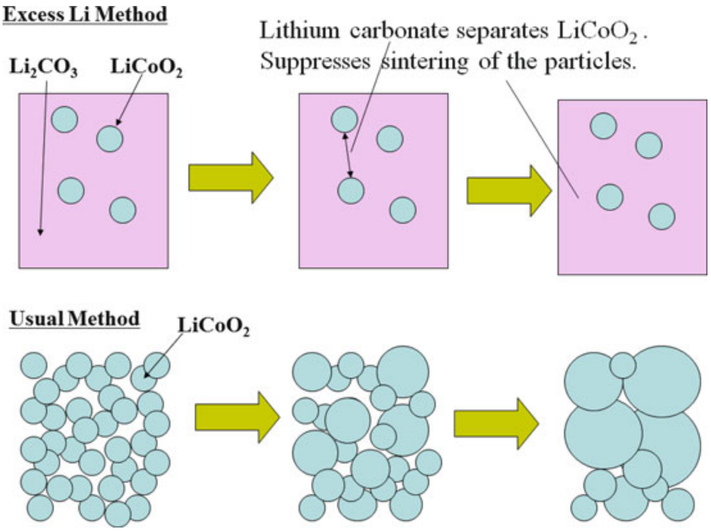

Fig. 2.2 Mechanism of excess Li method

The mechanism for obtaining nano-sized $LiCoO_2$ particles using the excess-lithium method is very simple. First, a large amount of $LiCH_3COO \cdot 2H_2O$ and a small quantity of $Co(CH_3COO)_2 \cdot 4H_2O$ are mixed uniformly with water. Next, the dried mixture is calcined. With calcination, $LiCoO_2$ is synthesized and any excess lithium acetate becomes lithium carbonate simultaneously. At that time, the excess lithium carbonate covers and separates the $LiCoO_2$ particles, and it suppresses the growth of $LiCoO_2$ particles, as shown in Fig. 2.2. After the lithium carbonate is removed, very fine $LiCoO_2$ powders are obtained. It is important to mix the lithium acetate and cobalt acetate uniformly and to calcine the mixture below the temperature of the melting point of lithium carbonate.

The cell performance was investigated to demonstrate the high rate capability of fine cathode particles.

2.3 Experimental Study of Discharge Performance of Nano-Sized $LiCoO_2$ Cathode Particles

2.3.1 Experimental Setup

The obtained powders are washed with a large amount of water to remove impurities (for example Li_2CO_3) and then dried. Without the washing process, the capacity of the nano-sized $LiCoO_2$ would be very small.

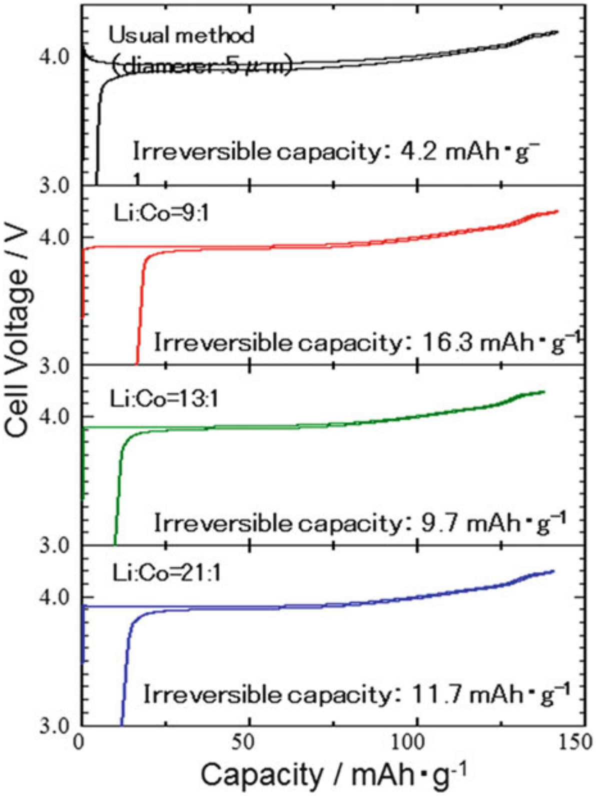

Fig. 2.3 First charge–discharge cycle of $LiCoO_2$ samples obtained using excess-lithium method (voltage range: 4.2–3.0 V, current density: 0.1 mA cm^{-2})

The electrochemical properties of $LiCoO_2$ powders were investigated using a Li/1 M $LiPF_6$ EC (ethylene carbonate) + DMC (dimethyle carbonate) (1:1 in volume)/ $LiCoO_2$ cell. A composite cathode was prepared by mixing the $LiCoO_2$ powder, acetylene black (AB), and polyvinylidene fluoride (PVDF) at a weight ratio of 90:5:5 in *n*-methylpyrrolidinone (NMP) and then coating the resultant paste on an Al foil. The coated cathode sheet was dried, pressed, and cut into samples 15 mm in diameter. Celgard 3501 (Celanese, Texas, United States) was used as a separator. The cell elements were fabricated into coin-type cells (20 mm in diameter, 3.2 mm thick) in a dry box filled with Ar gas. The cells were cycled using a cell cycler (HJSM6, HOKUTO DENKO, Tokyo, Japan) at a constant current density of 12 or 24 Ma cm^{-2} between 4.2 and 2.6 V at 25 °C.

2.3.2 Results and Discussion

The first charge–discharge cycle of the $LiCoO_2$ samples obtained using the excess-lithium method is shown in Fig. 2.3. The irreversible capacity was larger when

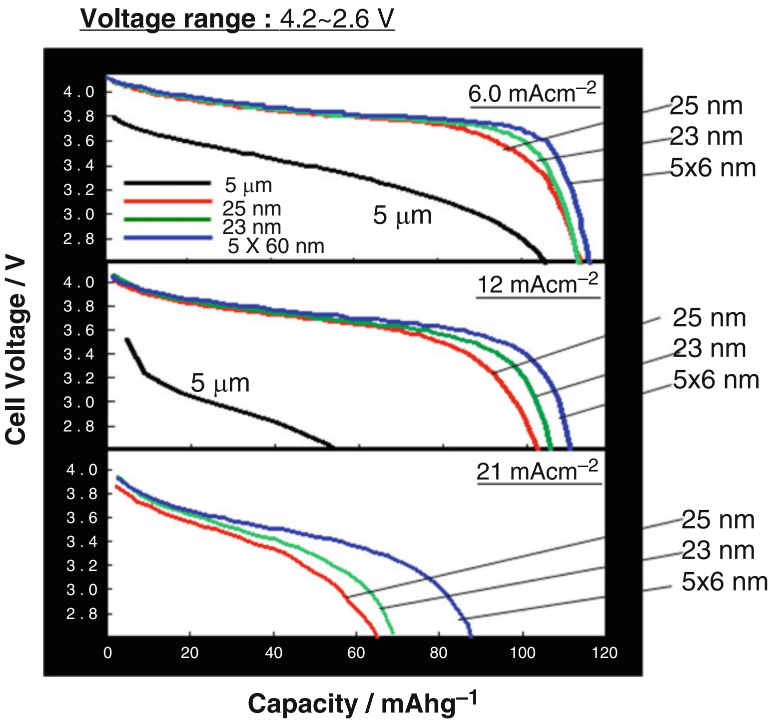

Fig. 2.4 Discharge profiles of large and nano-sized $LiCoO_2$ powders at first discharge

finer $LiCoO_2$ was used because of the larger surface area, which caused greater SEI formation.

Figure 2.4 shows the discharge profiles of large and nano-sized $LiCoO_2$ powders at the first discharge. The current densities are 6.0, 12, and 20 $mAcm^{-2}$. The capacity increased with a decrease in particle size of $LiCoO_2$.

The cathode electrode densities including $LiCoO_2$ particles obtained by mixing lithium acetate and cobalt acetate at a molar ratio of 9, 13, and 21 to 1 are 1.60, 1.47, and 1.52 g cm^{-3}, respectively. The cathode density including $LiCoO_2$ particles obtained by the usual solid phase method is 1.41 g cm^{-3}. The cathode thickness of all cells is approximately 80 μm.

Figure 2.5 shows the rate capability. After washing with water, nano-$LiCoO_2$ showed a larger capacity due to the removal of Li_2CO_3 from the surface and the separation of primary particles.

The effect of the amount of AB was also investigated. Three kinds of electrodes with 5 % of AB ($LiCoO_2$: AB : PVdF = 90 : 5 : 5), 10 % of AB ($LiCoO_2$: AB : PVdF = 85 : 10 : 5), and 15 % of AB ($LiCoO_2$: AB : PVdF = 75 : 15 : 5) were prepared. The result is shown in Fig. 2.6. Cathode utilization increased by adding a larger amount of AB.

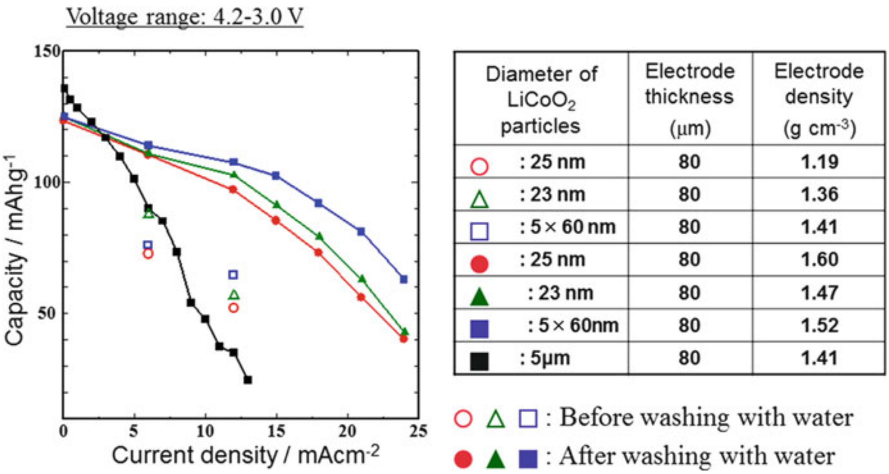

Diameter of $LiCoO_2$ particles	Electrode thickness (μm)	Electrode density (g cm^{-3})
○ : 25 nm	80	1.19
△ : 23 nm	80	1.36
□ : 5× 60 nm	80	1.41
● : 25 nm	80	1.60
▲ : 23 nm	80	1.47
■ : 5× 60nm	80	1.52
■ : 5μm	80	1.41

○ △ □ : Before washing with water
● ▲ ■ : After washing with water

Fig. 2.5 Rate capability of large and nano-sized $LiCoO_2$ powders

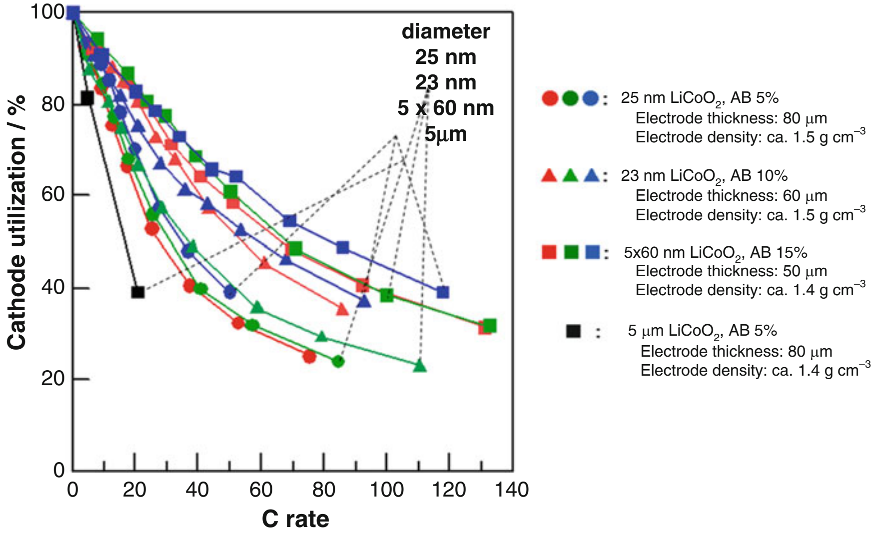

Fig. 2.6 Dependence of amount of AB in electrode on discharge capacity

2.4 Theoretical Study of Discharge Performance of Nano-Sized $LiCoO_2$ Cathode Particles

We prepared nano-sized $LiCoO_2$ particles by an excess-lithium method, and the rate performance was improved using the resultant nano-sized $LiCoO_2$ compared with that using micron-sized $LiCoO_2$ powder [3, 15]. However, the cell performance was

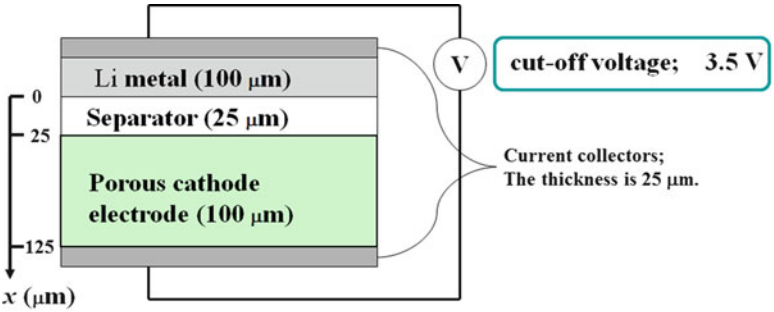

Fig. 2.7 Cell model for calculation

influenced by the particle size of the active materials and by other geometric factors such as the thickness of the electrode. Such inherent complications should be mainly due to the porous structure of the electrodes; the ohmic potential drop and mass transfer were very intricate, and there was no way to separate them. Some powerful methods are needed to review the experimental results methodically, which should contribute to the design of high-power batteries. It might be useful to simulate cell performance by calculation. Doyle et al. proposed a mathematical model of a Li/insertion electrode cell using a porous electrode theory and reported the simulation results [16, 17]. Newman et al. studied the charge/discharge characteristics of a dual-insertion cell of C/$LiMn_2O_4$ by numerical calculation and compared them with experimental data [18, 19].

In this session, the discharge characteristics of a Li/Li_yCoO_2 cell were studied by numerical calculation using the program proposed by Newman et al. [20].

2.4.1 Model Development

The program used (dual. f, version 4.0) is freely available from Newman's group through their Web site. The program is based on a cell model consisting of a porous positive electrode, a separator, and a lithium metal negative electrode. The porous electrode was composed of sphere-shaped particles of active materials, inert conductive additives, and polymer binder. The void space in the electrode was filled with an electrolyte solution. In the model, the one-dimensional transport of lithium-ion from the negative electrode to the positive electrode through the separator was considered, and the electrochemical insertion of lithium ion was assumed to occur at all points on the active materials. The program was composed of six differential equations, which are described elsewhere in detail [18, 20].

In the present work, $LiCoO_2$ was used as the active material for the porous positive electrode, and the negative electrode was Li metal.

The cell model is shown schematically in Fig. 2.7. The thickness of the separator and the positive electrode were set to 25 and 100 μm, respectively. The surface

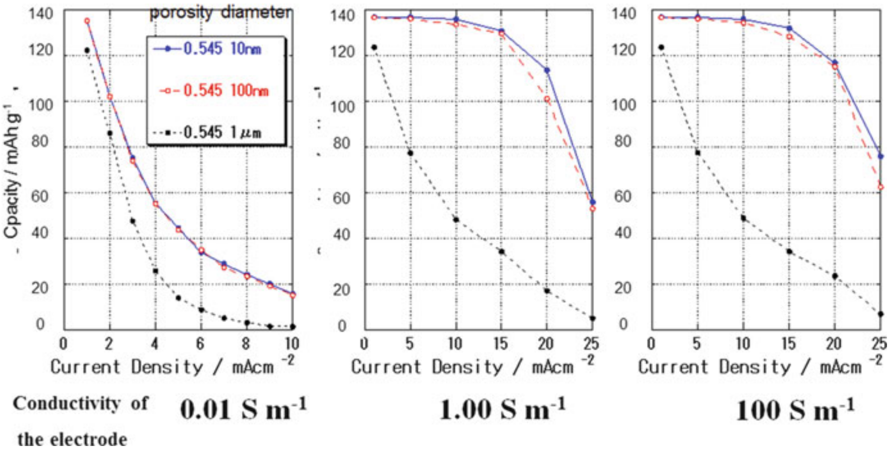

Fig. 2.8 Effect of particle size of $LiCoO_2$ on discharge capacity

of the Li negative electrode was defined as $x = 0$. The content of the $LiCoO_2$ active material is 80 % [active material $LiCoO_2$: (conductor (AB) + binder (PVdF)) = 80:20(wt.%)].

The diffusion coefficient of lithium ions within $LiCoO_2$ particles and a standard rate constant (k^0) were determined based on the literature [21]. The former was assumed to be constant at 1.0×10^{-16} m^2 s^{-1}. The latter was evaluated to be 1.5×10^{-6} A $mol^{-3/2}$ $m^{9/2}$ from the value for charge transfer resistance (R_{ct}).

The electrode density was changed to be 1.0, 1.5, 2.0, 2.5, and 3.0 g cm^{-3}; these values correspond to electrode porosities of 0.772, 0.659, 0.545, 0.431, and 0.318, respectively. The particle size was changed from 10 to 1000 nm and the conductivity of the electrode from 0.01 to 100 S m^{-1}.

2.4.2 Results and Discussion

The effect of the particle size of $LiCoO_2$ is shown in Fig. 2.8. The porosity used was 0.545. The discharge capacity increased as the particle size decreased.

Figures 2.9, 2.10, and 2.11 show the variation in discharge capacity with the current density at various porosity values ranging from 0.318 to 0.772. The electrode conductivity used in Figs. 2.9, 2.10, and 2.11 were 0.01, 1.00, and 100 S m^{-1}, respectively. The discharge capacity tended to increase with a decrease in porosity when the electrode conductivity was 0.01 S m^{-1} (Fig. 2.9). When the electrode conductivity was 1.00 S m^{-1} (Fig. 2.10), the porosity at which a maximum capacity could be obtained differed depending on the particle size of $LiCoO_2$; the particle size of 10 nm gave the largest capacities when the porosity was 0.545, and the corresponding values were 0.431 and 0.318 for 100 and 1 μm, respectively. In the case

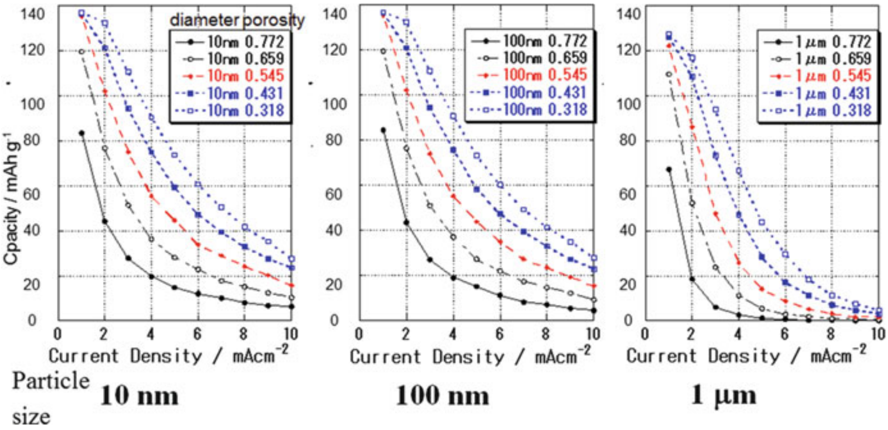

Fig. 2.9 Effect of porosity (electrode conductivity: 0.01 S m^{-1})

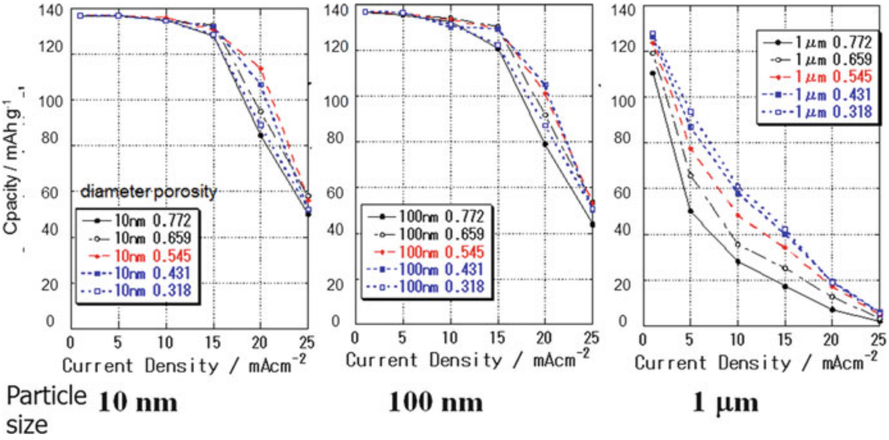

Fig. 2.10 Effect of porosity (electrode conductivity: 1.00 S m^{-1})

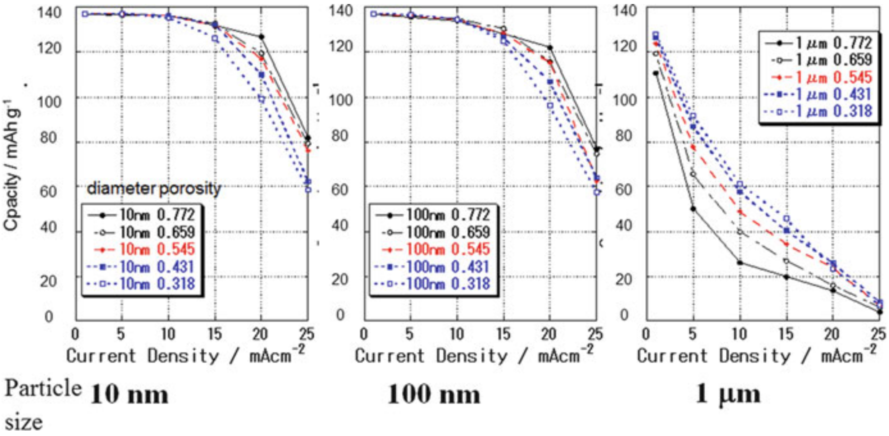

Fig. 2.11 Effect of porosity (electrode conductivity: 100 S m^{-1})

Fig. 2.12 Shape of $LiNiO_2$ cathode when a similar shape of unit cell was maintained

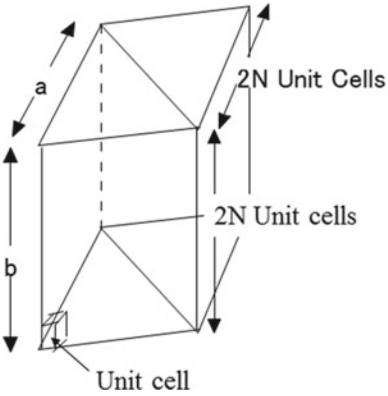

of 100 S m^{-1} (Fig. 2.11), the corresponding values of the maximum capacity were 0.772, 0.772, and 0.318 for 10, 100, and 1, respectively. These results suggest that there should be an optimal value for the porosity of a porous electrode to enhance the rate performance of batteries.

2.5 The Possibility of Open Circuit Potential Changes in Nano-Sized $LiNiO_2$ Cathode Particles

Recently, several studies have been published predicting the cell voltage of cathode active materials in lithium ion cells based on first-principles quantum chemistry [22–25]. The internal energy was calculated using first-principles quantum chemistry, and the Gibbs function was obtained. The researchers in these studies discussed phase separation using the Gibbs function. We studied voltage using a simpler method [26–28] – based on the Coulomb potential created by the atoms of a cathode active material.

We used this simple method to investigate the effect of cathode particle size on cell potential. $LiNiO_2$ was selected as a typical cathode of an ordered rock salt structure whose structure is similar to that of $LiCoO_2$. The calculation of voltage was performed for E_{int} of $LiNiO_2$ and $Li_{0.75}NiO_2$. The two-phase voltage from $x=1$ to 0.75 (Li_xNiO_2) was also calculated. The most reliable voltage is E_{int} of $LiNiO_2$. In this calculation, the outside layers are Li layers. To increase the size of $LiNiO_2$ from a unit cell, we examined three different cases.

2.5.1 *Increasing the Size of $LiNiO_2$ While Maintaining a Similar Shape of the Unit Cell*

The shape of a $LiNiO_2$ cathode is shown in Fig. 2.12 when a similar shape of the unit cell was maintained. The voltage increased as the size of $LiNiO_2$ decreased, as

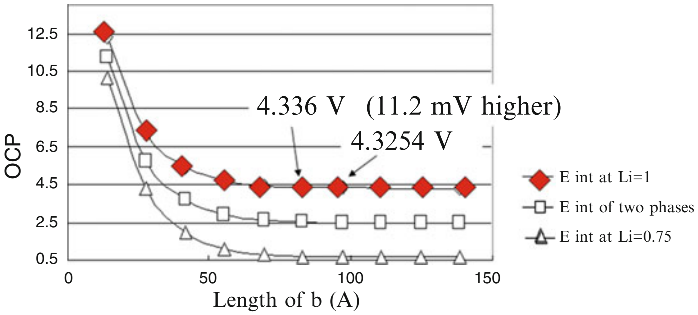

Fig. 2.13 Open circuit potential when a similar shape of unit cell was maintained

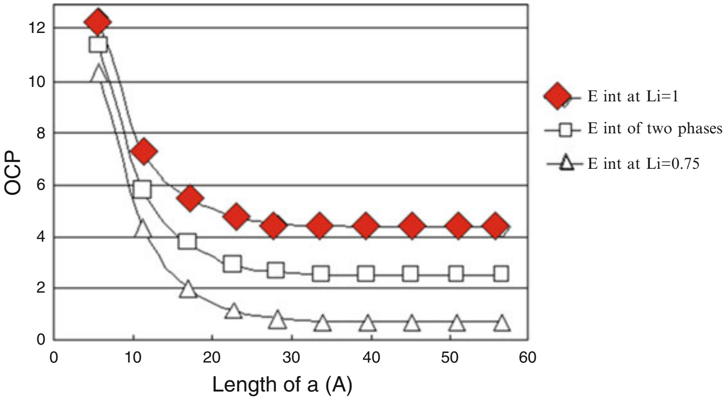

Fig. 2.14 Open circuit potential changing in-plane area and retaining the number of layers (20 layers)

shown in Fig. 2.13. The E_{int} of the $LiNiO_2$ increased very rapidly from 4.3 to 12.3 V as the size of $LiNiO_2$ decreased. The E_{int} of the $LiNiO_2$ was 4.3254 V at $b=139$ A and 4.3366 V at $b=97$ A. This means that the E_{int} of the $LiNiO_2$ increased for 11.2 mV as the size decreased from $b=139$ to 97 A. It is not very difficult to measure the 10 mV difference. Therefore, if we synthesize 100 A (10 μm) particles of $LiNiO_2$ experimentally, then we can check the voltage change. Experiments are currently under way to prove our theory.

2.5.2 Increasing the Size of $LiNiO_2$ While Changing the In-Plane Area and Keeping the Number of Layers (20 Layers)

The voltage increased as the size of the $LiNiO_2$ decreased, as shown in Fig. 2.14. The E_{int} of the $LiNiO_2$ increased very rapidly from 4.6 to 12.6 V as the size of the $LiNiO_2$ decreased.

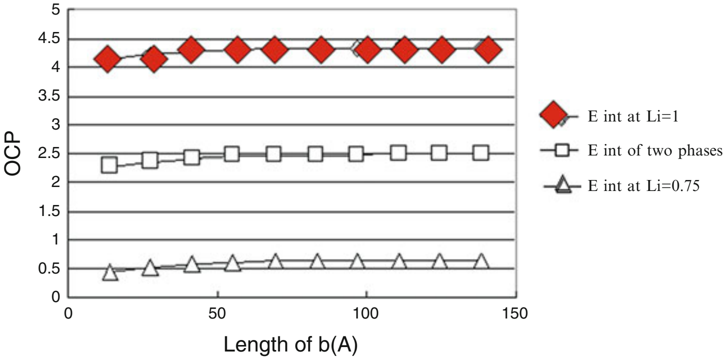

Fig. 2.15 Open circuit potential maintaining in-plane area (20×20 unit cells) and changing the number of layers

2.5.3 Increasing the Size of $LiNiO_2$ While Maintaining the In-Plane Area (20×20 Unit Cells) and Changing the Number of Layers

The voltage decreased slightly as the size of the $LiNiO_2$ decreased, as shown in Fig. 2.15. The E_{int} of the $LiNiO_2$ decreased from 4.3 to 4.1 V as the size of the $LiNiO_2$ decreased.

2.5.4 Discussion

Based on the results of this study, we conclude that the voltage changes when the size of $LiNiO_2$ becomes less than approximately 10 nm. The voltage increased as we decreased the in-plane size and decreased as we decreased the number of layers. From a practical point of view, the decrease in voltage is not good. We conclude, therefore, that reducing the number of layers is not a good way to synthesize nano-sized $LiNiO_2$. However, we must find a new electrolyte that has a higher oxidation potential when a high-voltage cathode is used.

2.5.5 Conclusion

We investigated a new method, the excess-lithium method, of preparing nano-sized $LiCoO_2$ powders. Using this method, we obtained nano-sized spherical $LiCoO_2$ particles with a diameter of approximately 25 and 23 nm at Li/Co molar ratios of 9/1 and 13/1, respectively. Needlelike $LiCoO_2$ particles with a diameter of approximately 5 nm and a length of approximately 60 nm appeared at Li/Co = 21/1. The rate capability of the Li cells was significantly improved using cathodes made of nano-sized $LiCoO_2$ compared with that of cathodes made with the usual 5 μm $LiCoO_2$.

Based on the program proposed by Newman's group, the discharge characteristics of a Li/Li_yCoO_2 cell were simulated by numerical calculations. The discharge performance was investigated using $LiCoO_2$ particles of various sizes, ranging from 10 nm to 1 μm. The porosity that gave the largest capacity differed depending on the particle size of the active materials.

We studied the voltage using a simpler method, based on the Coulomb potential created by the atoms of a cathode active material. Based on the results of this study, we conclude that the voltage changes when the size of $LiNiO_2$ becomes less than approximately 10 nm. The voltage increased as we decreased the in-plane size and decreased as we decreased the number of layers.

Acknowledgments This work was supported by CREST of the Japan Science and Technology Agency.

References

1. N. Li, C.R. Martin, B. Scrosati, J. Power Sources **97–98**, 240 (2001)
2. D. Larcher, C. Masquelier, D. Bonnin, Y. Chabre, V. Masson, J.B. Leriche, J.M. Tarascon, J. Electrochem. Soc. **150**(1), 133 (2003)
3. T. Kawamura, M. Makidera, S. Okada, K. Koga, N. Miura, J. Yamaki, J. Power Sources **146**, 27 (2005)
4. T. Doi, H. Fukudome, S. Okada, J. Yamaki, J. Power Sources **174**, 779 (2007)
5. J. Yamaki, Electrochemistry **78**(12), 988 (2010)
6. J. Yamaki, M. Makidera, T. Kawamura, M. Egashira, S. Okada, J. Power Sources **153**, 245 (2006)
7. P.N. Kumta, D. Gallet, A. Waghray, G.E. Blomgren, M.P. Setter, J. Power Sources **72**, 91 (1998)
8. E. Rossen, J.N. Reimers, J.R. Dahn, Solid State Ion. **62**, 53 (1993)
9. Z.S. Peng, C.R. Wan, C.Y. Jiang, J. Power Sources **72**, 215 (1998)
10. W.S. Yoon, K.B. Kim, J. Power Sources **81–82**, 517 (1999)
11. Y. Li, C. Wan, Y. Wu, C. Jiang, Y. Zhu, J. Power Sources **85**, 294 (2000)
12. H. Chen, X. Qiu, W. Zhu, P. Hagenmuller, Electrochem. Commun. **4**, 488 (2002)
13. A. Burukhin, O. Brylev, P. Hany, B.R. Churagulov, Solid State Ion. **151**, 259 (2002)
14. H. Arai, S. Okada, H. Ohtsuka, M. Ichimura, J. Yamaki, Solid State Ion. **80**, 261 (1995)
15. T. Tsuji, T. Kakita, T. Hamagami, T. Kawamura, J. Yamaki, M. Tsuji, Chem. Lett. **33**, 1136 (2004)
16. M. Doyle, T.F. Fuller, J. Newman, J. Electrochem. Soc. **140**, 1526 (1993)
17. M. Doyle, J. Newman, J. Appl. Electrochem. **27**, 846 (1997)
18. T.F. Fuller, M. Doyle, J. Newman, J. Electrochem. Soc. **141**, 1 (1994)
19. P. Arora, M. Doyle, A.S. Gozdz, R.E. White, J. Newman, J. Power Sources **88**, 219 (2000)
20. J. Newman, K.E. Thomas-Alyea, *Electrochemical Systems*, 3rd edn. (Wiley–Interscience, Hoboken, 2004)
21. Y.H. Rho, K. Kanamura, J. Electrochem. Soc. **151**, A1406 (2004)
22. E. Deiss, A. Wokaun, J.-L. Barras, C. Daul, P. Dufek, J. Electrochem. Soc. **144**, 3877 (1997)
23. M.K. Aydinol, A.F. Kohan, G. Ceder, J. Power Sources **68**, 664 (1997)

24. C. Wolverton, A. Zunger, J. Electrochem. Soc. **145**, 2424 (1998)
25. A. Van der Ven, M.K. Aydinol, G. Ceder, J. Electrochem. Soc. **145**, 2149 (1998)
26. J. Yamaki, M. Egashira, S. Okada, J. Power Sources **97–98**, 349 (2001)
27. J. Yamaki, M. Egashira, S. Okada, J. Power Sources **90**, 116 (2000)
28. J. Yamaki, M. Egashira, S. Okada, J. Electrochem. Soc. **147**, 460 (2000)

Chapter 3
Nano Aspects of Advanced Positive Electrodes for Lithium-Ion Batteries

Kuniaki Tatsumi

3.1 Introduction

In the last two decades, demand for rechargeable batteries with high specific energy or high energy density has been increasing for applications in portable electronic devices such as mobile phones (feature phones and smartphones), notebook personal computers (PCs), and tablet PCs. Since these electronic devices possess relatively large and bright display panels (liquid-crystal or organic electroluminescence), smaller and lighter rechargeable batteries are required to lengthen the devices' battery life. Furthermore, the need is rapidly increasing for electrochemical power sources applied to electric vehicles (EVs), hybrid electric vehicles (HEVs), and plug-in HEVs (PHEVs). In particular, the European Union (EU) CO_2 emission regulation proposed for 2020 has made a strong impact on future automotive power trains, and EVs and PHEVs are thought to be indispensable for meeting this regulation.

Concerning applications to vehicles, required specifications are often much more stringent than those for portable electronic devices. In particular, the calendar life favorable to vehicle application A calendar life of more than 10 years, which favors vehicles, is much longer than the calendar life of electronic devices. Hence, much effort has been devoted to understanding the degradation mechanisms that limit the calendar life of lithium-ion cells [1–18]. In recent years, it has been shown that changes at the nano-surface region of positive electrode materials play important roles in the power fading of lithium-ion batteries. From the viewpoint of lithium insertion/deinsertion of positive electrode materials, nano-surface effects on power fading are not surprising but rather reasonable. However, the nano-surface region of a material is generally too thin to be examined; conventional analysis methods are often insufficient to highlight such a shallow area.

K. Tatsumi (✉)
Research Institute for Ubiquitous Energy Devices, National Institute of Advanced Industrial Science and Technology (AIST), 1-8-31 Midorigaoka, 563-8577 Ikeda, Osaka, Japan
e-mail: tatsumi-kuniaki@aist.go.jp

T. Osaka and Z. Ogumi (eds.), *Nanoscale Technology for Advanced Lithium Batteries*, Nanostructure Science and Technology 182, DOI 10.1007/978-1-4614-8675-6_3,

This chapter focuses on the nano-surface area of positive electrode materials as a typical feature of the nano aspect of positive electrodes, and research results on the nano surface of positive electrode materials are reviewed. Moreover, nano-surface modification methods of positive electrode materials are summarized.

3.2 Interphase Between Positive Electrode Materials and Electrolytes

Solid-electrolyte interphase (SEI) [19] is a very important and fundamental model to explain how metallic lithium and lithiated negative electrodes, for example graphite and carbon, work as electrochemical electrodes in nonaqueous liquid electrolytes because these electrode materials instantly reduce and decompose electrolyte solutions. While the SEI works as a passivating layer between the electrode and the electrolyte, the SEI must pass through a Li^+ cation between the two phases (a negative electrode material and an electrolyte) as a Li^+-cation conductor. A SEI on negative electrodes at an electrochemical potential lower than approximately 1 V (versus Li^+/Li) is detectable by scanning electron microscope (SEM), and the chemical states of the SEI are examined by various spectroscopic methods such as Fourier transform infrared spectroscopy [20–34] and X-ray photoelectron spectroscopy [35–38]. Although the composition of SEIs on lithium or lithiated negative electrode materials lower than approximately 1 V is dependent on at least the type of negative electrode material, the composition of the electrolyte, and temperature, common components of SEIs include, for example, $(CH_2OCO_2Li)_2$, $ROCO_2Li$, Li_2CO_3, ROLi, LiF, and Li_2O [39].

Concerning the interface of positive electrode materials for lithium and lithium-ion cells versus electrolytes, even in the early stage of research on oxide positive electrode materials, a surface-layer model for positive electrode materials was proposed. In 1985, for example, Thomas et al. reported that electrochemical alternating current (AC) impedance spectroscopy results could be explained by a surface-layer model of $LiCoO_2$ electrodes [40]. They speculated that $LiCoO_2$ particles were covered with a surface film that was a Li^+-cation-conducting solid electrolyte consisting of polymers. Furthermore, they presented a high-resolution transmission electron micrograph of a cross section of a $LiCoO_2$ particle covered with some amorphous materials approximately 3 nm thick as evidence for their surface-layer model. However, a surface-layer or passivating film model on positive electrodes had not been related to the SEI model for negative electrodes because the SEI is thought to be formed by cathodic reduction of electrolytes on negative electrodes.

Since the late 1990s, surface phenomena of positive electrodes have become one of the most important issues for understanding the rate capability and power fades of positive electrode materials. Electrochemical impedance spectroscopic analysis of lithium insertion/deinsertion positive electrode materials, such as $LiCoO_2$, $LiNi_{1-x}Co_xO_2$, and $LiMn_2O_4$, has indicated the existence of a surface layer or surface film on positive electrode materials. The surface chemistry of positive electrode

Table 3.1 Chemical composition of surface layers on various positive electrode materials

Positive electrode material	Electrolyte	Detected chemical species of surface layer on positive electrode materials	Reference
$LiNiO_2$	$LiAsF_6$, $LiPF_6$, $LiC(SO_2CF_3)_3$/EC + DMC	Li_2CO_3, $ROCO_2Li$, $ROLi$, poly carbonates, LiF	[43]
$LiNi_{0.8}Co_{0.2}O_2$	$LiPF_6$/EC + DEC	Li_2CO_3, $ROCO_2Li$, poly carbonates, Li_xPF_y, $Li_xPF_yO_z$, LiF	[5]
$LiNi_{1-y-z}Co_yAl_zO_2$	$LiPF_6$/PC + DMC	Li_2CO_3, $ROCO_2Li$, polycarbonates, LiF	[13, 14]
	$LiPF_6$/EC + EMC	$ROCO_2Li$, Li_xPF_y, $Li_xPF_yO_z$, LiF	[11]
	$LiPF_6$/EC + DMC	Li_2CO_3	[44]
$LiMn_{1/2}Ni_{1/2}O_2$	$LiPF_6$/EC + DMC	Li_2CO_3, LiF	[45]
$LiMn_{1/3}Ni_{1/3}Co_{1/3}O_2$	$LiPF_6$/EC + DMC	Li_2CO_3, $ROCO_2Li$, polycarbonates	[18]
$LiMn_2O_4$	$LiAsF_6$, $LiPF_6$, $LiC(SO_2CF_3)_3$/EC + DMC	Li_2CO_3, $ROCO_2Li$, $ROLi$, polycarbonates, LiF	[43]
	$LiPF_6$, $LiBF_4$/EC + DMC	Polyether (PEO), $ROCO_2Li$, Li_2CO_3, P_2O_5, LiF	[42]
	$LiPF_6$/EC + DMC	LiF	[46]
$LiMn_{1.5}Ni_{0.5}O_4$	$LiPF_6$/EC + DEC	$Li_xP_yOF_z$, Li_2CO_3, LiF, $ROCO_2M$, $(CH_2O)_n$	[47]
$LiMn_{1.6}Ni_{0.4}O_4$	$LiPF_6$/EC + PC + DMC	LiF, organic compounds with $-CH_2$, C–O, O = C–O	[48]
$LiFePO_4$	$LiPF_6$/EC + DMC	very small amount of Li_2CO_3	[49]

materials has also been investigated by the same experimental techniques that were applied to characterize the composition and properties of SEIs on graphite or carbon negative electrode materials [41–43]. The chemical species of surface films on positive electrode materials are summarized in Table 3.1.

3.3 Transforming the Nano-Surface Structure of Positive Electrode Materials with Degradation

In the 1990s, the rate capability was not a very important requirement for lithium-ion batteries because almost all lithium-ion cells at that time were being used in portable electronic devices. On the other hand, HEVs, for instance, require rechargeable batteries possessing a rate capability 10 times greater than that of portable electronic devices. For such applications, power fading is one of the most important issues to determine the end of life of rechargeable batteries. Since lithium-ion cells have been recognized as promising candidates as power sources for HEVs, the power fade of lithium-ion cells has been a very important issue to be resolved.

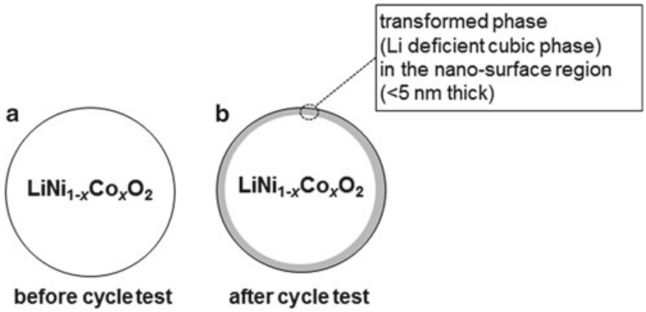

Fig. 3.1 Schematic representation of formation of transformed phase in nano-surface region of LiNi1-$_x$Co$_x$O$_2$-system positive electrode materials following charge–discharge cycle test

As mentioned in the previous section, electrochemical impedance spectroscopic analyses have indicated that the power fade (or increase in cell impedance) of lithium-ion cells with a conventional cell chemistry (carbon/graphite negative electrodes and lithium Ni-Co or Ni-Co-Al oxide positive electrode materials) is primarily due to a significant increase in the charge-transfer resistance in positive electrode materials [4, 50]. In contrast to the SEI of negative electrode materials, almost all surface films formed on positive electrode materials during the charge–discharge cycle are much thinner than the SEI on negative electrode materials. In addition, the chemical components of surface films on positive electrode materials are almost the same as those of the SEI on negative electrode materials. Therefore, surface films on positive electrode materials are not thought to be a major contributor to increases in the charge-transfer resistance of positive electrode materials.

To explicate the cause of the charge-transfer resistance rise of positive electrode materials, the surface of the materials has been studied. In particular, Li(NiCo)O_2 systems have been studied by several groups [51–54] because such systems, along with spinel manganese oxide systems, have been shown to be among the most promising candidate positive electrode materials of lithium-ion cells for vehicle applications. In 2003, Abraham et al. reported that a “modified” phase transformed from the layered structure of a $LiNi_{0.8}Co_{0.2}O_2$ positive electrode material was detected in the nano-surface region of 5 nm from the surface of $LiNi_{0.8}Co_{0.2}O_2$ particles following cycle tests by means of oxygen K-edge X-ray absorption spectroscopy (XAS) in the total electron yield (TEY) mode, high-resolution transmission electron microscopy (HRTEM), nanoprobe diffraction, and electron energy loss spectroscopy (EELS) [6]. Other research groups have also detected a transformed phase in the nano-surface region of a Li(NiCoAl)O_2 particle (Fig. 3.1) using XAS in the TEY mode and scanning TEM methods [52–58].

The crystal structure of the transformed phase is not thought to be a layered structure (R-3 m) but a lithium-deficient NiO-type cubic structure using nanoprobe diffraction and O K-edge XAS in the TEY mode. Since this transformed phase is thought to have no or very poor lithium-ion conductivity, area-specific impedance of the positive electrode materials should increase with increases in the transformed phase. Shikano et al. reported that the formation of a transformed phase in the nano-surface area also occurs in $LiNi_{1/3}Mn_{1/3}Co_{1/3}O_2$ positive electrode materials [18].

3.4 Coating Technology for Positive Electrode Materials

Surface film formation on a positive electrode material results from side reactions of an electrolyte. In addition, transformed phase formations in the nano-surface region of positive electrode materials are also thought to be related to side reactions between electrolytes and positive electrode materials. To suppress such side reactions between positive electrode materials and electrolytes, various surface coatings on positive electrode materials have been proposed and developed [59, 60]. The aim of surface coatings is mainly to modify surface chemistry [61, 62] or provide physical protection shields [63, 64]. Table 3.2 summarizes surface coating materials on typical positive electrode materials for lithium-ion batteries.

Many research groups have shown that surface coatings are effective at suppressing the capacity and power fades of positive electrode materials. However, the mechanisms of the coating for such effects are complicated and have not been explained sufficiently to design surface coating optima for positive electrode materials and cell chemistry. For example, Chen and Dahn reported that a rough coating of Al_2O_3 particles 10 nm in diameter on a $LiCoO_2$ particle also showed a clear effect for improving capacity retention during the charge–discharge cycle [61]. This result indicates that the role of surface coatings is not only to provide a physical protection shield but also to modify the surface chemistry of positive electrode materials.

Table 3.2 Surface coating materials on typical positive electrode materials for lithium-ion batteries

Positive electrode material	Coating materials	Reference
$LiCoO_2$	Li_2CO_3	[65]
	MgO	[66–70]
	Al_2O_3	[71–76]
	$AlPO_4$	[77–80]
	ZrO_2	[81–82]
	SnO_2	[83]
$LiNiO_2/LiNi_{1-x}Co_xO_2$	MgO	[84–85]
	$AlPO_4$	[79–86]
	SiO_x	[87]
	TiO_2	[88–90]
	ZrO_2	[66, 81, 91]
$LiMn_2O_4$	MgO	[92]
	Al_2O_3	[81, 92, 93]
	ZrO_2	[94]
	polymer	[95–97]
$LiMn_{1.5}Ni_{0.5}O_4$	ZnO	[98]

Chen et al. have reviewed the key mechanisms of surface coatings from the research literature on various coating materials for different positive electrode materials as follows [59]: (a) electron-conducting media that facilitate charge transfer at the surface of particles; (b) modification of the surface chemistry of positive electrode materials that improves performance; (c) hydrofluoric acid (HF) scavengers that reduce the acidity of nonaqueous electrolytes and suppresses metal dissolution of positive electrode materials; and (d) a physical protection barrier that impedes side reactions between positive electrode materials and nonaqueous electrolytes. All of the mechanisms that represent key functions in Chen et al.'s review are thought to have no exceptions. However, almost all surface coatings possess some key mechanisms shown earlier. Therefore, studies on the mechanisms of surface coatings are still very important for the purpose of advancing surface coating methods to achieve a more stable and longer life of the interface between positive electrode materials and electrolytes.

References

1. M.D. Levi, G. Salitra, B. Markovsky, H. Teller, D. Aurbach, U. Heider, L. Heider, J. Electrochem. Soc. **146**, 1279 (1999)
2. Z.Y. Chen, X.Q. Liu, L.Z. Gao, Z.L. Yu, Chin. J. Inorg. Chem. **17**, 325 (2001)
3. C.H. Chen, J. Liu, K. Amine, J. Power Sources **96**, 321 (2001)
4. K. Amine, C.H. Chen, J. Liu, M. Hammond, A. Jansen, D. Dees, I. Bloom, D. Vissers, G. Henriksen, J. Power Sources **97–8**, 684 (2001)
5. A.M. Andersson, D.P. Abraham, R. Haasch, S. MacLaren, J. Liu, K. Amine, J. Electrochem. Soc. **149**, A1358 (2002)
6. D.P. Abraham, R.D. Twesten, M. Balasubramanian, J. Kropf, D. Fischer, J. McBreen, I. Petrov, K. Amine, J. Electrochem. Soc. **150**, A1450 (2003)
7. G.V. Zhuang, G.Y. Chen, J. Shim, X.Y. Song, P.N. Ross, T.J. Richardson, J. Power Sources **134**, 293 (2004)
8. M.V. Reddy, G.V. Subba Rao, B.V.R. Chowdari. Solid State Ionics. The Sci. & Technol. of Ions in Motion, (Eds.) B.V.R. Chowdari, H.-I. Yoo, G.M. Choi, J.H. Lee, World Scientific, Singapore, **525** (2004)
9. D.P. Abraham, E.M. Reynolds, E. Sammann, A.N. Jansen, D.W. Dees, Electrochim. Acta **51**, 502 (2005)
10. Z.H. Chen, K. Amine, J. Electrochem. Soc. **153**, A316 (2006)
11. M. Kerlau, M. Marcinek, V. Srinivasan, R.M. Kostecki, Electrochim. Acta **52**, 5422 (2007)
12. D.P. Abraham, J.L. Knuth, D.W. Dees, I. Bloom, J.P. Christophersen, J. Power Sources **170**, 465 (2007)
13. M. Shikano, H. Kobayashi, S. Koike, H. Sakaebe, E. Ikenaga, K. Kobayashi, K. Tatsumi, J. Power Sources **174**, 795 (2007)
14. H. Kobayashi, M. Shikano, S. Koike, H. Sakaebe, K. Tatsumi, J. Power Sources **174**, 380 (2007)
15. D. Mori, H. Kobayashi, M. Shikano, H. Nitani, H. Kageyama, S. Koike, H. Sakaebe, K. Tatsumi, J. Power Sources **189**, 676 (2009)
16. P.L. Moss, G. Au, E.J. Plichta, J.P. Zheng, J. Electrochem. Soc. **157**, A1 (2010)
17. C. Qing, Y. Bai, J. Yang, W. Zhang, Electrochim. Acta **56**, 6612 (2011)
18. M. Shikano, H. Kobayashi, S. Koike, H. Sakaebe, Y. Saito, H. Hori, H. Kageyama, K. Tatsumi, J. Power Sources **196**, 6881 (2011)
19. E. Peled, J. Electrochem. Soc. **126**, 2047 (1979)

20. Y. Eineli, D. Aurbach, J. Power Sources **54**, 281 (1995)
21. T.P. Kumar, A.M. Stephan, P. Thayananth, V. Subramanian, S. Gopukumar, N.G. Renganathan, M. Raghavan, N. Muniyandi, J. Power Sources **97–8**, 118 (2001)
22. Y.K. Choi, K.I. Chung, W.S. Kim, Y.E. Sung, Microchem. J. **68**, 61 (2001)
23. H. Ota, A. Kominato, W.J. Chun, E. Yasukawa, S. Kasuya, J. Power Sources **119**, 393 (2003)
24. S.B. Lee, S.I. Pyun, J. Solid State Electrochem. **7**, 201 (2003)
25. G.V. Zhuang, K. Xu, T.R. Jow, P.N. Ross, Electrochem. Solid State Lett. **7**, A224 (2004)
26. G.R.V. Zhuang, K. Xu, H. Yang, T.R. Jow, P.N. Ross, J. Phys. Chem. B **109**, 17567 (2005)
27. H. Nakahara, S. Nutt, J. Power Sources **160**, 1355 (2006)
28. G. Kwak, J. Park, J. Lee, S.A. Kim, I. Jung, J. Power Sources **174**, 484 (2007)
29. B. Wang, Q.T. Qu, Q. Xia, Y.P. Wu, X. Li, C.L. Gan, T. van Ree, Electrochim. Acta **54**, 816 (2008)
30. N.-S. Choi, I.A. Profatilova, S.-S. Kim, E.-H. Song, Thermochim. Acta **480**, 10 (2008)
31. S.-W. Song, S.-W. Baek, Electrochim. Acta **54**, 1312 (2009)
32. J.-T. Li, S.-R. Chen, F.-S. Ke, G.-Z. Wei, L. Huang, S.-G. Sun, J. Electroanal. Chem. **649**, 171 (2010)
33. H. Choi, C.C. Nguyen, S.-W. Song, Bull. Korean Chem. Soc. **31**, 2519 (2010)
34. W. Xu, S.S.S. Vegunta, J.C. Flake, J. Power Sources **196**, 8583 (2011)
35. D. Aurbach, B. Markovsky, I. Weissman, E. Levi, Y. Ein-Eli, Electrochim. Acta **45**, 67 (1999)
36. K. Edstrom, A.M. Andersson, A. Bishop, L. Fransson, J. Lindgren, A. Hussenius, J. Power Sources **97–8**, 87 (2001)
37. V. Eshkenazi, E. Peled, L. Burstein, D. Golodnitsky, Solid State Ion. **170**, 83 (2004)
38. S. Menkin, D. Golodnitsky, E. Peled, Electrochem. Commun. **11**, 1789 (2009)
39. P. Verma, P. Maire, P. Novak, Electrochim. Acta **55**, 6332 (2010)
40. M. Thomas, P.G. Bruce, J.B. Goodenough, J. Electrochem. Soc. **132**, 1521 (1985)
41. K. Edstrom, T. Gustafsson, J.O. Thomas, Electrochim. Acta **50**, 397 (2004)
42. T. Eriksson, A.M. Andersson, A.G. Bishop, C. Gejke, T. Gustafsson, J.O. Thomas, J. Electrochem. Soc. **149**, A69 (2002)
43. D. Aurbach, K. Gamolsky, B. Markovsky, G. Salitra, Y. Gofer, U. Heider, R. Oesten, M. Schmidt, J. Electrochem. Soc. **147**, 1322 (2000)
44. Y. Saito, M. Shikano, H. Kobayashi, J. Power Sources **196**, 6889 (2011)
45. N. Dupre, J.-F. Martin, J. Oliveri, P. Soudan, A. Yamada, R. Kanno, D. Guyomard, J. Power Sources **196**, 4791 (2011)
46. K.Y. Chung, W.-S. Yoon, K.-B. Kim, B.-W. Cho, X.-Q. Yang, J. Appl. Electrochem. **41**, 1295 (2011)
47. H. Duncan, Y. Abu-Lebdeh, I.J. Davidson, J. Electrochem. Soc. **157**, A528 (2010)
48. R. Dedryvere, D. Foix, S. Franger, S. Patoux, L. Daniel, D. Gonbeau, J. Phys. Chem. C **114**, 10999 (2010)
49. N. Dupre, J. Oliveri, J. Degryse, J.-F. Martin, D. Guyomard, Ionics **14**, 203 (2008)
50. Y. Saito, J. Power Sources **146**, 770 (2005)
51. S. Muto, K. Tatsumi, Y. Kojima, H. Oka, H. Kondo, K. Horibuchi, Y. Ukyo, J. Power Sources **205**, 449 (2012)
52. S. Zheng, R. Huang, Y. Makimura, Y. Ukyo, C.A.J. Fisher, T. Hirayama, Y. Ikuhara, J. Electrochem. Soc. **158**, A357 (2011)
53. Y. Kojima, S. Muto, K. Tatsumi, H. Kondo, H. Oka, K. Horibuchi, Y. Ukyo, J. Power Sources **196**, 7721 (2011)
54. T. Nonaka, C. Okuda, Y. Seno, Y. Kondo, K. Koumoto, Y. Ukyo, J. Electrochem. Soc. **154**, A353 (2007)
55. T. Sasaki, T. Nonaka, H. Oka, C. Okuda, Y. Itou, Y. Kondo, Y. Takeuchi, Y. Ukyo, K. Tatsumi, S. Muto, J. Electrochem. Soc. **156**, A289 (2009)
56. S. Muto, Y. Sasano, K. Tatsumi, T. Sasaki, K. Horibuchi, Y. Takeuchi, Y. Ukyo, J. Electrochem. Soc. **156**, A371 (2009)
57. K. Tatsumi, Y. Sasano, S. Muto, T. Yoshida, T. Sasaki, K. Horibuchi, Y. Takeuchi, Y. Ukyo, Phys. Rev. B **78**, 045108 (2008)

58. T. Nonaka, C. Okuda, Y. Seno, K. Koumoto, Y. Ukyo, Ceram. Int. **34**, 859 (2008)
59. Z. Chen, Y. Qin, K. Amine, Y.-K. Sun, J. Mater. Chem. **20**, 7606 (2010)
60. C. Li, H.P. Zhang, L.J. Fu, H. Liu, Y.P. Wu, E. Ram, R. Holze, H.Q. Wu, Electrochim. Acta **51**, 3872 (2006)
61. Z.H. Chen, J.R. Dahn, Electrochim. Acta **49**, 1079 (2004)
62. Z.H. Chen, J.R. Dahn, Electrochem. Solid State Lett. **6**, A221 (2003)
63. Y.K. Sun, Y.C. Bae, S.T. Myung, J. Appl. Electrochem. **35**, 151 (2005)
64. J.M. Zheng, Z.R. Zhang, X.B. Wu, Z.X. Dong, Z. Zhu, Y. Yang, J. Electrochem. Soc. **155**, A775 (2008)
65. J. Zhang, Y.J. Xiang, Y. Yu, S. Xie, G.S. Jiang, C.H. Chen, J. Power Sources **132**, 187 (2004)
66. L.J. Fu, H. Liu, C. Li, Y.P. Wu, E. Rahm, R. Holze, H.Q. Wu, Prog. Mater Sci. **50**, 881 (2005)
67. Y. Iriyama, H. Kurita, I. Yamada, T. Abe, Z. Ogumi, J. Power Sources **137**, 111 (2004)
68. H.L. Zhao, G. Ling, W.H. Qiu, X.H. Zhang, J. Power Sources **132**, 195 (2004)
69. Z.X. Wang, L.J. Liu, L.Q. Chen, X.J. Huang, Solid State Ion. **148**, 335 (2002)
70. M. Mladenov, R. Stoyanova, E. Zhecheva, S. Vassilev, Electrochem. Commun. **3**, 410 (2001)
71. G.T.K. Fey, H.Z. Yang, T.P. Kumar, S.P. Naik, A.S.T. Chiang, D.C. Lee, J.R. Lin, J. Power Sources **132**, 172 (2004)
72. S. Oh, J.K. Lee, D. Byun, W.I. Cho, B.W. Cho, J. Power Sources **132**, 249 (2004)
73. L.J. Liu, L.Q. Chen, X.J. Huang, X.Q. Yang, W.S. Yoon, H.S. Lee, J. McBreen, J. Electrochem. Soc. **151**, A1344 (2004)
74. J. Cho, Y.J. Kim, B. Park, J. Electrochem. Soc. **148**, A1110 (2001)
75. J. Cho, Y.J. Kim, T.J. Kim, B. Park, Angew. Chem. Int. Ed. **40**, 3367 (2001)
76. J. Cho, Y.J. Kim, B. Park, Chem. Mater. **12**, 3788 (2000)
77. J.P. Cho, B. Kim, J.G. Lee, Y.W. Kim, B. Park, J. Electrochem. Soc. **152**, A32 (2005)
78. J. Cho, J.G. Lee, B. Kim, T.G. Kim, J. Kim, B. Park, Electrochim. Acta **50**, 4182 (2005)
79. J. Cho, H. Kim, B. Park, J. Electrochem. Soc. **151**, A1707 (2004)
80. G.T.K. Fey, T.P. Kumar, J. Ind. Eng. Chem. **10**, 1090 (2004)
81. H. Liu, Y.P. Wu, E. Rahm, R. Holze, H.Q. Wu, J. Solid State Electrochem. **8**, 450 (2004)
82. Y.J. Kim, J.P. Cho, T.J. Kim, B. Park, J. Electrochem. Soc. **150**, A1723 (2003)
83. J. Cho, C.S. Kim, S.I. Yoo, Electrochem. Solid State Lett. **3**, 362 (2000)
84. H.J. Kweon, S.J. Kim, D.G. Park, J. Power Sources **88**, 255 (2000)
85. H.J. Kweon, D.G. Park, Electrochem. Solid State Lett. **3**, 128 (2000)
86. J. Cho, T.J. Kim, J. Kim, M. Noh, B. Park, J. Electrochem. Soc. **151**, A1899 (2004)
87. H. Omanda, T. Brousse, C. Marhic, D.M. Schleich, J. Electrochem. Soc. **151**, A922 (2004)
88. H.S. Liu, Z.R. Zhang, Z.L. Gong, Y. Yang, Solid State Ion. **166**, 317 (2004)
89. Z.R. Zhang, H.S. Liu, Z.L. Gong, Y. Yang, J. Electrochem. Soc. **151**, A599 (2004)
90. Z.R. Zhang, Z.L. Gong, Y. Yang, J. Phys. Chem. B **108**, 17546 (2004)
91. J. Cho, T.J. Kim, Y.J. Kim, B. Park, Electrochem. Solid State Lett. **4**, A159 (2001)
92. A.M. Kannan, A. Manthiram, Electrochem. Solid State Lett. **5**, A167 (2002)
93. S.W. Lee, K.S. Kim, H.S. Moon, H.J. Kim, B.W. Cho, W.I. Cho, J.B. Ju, J.W. Park, J. Power Sources **126**, 150 (2004)
94. M.M. Thackeray, C.S. Johnson, J.S. Kim, K.C. Lauzze, J.T. Vaughey, N. Dietz, D. Abraham, S.A. Hackney, W. Zeltner, M.A. Anderson, Electrochem. Commun. **5**, 752 (2003)
95. R. Vidu, P. Stroeve, Ind. Eng. Chem. Res. **43**, 3314 (2004)
96. C. Arbizzani, A. Balducci, M. Mastragostino, M. Rossi, F. Soavi, J. Electroanal. Chem. **553**, 125 (2003)
97. M. Nishizawa, K. Mukai, S. Kuwabata, C.R. Martin, H. Yoneyama, J. Electrochem. Soc. **144**, 1923 (1997)
98. Y.K. Sun, Y.S. Lee, M. Yoshio, K. Amine, Electrochem. Solid State Lett. **5**, A99 (2002)

Chapter 4
Nano-Aspects of Carbon Negative Electrodes for Li Ion Batteries

Takeshi Abe and Zempachi Ogumi

Carbon negative electrodes have been used as negative electrodes since lithium-ion batteries were commercialized. Various carbonaceous materials have been extensively investigated for practical use as negative electrodes. The negative electrode performance of carbons depends to a large extent on their microstructures. Less crystallized carbons show capacities exceeding 700 mAh/g, but these carbons were not commercialized due to their poor cycle performance. Intermediate crystallized carbons show a high cycle performance and high rate capability, but the capacities are around 200 mAh/g. Among carbonaceous materials, in particular graphitized carbonaceous materials, henceforth called graphite, have been used because graphite negative electrodes demonstrate, for example, a good cycle performance and a high reversible capacity of 372 mAh/g. This chapter describes mainly the electrochemical properties of graphite negative electrodes.

4.1 Carbonaceous Materials

Carbons can be obtained by heating organic polymers or hydrocarbon precursors under inert atmosphere. By changing the heat-treatment temperatures, low to high crystallized carbons with various microstructures are synthesized. Increases in the heat-treatment temperatures up to 3,000 °C make it possible to synthesize graphitized carbons, and these carbons are called artificial graphite. Some organic materials, such as phenolic resin, cannot be graphitized even at high heat-treatment temperatures. The precursor of phenolic resin is heated to be nongraphitizable carbons. In contrast to these carbons, natural graphite is produced, for example, in China, Madagascar, and Ceylon. A schematic of carbon microstructures is shown

---

T. Abe (✉) • Z. Ogumi
Society-Academia Collaboration for Innovation,
Kyoto University, Gokasho, Uji 611-0011, Japan
e-mail: abe@elech.kuic.kyoto-u.ac.jp; ogumi@scl.kyoto-u.ac.jp

T. Osaka and Z. Ogumi (eds.), *Nanoscale Technology for Advanced Lithium Batteries*,
Nanostructure Science and Technology 182, DOI 10.1007/978-1-4614-8675-6_4,

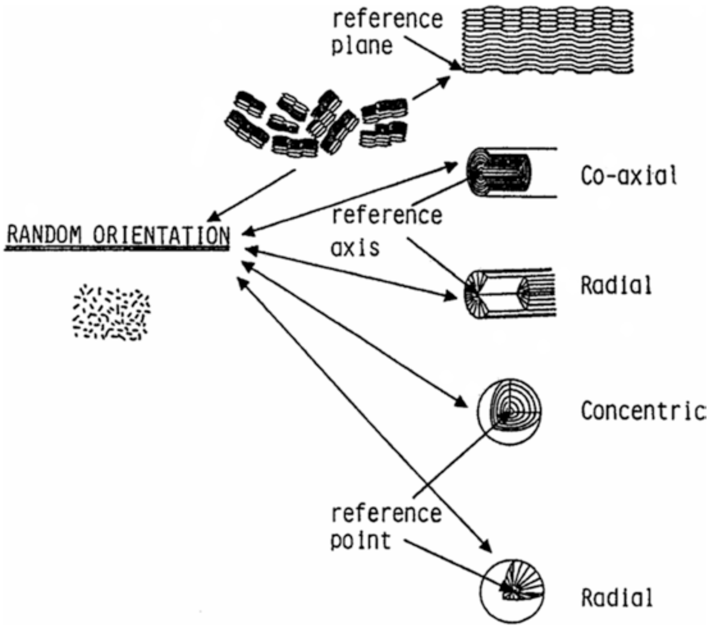

Fig. 4.1 Microstructures of carbons [1]

in Fig. 4.1 [1]. Most natural graphite and highly oriented pyrolytic graphite (so-called HOPG) show a plane orientation. Axial orientation is found in carbon fibers. Two cross-sectional surfaces, coaxial and radial types, can be seen in carbon fibers. Vapor-grown carbon fibers are typical of a coaxial type, and pitch-based carbon fibers are of a radial type. Carbon black is known as a conductive additive and has a point orientation with a concentric type. Mesocarbon microbeads (MCMBs) possess a point orientation with a radial type. Nongraphitizable carbons show a random orientation. The differences in their microstructures play an important role in the electrochemical properties of carbon negative electrodes.

4.2 Capacities of Carbon Negative Electrodes

As described earlier, carbons can be synthesized by heating organic materials. These carbons are categorized as soft and hard carbons. Soft carbons can be graphitized by heat treatment, whereas hard carbons are nongraphitizable carbons.

The capacities of carbon negative electrodes depend largely on the heat-treatment temperatures. Dahn et al. [2] studied the capacities of carbon negative electrodes and summarized them as shown in Fig. 4.2. At low temperatures of approximately

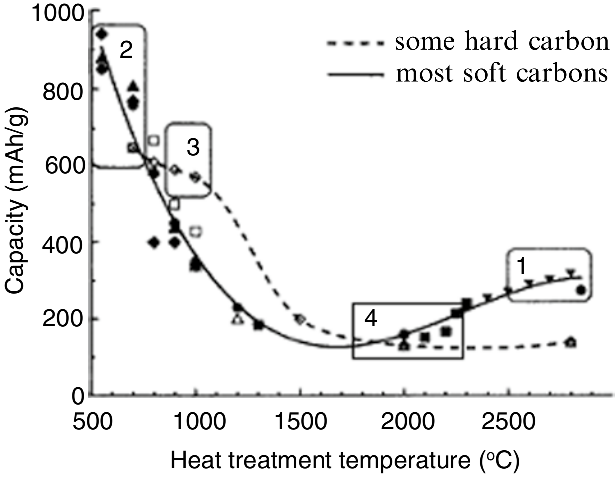

Fig. 4.2 Capacities versus heat-treatment temperatures [2]

700 °C, the capacities of carbons are larger than 372 mAh/g of the theoretical value of graphite. Several models were proposed to explain large capacities. Among them, two models [3, 4] are described. One is that lithium can be accommodated in nano-sized cavities of carbons [3], and the other is that lithium can adsorb onto both sides of single graphitelike sheets [4]. A detailed understanding of high capacities is still lacking because the bulk and surface structures, compositions, and so forth vary according to the heat-treatment process. These carbons heat-treated below 700 °C were not commercialized due to, for example, hysteresis in the potentials during charge and discharge, poor cycle performance, and deterioration of reversible capacities. As shown in Fig. 4.2, the capacities of carbons decrease as the heat-treatment temperatures increase from 1,000 up to 1,700–2,000 °C. The decrease in the capacities can be explained by the decrease in the nano-sized cavities or the decrease in the adsorption sites as described earlier. Carbons that are heat-treated above 2,000 °C show graphite structures. The graphitization degree increases with increases in the heat-treatment temperature. The capacities are correlated with the P1 parameter (probability for the nearest-neighbor pairs of layers having a graphitic relationship, the ratio of AB, or ABC sequences) in the carbons, and therefore the capacities increase as the heat-treatment temperatures increase [5]. The capacity increases to almost 372 mAh/g of a theoretical value of graphite. Carbons heat-treated at around 2,000 °C have not attracted attention due to their low capacities, and little work has been done in this area. However, Panasonic and Osaka Gas collaborated on cokes heat-treated at around 2,000 °C for lithium-ion batteries in hybrid electric vehicles. The cokes showed excellent rate performance, although the reversible capacities were not high.

4.3 Graphite Negative Electrodes

4.3.1 Characteristics of Graphite Negative Electrodes

Graphite negative electrodes have been used in most lithium-ion batteries. Figure 4.3 shows the typical charge–discharge curves of flaky natural graphite (plane orientation) in 1 mol dm^{-3} $LiPF_6$/EC (ethylene carbonate) + DMC (dimethyl carbonate) (1:1 by vol.). Although the irreversible capacities (Q_{irr}) appear at the first cycle due to the formation of solid electrolyte interphase (SEI) [6], the reversibility after the second cycle is as high as around 100 %. The characteristics of graphite negative electrodes are as follows:

1. Charge (lithium-ion intercalation) and discharge (de-intercalation) reactions mainly proceed at the potentials as low as lithium metal: the low potentials of lithiated graphite result in the high voltage of lithium-ion batteries.
2. Volumetric capacity is relatively high (> 800 mAh cm^{-3}).
3. Volume expansion is small (around 10 % along the *c*-axis): when a lithium ion is fully intercalated into graphite, the interlayer distance between the nearest graphene sheet increases from 0.335 to 0.370 nm. The in-plane C-C distance is almost unchanged.
4. The potential profile is very flat, as shown in Fig. 4.3. Through the lithium-ion intercalation/deintercalation at the graphite electrode, the stage transformation

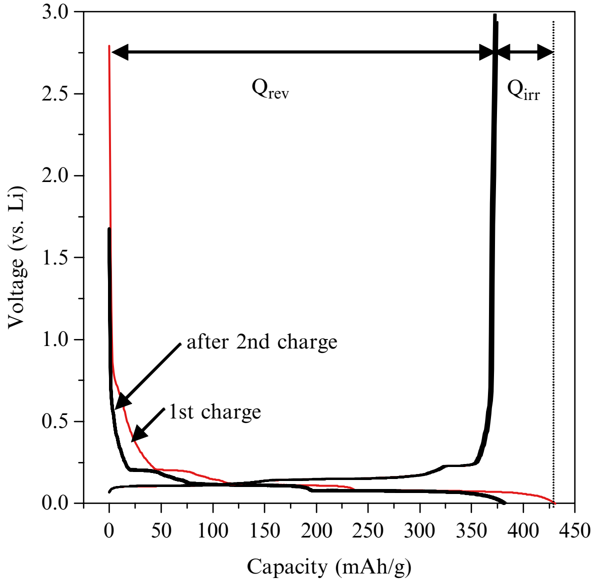

Fig. 4.3 Typical charge and discharge curves of graphite electrode

of lithium-graphite intercalation compounds proceeds. The potential during charge–discharge at the graphite negative electrode becomes flat due to the coexistence of two different stages (phases).

5. Graphite, in particular natural graphite, is inexpensive.

Due to these advantages, graphite negative electrodes are superior to other negative electrode candidates such as, for example, metal alloys and oxides, although some metal alloys and oxides show much higher capacities than graphite.

4.3.2 Surface Film Formation

As shown in Fig. 4.3, the potential of lithiated graphite is as low as that of lithium metal. The low potential indicates that its reductive ability is very strong, resulting in the decomposition of electrolytes used in lithium-ion batteries. At the first charge, the electrolyte decomposes at a potential of around 1 V versus Li/Li^+, followed by the formation of a surface film, the so-called SEI. The SEI formation is principally responsible for the irreversible capacity at the first cycle, and therefore considerable work has been done on the SEI formation mechanism, composition, and so forth.

Besenhard's group used a dilatometer during the charge–discharge reactions of graphite negative electrodes and found the volume expansion at a potential of around 1 V versus Li/Li^+ [7]. Based on the results, they proposed a solvated lithium-ion intercalation model (Fig. 4.4). Solvated lithium-ion intercalation is thermodynamically preferable to only lithium-ion intercalation in graphite. Therefore, it could very well be that solvated lithium-ion intercalates in graphite prior to lithium-ion intercalation. The solvated lithium ion decomposes with a decrease in the potential below 1.0 V to form SEI at the graphite negative electrode. Many studies have supported this model, but direct evidence of solvated lithium-ion intercalation by X-ray diffraction has not been reported so far.

Aurbach's group has reported excellent work on the composition of SEI using Fourier transform infrared techniques [8]. They found that inorganic and organic compounds, such as Li_2CO_3, Li_2O, and alkyl carbonates, served as SEI and stabilized the graphite negative electrode toward the reaction with the electrolyte.

Fabrication of stable SEI is one of the key issues in enhancing battery performance. Therefore, many additives for the formation of SEI on graphite negative electrodes have been studied, and some of them have been commercialized. The concept of additives involves the formation of additive-derived SEI prior to that of electrolyte-derived SEI. As described earlier, electrolyte decomposition takes place at around 1.0 V versus Li/Li^+, and therefore the additives are designed to be decomposed at potentials higher than 1.0 V. The typical additives are vinylene carbonate (VC), ethylene sulfite, fluoroethylene carbonate, and others. VC has been used in many lithium-ion batteries.

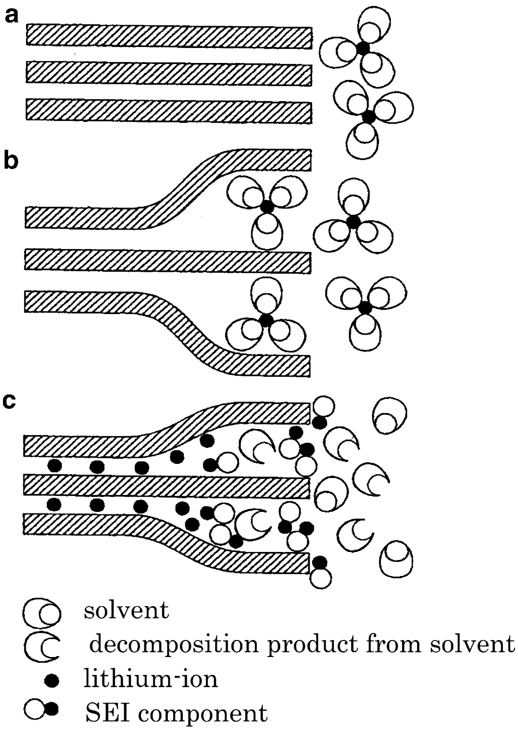

Fig. 4.4 Solvated intercalation model (Besenhard model [7])

4.3.3 *Diffusivity of Lithium Ions*

The diffusion of lithium ions in active materials plays a crucial role in the rate capabilities of lithium-ion batteries. Much work has been done on elucidating the diffusion coefficients of lithium ions in graphite. Various values ranging from 10^{-7} to 10^{-12} cm^2/s have been reported. This large difference is mainly due to the method used to evaluate the diffusion coefficients.

Dokko et al. [9] used a single particle of artificial graphite of around 18 μm to evaluate the electrochemical properties. Discharge curves of the single particle are shown in Fig. 4.5. When the applied current was between 3 and 200 nA, a capacity of 2 nAh was observed. Therefore, the maximum discharge capacity of this single particle should be 2 nAh. With an increase in the current up to 2,000 nAh, approximately 1.7 nAh of capacity was shown. The current corresponds to a 1,000 C rate, indicating that the diffusion of lithium ions in graphite should be very fast. In fact, Dokko et al. [9] conducted impedance spectroscopy measurements and obtained the diffusion coefficient exceeding 10^{-8} cm^2/s. On the basis of these results, the diffusivity of graphite is concluded to be very fast.

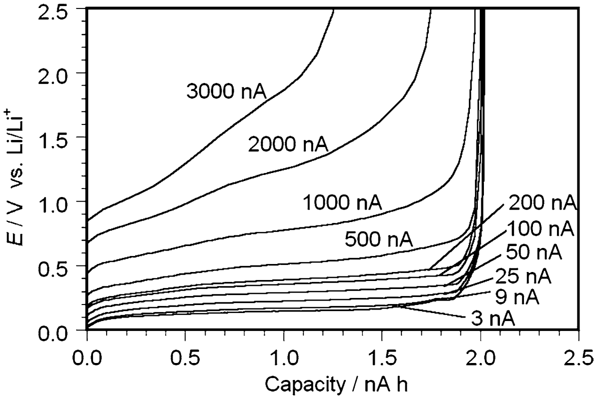

Fig. 4.5 Discharge curves of single particle of mesocarbon microbeads. Charge current was set at 3 nA and discharge currents ranged from 3 to 3,000 nA [9]

4.4 Charge (Lithium-Ion) Transfer Reaction

An increase in the rate performance of lithium-ion batteries can be attained by a decrease in the internal resistances caused by the processes of electron and ion transfer through charge–discharge reactions. The former processes consist of (1) electron transfer in positive and negative electrodes and (2) electron transfer between a current collector and electrode. These electron-transfer processes are generally fast or devised to be fast when the active materials in positive and negative electrodes are insulators. The latter processes are divided into four groups: (3) lithium-ion diffusion in active materials, (4) lithium-ion (charge) transfer at an electrode/electrolyte interface, (5) lithium-ion transport in an electrolyte penetrated in a composite electrode, and (6) lithium-ion transport in an electrolyte (separator).

As described in the previous section, the diffusivities of lithium ions in active materials are a very important issue for the rate performance of lithium-ion batteries, and therefore many studies have been conducted on the evaluation of the diffusion coefficients of lithium ions in various active materials. Practically, fine particles are adopted for the active materials to shorten the diffusion path of lithium ions in active materials. Resistances from the lithium-ion transport processes (5 and 6) can be reduced by a thinner composite electrode and separator. Among the four lithium-ion processes, less attention has been paid to the interfacial lithium-ion transfer process (4).

Lithium-ion transfer resistance, that is, the charge transfer resistance of R_{ct}, can be expressed by the following equation:

$$1/R_{ct} = A\exp\left(-E_{\mathrm{a}}/RT\right), \tag{4.1}$$

where A is the preexponential factor, Ea is the activation energy, R is the gas constant, and T is the absolute temperature. Equation 4.1 shows that the charge transfer

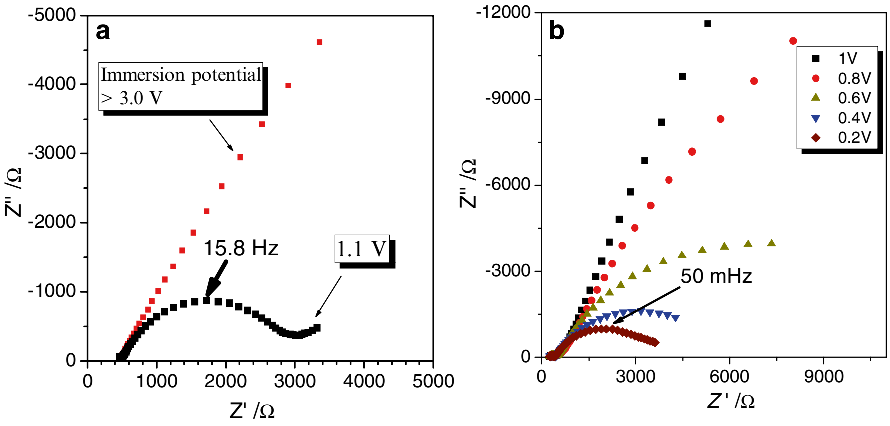

Fig. 4.6 Comparison of Nyquist plots of HOPG electrode in (**a**) 1 mol dm^{-3} $LiCF_3SO_3$/DME and (**b**) 1 mol dm^{-3} $LiClO_4$/EC + DEC

resistance decreases with an increase in A. The preexponential factor depends on the number of reaction sites of the positive and negative electrodes, the wettability of the electrodes in relation to the electrolyte, and the activities of the lithium ions. Therefore, an increase in the electrode area and the use of fine particles of active materials are practically effective in the decrease in R_{ct}. As shown by Eq. 4.1, a decrease in activation energies for lithium-ion transfer at electrodes can drastically reduce R_{ct}. Then, it is very important to elucidate the activation energies for lithium-ion transfer at electrodes in lithium-ion batteries.

We elucidated the activation energies of lithium-ion transfer at graphite electrodes [10]. Highly oriented pyrolytic graphite (HOPG) was used as a model graphite electrode because a porous composite electrode consisting of active material, a conductive additive, and a polymer often causes difficulties in the precise interpretation of Nyquist plots obtained by electrochemical impedance spectroscopy (EIS). Lithium-ion transfer at the interface between HOPG and an organic electrolyte of 1 mol dm^{-3} $LiClO_4$/EC (ethylene carbonate) + DEC (diethyl carbonate) was studied using a three-electrode cell consisting of a working electrode of HOPG and counter and reference electrodes of lithium metal. Then the electrochemical measurements were conducted by a three-electrode cell and the potential was referred to lithium metal unless otherwise stated. Organic electrolytes of 1 mol dm^{-3} $LiCF_3SO_3$/1,2-dimethoxyethane (DME) or dimethyl sulfoxide (DMSO) were also used. In these electrolytes, intercalation and deintercalation of solvated lithium ions take place at graphite electrodes due to the strong interaction between lithium ions and solvents of DME and DMSO. Figure 4.6 shows a comparison of Nyquist plots of HOPG electrodes in (a) 1 mol dm^{-3} $LiCF_3SO_3$/DME and (b) 1 mol dm^{-3} $LiClO_4$/EC + DEC. As shown in Fig. 4.6a, b, a blocking-electrode-type behavior was observed at higher potentials. When the potential decreased to 1.1 V (Fig. 4.6a) and 0.4 V (Fig. 4.6b), semicircles are observed. These semicircles were dependent on the electrode

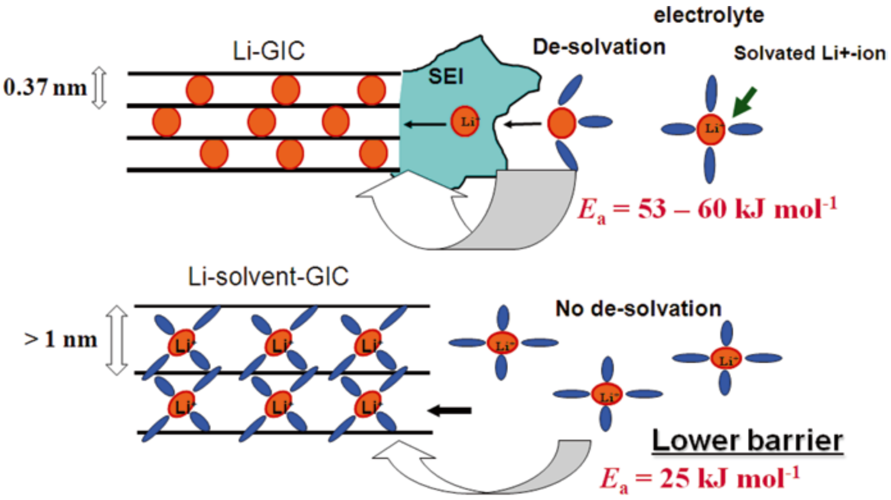

Fig. 4.7 Schematic of lithium-ion and solvated lithium-ion transfers at graphite electrodes. The activation energies for solvated lithium-ion transfer are much lower than those for lithium-ion transfer

potentials and salt concentrations, and therefore we assigned these semicircles as lithium-ion transfer resistances. By the temperature dependency of the lithium-ion transfer resistances, the activation energies for lithium-ion and solvated lithium-ion transfer were obtained as 53–59 kJ mol^{-1} and 25 kJ mol^{-1}, respectively. The activation barrier for solvated lithium-ion transfer was much smaller than that for only lithium-ion transfer. Figure 4.7 shows a schematic illustration of lithium-ion and solvated lithium-ion transfers. It should be noted that a solvated lithium-ion transfer gives a larger volume expansion of graphite along the *c*-axis, indicating that a large expansion of graphite layers does not cause high activation barriers for lithium-ion transfer at graphite electrodes. Then, an intuitively plausible explanation for the large activation barriers can be made by considering the desolvation process because lithium ions are a strong Lewis acid and are solvated strongly by a Lewis base of organic solvent. In addition, SEI on graphite electrodes may retard lithium-ion kinetics at graphite electrodes [11].

References

1. M. Inagaki, Tanso **122**, 114 (1985)
2. J.R. Dahn, T. Zheng, Y. Liu, J.S. Xue, Science **270**, 590 (1995)
3. A. Mabuchi, K. Tokumitsu, H. Fujimoto, T. Kasuh, J. Electrochem. Soc. **142**, 1041 (1995)
4. Y. Liu, J.S. Xue, T. Zheng, J.R. Dahn, Carbon **34**, 193 (1996)
5. K. Tatsumi, N. Iwashita, H. Sakaebe, H. Shioyama, S. Higuchi, A. Mabuchi, H. Fujimoto, J. Electrochem. Soc. **142**, 716 (1995)

6. E. Peled, J. Electrochem. Soc. **126**, 2047 (1979)
7. J.O. Besenhard, M. Winter, J. Yang, W. Biberacher, J. Power Sources **54**, 228 (1995)
8. D. Aurbach, B. Markovsky, I. Weissman, E. Levi, Y. Ein-Eli, Electrochim. Acta **45**, 67 (1999)
9. K. Dokko, N. Nakata, Y. Suzuki, K. Kanamura, J. Phys. Chem. C **114**, 8649 (2010)
10. T. Abe, H. Fukuda, Y. Iriyama, Z. Ogumi, J. Electrochem. Soc. **151**(8), A1120 (2004)
11. Y. Yamada, Y. Iriyama, T. Abe, Z. Ogumi, Langmuir **25**(21), 12766 (2009)

Chapter 5
Advanced Negative Electrodes of Nano-Scale Chemical Design for Lithium Batteries

Toshiyuki Momma and Tetsuya Osaka

5.1 Introduction

Li-ion batteries (LIBs) have extended their application fields to portable electronic devices due to their high energy density. Portable computers, cellular phones, and other mobile devices now use LIBs as their energy pack. In addition, for energy storage, electric vehicles and hybrid vehicles are starting to mount LIBs. For longer operation with one charge and for longer life cycle through the replacement of the energy module in vehicles and electric devices, there is strong demand for a novel electrochemical system for batteries having superior performance compared with conventional LIBs, which have systems of lithium metal oxide as the cathodes and carbon as the anodes. One of the candidates for anodes is, of course, lithium metal, and for now much effort is still being devoted to ensuring adequate safety of batteries. Another approach is to use the electrochemical alloying–dealloying reactions of lithium and another metal as the anode reaction. In this chapter, reports on proposals for a metallic anode for lithium batteries are reviewed.

5.2 Metallic Anode for Lithium Batteries

The electrochemical alloying–dealloying process has been investigated and applied to anode reactions of lithium batteries. The alloy of Al and Li is one of the most investigated materials for anodes of Li batteries. Gay investigated and reported that

---

T. Momma (✉)
Waseda University, Tokyo, Japan
e-mail: momma@waseda.jp; osakatets@waseda.jp

T. Osaka
Waseda University, Faculty of Science and Engineering,
Shinjuku-ku Tokyo, 169-8555, Japan

T. Osaka and Z. Ogumi (eds.), *Nanoscale Technology for Advanced Lithium Batteries*,
Nanostructure Science and Technology 182, DOI 10.1007/978-1-4614-8675-6_5,

Table 5.1 Lithium alloys and volumetric change during cycling [3] (Reprinted from ref. 3, Copyright (1990), with permission from Elsevier)

Host material	Charged state	Volumetric change (%)	Molar volume of Li (cm^3)
Al	LiAl	96.78	19.67
As	LiAs	91.63	24.88
	Li_3As	95.59	8.47
Bi	LiBi	75.88	29.06
	Li_3Bi	176.51	15.22
C	LiC_6	9.35	35.82
Cd	$LiCd_3$	17.60	45.89
	Li_3Cd	267.71	15.92
In	LiIn	52.29	23.53
Pb	LiPb	44.70	26.43
	$Li_{22}Pb_5$	233.66	13.85
Sb	Li_3Sb	147.14	14.99
Si	Li_2Si	175.12	15.15
	Li_4Si	322.57	11.64
Sn	$Li_{22}Sn_5$	676.31	28.75
Zn	$LiZn_4$	11.33	40.81
	LiZn	70.64	17.30

Li spontaneously alloyed with other metals [1], and a Li-Al alloy was proposed as an anode of a high-energy-density battery system [2]. Other Li-alloy systems have also been investigated, and the problem of these systems have been demonstrated to be the volmetric change during charging and discharging, as summarized in Table 5.1 [3]. Most of the systems listed in Table 5.1 show high values of volumetric change caused by lithiation into the host matrix, while C shows a slight change in volume. The huge change in volume of the material during the alloying–dealloying process leads to the pulverization of the matrix of the anode material, which subsequently leads to peeling off of the active material from the electrode, or a lack of electrical path from the current collector to the active material. Due to the dimensional stability, carbon was selected for the long cycle life anodes of LIBs.

There is a need to expand the energy density of batteries, with finding anode material having a superior energy density, power density, long cycle life, and safety. Tin (Sn) and Silicon (Si) are the elements of anode materials in lithium batteries that have attracted the attention of many researchers due to their high energy density values. However as an anode, pure Sn or Si is too fragile due to its large volumetric change during alloying and dealloying with Li.

5.3 Sn-Based Material with Conversion Reaction for Lithium Battery Anode

Researchers found a way to use Sn for the host of Li alloys without degrading the reversible capacity in continuous cycling. A reductively converted matrix from SnM_xO_y was proposed by Itoda et al. [4]. A fine Sn cluster was formed in an oxide matrix by electrochemical reduction of SnO_2-based material in the presence of Li^+. Following electrochemical reductive conversion, the electrode showed high cyclability as an anode of a Li battery. The process of electrochemical reduction of Sn-based oxide formed a Li_2O matrix embedding fine metallic clusters. Both the small size of the alloying metallic clusters and the Li_2O matrix are considered to lead the properties to endure the volumetric changes in the metal in the anode layer on the current collector. Based on the idea of converting the Sn oxide electrochemically to form an anode bearing the stress during charging–discharging, $SnSO_4$ and SnS_x were also reported as potential anode materials [5, 6]. Anodes using these materials are considered to work as follows. The starting materials of Sn compounds (here expressed as Sn-X) with Sn in an oxide state are reduced in the initial reduction process to form Li-X with fine metallic Sn particles in the presence of Li^+. Following this conversion reaction, Sn is then electrochemically reduced by the formation of an alloy of Li_ySn. After complete lithiation of Sn, Li_ySn will play a role in the anode active phase during the subsequent discharging–charging steps. Due to the conversion process in the initial reduction of the starting material, an irreversible reducing charge is essential to utilize these materials. The formed Li-X matrix is considered to provide mechanical capacity to the converted layer of Li-X and Sn. With the formation of the Li_ySn alloy and the dealloying of Li from Sn, the metallic phase should expand and shrink in volume. The internal stress of the Li-X layer embedding the fine metallic Sn particles is imagined to be reduced due to the physical properties of the Li-X layer. The converted anodes consisting of Li-X and metallic Sn particles were demonstrated to work as anodes of Li batteries for hundreds of charge–discharge cycles without the breaking of their structure. A representative charge–discharge performance of Sn-S–based material as an anode of a Li battery is illustrated in Fig. 5.1 [6]. The SnS_2 was converted into a Li_2S matrix embedding Sn-Li during the first reduction in the first charging process. The conversion requires an irreversible cathodic charge and in subsequent continuous cycling a current efficiency increase of up to 100 % with stable charge–discharge cycling. The potential of the electrode is around 1.3 V versus Li/Li^+ during the conversion reaction, while the potential of the anode during continuous charging and discharging remains around 0.5 V versus Li/Li^+; this value indicates that the reaction represents the alloying–dealloying of Sn with Li. The reversible discharge capacity in the continuous operation suggests that a Li_2S matrix works well in maintaining the electrode structure during the alloying–dealloying of Sn with Li.

5.4 Sn-Based Anode in Metallic State

The use of materials consisting of metallic Sn as the anode without a conversion reaction has also been studied. To prevent the pulverization of the anode matrix, which is observed in a pure Sn layer, during the continuous charge–discharge cycling, the alloying of Sn with another metallic element was proposed [7] and examined.

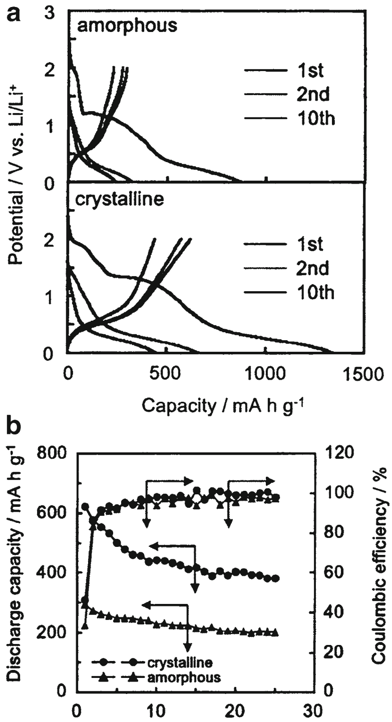

Fig. 5.1 Charge–discharge curves (**a**) and cycle performance (**b**) of SnS_2 electrode in 1 M $LiClO_4$/EC+PC(1:1) in potential range of 0–2 V versus Li/Li^+ under a loading current density of 50 mA g^{-1} (Reprinted from ref. 6, Copyright (2001), with permission from Elsevier)

Elements that are inactive against Li are assumed to effectively suppress the volumetric change without much irreversible capacity [8]. The use of Sn compounds with elements such as Fe, Cu, Mn, and Co has been investigated based on this assumption [9–18]. Ni is a typical element that does not react with Li. Therefore, this element can be expected to serve as an appropriate matrix to improve the cyclability of an electrode without a high initial irreversible capacity. Studies have been conducted on Ni-Sn compounds prepared by ball milling [8, 19] and electroplating [20]. An electrodeposited Ni-Sn alloy was demonstrated to be a candidate for the anodes of lithium batteries with a long cycle life [21]. The current efficiency of Ni-Sn anodes with a variation in the Sn content during continuous cycling is illustrated in Fig. 5.2 [21, 22]. In contrast to SnO and SnSx materials, the metallic Sn alloy shows a high discharge capacity from the first cycle of charge–discharge tests. The morphology observation of Ni-Sn anode before and after operation as the anode of a Li battery revealed that the matrix withstood the stress caused by a volumetric change during cycling [23]. In this Ni-Sn system, Ni was selected due to its unreactivity with Li to form an alloy phase and as a possible matrix that would retain the fine Li-Sn grains as the charged state of the anode. A crystallographic characterization of the Ni-Sn electrode with or without electrochemical alloying with Li revealed that the metastable phase M1 is a Ni-Sn phase with a composition ratio of almost 50:50, and the metastable phase M2 is a phase where Ni is melted into Sn crystals. Samples with higher Sn content were confirmed to have a structure similar to that of 100 atom.% Sn.

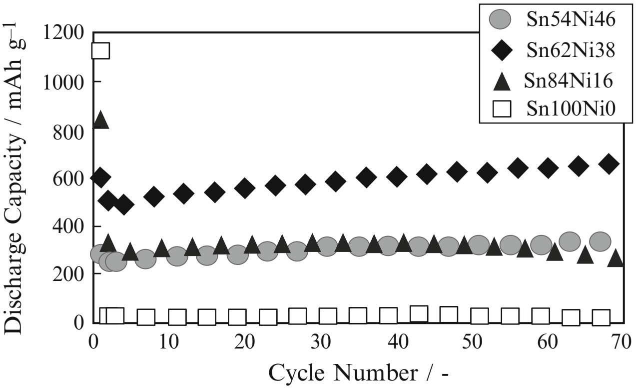

Fig. 5.2 Cycle performance of electrodes with various Ni/Sn ratios at a constant current density of 50 mA/g in potential range of 0–3 V versus Li/Li^+ in 1 M $LiClO_4$/EC + PC(1:1) organic electrolyte (Reprinted from ref. 22, Copyright (2005), with permission from Elsevier)

A reaction mechanism of Ni-Sn alloys was suggested from Ni-Sn alloys with different compositions ($Sn_{54}Ni_{46}$, $Sn_{62}Ni_{38}$, and $Sn_{84}Ni_{16}$) that show different anode properties. When Li^+ is inserted during the charge process, Sn atoms segregate from the Ni-Sn alloy structure and alloys with Li to form the Li-Sn alloy phase. This reaction should be reversible, and upon discharge, the Li^+ is extracted from the Li-Sn alloy phase, and the dealloyed Sn atom gets absorbed into the Ni matrix, again forming the Ni-Sn alloy phase.

These analyses suggest that the structure of $Sn_{54}Ni_{46}$ was unable to free the Sn from the metastable Ni-Sn alloy crystal to allow its full alloying with Li. For $Sn_{84}Ni_{16}$, pure Sn phases were observed that clearly did not alloy with Ni, hence leading to a large capacity drop following the second cycle. This indicates that the structure that allows Li and Sn, and Sn and Ni, to reversibly alloy/dealloy is the key to obtaining high-capacity, long-life anode materials. The Ni_3Sn_4 phase may realize such reversible reactions, and $Sn_{62}Ni_{38}$, which is mainly composed of this Ni_3Sn_4 structure, results in high capacity. It was also indicated that the lithiation procedure has the effect of lowering the crystallinity of electrodes. The formation of surface cracks during cycling was also confirmed with cycling. This generation of cracks may be one of the reasons for the increase in capacity with cycling seen in the cycle performance of electrodeposited Ni-Sn alloy anodes.

5.5 Si Thin Anodes

To realize a metallic pure Si anode, a thin layer or submicron-sized particles to bear the internal stress due to the alloying–dealloying of Si with Li during charging or discharging was examined.

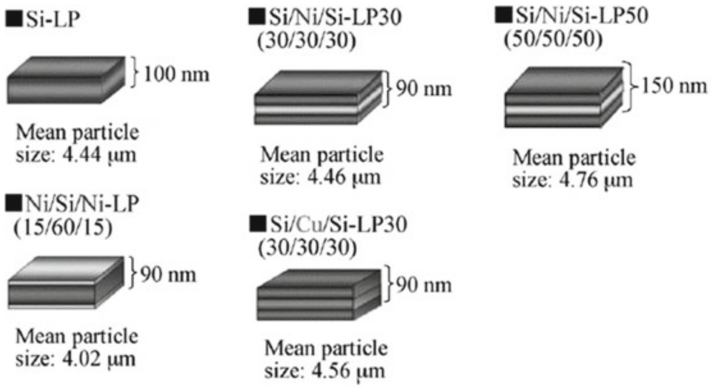

Fig. 5.3 Schematic illustration of Si thin platelets [27] (Reprinted from ref. [27], Copyright (2011), with permission from Elsevier)

The theoretical capacity of Si as a Li battery anode is 4,200 mAh g^{-1}, and many attempts to realize longlasting Si anodes have been made by forming a thin layer of Si by physical processes [24]. A thin n-Si anode with 2,000 mAh g^{-1} of capacity for more than 3,000 cycles using a sputtering process with a thickness as low as 50 nm has been reported [25]. Although Si reported demonstrates a good cycle life, it was shown that the thickness of a Si film should be less than several micrometers for continuous cycling because this determines the limitations of the anode's capacity. Amorphous Si deposited by chemical vapor deposition (CVD) using SiH_4 was also considered as an anode material [26]. A rather thicker film of 1.2 μm with amorphous Si was formed and possessed 1,000 mAh g^{-1} of discharge capacity in the initial cycling. However, the reversible capacity faded dramatically as the number of cycles increased, and at the 20th cycle, it dropped to 200 mAh g^{-1}. The authors concluded that modification of the microstructure would be the key factor in improving the cycle life. With the aim of regulating the thickness of the Si layer, Inaba et al. proposed anodes of Si platelets (leaflets) or Si/Ni/Si sandwich-type platelets regulating the Si thickness [27]. Figure 5.3 presents a schematic image of such a platelet. The platelet particles have a mean size of more than a few microns with a thickness of approximately 100 nm. These powders with small Si thicknesses have a merit to maintain the structure during repeated charge–discharge processes and can reduce the Li^+ diffusion length within the powder. Three-dimensional control of the morphology of Si has also been reported. Kim et al. proposed the introduction of a mesoporous structure into a Si/SiO_2 composite anode material [28]. A SiO_2/Si composite with a porous structure having a high surface area was achieved and exhibited a capacity of more than 2,800 mAh g^{-1} at a loading current density of 0.2 C with almost 100 % coulombic efficiency. Nanowire-structured Si was also examined for its potential as an anode in Li batteries. Peng et al. proposed Si nanowires as an anode material [29]. These materials are designed and demonstrated to have a potentially long cycling life because of their fine structures, which are able to bear stress during charging–discharging with huge volumetric changes.

5.6 Si-Based Composite Material Prepared by Electrodeposition

To produce an anode material with a fine Si cluster embedded in a soft matrix, deposition of the matrix with a Si cluster was attempted. An electrodeposition method was used to simulate the deposition of a matrix with Si. The idea of adopting the electrodeposition method from an organic solution to form a Si-containing anode is proposed as follows. A composite of Si with an organic/inorganic compound would withstand stress during anode operation. The organic/inorganic compounds formed by the reduction of an organic solvent, which results in the formation of a solid electrolyte interphase (SEI) layer on anodes in Li-ion batteries, are known to possess Li^+ permeability as well as chemical/electrochemical stability against anodes and electrolytes. With these considerations, producing a Si and organic/inorganic compound that would buffer stress and indicate a Li^+ permeability, electrochemical coreduction of Si and a solvent was performed to deposit directly onto the current collector [30], as shown in Fig. 5.4 [31].

A Si anode formed by electrodeposition was reported by Martin et al., and the reversible capacity and cycle life reported were low compared to conventional carbon anodes [32]. After several attempts, it was revealed that it is not easy to obtain pure Si by electrodeposition from conventional organic electrolyte systems. In contrast, with optimization of solution and operating condition the deposit, which is the mixture of reductive decomposed products of electrolyte and Si was found to work well as an anode of Li batteries.

Analysis of the electrodeposited SiOC from an organic electrolyte solution containing $SiCl_4$ revealed that the SiOC had a homogeneous dispersion of SiOx and organic/inorganic compounds at the nanometer scale. The structural uniformity

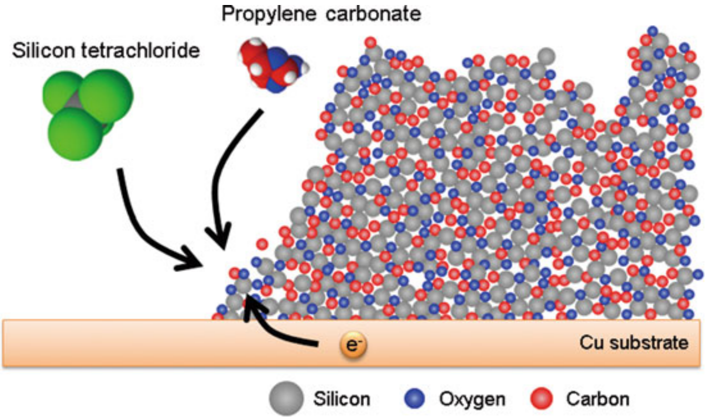

Fig. 5.4 Schematic image of SiOC preparation by $SiCl_4$ reduction with reductive decomposition of organic solvent [31] (Reproduced by permission of The Royal Society of Chemistry)

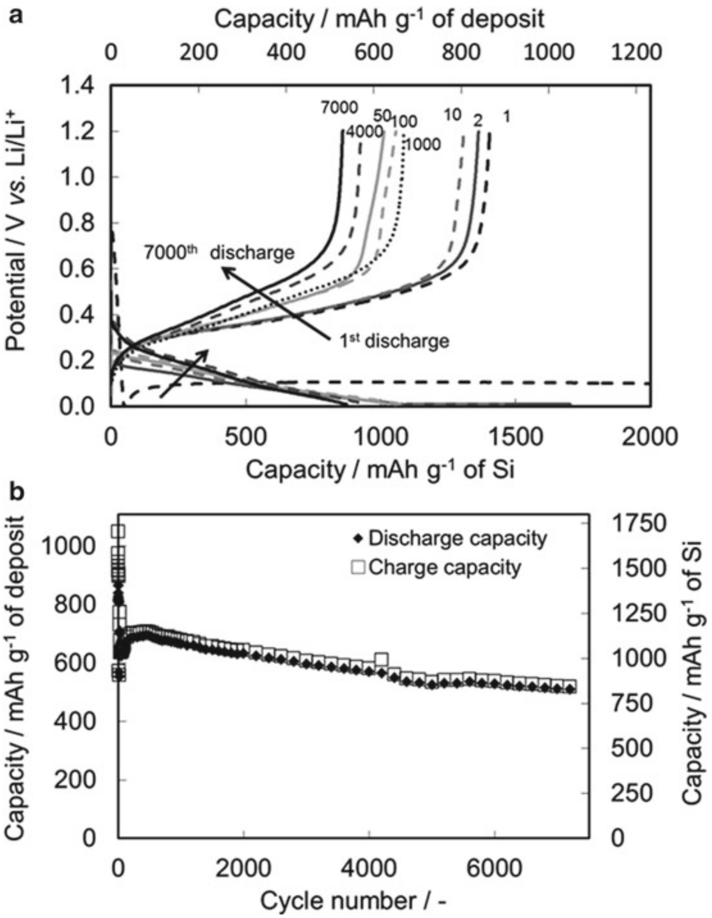

Fig. 5.5 Charge–discharge performance of SiOC composite anode for Li batteries. Chronopotentiogram (**a**) and capacity during continuous cycling (**b**) are illustrated. The capacity values were normalized with respect to the weight of the initial deposit or the calculated amount of Si in the deposit. The applied current density was 250 mA cm^{-2} (1.0 C-rate). (Reproduced by permission of The Royal Society of Chemistry)

of the SiOC composite was believed to have suppressed the formation of cracks attributable to the stress resulting from the reaction of Si with Li during charge–discharge cycles. The charge–discharge cycling tests of the SiOC anode was demonstrated with more than 7,200 cycles with a capacity of approximately 800 mAh/g of Si, as shown in Fig. 5.5 [31].

The deposition of SiOC by the reduction of $SiCl_4$ from an organic electrolyte solution made it possible to produce a Si cluster embedded in a stress-absorbing matrix and the deposit showed a high reversible capacity during a long cycle life as an anode of Li batteries.

References

1. A.N. Gay, J. Electrochem. Soc. **118**, 1547–1549 (1971)
2. E. Gay, D. Vissers, F. Martino, K. Anderson, J. Electrochem. Soc. **123**, 1591–1596 (1976)
3. J.O. Bensenhard, M. Hess, P. Komenda, Solid State Ion. **40**(41), 525–529 (1990)
4. Y. Idota, T. Kubota, A. Matsufuji, Y. Maekawa, T. Miyasaka, Science **276**, 1395–1397 (1997)
5. M. Nagayama, T. Morita, H. Ikuta, M. Wakihara, M. Takano, S. Kawasaki, Solid State Ion. **106**, 33–38 (1998)
6. T. Momma, N. Shiraishi, A. Yoshizawa, T. Osaka, A. Gedanken, J. Zhu, L. Sominski, J. Power, Sources **97–98**, 198–200 (2001)
7. J. Yang, M. Winter, J.O. Bensenhard, Solid State Ion. **90**, 281–287 (1996)
8. J. Ahn, Y. Kim, G. Wang, M. Lindsay, H.K. Liu, S. Dou, Mater. Trans. **43**(1), 63 (2002)
9. O. Mao, R.L. Turner, I.A. Courtney, B.D. Fredericksen, M.I. Buckett, L.J. Krause, J.R. Dahn, Electrochem. Solid State Lett. **2**(1), 3 (1999)
10. O. Mao, R.A. Dunlap, J.R. Dahn, J. Electrochem. Soc. **146**(2), 405 (1999)
11. O. Mao, R.A. Dunlap, J.R. Dahn, J. Electrochem. Soc. **146**(2), 414 (1999)
12. O. Mao, R.A. Dunlap, J.R. Dahn, J. Electrochem. Soc. **146**(2), 423 (1999)
13. D. Larcher, L.Y. Beaulieu, O. Mao, A.E. George, J.R. Dahn, J. Electrochem. Soc. **147**(5), 1703 (2000)
14. K.D. Kepler, J.T. Vaughey, M.M. Thackeray, Electrochem. Solid State Lett. **2**(7), 307 (1999)
15. D. Larcher, L.Y. Beaulieu, D.D. MacNeil, J.R. Dahn, J. Electrochem. Soc. **147**(5), 1658 (2000)
16. G.X. Wang, L. Sun, D.H. Bradhurst, S.X. Dou, H.K. Liu, J. Alloy Compd. **299**, L12 (2000)
17. N. Tamura, R. Ohshita, M. Fujimoto, S. Fujitani, M. Kamino, I. Yonezu, J. Power Sources **107**, 48 (2002)
18. L. Beaulieu, D. Larcher, R.A. Dunlap, J.R. Dahn, J. Alloys Compd. **297**, 122 (2000)
19. G.M. Ehrlich, C. Durand, X. Chen, T.A. Hugener, F. Spiess, S.L. Suib, J. Electrochem. Soc. **147**(3), 886 (2000)
20. O. Crosnier, T. Brousse, X. Devaux, P. Fragnaud, D.M. Schleich, J. Power Sources **94**, 169 (2001)
21. H. Mukaibo, T. Sumi, T. Yokoshima, T. Momma, T. Osaka, Electrochem. Solid State Lett. **6**, A218–A220 (2003)
22. H. Mukaibo, T. Momma, T. Osaka, J. Power Sources **146**, 457–463 (2005)
23. H. Mukaibo, T. Momma, M. Mohamedi, T. Osaka, J. Electrochem. Soc. **152**, A560–A565 (2005)
24. U. Kasavajjula, C. Wang, A.J. Appleby, J. Power Sources **163**, 1003–1039 (2007)
25. T. Takamura, M. Uehara, J. Suzuki, K. Sekine, K. Tamura, J. Power, Sources **158**, 1401–1404 (2006)
26. S. Bourderau, T. Brousse, D.M. Schleich, J. Power Sources **81–82**, 233–236 (1999)
27. M. Saito, K. Nakai, T. Yamada, T. Takenaka, M. Hirota, A. Kamei, A. Tasaka, M. Inaba, J. Power, Sources **196**, 6637–6643 (2011)
28. H. Kim, B. Han, J. Choo, J. Cho, Angew. Chem. Int. Ed. **47**, 10151–10154 (2008)
29. K. Peng, J. Jie, W. Zhang, S.-T. Lee, Appl. Phys. Lett. **93**, 033105 (2008)
30. T. Momma, S. Aoki, H. Nara, T. Yokoshima, T. Osaka, Electrochem. Commn. **13**, 969–972 (2011)
31. H. Nara, T. Yokoshima, T. Momma, T. Osaka, Energy Env. Sci. **5**, 6500–6505 (2012)
32. M. Schmuck, A. Balducci, B. Rupp, W. Kern, S. Passerini, M. Winter, J. Solid State Electrochem. **14**, 2203–2207 (2010)

Chapter 6
Polymer and Ionic Liquid Electrolytes for Advanced Lithium Batteries

Shiro Seki and Masayoshi Watanabe

6.1 Introduction

Environmentally benign energy generation methods, for example wind and photovoltaic power, are extremely valuable in terms of not only their contributions to improving the self-sufficiency ratio in energy supply and preventing global warming but also for their advantage of being energy-dispersive systems. However, these new energy generation methods are affected by nature (particularly, the weather and seasons), resulting in the instability of their output performance. For example, if electric power systems were supplied with a large amount of energy generated by these methods, not only the maintenance of operation frequency but also the power supply would become more difficult to maintain compared with systems based on thermal power generation. Therefore, when a large amount of energy supplied by such methods is introduced, output smoothing by storage control and the accumulation of energy are required during times of light loads such at night.

Given such a background, lithium-ion secondary batteries have significant advantages, such as a high energy density and a long cycle life, and are used in laptop personal computers, cellular phones, and in household electronics and appliances [1, 2]. Furthermore, in recent years, investigation of the use of high-power lithium-ion secondary batteries for hybrid electric vehicles (HEVs), plug-in hybrid electric vehicles (PHEVs), and electric vehicles (EVs) has been widely promoted on a

---

S. Seki (✉)
Materials Science Research Laboratory, Central Research Institute of Electric Power Industry (CRIEPI), 2-11-1, Iwado-kita, Komae, Tokyo 201-8511, Japan
e-mail: s-seki@criepi.denken.or.jp

M. Watanabe
Department of Chemistry and Biotechnology, Yokohama National University, Yokohama, Kanagawa 240-8501, Japan
e-mail: mwatanab@ynu.ac.jp

T. Osaka and Z. Ogumi (eds.), *Nanoscale Technology for Advanced Lithium Batteries*, Nanostructure Science and Technology 182, DOI 10.1007/978-1-4614-8675-6_6,

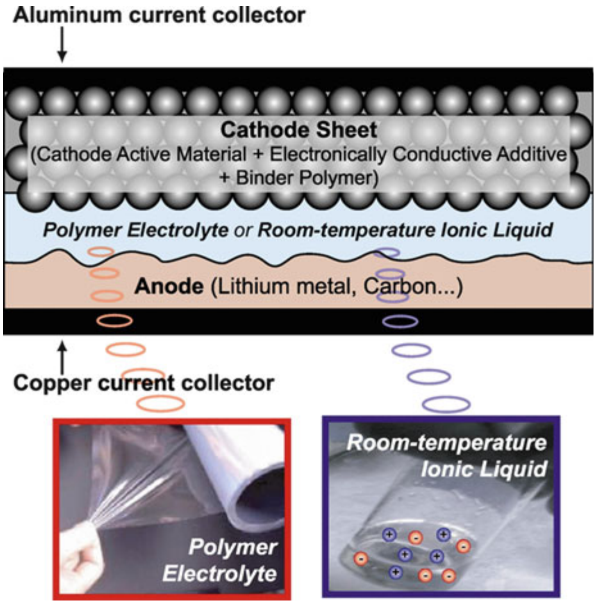

Fig. 6.1 Cross-sectional images of highly safe lithium secondary batteries using solid polymer electrolyte and room-temperature ionic liquid

global scale [3–6]. Certainly, current lithium-ion secondary batteries are also attractive from the viewpoint of large-scale energy storage such as in electric power load-leveling systems [7, 8]. However, many accidents caused by the electrical short circuit of commercially available cells used in portable systems have been reported, and safety management and performance are now recognized as an important problem. Furthermore, when battery systems are enlarged, for example to megawatt-class battery systems, safety becomes a much more important issue. Given such a background, solid polymer electrolytes and room-temperature ionic liquids (room-temperature molten salts) have been attracting attention as safe lithium secondary battery electrolytes for large-scale electrochemical energy storage devices (Fig. 6.1).

The important requirements that must be satisfied for solid polymer electrolytes and room-temperature ionic liquid electrolytes to act as electrolyte materials in high-performance lithium batteries are as follows.

1. Electrochemical stability up to the reduction potential of the negative electrode (anode) material (e.g., lithium metal, graphite, hard carbon, $Li_4Ti_5O_{12}$) (Fig. 6.2);
2. Electrochemical stability up to the oxidation potential of the positive electrode (cathode) active material (e.g., $LiCoO_2$, $LiMn_2O_4$, $LiNi_{1/3}M_{1/3}Co_{1/3}O_2$, $LiFePO_4$) (Fig. 6.2);
3. High lithium cationic conductivity of electrolytes composed of lithium salt/solid polymers or room-temperature ionic liquids.

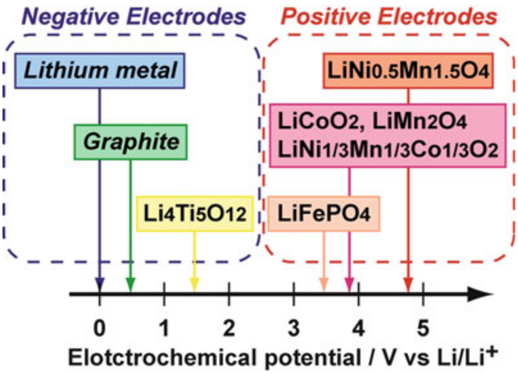

Fig. 6.2 Electrochemical potentials of various electrode materials for lithium secondary batteries

6.2 Solvent-Free, All-Solid-State Lithium Polymer Secondary Batteries

Conventional solvent-free polymer electrolytes for lithium polymer secondary batteries (all-solid-state lithium polymer batteries) utilize poly(ethylene oxide) (PEO) and its derivatives as their matrix polymers. Many polyether-based polymer electrolytes have a low glass transition temperature (170–230 K). Therefore, solid polymer electrolytes are flexible at room temperature and can be processed into a thin film. In the initial stage of research and development (R&D) of solid polymer electrolytes, the reported ionic conductivities were on the order of 10^{-8} S cm^{-1} at room temperature [9], and since the proposal to apply them to lithium secondary battery electrolytes [10], extensive studies have been carried out. For example, to improve the ionic conductivity of solid polymer electrolytes, the introduction of a comb-branched polyether structure to the PEO backbone [11–13] (Fig. 6.3) was found to be effective. Applications of siloxane [14, 15] or phosphazene [16–19] having lower glass transition temperatures than the main chain of comb-branched polyethers were quite effective at improving the electrolyte bulk ionic conductivity. The comb-branched structure of solid polymer electrolytes contributes not only to enhancing the bulk ionic conductivities but also to the stabilization and reduction of the interfacial charge transfer resistance with electrode materials [20]. Furthermore, the introduction of free-chain ends facilitates the interfacial charge transfer process with metallic lithium electrodes [12]. On the other hand, Scrosati and coworkers have reported increases in ionic conductivity and lithium cationic transport number, as well as a decrease in the interfacial resistance between lithium electrodes, by the addition of an inorganic filler (e.g., γ-$LiAlO_2$ [21–23], TiO_2 [24–26], Al_2O_3 [24, 26], and SiO_2 [26]) to PEO. At present, the highest ionic conductivities of solid polymer electrolytes have been reported in so-called decoupling polymer electrolytes (rigid polycarbonate [27], and poly[2,6-dimethoxy-*N*-(4-vinylphenyl)benzamide [28]) and siloxane-based electrolytes (semi-interpenetrating polymer network [29]), branched side chain electrolytes [30], and so on.

On the other hand, electrochemical stabilities for both anodic and cathodic sides still remain problematic for practical applications. The oxidation decomposition of

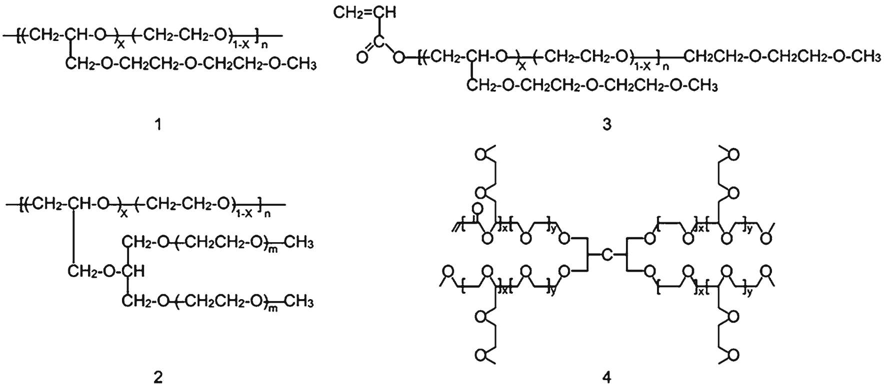

Fig. 6.3 Chemical structures of various comb-branched poly(ethylene oxide)-based polymer electrolytes

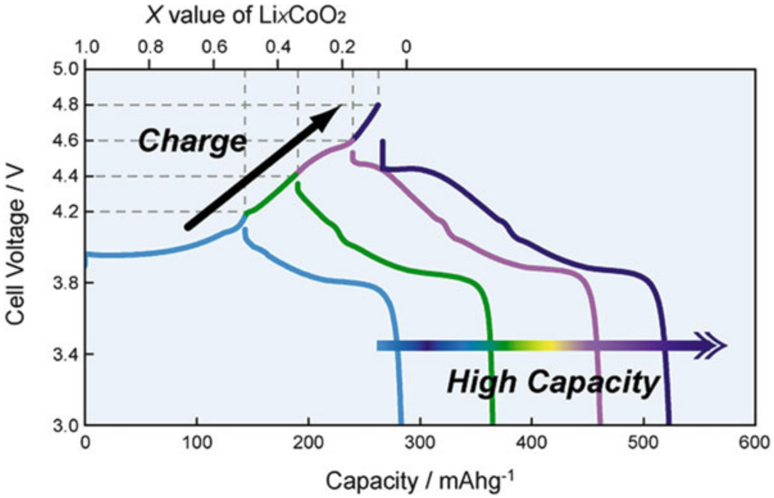

Fig. 6.4 Conceptual image figure for relationships between upper cutoff voltage and charge–discharge capacity of $LiCoO_2$

a PEO-based solid polymer electrolyte takes place at over 4 V vs. Li/Li^+ [11]. Therefore, the most commonly reported positive electrode materials for lithium polymer batteries using solid polymer electrolytes have been 3 V-class ones (e.g., V_2O_5 [31, 32] and $LiFePO_4$ [33]), and the R&D (laboratory scale) of stable 4 V-class positive electrode | polymer electrolyte interfaces is now in progress (e.g., $LiCoO_2$ [34, 35] and $LiMn_2O_4$ [36]). To improve the charge–discharge properties (higher capacities) under high oxidation conditions (high voltage over 4 V in the case of $LiCoO_2$: image figure) (Fig. 6.4), the polymer electrolyte/inorganic electrolyte composite concept was proposed as a guiding principle for the design of a battery with the capacity for high-voltage operation.

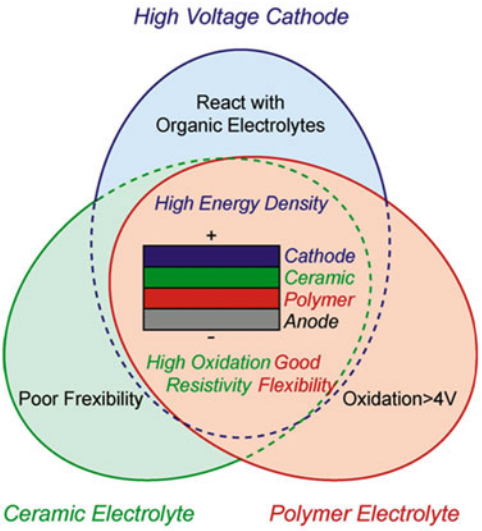

Fig. 6.5 A schematic image of inorganic/polymer composite concept

The reversibility of lithium polymer batteries in high-voltage charge–discharge operation was improved by placing an inorganic electrolyte between a positive electrode active material and a solid polymer electrolyte by spray coating [37, 38] or solid coating [39, 40] and by simple mixing [41, 42] (Fig. 6.5) with the surface of positive electrode active materials. On the other hand, electrochemical study with carbon-based negative electrode materials, which are used in commercially available lithium-ion secondary batteries with aprotic organic liquid electrolytes (e.g., EC/DMC-$LiPF_6$), is still in the early stages. Recently, Imanishi et al. reported good electrochemical reversibility between PEO-based electrolyte and surface-modified mesocarbon microbeads (MCMB) [43]. Our research group has also reported stable charge–discharge operation with [$LiFePO_4$ positive electrode | PEO-based electrolyte | graphite negative electrode] cells [44]. The use of carbon-based negative electrode materials, as in commercially available lithium-ion secondary batteries, makes it possible to utilize existing production facilities (e.g., electrode sheet coater), which may contribute to reducing production costs.

6.3 Highly Safe Lithium Secondary Batteries Using Room-Temperature Ionic Liquids

Room-temperature ionic liquids (RTILs) are liquid salts consisting entirely of cations (positive ions) and anions (negative ions) with interesting properties such as low flammability and low volatility (negligible vapor pressure), high ionic conductivity, and thermal and electrochemical stability [45]. Moreover, RTILs are known as designer solvents because their properties can be tuned by varying the

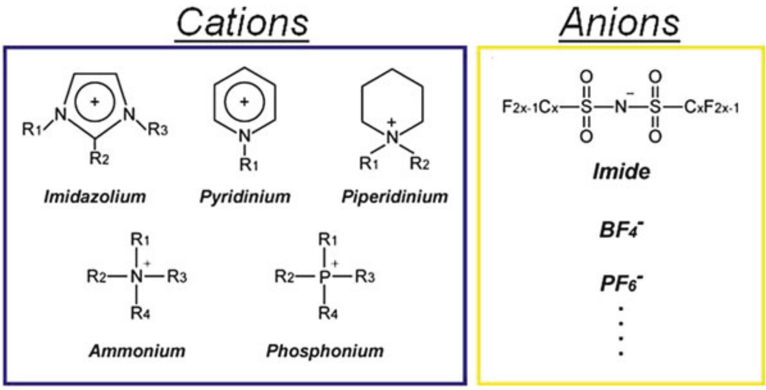

Fig. 6.6 Chemical structures of typical cations and anions for room-temperature ionic liquids

combinations of the cations and anions (typical chemical structures of cations and anions; Fig. 6.6). It has already been pointed out that the numbers of combinations exceed one million species.

In materials chemistry, RTILs have attracted much attention because of their promising physicochemical properties and various applications. For instance, studies on ionic aggregation [46–50] in RTILs and on their hybrid materials with polymers [51–54], glasses [55], and inorganic materials [56] have been reported. There has also been wide-ranging R&D of RTILs as solvents for synthesis [57, 58], as catalysts [59–61] (reaction field), and in energy storage-conversion systems as new task-specific electrolytes including lithium secondary batteries, electric double-layer capacitors [62–64], dye-sensitized solar cells [65, 66], fuel cells [67–70], electrochromic devices [71], and organic field-effect transistors [72]. In particular, the number of studies on lithium secondary battery electrolytes has increased in recent years.

The RTILs that have been reported so far (e.g., imidazolium-cation-based RTILs) lack electrochemical stability up to the reduction potential of lithium ions. Thus, various battery systems with different negative materials have been proposed. Nakagawa et al. [73] and Garcia et al. [74] have developed [$LiCoO_2$ | imidazolium-based RTIL | $Li_4Ti_5O_{12}$] cells to solve the problem of the reduction limit of imidazolium cations. In addition, Sato et al. reported a battery using a carbon anode on which a solid electrolyte interphase was formed with the addition of vinylene carbonate and ethylene carbonate to RTILs [75]. To increase the reduction potential, Sakaebe and Matsumoto proposed a RTIL mixture, *N*-methyl-*N*-propylpiperidinium bis(trifluoromethylsulfonyl)amide (PP_{13}-TFSA), containing lithium bis(trifluoromethylsulfonyl)amide (LiTFSA), and prepared [$LiCoO_2$ positive electrode | PP_{13}-TFSA/LiTFSA | lithium metal negative electrode] cells [76]. In this report, 30 charge–discharge cycles with a coulombic efficiency higher than 97 % is demonstrated. Also, Matsumoto et al. reported a mixture of a RTIL based on alkyl ammonium cations having an ether structure and a lithium salt for lithium battery electrolytes owing to the wide electrochemical window (particularly reduction potential) [77]. Our groups have also so far reported on advanced batteries with a long charge/discharge cycle life that use quaternary ammonium cations based on (*N*,*N*-diethyl-*N*-methyl-*N*-(2-methoxyethyl) ammonium) (DEME-TFSA) [78, 79] and imidazolium cations based on (1,2-dimethyl-3-propylimidazolium bis(trifluoromethylsulfonyl)amide) (DMPIm-TFSA) [80, 81].

In lithium secondary batteries that use RTILs, the application of graphite negative electrode materials results in incomplete interfacial formation. Therefore, the use of other negative electrode materials (e.g., lithium metal, $Li_4Ti_5O_{12}$) has been reported. On the other hand, Ishikawa et al. [82] and Guerfi et al. [83] have recently reported the favorable charge/discharge operation of [graphite electrode | room-temperature ionic liquid electrolyte | lithium metal electrode] cells using bis(fluorosulfonyl)amide (FSA) anion-based RTILs. The FSA anion-based RTILs have very low viscosity compared with those based on typical imide anions (e.g., TFSA) and are extremely promising RTILs from the viewpoint of realizing batteries with high-rate output characteristics [84].

Recently, it has been reported that one-to-one complexes of certain glymes (oligoethers) and lithium salts are liquid at room temperature and have high thermal stability, low volatility, and low flammability, which are promising for new electrolyte materials of lithium secondary batteries [85, 86]. These molten complexes behave like RTILs because all the glymes complex with lithium cations to form a complex cation, $[Li(glyme)]^+$, and there are no free glyme molecules.

Electrolytes are key materials for the improvement of the safety, cycle life, and power density of lithium-ion secondary batteries. These electrolytes are becoming increasingly important as battery sizes increase. The proper choice and design of electrolytes using a wide range of materials, including molecular liquids, ionic liquids, polymer electrolytes, inorganic solid electrolytes, and their hybrids, are essential for future development.

References

1. J.M. Tarascon, M. Armand, Building better batteries. Nature **451**, 652–657 (2001)
2. M. Winter, R.J. Brodd, What are batteries, fuel cells, and supercapacitors? Chem. Rev. **104**, 4245–4270 (2004)
3. J.F. Cousseau, C. Siret, P. Biensan, M. Broussely, Recent developments in Li-ion prismatic cells. J. Power. Sources **162**, 790–796 (2006)
4. D.P. Abraham, E.M. Reynolds, P.L. Schultz, A.N. Jansen, D.W. Dees, Temperature dependence of capacity and impedance data from fresh and aged high-power lithium-ion cells. J. Electrochem. Soc. **153**, A1610–A1616 (2006)
5. K. Zaghib, P. Charest, A. Guerfi, J. Shim, M. Perrier, K. Striebel, Safe Li-ion polymer batteries for HEV applications. J. Power. Sources **134**, 124–129 (2004)
6. K. Takei, K. Ishihara, K. Kumai, T. Iwahori, K. Miyake, T. Nakatsu, N. Terada, N. Arai, Performance of large-scale secondary lithium batteries for electric vehicles and home-use load-leveling systems. J. Power. Sources **119–121**, 887–892 (2003)
7. K. Adachi, H. Tajima, T. Hashimoto, K. Kobayashi, Development of 16 kWh power storage system applying Li-ion batteries. J. Power. Sources **119–121**, 897–901 (2003)

8. N. Terada, T. Yanagi, S. Arai, M. Yoshikawa, K. Ohta, N. Nakajima, A. Yanai, N. Arai, Development of lithium batteries for energy storage and EV applications. J. Power. Sources **100**, 80–92 (2001)
9. D.E. Fenton, J.M. Parker, P.V. Wright, Complexes of alkali metal ions with poly(ethylene oxide). Polymer **14**, 589 (1973)
10. M.B. Armand, J.M. Chabagno, M.J. Duclot, in *Fast Ion Transport in Solids*, ed. by P. Vashishta, J.-N. Mundy, G.K. Shenoy (Elsevier, New York, 1979), pp. 131–136
11. A. Nishimoto, K. Agehara, N. Furuya, T. Watanabe, M. Watanabe, High ionic conductivity of polyether-based network polymer electrolytes with hyperbranched side chains. Macromolecules **32**, 1541–1548 (1999)
12. M. Kono, E. Hayashi, M. Watanabe, Network polymer electrolytes with free chain ends as internal plasticizer. J. Electrochem. Soc. **145**, 1521–1527 (1998)
13. M. Watanabe, T. Hirakimoto, S. Mutoh, A. Nishimoto, Polymer electrolytes derived from dendritic polyether macromonomers. Solid State Ion. **148**, 399–404 (2002)
14. R. Spindler, D.F. Shriver, Investigations of a siloxane-based polymer electrolyte employing ^{13}C, ^{29}Si, ^{7}Li, and ^{23}Na solid-state NMR spectroscopy. J. Am. Chem. Soc. **110**, 3036–3043 (1988)
15. G.C. Rawsky, T. Fujinami, D.F. Shriver, Aluminosilicate/poly(ethylene glycol) copolymers: A new class of polyelectrolytes. Chem. Mater. **6**, 2208–2209 (1994)
16. P.M. Blonsky, D.F. Shriver, P. Austin, H.R. Allcock, Polyphosphazene solid electrolytes. J. Am. Chem. Soc. **106**, 6854–6855 (1984)
17. H.R. Allcock, S.E. Kuharcik, C.S. Reed, M.E. Napierala, Synthesis of polyphosphazenes with ethyleneoxy-containing side groups: New solid electrolyte materials. Macromolecules **29**, 3384–3389 (1996)
18. H.R. Allcock, W.R. Laredo, I.I.I.E.C. Kellam, R.V. Morford, Polynorbornenes bearing pendent cyclotriphosphazenes with oligoethyleneoxy side groups: Behavior as solid polymer electrolytes. Macromolecules **34**, 787–794 (2001)
19. H.R. Allcock, R. Prange, T.J. Hartle, Poly(phosphazene-ethylene oxide) di- and triblock copolymers as solid polymer electrolytes. Macromolecules **34**, 5463–5470 (2001)
20. M. Watanabe, T. Endo, A. Nishimoto, K. Miura, M. Yanagida, High ionic conductivity and electrode interface properties of polymer electrolytes based on high molecular weight branched polyether. J. Power. Sources **81–82**, 786–789 (1999)
21. F. Capuano, F. Croce, B. Scrosati, Composite polymer electrolytes. J. Electrochem. Soc. **138**, 1918–1922 (1991)
22. F. Croce, B. Scrosati, G. Mariotto, Electrochemical and spectroscopic study of the transport properties of composite polymer electrolytes. Chem. Mater. **4**, 1134–1136 (1992)
23. M.C. Borghini, M. Mastragostino, S. Passerini, B. Scrosati, Electrochemical properties of polyethylene oxide-$\mathrm{Li[(CF_3SO_2)_2N]}$-$\gamma$-$\mathrm{LiAlO_2}$ composite polymer electrolytes. J. Electrochem. Soc. **142**, 2118–2121 (1995)
24. F. Croce, G.B. Appetecchi, L. Persi, B. Scrosati, Nanocomposite polymer electrolytes for lithium batteries. Nature **394**, 456–458 (1998)
25. F. Croce, R. Curini, A. Martinelli, L. Persi, F. Ronci, B. Scrosati, R. Caminiti, Physical and chemical properties of nanocomposite polymer electrolytes. J. Phys. Chem. B **103**, 10632–10638 (1999)
26. B. Scrosati, F. Croce, L. Persi, Impedance spectroscopy study of PEO-based nanocomposite polymer electrolytes. J. Electrochem. Soc. **147**, 1718–1721 (2000)
27. X. Wei, D.F. Shriver, Highly conductive polymer electrolytes containing rigid polymers. Chem. Mater. **10**, 2307–2308 (1998)
28. A. Sato, T. Okumura, S. Nishimura, H. Yamamoto, N. Ueyama, Lithium ion conductive polymer electrolyte by side group rotation. J. Power. Sources **146**, 423–426 (2005)
29. K. Noda, T. Yasuda, Y. Nishi, Concept of polymer alloy electrolytes: Towards room temperature operation of lithium-polymer batteries. Electrochim. Acta **50**, 243–246 (2004)
30. S. Matsui, T. Muranaga, H. Higobashi, S. Inoue, T. Sakai, Liquid-free rechargeable Li polymer battery. J. Power. Sources **97–98**, 772–774 (2001)
31. P. Villano, M. Carewska, G.B. Appetecchi, S. Passerini, PEO-$\mathrm{LiN(SO_2CF_2CF_3)_2}$ polymer electrolytes III. Test in batteries. J. Electrochem. Soc. **149**, A1282–A1285 (2002)

32. P. André, P. Deniard, R. Brec, S. Lascaud, Study of the interface nickel/composite cathode of industrially made Li/V_2O_5 polymer (POE) batteries working at 90 °C. J. Power. Sources **105**, 66–74 (2002)
33. H. Miyashiro, Y. Kobayashi, T. Nakamura, S. Seki, Y. Mita, A. Usami, Basic properties of all-solid-state lithium polymer secondary batteries using $LiFePO_4$. Electrochemistry **74**, 321–325 (2006)
34. Y. Matoba, S. Matsui, M. Tabuchi, T. Sakai, Electrochemical properties of composite polymer electrolyte applied to rechargeable lithium polymer battery. J. Power. Sources **137**, 284–287 (2004)
35. Y. Aihara, J. Kuratomi, T. Bando, T. Iguchi, H. Yoshida, T. Ono, K. Kuwana, Investigation on solvent-free solid polymer electrolytes for advanced lithium batteries and their performance. J. Power. Sources **114**, 96–104 (2003)
36. Y. Kang, H.J. Kim, E. Kim, B. Oh, J.H. Cho, Photocured PEO-based solid polymer electrolyte and its application to lithium-polymer batteries. J. Power. Sources **92**, 255–259 (2001)
37. Y. Kobayashi, S. Seki, A. Yamanaka, H. Miyashiro, Y. Mita, T. Iwahori, Development of high-voltage and high-capacity all-solid-state lithium secondary batteries. J. Power. Sources **146**, 719–722 (2005)
38. H. Miyashiro, Y. Kobayashi, S. Seki, Y. Mita, A. Usami, M. Nakayama, M. Wakihara, Fabrication of all-solid-state lithium polymer secondary batteries using Al_2O_3-coated $LiCoO_2$. Chem. Mater. **17**, 5603–5605 (2005)
39. Y. Kobayashi, S. Seki, M. Tabuchi, H. Miyashiro, Y. Mita, T. Iwahori, High-performance genuine lithium polymer battery obtained by fine-ceramic-electrolyte coating of $LiCoO_2$. J. Electrochem. Soc. **152**, A1985–A1988 (2005)
40. S. Seki, Y. Kobayashi, H. Miyashiro, Y. Mita, T. Iwahori, Fabrication of high-voltage, high-capacity all-solid-state lithium polymer secondary batteries by application of the polymer electrolyte/inorganic electrolyte composite concept. Chem. Mater. **17**, 2041–2045 (2005)
41. S. Seki, Y. Kobayashi, H. Miyashiro, A. Usami, Y. Mita, N. Terada, Improvement in high-voltage performance of all-solid-state lithium polymer secondary batteries by mixing inorganic electrolyte with cathode materials. J. Electrochem. Soc. **153**, A1073–A1076 (2006)
42. H. Miyashiro, S. Seki, Y. Kobayashi, Y. Ohno, Y. Mita, A. Usami, All-solid-state lithium polymer secondary battery with $LiNi_{0.5}Mn_{1.5}O_4$ by mixing of Li_3PO_4. Electrochem. Commun. **7**, 1083–1086 (2005)
43. N. Imanishi, Y. Ono, K. Hanai, R. Uchiyama, Y. Liu, A. Hirano, Y. Takeda, O. Yamamoto, Surface-modified meso-carbon microbeads anode for dry polymer lithium-ion batteries. J. Power. Sources **178**, 744–750 (2008)
44. Y. Kobayashi, S. Seki, Y. Mita, Y. Ohno, H. Miyashiro, P. Charest, A. Guerfi, K. Zaghib, High reversible capacities of graphite and SiO/graphite with solvent-free solid polymer electrolyte for lithium-ion batteries. J. Power. Sources **185**, 542–548 (2008)
45. K.E. Johnson, What's an ionic liquid ? Electrochem. Soc. Interface **16**, 38–41 (2007)
46. A. Noda, K. Hayamizu, M. Watanabe, Pulsed-gradient spin-echo ^{1}H and ^{19}F NMR ionic diffusion coefficient, viscosity, and ionic conductivity of non-chloroaluminate room-temperature ionic liquids. J. Phys. Chem. B **105**, 4603–4610 (2001)
47. H. Tokuda, K. Hayamizu, K. Ishii, M.A.B.H. Susan, M. Watanabe, Physicochemical properties and structures of room temperature ionic liquids. 1. Variation of anionic species. J. Phys. Chem. B **108**, 16593–16600 (2004)
48. H. Tokuda, K. Hayamizu, K. Ishii, M.A.B.H. Susan, M. Watanabe, Physicochemical properties and structures of room temperature ionic liquids. 2. variation of alkyl chain length in imidazolium cation. J. Phys. Chem. B **109**, 6103–6110 (2005)
49. H. Tokuda, K. Ishii, M.A.B.H. Susan, S. Tsuzuki, K. Hayamizu, M. Watanabe, Physicochemical properties and structures of room-temperature ionic liquids. 3. Variation of cationic structures. J. Phys. Chem. B **110**, 2833–2839 (2006)

50. H. Tokuda, S. Tsuzuki, M.A.B.H. Susan, K. Hayamizu, M. Watanabe, How ionic are room-temperature ionic liquids? An indicator of the physicochemical properties. J. Phys. Chem. B **110**, 19593–19600 (2006)
51. A. Noda, M. Watanabe, Highly conductive polymer electrolytes prepared by in situ polymerization of vinyl monomers in room temperature molten salts. Electrochim. Acta **45**, 1265–1270 (2000)
52. S. Washiro, M. Yoshizawa, H. Nakajima, H. Ohno, Highly ion conductive flexible films composed of network polymers based on polymerizable ionic liquids. Polymer **45**, 1577–1582 (2004)
53. M.A.B.H. Susan, T. Kaneko, A. Noda, M. Watanabe, Ion gels prepared by in situ radical polymerization of vinyl monomers in an ionic liquid and their characterization as polymer electrolytes. J. Am. Chem. Soc. **127**, 4976–4983 (2005)
54. T. Fukushima, A. Kosaka, Y. Ishimura, T. Yamamoto, T. Takigawa, N. Ishii, T. Aida, Molecular ordering of organic molten salts triggered by single-walled carbon nanotubes. Science **300**, 2072–2074 (2003)
55. A. Hayashi, M. Yoshizawa, C.A. Angell, F. Mizuno, T. Minami, M. Tatsumisago, High conductivity of superionic-glass-in-ionic-liquid solutions. Electrochem. Solid-State Lett. **6**, E19–E22 (2003)
56. Y. Tominaga, S. Asai, M. Sumita, S. Panero, B. Scrosati, Fast ionic conduction in PEO-based composite electrolyte filled with ionic liquid-modified mesoporous silica. Electrochem. Solid-State Lett. **8**, A22–A25 (2005)
57. K.R. Seddon, A. Stark, M.J. Torres, Influence of chloride, water, and organic solvents on the physical properties of ionic liquids. Pure Appl. Chem. **72**, 2275–2287 (2000)
58. J. Dupont, R.F. De Souza, P.A.Z. Suarez, Ionic liquid (molten salt) phase organometallic catalysis. Chem. Rev. **102**, 3667–3692 (2002)
59. P. Wasserscheid, W. Keim, Ionic liquids – new 'solutions' for transition metal catalysis. Angew. Chem. Int. Ed. **39**, 3773–3789 (2000)
60. T. Welton, Ionic liquids in catalysis. Coord. Chem. Rev. **248**, 2459–2477 (2004)
61. R.A. Sheldon, R. Madeira Lau, M.J. Sorgedrager, F. Van Rantwijk, K.R. Seddon, Biocatalysis in ionic liquids. Green Chem. **4**, 147–151 (2002)
62. A.B. McEwen, H.L. Ngo, K. LeCompte, J.L. Goldman, Electrochemical properties of imidazolium salt electrolytes for electrochemical capacitor applications. J. Electrochem. Soc. **146**, 1687–1695 (1999)
63. M. Ue, M. Takeda, T. Takahashi, M. Takehara, Ionic liquids with low melting points and their application to double-layer capacitor electrolytes. Electrochem. Solid-State Lett. **5**, A119–A121 (2002)
64. M. Ue, M. Takeda, A. Toriumi, A. Kominato, R. Hagiwara, Y. Ito, Application of low-viscosity ionic liquid to the electrolyte of double-layer capacitors. J. Electrochem. Soc. **150**, A499–A502 (2003)
65. D. Kuang, P. Wang, S. Ito, S.M. Zakeeruddin, M. Grätzel, Stable mesoscopic dye-sensitized solar cells based on tetracyanoborate ionic liquid electrolyte. J. Am. Chem. Soc. **128**, 7732–7733 (2006)
66. T. Kato, T. Kado, S. Tanaka, A. Okazaki, S. Hayase, Quasi-solid dye-sensitized solar cells containing nanoparticles modified with ionic liquid-type molecules. J. Electrochem. Soc. **153**, A626–A630 (2006)
67. M. Doyle, S.K. Choi, G. Proulx, High-temperature proton conducting membranes based on perfluorinated ionomer membrane-ionic liquid composites. J. Electrochem. Soc. **147**, 34–37 (2000)
68. A. Noda, M.A.B.H. Susan, K. Kudo, S. Mitsushima, K. Hayamizu, M. Watanabe, Brønsted acid–base ionic liquids as proton-conducting nonaqueous electrolytes. J. Phys. Chem. B **107**, 4024–4033 (2003)
69. R. Hagiwara, T. Nohira, K. Matsumoto, Y. Tamba, A fluorohydrogenate ionic liquid fuel cell operating without humidification. Electrochem. Solid-State Lett. **8**, A231–A233 (2005)

70. M.A. Navarra, S. Panero, B. Scrosati, Novel, ionic-liquid-based, gel-type proton membranes. Electrochem. Solid-State Lett. **8**, A324–A327 (2005)
71. W. Lu, A.G. Fadeev, B. Qi, B.R. Mattes, Fabricating conducting polymer electrochromic devices using ionic liquids. J. Electrochem. Soc. **151**, H33–H39 (2004)
72. S. Ono, S. Seki, R. Hirahara, Y. Tominari, J. Takeya, High-mobility, low-power, and fast-switching organic field-effect transistors with ionic liquids. Appl. Phys. Lett. **92**, 103313-1-3 (2008).
73. H. Nakagawa, S. Izuchi, K. Kuwana, T. Nukuda, Y. Aihara, Liquid and polymer gel electrolytes for lithium batteries composed of room-temperature molten salt doped by lithium salt. J. Electrochem. Soc. **150**, A695–A700 (2003)
74. B. Garcia, S. Lavallée, G. Perron, C. Michot, M. Armand, Room temperature molten salts as lithium battery electrolyte. Electrochim. Acta **49**, 4583–4588 (2004)
75. T. Sato, T. Maruo, S. Marukane, K. Takagi, Ionic liquids containing carbonate solvent as electrolytes for lithium ion cells. J. Power. Sources **138**, 253–261 (2004)
76. H. Sakaebe, H. Matsumoto, *N*-methyl-*N*-propylpiperidinium bis(trifluoromethanesulfonyl) imide (PP13-TFSI) – novel electrolyte base for Li battery. Electrochem. Commun. **5**, 594–598 (2004)
77. H. Matsumoto, M. Yanagida, K. Tanimoto, M. Nomura, Y. Kitagawa, Y. Miyazaki, Highly conductive room temperature molten salts based on small trimethylalkylammonium cations and bis(trifluoromethylsulfonyl)imide. Chem. Lett. **29**, 922–923 (2000)
78. S. Seki, Y. Kobayashi, H. Miyashiro, Y. Ohno, Y. Mita, A. Usami, N. Terada, M. Watanabe, Reversibility of lithium secondary batteries using a room-temperature ionic liquid mixture and lithium metal. Electrochem. Solid-State Lett. **8**, A577–A578 (2005)
79. S. Seki, Y. Ohno, H. Miyashiro, Y. Kobayashi, A. Usami, Y. Mita, N. Terada, K. Hayamizu, S. Tsuzuki, M. Watanabe, Quaternary ammonium room-temperature ionic liquid/lithium salt binary electrolytes: electrochemical study. J. Electrochem. Soc. **155**, A421–A427 (2008)
80. S. Seki, Y. Kobayashi, H. Miyashiro, Y. Ohno, A. Usami, Y. Mita, N. Kihira, M. Watanabe, N. Terada, Lithium secondary batteries using modified-imidazolium room-temperature ionic liquid. J. Phys. Chem. B **110**, 10228–10230 (2006)
81. S. Seki, Y. Ohno, Y. Kobayashi, H. Miyashiro, A. Usami, Y. Mita, H. Tokuda, M. Watanabe, K. Hayamizu, S. Tsuzuki, M. Hattori, N. Terada, Imidazolium-based room-temperature ionic liquid for lithium secondary batteries. J. Electrochem. Soc. **154**, A173–A177 (2007)
82. M. Ishikawa, T. Sugimoto, M. Kikuta, E. Ishiko, M. Kono, Pure ionic liquid electrolytes compatible with a graphitized carbon negative electrode in rechargeable lithium-ion batteries. J. Power. Sources **162**, 658–662 (2006)
83. A. Guerfi, S. Duchesne, Y. Kobayashi, A. Vijh, K. Zaghib, $LiFePO_4$ and graphite electrodes with ionic liquids based on bis(fluorosulfonyl)imide (FSI)- for Li-ion batteries. J. Power. Sources **175**, 866–873 (2008)
84. H. Matsumoto, H. Sakaebe, K. Tatsumi, M. Kikuta, E. Ishiko, M. Kono, Fast cycling of $Li/LiCoO_2$ cell with low-viscosity ionic liquids based on bis(fluorosulfonyl)imide $[FSI]^-$. J. Power. Sources **160**, 1308–1313 (2006)
85. T. Tamura, T. Hachida, K. Yoshida, N. Tachikawa, K. Dokko, M. Watanabe, New glyme-cyclic imide lithium salt complexes as thermally stable electrolytes for lithium batteries. J. Power. Sources **195**, 6095 (2010)
86. T. Tamura, K. Yoshida, T. Hachida, M. Tsuchiya, M. Nakamura, Y. Kazue, N. Tachikawa, K. Dokko, M. Watanabe, Physicochemical properties of glyme-Li salt complexes as a new family of room-temperature ionic liquids. Chem. Lett. **39**, 753 (2010)

Chapter 7
Development of Glass-Based Solid Electrolytes for Lithium-Ion Batteries

Masahiro Tatsumisago and Akitoshi Hayashi

7.1 Introduction

Lithium-ion batteries are widely used as a power source with a high energy density and high power density [1]. To reduce the emission of CO_2, large-scale lithium-ion batteries have been developed for application in automotive propulsion and stationary load leveling for intermittent power generation from solar or wind energy. The safety of lithium-ion batteries has become more serious with increases in their size. All-solid-state rechargeable lithium batteries have attracted much attention because the replacement of an organic liquid electrolyte with a safer and more reliable inorganic solid electrolyte simplifies battery design and improves the safety and durability of the battery [2, 3]. A key material in developing solid-state batteries is a solid electrolyte with high Li^+ ion conductivity at room temperature. Inorganic solid electrolytes have been widely studied, and several solid electrolytes with high Li^+ ion conductivity have been reported so far [4–6]. Figure 7.1 shows the temperature dependence of the electrical conductivity of typical inorganic solid electrolytes. In general, sulfide electrolytes have higher conductivity than oxide materials, although limited oxide crystalline electrolytes exhibit high conductivity. Sulfide crystals, glasses, and glass ceramics (crystallized glasses) with high Li^+ ion concentration basically show a high Li^+ ion conductivity of over 10^{-4} S cm^{-1} at room temperature. In particular, glass-ceramic electrolytes in a Li_2S-P_2S_5 system have a maximum conductivity of 5.4×10^{-3} S cm^{-1}. Moreover, inorganic solid electrolytes have an advantage in the lithium transport number of unity: only target ions (Li^+ ion) are mobile in solid electrolytes. A conventional organic liquid electrolyte, such as 1 M $LiPF_6$ in carbonate solvents, has a conductivity of 10^{-2} S cm^{-1}, as shown in Fig. 7.1.

M. Tatsumisago (🖂) • A. Hayashi
Department of Applied Chemistry, Osaka Prefecture University,
1-1 Gakuen-cho, Naka-ku, Sakai, Osaka 599-8531, Japan
e-mail: tatsu@chem.osakafu-u.ac.jp

T. Osaka and Z. Ogumi (eds.), *Nanoscale Technology for Advanced Lithium Batteries*,
Nanostructure Science and Technology 182, DOI 10.1007/978-1-4614-8675-6_7,

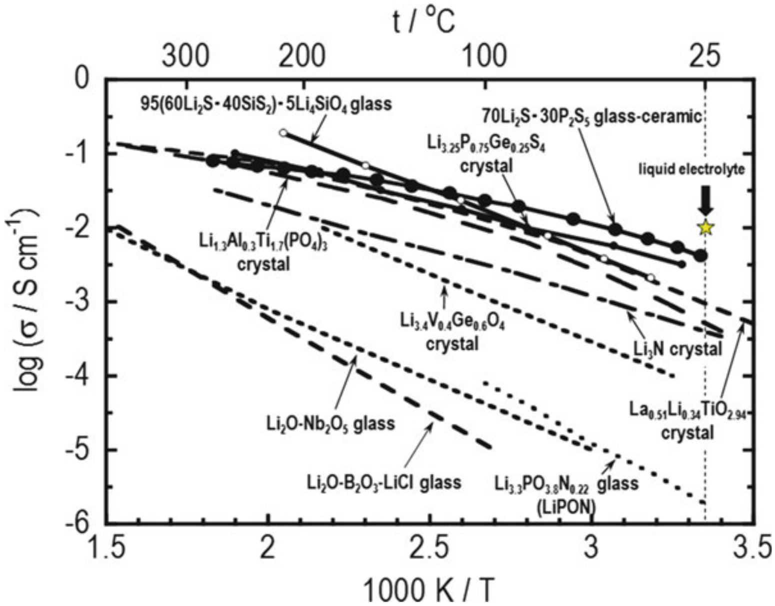

Fig. 7.1 Temperature dependence of conductivity for typical inorganic solid electrolytes

However, liquid electrolytes are a dual ion conductor, and their lithium transference numbers are thus below 0.5. On the basis of the lithium transference number, Li_2S-P_2S_5 glass-ceramic electrolytes are revealed to have almost the same Li^+ ion conductivity as organic liquid electrolytes. Sulfide electrolytes also have a wide electrochemical window of over 5 V.

In this chapter, the development of inorganic solid electrolytes is reviewed. Their advantages as a solid electrolyte and preparation techniques of glass-based solid electrolytes are described. The recent development of sulfide glass-ceramic electrolytes with the highest Li^+ ion conductivity is demonstrated. Finally, the application of glass-ceramic electrolytes for all-solid-state rechargeable lithium batteries is reported.

7.2 Classification of Inorganic Solid Electrolytes

Several types of inorganic compounds in crystalline, glass, and glass-ceramic forms have been used as Li^+ ion conductors. Oxide and sulfide compounds have been widely studied as solid electrolytes. The conductivity at 25 °C of typical oxide and sulfide solid electrolytes are listed in Table 7.1 [7–22]. The greatest merit of oxide electrolytes is their high chemical stability in air. Some crystalline phosphates with a NASICON (*Na* *s*uper *i*onic *con*ductor)-type structure, such as $Li_{1+x}Al_xTi_{2-x}(PO_4)_3$

Table 7.1 Conductivity at 25 °C of oxide and sulfide solid electrolytes

Composition	Conductivity at 25 °C (S cm^{-1})	Classification	Reference
$La_{0.51}Li_{0.34}TiO_{2.94}$	1.4×10^{-3}	Crystal (perovskite)	[7]
$Li_{1,3}Al_{0.3}Ti_{1.7}(PO_4)_3$	7×10^{-4}	Crystal (NASICON)	[8]
$Li_7La_3Zr_2O_{12}$	3×10^{-4}	Crystal (garnet)	[9]
$42.5Li_2O \cdot 57.5B_2O_3$	7.1×10^{-8}	Glass	[4]
$50Li_4SiO_4 \cdot 50Li_3BO_3$	4.0×10^{-6}	Glass	[10]
$Li_{2.9}PO_{3.3}N_{0.46}$	3.3×10^{-6}	Amorphous (thin film)	[11]
$Li_{3.6}Si_{0.6}P_{0.4}O_4$	5.0×10^{-6}	Amorphous (thin film)	[12]
$Li_{1.07}Al_{0.69}Ti_{1.46}(PO_4)_3$	1.3×10^{-3}	Glass-ceramic	[13]
$Li_{1.5}Al_{0.5}Ge_{1.5}(PO_4)_3$	4.0×10^{-4}	Glass-ceramic	[14]
$Li_{3.25}Ge_{0.25}P_{0.25}S_4$	2.2×10^{-3}	Crystal (thio-LISICON)	[15]
$50Li_2S \cdot 50GeS_2$	4.0×10^{-5}	Glass	[16]
$70Li_2S \cdot 30P_2S_5$	1.6×10^{-4}	Glass	[17]
$30Li_2S \cdot 26B_2S_3 \cdot 44LiI$	1.7×10^{-3}	Glass	[18]
$63Li_2S \cdot 36SiS_2 \cdot 1Li_3PO_4$	1.5×10^{-3}	Glass	[19]
$57Li_2S \cdot 38SiS_2 \cdot 5Li_4SiO_4$	1.0×10^{-3}	Glass	[20]
$Li_{3.25}P_{0.95}S_4$	1.3×10^{-3}	Glass-ceramic	[21]
$Li_7P_3S_{11}$	5.4×10^{-3}	Glass-ceramic	[22]

(LATP) and $Li_{1+x}Al_xGe_{2-x}(PO_4)_3$ (LAGP), are excellent Li^+ ion conductors. Perovskite $Li_{0.5-3x}La_{0.5+x}TiO_3$ (LLT) exhibits a high level of bulk conductivity of 10^{-3} S cm^{-1}, but total conductivity decreases by two orders of magnitude. The higher bulk conductivity indicates that grain boundaries impede the transport of lithium ions. Effective sintering to decrease the grain boundary is important to increase the total conductivity of those oxide crystalline electrolytes. An alternative idea is the use of glass-ceramic electrolytes. By crystallizing the LATP or LAGP phase from a precursor glass, the effect of grain-boundary resistance on total conductivity is highly reduced. Most oxide crystalline electrolytes with high conductivity include transition metal elements such as Ti, and this restricts the operating voltage range in solid-state batteries. Those electrolytes are not compatible with Li metal negative electrode because of the easy reduction of the transition metal. Some oxides forming a garnet-related structure also have a high Li^+ ion conductivity. The garnet crystal $Li_7La_3Zr_2O_{12}$ has the advantage of a relatively high conductivity of 3×10^{-4} S cm^{-1} and a high stability with Li metal. Most oxide glass electrolytes show low conductivity at room temperature, but some glasses with high Li^+ ion concentration, such as lithium ortho-oxosalts, have a relatively high conductivity of 10^{-6} S cm^{-1}. LiPON (*li*thium *p*hosphorous *o*xy*n*itride) amorphous thin film also has the same level of conductivity. LiPON has been used in thin-film batteries because reducing the electrolyte thickness decreases the resistance.

Sulfide solid electrolytes have the benefit of a high conductivity of over 10^{-4} S cm^{-1}, although the preparation and storage of sulfide compounds should be done in an inert-gas atmosphere. Another merit of sulfide electrolytes is the easy reduction of grain-boundary resistance by conventional cold-press of electrolyte powders. Sulfide crystals, which are referred to as thio-LISICON, have been reported, and $Li_{3.25}Ge_{0.25}P_{0.75}S_4$ has a high conductivity of 2.2×10^{-3} S cm^{-1}. Sulfide glasses with a high Li^+ ion concentration show high conductivity. In particular, the addition of lithium halides, such as LiI, and lithium ortho-oxosalts, such as Li_4SiO_4, increases the conductivity to more than 10^{-3} S cm^{-1}. Sulfide glass ceramics with $Li_7P_3S_{11}$ phases have the highest conductivity, 5.4×10^{-3} S cm^{-1}. Very recently, it was revealed that selected compositions of Li_2S-P_2S_5 electrolytes had a relatively high chemical stability in air [23]. Further improvement in the chemical stability as well as conductivity of sulfide electrolytes is desired. Oxysulfide glass and sulfide glass-ceramic electrolytes will be demonstrated in detail in Sect. 7.5.

7.3 Advantage of Glass Solid Electrolytes

Glasses have several advantages as solid electrolytes for all-solid-state batteries. Glass electrolytes show a relatively high conductivity in a wide composition range, whereas crystalline electrolytes have a high conductivity at a limited composition, giving favorable conduction paths for lithium ions. A principal strategy to develop the conductivity of glass electrolytes is to increase the number and mobility of lithium ions. Figure 7.2 shows the composition dependence of electrical conductivity at 25 °C for the oxide and sulfide glasses in the systems Li_2O-SiO_2, Li_2O-P_2O_5, Li_2S-SiS_2, and Li_2S-P_2S_5. By increasing the lithium-ion concentration in the glasses, the conductivity of the glasses in all the systems monotonously increases. The

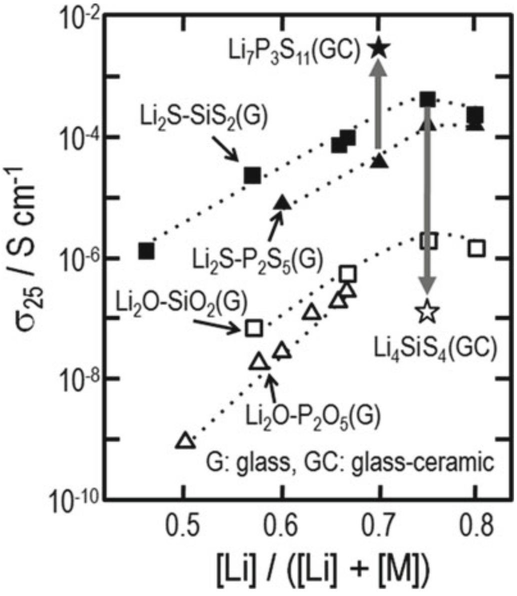

Fig. 7.2 Composition dependence of conductivity at 25 °C for oxide and sulfide glass-based electrolytes

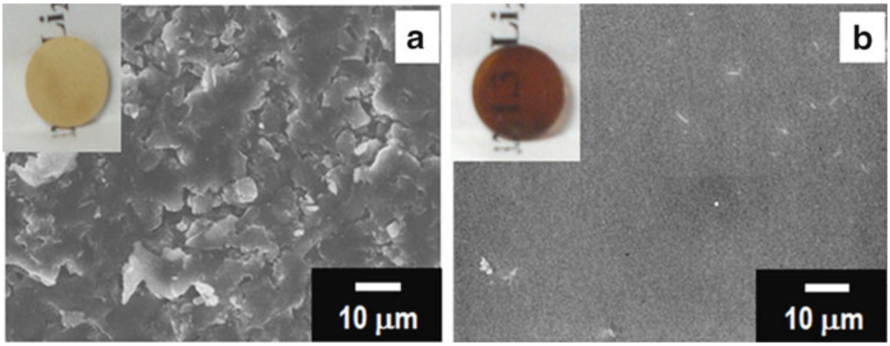

Fig. 7.3 SEM images of cross section of a powder-compressed pellet of Li_2S-P_2S_5 glass prepared by (**a**) cold press at room temperature and (**b**) hot press at 210 °C for 4 h. Inset figure shows photographs of pellet

conductivity drastically increases by changing the glass matrix from oxides to sulfides. Lithium ions acting as a so-called hard acid, which is classified from the viewpoint of the hard and soft acid and base theory of Pearson, would be more compatible with sulfide ions acting as a soft base [24]. The conductivity of Li_2S-SiS_2 sulfide glass at a composition of $[Li]/([Li]+[M])=0.75$ is on the order of 10^{-4} S cm^{-1}, which is two orders of magnitude higher than that of Li_2O-SiO_2 oxide glass with the same lithium-ion concentration. The activation energy for conduction of the sulfide glass (33 kJ mol^{-1}) was lower than that of the oxide glass (48 kJ mol^{-1}), suggesting that the mobility of lithium ions increases by replacing the oxide matrix with a sulfide one. The conductivity of sulfide glass ceramics as shown in this figure will be discussed in Sect. 7.5.2.

Glasses have another benefit – easy softening at the glass transition temperature (T_g). In general, glass transforms into supercooled liquid beyond T_g. Figure 7.3 shows SEM images of a cross section of a compressed powder pellet of Li_2S-P_2S_5 glass prepared by (a) cold press at room temperature and (b) hot press at 210 °C for 4 h [25]. The inset figure shows photographs of the pellets. A yellowish pellet was obtained by cold press, while a translucent pellet was obtained by hot press. The cross-sectional SEM image reveals that the cold-pressed pellet has grain boundary. On the other hand, a smooth cross section is observed in the hot-pressed pellet. Softening adhesion among $80Li_2S{\cdot}20P_2S_5$ glass particles occurred by pressing at around T_g, and obvious grain boundaries and voids almost disappeared. The hot-pressed pellet showed a higher conductivity of 8.8×10^{-4} S cm^{-1} at 25 °C compared to a conductivity of 3.7×10^{-4} S cm^{-1} in the cold-pressed pellet. The electrical conductivity increased by decreasing the grain boundary and voids. Moreover, this softening technique is applicable to form intimate contact at the electrode/electrolyte interface in all-solid-state batteries. Using the viscous flow of the supercooled liquid of electrolytes onto solid-state active materials is effective in forming a liquid–solid interface, and the interface would give close solid–solid contact by cooling down to room temperature.

By heating of a supercooled liquid of electrolyte, a metastable or high-temperature phase with high conductivity tends to precipitate as a primary crystal. As a typical example, α-AgI (high-temperature phase) with extremely high Ag^+ ion conductivity was stabilized at room temperature by crystallization of AgI-based oxide glasses [26]. For Li^+ ion conductors, a high-temperature phase of $Li_7P_3S_{11}$ was prepared by careful heat treatment of Li_2S-P_2S_5 glass electrolytes, and the obtained glass-ceramic electrolyte exhibited an extremely high conductivity of 5.4×10^{-3} S cm^{-1}, as shown in Fig. 7.1 and Table 7.1. Therefore, glass electrolytes are quite useful as precursors for precipitating superionic crystals, which are difficult to synthesize by conventional solid-state reactions.

7.4 Preparation Technique for Glass Electrolytes

A conventional technique to prepare glass electrolytes is the melt quenching method. Increasing the lithium-ion concentration in glasses is a key point in achieving a higher electrical conductivity and lower activation energy for Li^+ transport. To synthesize glass electrolytes with a high Li^+ ion concentration, a rapid quenching technique using a twin-roller apparatus (the cooling rate is greater than 10^5 K s^{-1}) is useful to inhibit crystallization during the cooling process from the melt and expand the glass-forming region [27]. However, amorphization of lithium ortho-oxosalts such as Li_3PO_4 with the highest Li^+ ion concentration is difficult to achieve by rapid quenching. The combination of two lithium oxosalts is effective in facilitating glass preparation by rapid quenching. For example, the ionic glasses in a Li_4SiO_4-Li_3BO_3 system were prepared using this technique. A further advantage of combining two ortho-oxosalts is the enhancement of conductivity; this phenomenon is called the mixed anion effect [10]. Figure 7.4 shows the composition dependence of conductivity at 400 K and the Li^+ ion concentration for oxide glasses in a Li_4SiO_4-Li_3BO_3 system. The glass exhibited the maximum conductivity in a composition with equal moles of two anions of SiO_4^{4-} and BO_3^{3-}, despite a constant lithium-ion concentration. An alternative technique for synthesizing amorphous lithium ortho-oxosalts is a gas-phase process. Amorphous thin films such as Li_4SiO_4-Li_3PO_4 have been prepared by pulsed laser deposition [28] and RF magnetron sputtering [12], and their conductivities are 10^{-6} S cm^{-1} at room temperature.

Mechanochemical synthesis using a planetary ball mill apparatus has the advantages as a new glass preparation technique that the whole process is performed at room temperature and fine electrolyte powders that can be directly applied to solid-state batteries are obtained without an additional pulverizing procedure. The Li_2S-P2S5 glasses can be prepared by a quenching method, but the melting reaction must be carried out in sealed quartz tubes because of the high vapor pressure of P_2S_5 at high temperatures. These glasses were synthesized by mechanical milling at room temperature and normal pressure [29]. The $75Li_2S \cdot 25P_2S_5$ (mol%) glass at an ortho-composition was prepared via mechanochemistry, while glass preparation for this composition is difficult by melt quenching. The local structure around the

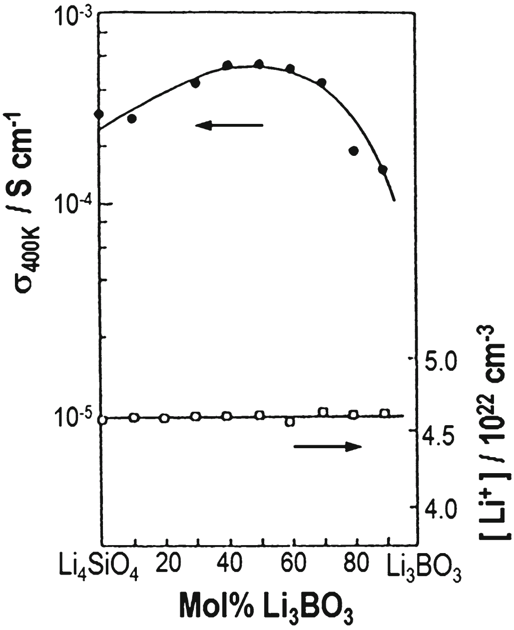

Fig. 7.4 Composition dependence of conductivity at 400 K and lithium-ion concentration of oxide glasses in Li_4SiO_4-Li_3BO_3 system

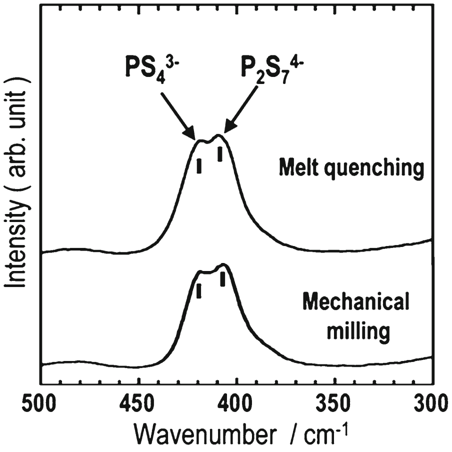

Fig. 7.5 Raman spectra of $70Li_2S{\cdot}30P_2S_5$ glasses prepared by mechanical milling and melt quenching

phosphorus atoms of the milled glass was almost the same as that of the melt-quenched glass. Figure 7.5 shows the Raman spectra of the $70Li_2S{\cdot}30P_2S_5$ glasses prepared by mechanical milling and melt quenching. The spectrum of the milled glass is quite similar to that of the quenched glass, and both glasses are composed of two thiophosphate ions of PS_4^{3-} and $P_2S_7^{4-}$.

The optimization of mechanical-milling conditions is important to prepare homogeneous glass electrolytes. Figure 7.6 shows the differential thermal analysis

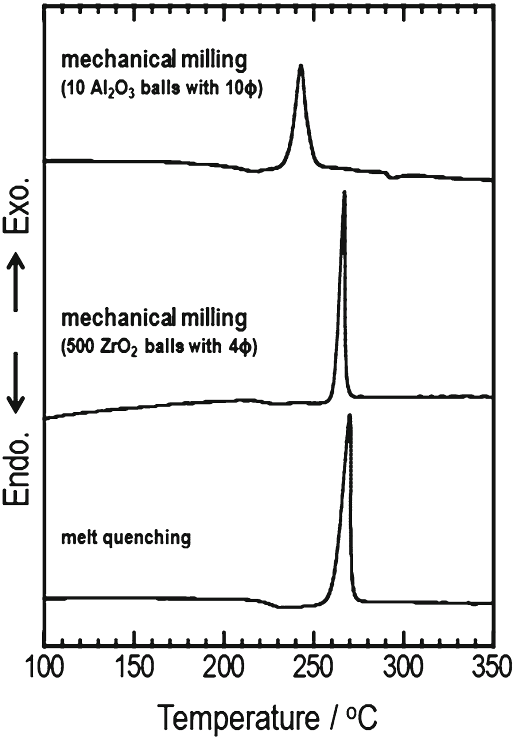

Fig. 7.6 Differential thermal analysis curves of $70Li_2S{\cdot}30P_2S_5$ glasses prepared by mechanical milling with ZrO_2 or Al_2O_3 media. A curve of the glass prepared by melt quenching is also shown for comparison

(DTA) curves of the $70Li_2S{\cdot}30P_2S_5$ glasses prepared by mechanical milling with two different experimental conditions [22]. A high-energy planetary ball mill apparatus was used, and the milling process was carried out at room temperature in a dry Ar-filled glove box. The curve of the $70Li_2S{\cdot}30P_2S_5$ glass prepared by melt quenching is also shown for comparison. The glass prepared by milling using an Al_2O_3 vessel and 10 Al_2O_3 balls (10 mm in diameter) at a rotation speed of 370 rpm shows a glass transition temperature (T_g) of 200 °C and a crystallization temperature (T_c) of 235 °C. These temperatures are somewhat lower than those of the glass prepared by melt quenching. On the other hand, the glass prepared by milling with a ZrO_2 vessel and 500 ZrO_2 balls (4 mm in diameter) at a rotation speed of 510 rpm exhibits a T_g of 218 °C and T_c of 255 °C, which are almost the same as those of the glass prepared by melt quenching. The glass prepared with ZrO_2 media shows clearer glass transition and crystallization than the glass prepared with Al_2O_3 media, suggesting that a homogeneous glass with narrowly distributed T_g was obtained using ZrO_2 media. The milling time to obtain glasses in the former case was 8 h, which is shorter than that in the latter case, which was 20 h. The glass ceramics were prepared by heating the obtained glasses at 360 °C. The glass ceramic derived from the glass with ZrO_2 media exhibited a higher conductivity of 5.4×10^{-3} S cm^{-1} than that with Al_2O_3 media (3.2×10^{-3} S cm^{-1}).

7.5 Development of Glass-Based Electrolytes

In glass-based solid electrolytes, oxysulfide glasses and sulfide glass ceramics have a high conductivity of over 10^{-3} S cm^{-1} at room temperature (Fig. 7.1 and Table 7.1). The glass-based materials are promising solid electrolytes for all-solid-state rechargeable lithium batteries. In this section, the relationship between the conductivity and structure for those glass-based electrolytes is demonstrated.

7.5.1 Oxysulfide Glass Electrolytes

Oxysulfide glasses at a composition of (100-z)($0.6Li_2S \cdot 0.4SiS_2$)·zLi_xMO_y (Li_xMO_y: lithium ortho-oxosalt) were prepared by rapid quenching with a twin-roller apparatus [30, 31]. A flakelike glass with a thickness of 20 μm was obtained. Figure 7.7 shows the composition dependence of the conductivity at room temperature (σ_{25}) and activation energy for conduction (Ea) for the oxysulfide glasses.

The addition of 5 mol% of Li_4SiO_4, Li_3PO_4, Li_4GeO_4, Li_3BO_3, and Li_3AlO_3 to $60Li_2S \cdot 40SiS_2$ increases the glass conductivity. The obtained oxysulfide glass shows a high conductivity of 1.0×10^{-3} S cm^{-1} at room temperature. The addition of larger amounts of Li_xMO_y to the Li_2S-SiS_2 sulfide system decreases the conductivity. The composition dependence of Ea corresponds to that of the conductivity. The addition of oxide to sulfide is expected to monotonically decrease the conductivity because oxide glasses have a much lower conductivity than sulfide glasses. It is noteworthy that oxysulfide glasses with 5 mol% of Li_xMO_y maintain a high

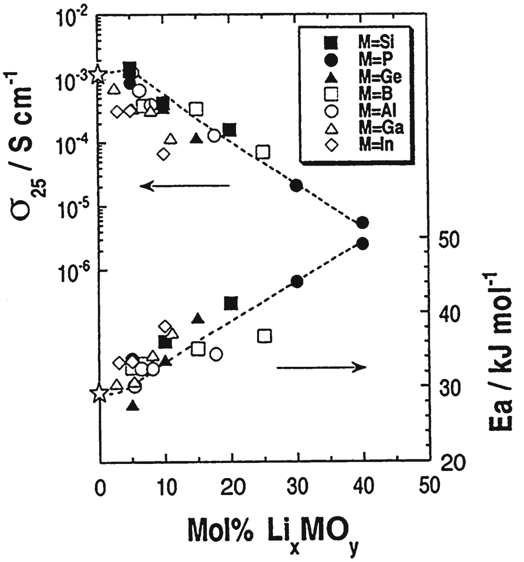

Fig. 7.7 Composition dependence of conductivity at room temperature (σ_{25}) and activation energy for conduction (Ea) for (100-z) ($0.6Li_2S \cdot 0.4SiS_2$)·zLi_xMO_y oxysulfide glasses

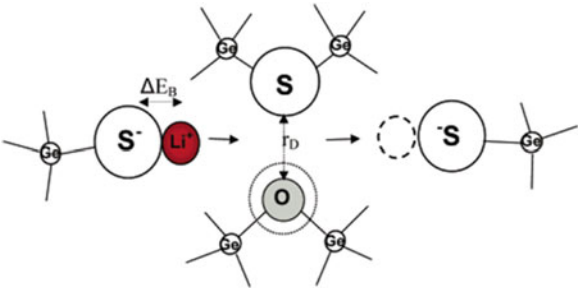

Fig. 7.8 Simplified pictorial view of ionic conduction energy for $50Li_2S{\cdot}45GeS_2{\cdot}5GeO_2$ oxysulfide glass [32]

conductivity of 10^{-3} S cm^{-1}. The local structure of the oxysulfide glass with 5 mol% Li_4SiO_4 was analyzed by nuclear magnetic resonance and X-ray photoelectron spectroscopy [30, 31]. The main structural units of $Si_2OS_6^{6-}$, where silicon atoms are coordinated with nonbridging sulfur atoms and a bridging oxygen atom, would give favorable conduction paths for Li^+ ions in the oxysulfide glass.

Conductivity enhancement was also reported in a Li_2S-GeS_2-GeO_2 oxysulfide system. The replacement of 5 mol% GeS_2 with GeO_2 increased conductivity and decreased activation energy for the conduction of $50Li_2S{\cdot}(50\text{-}x)GeS_2{\cdot}xGeO_2$ oxysulfide glasses. A conduction mechanism of Li^+ ions in oxysulfide glass has been proposed on the basis of the Anderson and Stuart energy barrier model. Figure 7.8 shows a simplified pictorial view of the ionic conduction energy for the $50Li_2S{\cdot}45GeS_2{\cdot}5GeO_2$ oxysulfide glass [32]. Ionic conduction requires the electrostatic binding energy (ΔE_B) to separate the Li^+ ion from its charge-compensating anion site (nonbridging sulfur) and move to the next site and the strain energy (ΔE_S) to open up a doorway (doorway radius: r_D) in the structure large enough for the ions to pass through. The introduction of bridging oxygen instead of bridging sulfur expands the conduction path, and a slightly increasing r_D in the strain energy term is proposed as a cause of the decreasing activation energy, which results in increasing ionic conductivity.

7.5.2 Sulfide Glass-Ceramic Electrolytes

An effective way to improve the conductivity of solid electrolytes is by the precipitation of a metastable or high-temperature phase from a glass precursor by crystallization. In general, crystallization of glass materials is known to decrease ionic conductivity. As shown in Fig. 7.2, the crystallization of the $60Li_2S{\cdot}40SiS_2$ glass decreased the conductivity by three orders of magnitude [33]. On the other hand, enhancement of conductivity by crystallization was found in $70Li_2S{\cdot}30P_2S_5$ ($Li_7P_3S_{11}$) glass [21]. The enhancement in conductivity is attributable to the

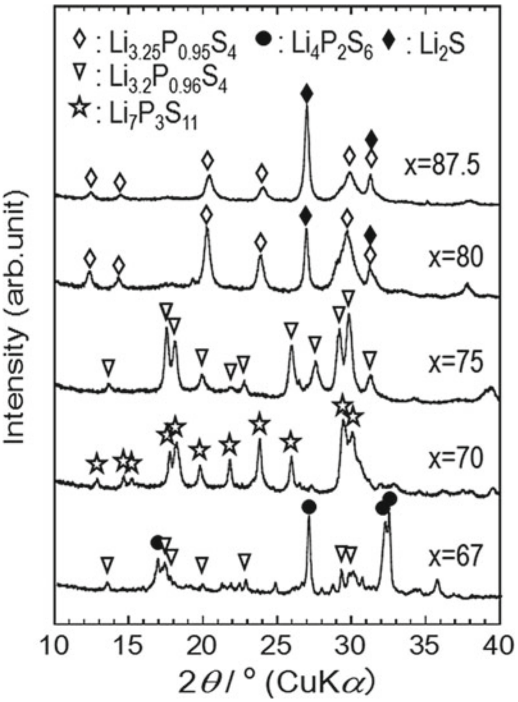

Fig. 7.9 X-ray diffraction (XRD) patterns of $xLi_2S \cdot (100\text{-}x)P_2S_5$ (x = 67, 70, 75, 80, and 87.5 mol%) glass ceramics

conductivity of precipitated crystalline phases. Thus, the relationship between the conductivity and the crystalline phase for a Li_2S-P_2S_5 glass-ceramic system was investigated.

Figure 7.9 shows the X-ray diffraction (XRD) patterns of the $xLi_2S \cdot (100\text{-}x)$ P_2S_5 (x = 67, 70, 75, 80, and 87.5 mol%) glass ceramics [21]. The $Li_4P_2S_6$ crystal was mainly precipitated in the glass ceramic with 67 mol% Li_2S, whereas the $Li_7P_3S_{11}$ crystal was formed in the glass ceramic with 70 mol % Li_2S. In glass ceramics with 75 mol% Li_2S or more, crystals analogous to thio-LISICON $Li_{3+x}Ge_xP_{1-x}S_4$ solid solution [15] were precipitated. In a binary Li_2S-P_2S_5 system with no Ge atoms, $Li_{3+5y}P_{1-y}S_4$ with phosphorus deficiency would form; a thio-LISICON region III ($Li_{3.2}Ge_{0.2}P_{0.8}S_4$) analog, a $Li_{3.2}P_{0.96}S_4$ crystal, was precipitated in a glass ceramic of x = 75, while a thio-LISICON region II ($Li_{3.25}Ge_{0.25}P_{0.75}S_4$) analog, a $Li_{3.25}P_{0.95}S_4$ crystal, was precipitated in glass ceramics of x = 80 and 87.5. A Li_2S crystal was observed in glass ceramics at compositions with 80 mol% Li_2S or more, and this is because the corresponding glasses partially include the Li_2S phase as a starting material. New crystalline $Li_7P_3S_{11}$ and thio-LISICON analogs of $Li_{3.25}P_{0.95}S_4$ have not been synthesized by conventional solid-state reaction. Glass electrolytes have an advantage as precursors because they stabilize at room temperature of a high-temperature phase of $Li_7P_3S_{11}$ or metastable phase of $Li_{3.25}P_{0.95}S_4$. The crystal structure of $Li_7P_3S_{11}$ was clarified by Rietveld analysis based on synchrotron XRD measurements [34]. The compound crystallized in a

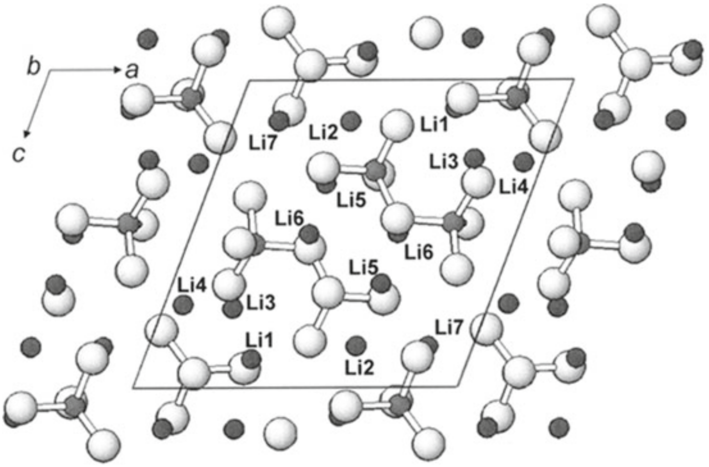

Fig. 7.10 Structure of $Li_7P_3S_{11}$ viewed along [010] direction

triclinic cell with a space group of *P*-1 and contained P_2S_7 ditetrahedra and PS_4 tetrahedra, similar to the case of the Ag^+ ion conductor $Ag_7P_3S_{11}$ (monoclinic, space group C2/c). A projection of the whole structure of $Li_7P_3S_{11}$ is shown in Fig. 7.10. The lithium atoms are located around the P_2S_7 ditetrahedra and PS_4 tetrahedra and surrounded by three to five sulfur atoms.

Crystals such as Li_3PS_4 and $Li_4P_2S_6$ showed low conductivity of less than 10^{-7} S cm^{-1} at room temperature, resulting in a lower conductivity of the glass ceramic of $x=67$. The thio-LISICON region II and III crystals were reported to show a high conductivity of 2.2×10^{-3} S cm^{-1} and 6.4×10^{-4} S cm^{-1}, respectively. The formation of highly conductive thio-LISICON analogs is responsible for the enhancement of conductivity (around 10^{-3} S cm^{-1}) by crystallization at compositions with 75 mol% Li_2S or more. A glass ceramic of $x=70$ with $Li_7P_3S_{11}$ showed the highest conductivity of 5.4×10^{-3} S cm^{-1} at room temperature. The electronic conductivity of the $Li_7P_3S_{11}$ glass ceramic was three orders of magnitude lower than the ionic conductivity, suggesting that the ion transference number is almost unity. The electrochemical stability of the $Li_7P_3S_{11}$ glass-ceramic electrolyte was examined by cyclic voltammetry. A stainless-steel disk as a working electrode and a lithium foil as a counter electrode were attached on each face of a pelletized electrolyte. The potential sweep was performed using a potentiostat/galvanostat device with a scanning rate of 1 mV s^{-1}. A cyclic voltammogram of the glass ceramic at the first cycle is shown in Fig. 7.11. A cathodic current peak due to lithium deposition and an anodic current peak due to lithium dissolution are observed reversibly at around 0 V (vs. Li^+/Li). There is no large current peak except for those peaks over the whole range from –0.1 to 5.0 V. It is concluded that glass-ceramic electrolytes have a wide electrochemical window of over 5 V and good compatibility with lithium metal.

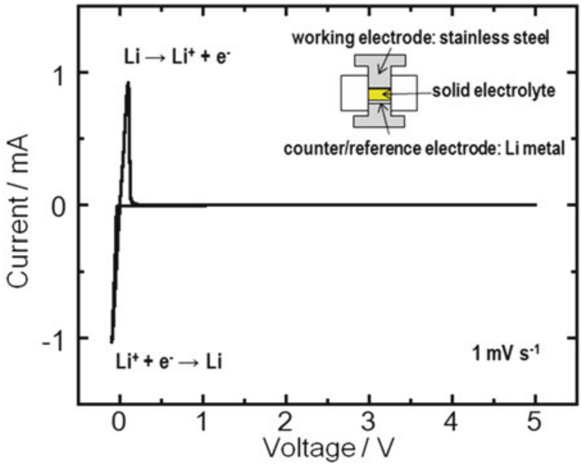

Fig. 7.11 Cyclic voltammogram of $Li_7P_3S_{11}$ glass ceramic at first cycle

7.6 All-Solid-State Rechargeable Lithium Batteries with Glass-Based Electrolytes

A bulk-type, solid-state battery composed of compressed powder electrode/electrolyte layers was studied. Compared to a thin-film battery, a bulk-type battery attracts a lot of attention because the battery is suitable for large-sized energy-storage devices. Li_2S-based sulfide materials with high Li^+ ion conductivity are promising solid electrolytes for bulk-type, solid-state batteries. The electrochemical performance of solid-state In/$LiCoO_2$ cells with Li_2S-SiS_2-Li_3PO_4 oxysulfide glasses was first reported in 1994 [35], and then these cells with sulfide electrolytes were developed. Intimate contact at the solid–solid interface between electrode and electrolyte is key to improving battery performance. A composite electrode composed of an active material, a solid electrolyte, and a conductive additive is commonly used in solid-state batteries to form continuous lithium-ion- and electron-conducting paths. A schematic of a typical all-solid-state electrochemical cell is shown in Fig. 7.12. The cell consists of a three-layer compressed powder pellet. The first layer is a Li-In alloy as a counter electrode. The second layer is a Li_2S-P_2S_5 glass-ceramic powder with a high conductivity as a solid electrolyte (SE). The third layer is a composite powder as a working electrode. To achieve a smooth electrochemical reaction in the cell, we prepared a composite electrode composed of three kinds of powders: the active material, the SE powder providing the lithium-ion-conduction path, and the conductive additive providing electron-conduction path. Figure 7.13 shows an example of a charge–discharge curve at the 100th cycle (inset) and the cycle performance of the all-solid-state Li-In/glass-ceramic/$Li_4Ti_5O_{12}$ cell [36]. A composite positive electrode consisting of $Li_4Ti_5O_{12}$, SE, and vapor grown carbon fiber (VGCF) powders with a weight ratio of 38 : 58 : 4

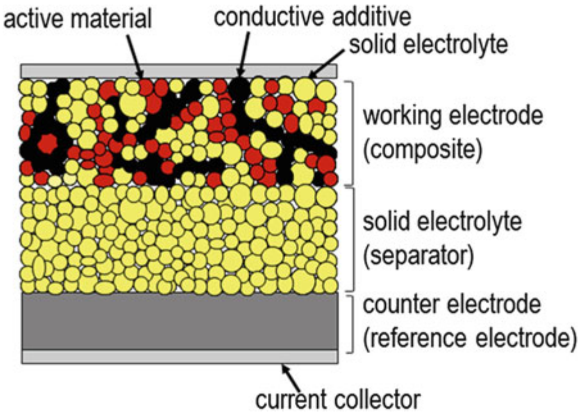

Fig. 7.12 Schematic of typical all-solid-state electrochemical cell

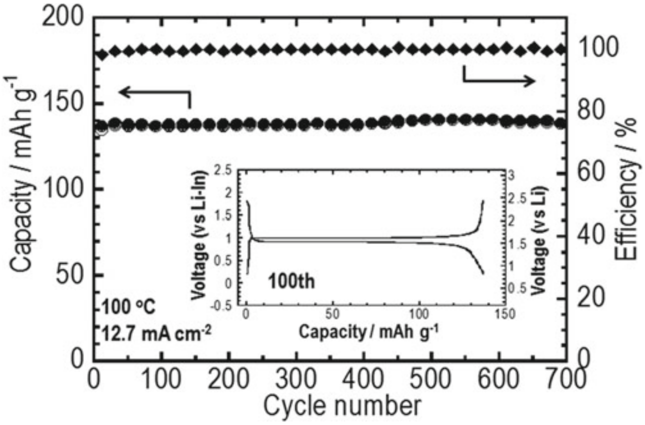

Fig. 7.13 Charge–discharge curve at 100th cycle (inset) and cycle performance of all-solid-state Li-In/Li_2S-P_2S_5 glass-ceramic/$Li_4Ti_5O_{12}$ cell

was used for all-solid-state cells. The measurement was carried out under a constant current density of 12.7 mA cm^{-2} at 100 °C. The cell operates reversibly for 700 cycles with a charge–discharge efficiency of 100 % under a high current density of over 10 mA cm^{-2} and a high temperature of 100 °C. The cell demonstrates a discharge and charge capacity of approximately 140 mAh g^{-1} and maintains a capacity for 700 cycles with no degradation. Solid-state cells exhibit excellent electrochemical performance with a long cycle life. There are few reports on the high temperature operation of batteries, and all-solid-state batteries using glass-ceramic electrolytes have the benefit of high-temperature application.

To improve the energy density of solid-state batteries, the use of active materials with a high capacity is indispensable. Elemental sulfur has been of great interest as

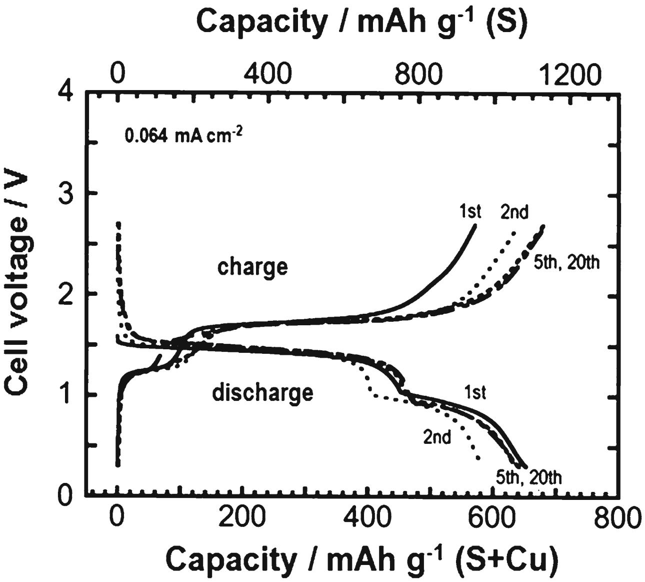

Fig. 7.14 Cycling performance of an all-solid-state Li-In/Li_2S-P_2S_5 glass-ceramic/S-Cu cell

a positive electrode material because of its large theoretical capacity of 1,672 mAh g^{-1}, low cost, and environmental friendliness. Unfortunately, Li/S batteries with conventional liquid electrolytes suffer from rapid capacity fading on cycling because polysulfides formed during a discharge process are dissolved into liquid electrolytes. The use of inorganic solid electrolytes resolves a key problem in Li/S batteries. The glass-based solid electrolytes in Li_2S-SiS_2 [37] and Li_2S-P_2S_5 systems [38] have been used for all-solid-state Li/S batteries. Figure 7.14 shows the cycling performance of an all-solid-state Li-In/Li_2S-P_2S_5 glass-ceramic/S-Cu cell [38]. The positive electrode materials with S particles covered with CuS were prepared by ball milling for the mixture of S and Cu powders (S/Cu = 3). All-solid-state cells work as rechargeable lithium batteries at room temperature under a constant current density of 0.064 mA cm^{-2}. The cell retains a high reversible capacity over 650 mAh per weight of S + Cu for 20 cycles. This capacity corresponds to approximately 1,100 mAh per weight of sulfur, and 65 % of theoretical capacity of sulfur is available. Sulfide solid electrolytes are useful for achieving a good cyclability of Li/S batteries. The use of sulfur-carbon composite electrodes instead of the sulfur-copper composite electrodes mentioned earlier improves the rate capability and reversible capacity of all-solid-state Li/S batteries [39]. Lithium sulfide, Li_2S, which is a reaction product following discharge for sulfur active materials, has also been used as a positive electrode in all-solid-state batteries [40]; the advantage of Li_2S over S is its compatibility with various negative electrodes without lithium sources such as graphite. The development of all-solid-state Li/S batteries will meet the demand for battery applications with a high energy density.

7.7 Concluding Remarks

Inorganic glass-based solid electrolytes with a high level of conductivity in an organic liquid electrolyte have been developed. Glass-based electrolytes in all-solid-state batteries have several advantages: high conductivity, single Li^+ ion conduction, wide electrochemical window, and intimate solid–solid contact. Sulfide glass-ceramic electrolytes in a Li_2S-P_2S_5 system was used in bulk-type, solid-state batteries, and the batteries exhibited excellent cycle performance. All-solid-state rechargeable batteries have many merits: high safety, high reliability, and simple design due to the absence of leakage and flammability of the cell components. The use of active materials with a high capacity, which is not available in conventional cells using a liquid electrolyte, is another advantage of solid-state batteries.

The next issues to be addressed in developing all-solid-state batteries for practical use include further increases in the Li^+ ion conductivity of glass-based solid electrolytes and the formation of good electrode–electrolyte interfaces to achieve rapid charge transfer by appropriate surface modification. Control of the size, morphology, and dispersibility of both solid electrolytes and active materials is also important for establishing intimate solid-solid contact. Development of an effective approach to decreasing the amount of solid electrolyte in a composite electrode layer will achieve essential improvements in the energy density and power density of solid-state batteries.

References

1. J.M. Tarascon, M. Armand, Issues and challenges facing rechargeable lithium batteries. Nature **414**, 359–367 (2001)
2. C. Julien, G.A. Nazri, *Solid State Batteries: Materials Design and Optimization* (Kluwer Academic Publishers, Boston, 1994)
3. T. Minami, M. Tatsumisago, M. Wakihara, C. Iwakura, S. Kohjiya, I. Tanaka, *Solid State Ionics for Batteries* (Springer, Tokyo, 2005)
4. H.L. Tuller, D.P. Button, D.R. Uhlmann, Fast ion transport in oxide glasses. J. Non-Cryst. Solids **40**, 93–118 (1980)
5. A.D. Robertson, A.R. West, A.G. Ritchie, Review of crystalline lithium-ion conductors suitable for high temperature battery applications. Solid State Ion. **104**, 1–11 (1997)
6. J.W. Fergus, Ceramic and polymeric solid electrolytes for lithium-ion batteries. J. Power. Sources **195**, 4554–4569 (2010)
7. M. Ito, Y. Inaguma, W.H. Jung, L. Chen, T. Nakamura, High lithium ion conductivity in the perovskite-type compounds $Ln_{1/2}Li_{1/2}TiO_3$ (Ln = La, Pr, Nd, Sm). Solid State Ion. **70–71**, 203–207 (1994)
8. H. Aono, E. Sugimono, Y. Sadaoka, N. Imanaka, G. Adachi, Ionic conductivity of solid electrolytes based on lithium titanium phosphate. J. Electrochem. Soc. **137**, 1023–1027 (1990)
9. R. Murugan, W.W. Thangadural, Fast lithium ion conduction in garnet-type $Li_7La_3Zr_2O_{12}$. Angew. Chem. Int. Ed. **46**, 7778–7781 (2007)
10. M. Tatsumisago, N. Machida, T. Minami, Mixed anion effect in conductivity of rapidly quenched Li_4SiO_4-Li_3BO_3 glasses. J. Ceram. Soc. Jpn **95**, 197–201 (1987)
11. X. Yu, J.B. Bates, G.E. Jellison, F.X. Hart, A stable thin-film lithium electrolyte: Lithium phosphorus oxynitride. J. Electrochem. Soc. **144**, 524–532 (1997)

12. K. Kanehori, K. Matsumoto, K. Miyauchi, T. Kudo, Thin film solid electrolyte and its application to secondary lithium cell. Solid State Ion. **9–10**, 1445–1448 (1983)
13. J. Fu, Superionic conductivity of glass-ceramics in the system Li_2O-Al_2O_3-TiO_2-P_2O_5. Solid State Ion. **96**, 195–200 (1997)
14. J. Fu, Fast Li^+ ion conducting glass-ceramics in the sytem Li_2O-Al_2O_3-GeO_2-P_2O_5. Solid State Ion. **104**, 191–194 (1997)
15. R. Kanno, M. Murayama, Lithium ionic conductor thio-LISICON; the Li_2S-GeS_2-P_2S_5 system. J. Electrochem. Soc. **148**, A742–A746 (2001)
16. M. Ribes, B. Barrau, J.L. Souquet, Sulfide glasses: Glass forming region, structure and ionic conduction of glasses in Na_2S-XS_2 (X = Si; Ge), Na_2S-P_2S_5 and Li_2S-GeS_2 systems. J. Non-Cryst. Solids **38–39**, 271–276 (1980)
17. Z. Zhang, J.H. Kennedy, Synthesis and characterization of the B_2S_3-Li_2S, the P_2S_5-Li_2S and the B_2S_3-P_2S_5-Li_2S glass systems. Solid State Ion. **38**, 217–224 (1990)
18. H. Wada, M. Menetrier, A. Levasseur, P. Hagenmuller, Preparation and ionic conductivity of new B_2S_3-Li_2S-LiI glasses. Mater. Res. Bull **18**, 189–193 (1983)
19. N. Aotani, K. Iwamoto, K. Takada, S. Kondo, Synthesis and electrochemical properties of lithium ion conductive glass, Li_3PO_4-Li_2S-SiS_2. Solid State Ion. **68**, 35–39 (1994)
20. K. Hirai, M. Tatsumisago, T. Minami, Thermal and electrical properties of rapidly quenched glasses in the system Li_2S-SiS_2-Li_xMO_y ($Li_xMO_y = Li_4SiO_4$, Li_2SO_4). Solid State Ion. **78**, 269–273 (1995)
21. F. Mizuno, A. Hayashi, K. Tadanaga, M. Tatsumisago, High lithium ion conducting glass-ceramics in the system Li_2S-P_2S_5. Solid State Ion. **177**, 2721–2725 (2006)
22. A. Hayashi, K. Minami, S. Ujiie, M. Tatsumisago, Preparation and ionic conductivty of $Li_7P_3S_{11\text{-}z}$ glass-ceramic electrolytes. J. Non-Cryst. Solids **356**, 2670–2673 (2010)
23. H. Muramatsu, A. Hayashi, T. Ohtomo, S. Hama, M. Tatsumisago, Structural change of Li_2S-P2S5 sulfide solid electrolytes in the atmosphere. Solid State Ion. **182**, 116–119 (2011)
24. N. Machida, T. Minami, Electrical properties of superionic conducting glasses in the pseudo-binary system CuI-Cu_2MoO_4. J. Am. Ceram. Soc. **71**, 784–788 (1988)
25. H. Kitaura, A. Hayashi, T. Ohtomo, S. Hama, M. Tatsumisago, Fabrication of electrode-electrolyte interfaces in all-solid-state rechargeable lithium batteries by using a supercooled liquid state of the glassy electrolytes. J. Mater. Chem. **21**, 118–124 (2011)
26. M. Tatsumisago, T. Saito, T. Minami, Stabilization of α-AgI at room temperature by heating of AgI-Ag_2O-MoO_3 glasses. Chem. Lett. 790–791 (2001).
27. M. Tatsumisago, T. Minami, Lithium ion conducting glasses prepared by rapid quenching. Mater. Chem. Phys. **18**, 1–17 (1987)
28. Y. Sakurai, A. Sakuda, A. Hayashi, M. Tatsumisago, Preparation of amorphous Li_4SiO_4-Li_3PO_4 thin films by pulsed laser deposition for all-solid-state lithium secondary batteries. Solid State Ion. **182**, 59–63 (2011)
29. A. Hayashi, S. Hama, H. Morimoto, M. Tatsumisago, T. Minami, Preparation of Li_2S-P_2S_5 amorphous solid electrolytes by mechanical milling. J. Am. Ceram. Soc. **84**, 477–479 (2001)
30. T. Minami, A. Hayashi, M. Tatsumisago, Preparation and characterization of lithium ion-conducting oxysulfide glasses. Solid State Ion. **136–137**, 1015–1023 (2000)
31. T. Minami, A. Hayashi, M. Tatsumisago, Recent progress of glass and glass-ceramics as solid electrolytes for lithium secondary batteries. Solid State Ion. **177**, 2715–2720 (2006)
32. Y. Kim, J. Saienga, S.W. Martin, Anomalous ionic conductivity increase in $Li_2S + GeS_2 + GeO_2$ glasses. J. Phys. Chem. B **110**, 16318–16325 (2006)
33. A. Hayashi, M. Tatsumisago, T. Minami, Electrochemical properties for the lithium ion conductive $(100\text{-}x)(0.6Li_2S \cdot 0.4SiS_2) \cdot xLi_4SiO_4$ oxysulfide glasses. J. Electrochem. Soc. **146**, 3472–3475 (1999)
34. H. Yamane, M. Shibata, Y. Shimane, T. Junke, Y. Seino, S. Adams, K. Minami, A. Hayashi, M. Tatsumisago, Crystal structure of a superionic conductor, $Li_7P_3S_{11}$. Solid State Ion. **178**, 1163–1167 (2007)
35. K. Iwamoto, N. Aotani, K. Takada, S. Kondo, Rechargeable solid state battery with lithium conductive glass, Li_3PO_4-Li_2S-SiS_2. Solid State Ion. **70–71**, 658–661 (1994)

36. K. Minami, A. Hayashi, S. Ujiie, M. Tatsumisago, Electrical and electrochemical properties of glass-ceramic electrolytes in the systems Li_2S-P_2S_5-P_2S_3 and Li_2S-P_2S_5-P_2O_5. Solid State Ion. **192**, 122–125 (2011). doi:10.1016/j.ssi.2010.06.018
37. N. Machida, K. Kobayashi, Y. Nishikawa, T. Shigematsu, Electrochemical properties of sulfur as cathode materials in a solid-state lithium battery with inorganic solid electrolytes. Solid State Ion. **175**, 247–250 (2004)
38. A. Hayashi, T. Ohtomo, F. Mizuno, K. Tadanaga, M. Tatsumisago, All-solid-state Li/S batteries with highly conductive glass-ceramic electrolytes. Electrochem. Commun. **5**, 701–705 (2003)
39. M. Nagao, A. Hayashi, M. Tatsumisago, Sulfur-carbon composite electrode for all-solid-state Li/S battery with Li_2S-P_2S_5 solid electrolyte. Electrochim. Acta. **56**, 6055–6059 (2011)
40. A. Hayashi, R. Ohtsubo, T. Ohtomo, F. Mizuno, M. Tatsumisago, All-solid-state rechargeable lithium batteries with Li_2S as a positive electrode material. J. Power. Sources **183**, 422–426 (2008)

Chapter 8
3DOM Structure for Battery Electrodes and Electrolytes

Kiyoshi Kanamura

8.1 Introduction

The capacity of lithium-ion batteries, especially at high rates, critically depends on the morphology of the battery active materials and the microstructure of the electrode [1]. A three-dimensionally ordered macroporous (3DOM) structure is an ideal structure due to its high porosity and regularity, which provide a large contact area between the electrode and electrolyte and a uniform current distribution, respectively. This chapter describes 3DOM anodes and 3DOM solid electrolyte-active material electrodes.

8.1.1 3DOM Anode

8.1.1.1 3DOM $Li_4Ti_5O_{12}$ Anode

$Li_4Ti_5O_{12}$ has been investigated as an anode material for lithium batteries [2–5]. $Li_4Ti_5O_{12}$ has a spinel-related structure (space group: *Fd*3*m*), and Li^+ ions can be inserted into the crystallographic structure reversibly at an electrode potential of 1.55 V versus Li/Li^+. It is well known that $Li_4Ti_5O_{12}$ shows a very small volumetric change during charge and discharge [2].

3DOM $Li_4Ti_5O_{12}$ was prepared by a colloidal crystal templating method combined with a sol–gel method. At first, monodispersed polystyerene (PS) latex was filtered. Following filtration, the PS deposit was heat-treated at 110 °C to interconnect all the PS particles. In the prepared PS membrane, PS particles were

---

K. Kanamura (✉)
Department of Applied Chemistry, Tokyo Metropolitan University, Hachioji, Tokyo, Japan
e-mail: kanamura@tmu.ac.jp

T. Osaka and Z. Ogumi (eds.), *Nanoscale Technology for Advanced Lithium Batteries*, Nanostructure Science and Technology 182, DOI 10.1007/978-1-4614-8675-6_8,

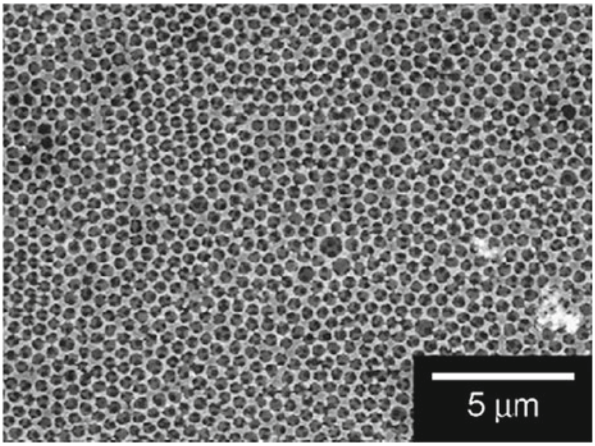

Fig. 8.1 SEM image of 3DOM $Li_4Ti_5O_{12}$

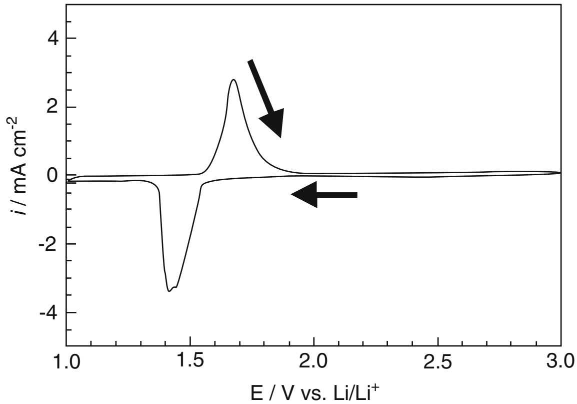

Fig. 8.2 SEM image of 3DOM $Li_4Ti_5O_{12}$

close-packed and there was a 26 vol.% void space for penetration by fluid precursor. A precursor sol for $Li_4Ti_5O_{12}$ was injected into the void space. After gelation, the gel-PS composite was calcined to remove the PS template and convert the gel into $Li_4Ti_5O_{12}$.

A cross-sectional scanning electron microscope (SEM) image of 3DOM $Li_4Ti_5O_{12}$ is displayed in Fig. 8.1. The inverse opal structure can be seen, and the interconnected pores with uniform size were clearly observed on the entire region.

A cyclic voltammogramm of 3DOM $Li_4Ti_5O_{12}$ clearly shows reversible redox peaks at 1.55 V versus Li/Li^+ due to the solid-state reaction of $Ti^{3+/4+}$ in the spinel structure (Fig. 8.2). Figure 8.3 shows the charge and discharge curves of a 3DOM $Li_4Ti_5O_{12}$ electrode measured at various currents. The charge and discharge curves

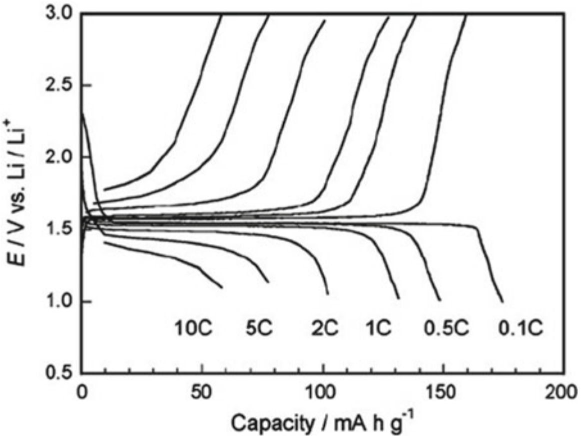

Fig. 8.3 Charge and discharge curves of 3DOM $Li_4Ti_5O_{12}$

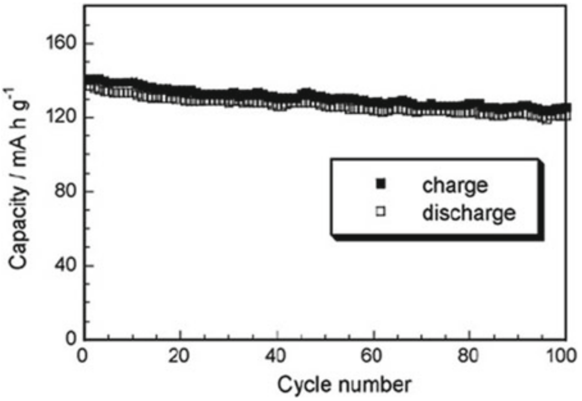

Fig. 8.4 Charge and discharge cycle stability of 3DOM $Li_4Ti_5O_{12}$ evaluated at 0.1 C

show a very flat plateau at a potential of 1.55 V. The very flat plateau indicates a characteristic of two-phase reactions. It has been proposed that Li^+ ions are inserted into $Li_4Ti_5O_{12}$, which convert into $Li_7Ti_5O_{12}$ [3]. The charge and discharge capacities at a 0.1 C rate (a 1 C rate corresponds to a current that can perform full charge or full discharge of the battery for 1 h) were 173 and 159 mA h g^{-1}, respectively, which were close to the theoretical capacity of 167 mA h g^{-1}. This means that the three-dimensional network of $Li_4Ti_5O_{12}$ was well developed, and the Li^+ ion insertion and extraction took place throughout the entire porous $Li_4Ti_5O_{12}$ membrane. Figure 8.4 reveals the charge–discharge cycle stability of the electrode as a function of the cycle number. The 3DOM $Li_4Ti_5O_{12}$ electrode showed good cycle stability. This indicated that the 3D network of $Li_4Ti_5O_{12}$ was maintained during the charge–discharge cycles because of the zero strain during Li^+ ion insertion and extraction.

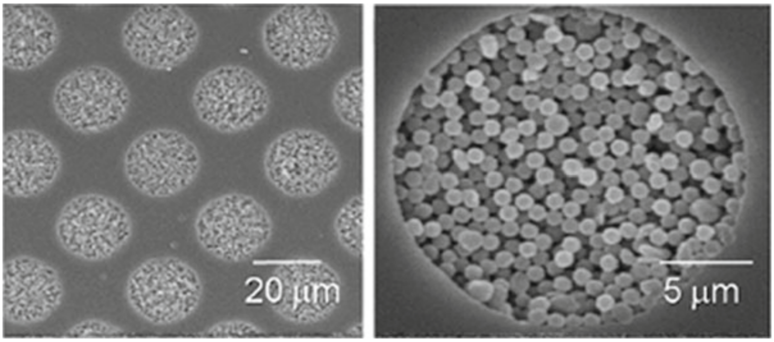

Fig. 8.5 SEM images of polystyerene beads injected into hole of photoresist substrate

8.1.1.2 3DOM Sn-Ni Anode

Sn has received much attention due to its high capacity (max. 994 mA h g^{-1}) [6]. However, Sn anodes undergo severe volumetric changes during alloying and dealloying with Li, causing poor cyclability. A 3DOM structure is expected to improve the cyclability even with the huge volumetric change during charge and discharge cycles. Here, a highly patterned Sn-Ni alloy anode with a 3DOM structure is introduced.

A 3DOM Sn-Ni alloy was prepared on a Cu plate using a colloidal crystal templating method combined with electroplating. A PS latex was electrodeposited onto a photoresist substrate that had regularly opened holes 20 µm in diameter (Fig. 8.5). Then, Sn-Ni was electrodeposited into the void space of the PS template. The plated photoresist substrate was immersed into toluene to eliminate the PS template.

Figure 8.6 shows a SEM image of a prepared 3DOM Sn-Ni alloy. The highly patterned 3DOM Sn-Ni alloy was prepared in the holes of the photoresist substrate. The composition of the Sn-Ni alloy was 60 at.% Sn, as determined by X-ray fluorescence (XRF) analysis. Figure 8.7 displays charge and discharge curves of a highly patterned 3DOM Sn-Ni alloy at a current density of 0.1 mA cm^{-2} (0. 1 mA cm^{-2} corresponds to a current density of approximately a 0.1 C rate). The charge and discharge curves show a clear potential plateau at around 0.4 V versus Li/Li^{+}, indicating the lithiation and delithiation processes into (from) Sn in the Ni-Sn alloy anode [7, 8]. The process of lithiation into Sn involves the formation of a Li$_x$Sn alloy within a Li-inactive Ni matrix. The crystallographic structure of Li$_x$Sn as it changes with the value of x during lithiation into Sn has been reported. An intermetallic Ni$_3$Sn$_4$ phase is reformed during the delithiation process [7]. In any case, seven kinds of intermetallic phase of Li$_x$Sn take place during the charge and discharge cycles [9–11]. The initial charge capacity was 747 mA h g^{-1}. This value was close to the theoretical value of 60 at.% Sn [12]. The discharge capacity of the highly patterned cylindrical Sn-Ni alloy anode was 632 mA h g^{-1} with a coulombic

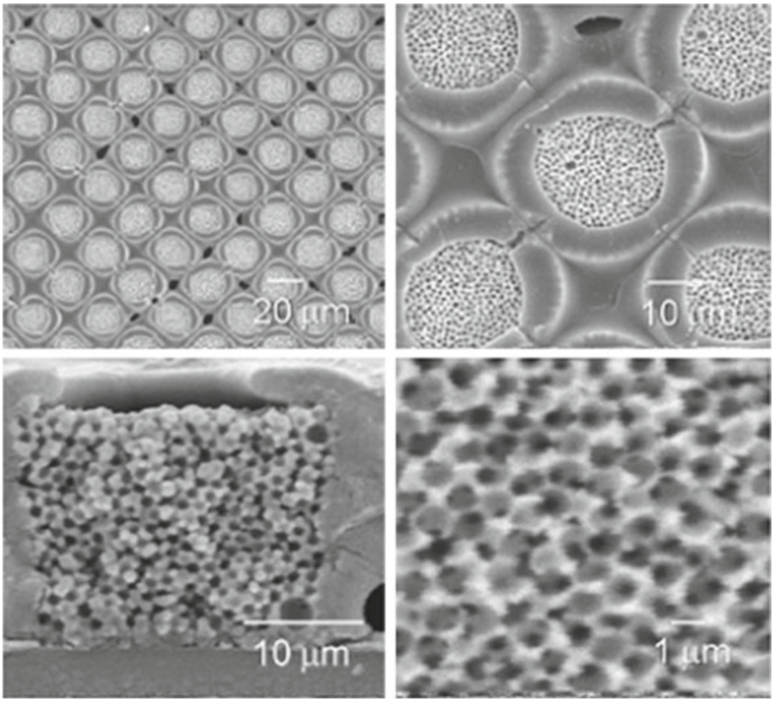

Fig. 8.6 SEM images of highly patterned Sn-Ni alloy

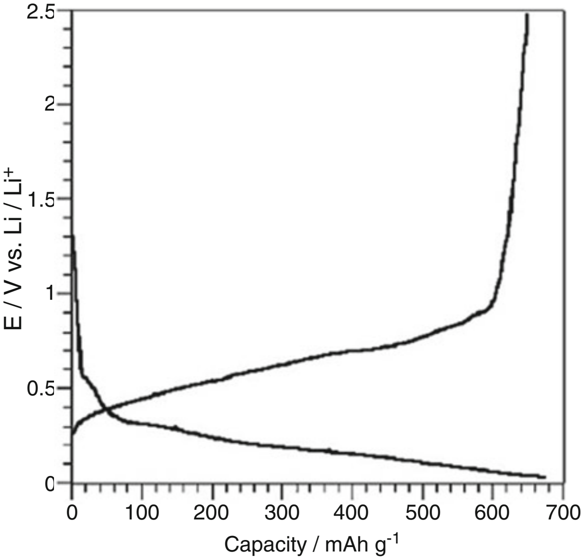

Fig. 8.7 Charge and discharge curves of highly patterned Sn-Ni alloy

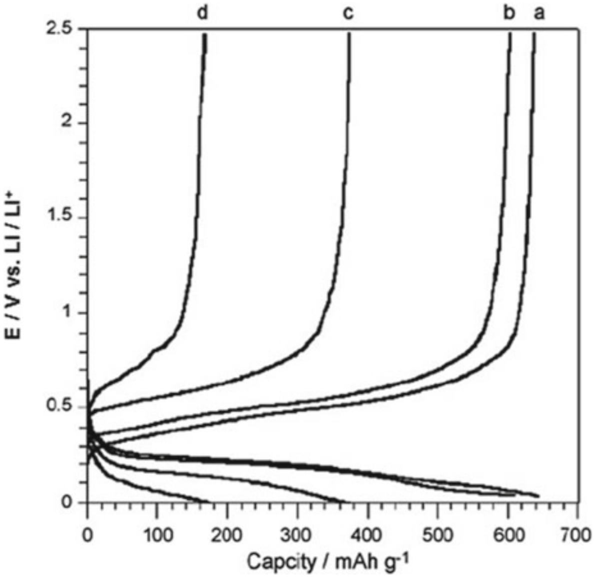

Fig. 8.8 Charge and discharge curves of highly patterned Sn-Ni alloy at various rates: (**a**) 0.2, (**b**) 0.5, (**c**) 1.0, and (**d**) 2.0 mA cm^{-2}

efficiency of 84 % as compared with its charge capacity. A large irreversible capacity during the initial cycle may be caused by the formation of solid electrolyte interphase (SEI) or the reduction of SnO_2 impurity to Li_2O and Sn on the surface of the Sn-Ni alloy anode [13–15]. Figure 8.8 displays the charge and discharge curves of a highly patterned cylindrical Sn-Ni alloy anode with a 3DOM structure measured at various current densities. The reversible discharge capacity of the highly patterned cylindrical Sn-Ni alloy anode was as high as 600 mA h g^{-1} with a good coulombic efficiency of over 98 % at low current densities of 0.2 and 0.5 mA cm^{-2}. However, the charge and discharge capacities gradually decreased as the current density increased. In other words, the termination of charge occurred before the maximum capacity of the Sn-Ni alloy anode was reached. Figure 8.9 shows the cycle performance of highly patterned cylindrical Sn-Ni alloy anodes with a 3DOM structure measured at a current density of 0.1 mA cm^{-2} for 200 cycles. To investigate the efficiency of a 3DOM cylinder structure for the relaxation of mechanical stress caused by volume expansion during charge and discharge processes, the state of charge (SOC) in a Sn-Ni alloy anode was controlled at 100 %, 80 %, and 67 %, respectively. For example, at 80 % SOC, the galvanostatic charging time was cut off as 80 % of the full charging time on the basis of the theoretical capacity of 747 mAh g^{-1} in the Sn-Ni alloy (60 at.% Sn). The Sn-Ni alloy anode cycle test at 67 % SOC showed an excellent cycle stability even at 200 cycles, and the coulombic efficiency was more than 99 %. A SEM image of highly patterned cylindrical Sn-Ni alloy anodes after 200 cycles of charge and discharge at 67 % SOC is shown in Fig. 8.10. The macropores within the Sn-Ni alloy cylinder was maintained, and the

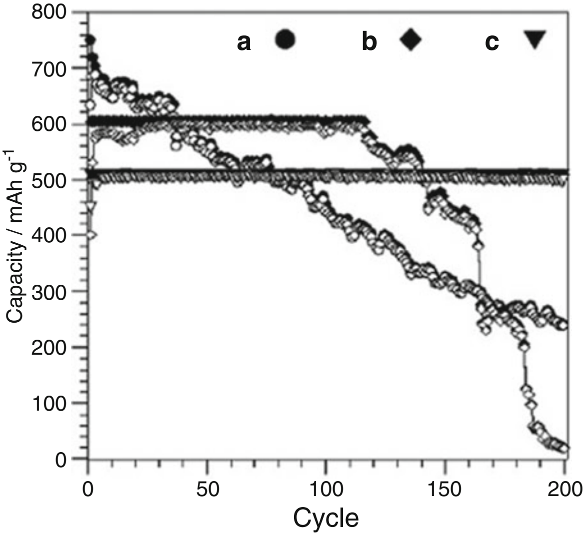

Fig. 8.9 Cycle stability of highly patterned cylindrical 3DOM Sn-Ni alloy at a 0.1 mA cm^{-2} under the SOC controlled at (**a**) 100 % (**b**), 80 %, and (**c**) 67 %

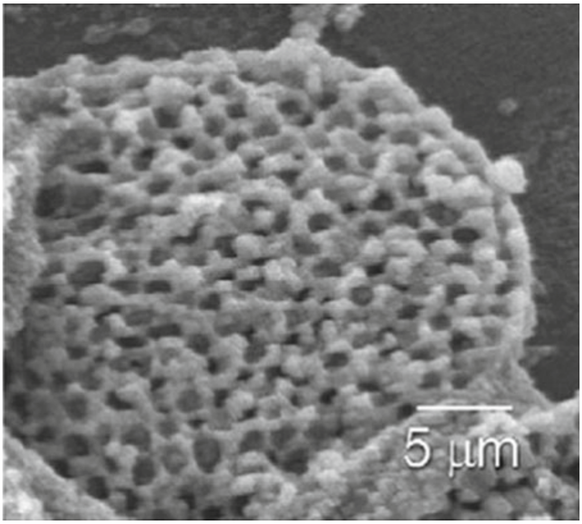

Fig. 8.10 SEM image of highly patterned cylindrical 3DOM Sn-Ni alloy after 200 cycles at state of charge of 67 %

size of the macropore hardly changed even after 200 cycles. It is considered that the 3DOM cylinder structure of the Sn-Ni alloy is effective for the relaxation of volumetric change with no crack formation during charge and discharge cycles.

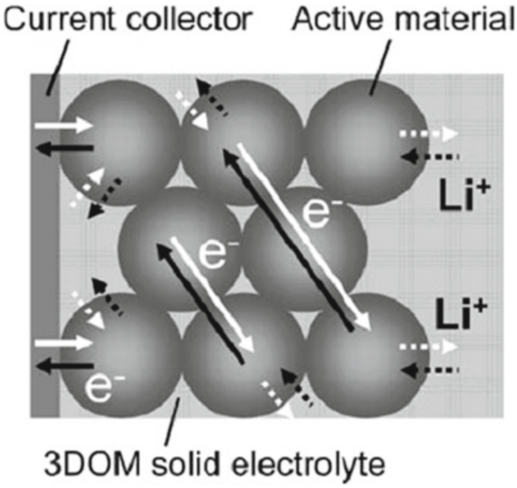

Fig. 8.11 Schematic illustration of composite electrode system with 3DOM solid electrolyte

8.1.2 3DOM Solid Electrolyte: Active Material Composite Electrode

One of the serious problems in realizing all-solid-state lithium-ion batteries using a ceramic electrolyte is the poor contact between the solid electrolyte and active materials [16]. The poor contact increases the internal resistance of the battery. In other words, the electrochemical interface in the electrode system used in all-solid-state batteries should be enlarged to realize a high electrode performance. A ceramic electrolyte with a 3DOM structure has a large surface area. By injecting an active material into the macropores of the 3DOM electrolyte, a large contact area between the active material and ceramic electrolyte can be obtained (Fig. 8.11). In this section, a 3DOM ceramic electrolyte-active material composite electrodes using $Li_{1.5}Al_{0.5}Ti_{1.5}(PO_4)_3$ (LATP) and $Li_{0.35}La_{0.55}TiO_3$ (LLT) prepared by suspension filtration and colloidal crystal templating methods, respectively, are described.

8.1.3 $LiMn_2O_4$: 3DOM LATP Composite Electrode

LATP has a Na super ionic conductor (NASICON)-type structure and is considered a promising solid electrolyte due to its high Li-ion conductivity (approximately 10^{-3} S cm^{-1}) [17]. A 3DOM LATP was prepared by a suspension filtration method. In the suspension filtration method, a mixture of precursor powder for a LATP and PS template was filtered, and the deposition on the filter was calcined at 950 °C for 12 h. A SEM image of the obtained 3DOM LATP is shown in Fig. 8.12. An interconnecting window was observed on the entire part of the LATP membrane. The macropore size was approximately 2 μm, which was smaller than that of the PS particle used as a template (3 μm), indicating that the shrinkage of the 3DOM LATP

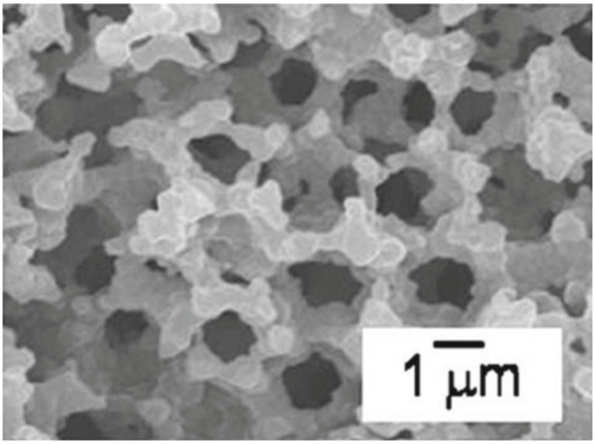

Fig. 8.12 Cross-sectional SEM image of 3DOM LATP

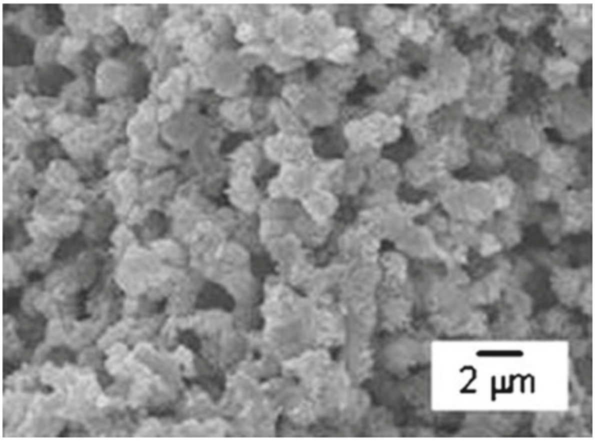

Fig. 8.13 Cross-sectional SEM image of composite electrode system between 3DOM LATP and $LiMn_2O_4$

took place during calcination. The porosity of the 3DOM LATP was estimated to be 73 % from the volume and weight of the membrane and the theoretical density of LATP, which was almost identical to the theoretical value (74 %). The ionic conductivity of 3DOM LATP was 5.3×10^{-5} S cm^{-1}, which was lower than the reported value [18]. This low value was attributed to defects in the 3DOM LATP, which break down a part of the ion-conduction network. A composite electrode consisting of 3DOM LATP and $LiMn_2O_4$ was prepared via a sol–gel process. The 3DOM LATP was immersed in the precursor sol under vacuum to inject the sol into the pore of 3DOM LATP. After gelation of the sol, the composite of 3DOM LATP and the gel was calcined at 450 °C for 30 min. This procedure was repeated four times to increase the filling ratio of $LiMn_2O_4$ in the 3DOM LATP. Finally, the composite was annealed at 450 °C for 1 h. By comparing the SEM image of the composite

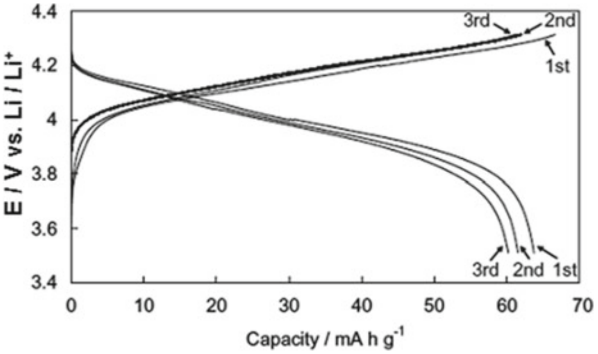

Fig. 8.14 Charge and discharge curves of composite between 3DOM LATP and $LiMn_2O_4$ at 0.1 °C (0.2 mA cm^{-2})

electrode system (Fig. 8.13) with that of the 3DOM LATP (Fig. 8.12), it was found that $LiMn_2O_4$ was injected into the pore of the 3DOM LATP. However, voids were still observed in the composite electrode. Because the Li-Mn-O sol used for injection of $LiMn_2O_4$ into the pore of the 3DOM LATP contained a large amount of solvent, voids remained as a result of evaporation of the solvent during the heat treatment. Figure 8.14 shows the charge–discharge curves of the composite electrode system. The potential plateaus were observed around 4.0 V. These plateaus were due to the redox reaction of $Mn^{3+/4+}$ in $LiMn_2O_4$, indicating that Li intercalation/deintercalation into/from $LiMn_2O_4$ occurred in the composite electrode system, which was produced by only ceramics. However, only one plateau was observed in the charge and discharge curves. $LiMn_2O_4$ has two redox potentials at 4.0 and 4.1 V versus Li/Li$^+$. This is due to the comparatively lower ionic conductivity of LATP compared with organic electrolytes. The low ionic conductivity of LATP causes a large polarization of the prepared cell. Such a large polarization sometimes makes it very difficult to identify two distinct potential plateaus. Incidentally, the first discharge capacity was 64 mA h g^{-1}, which was lower than the theoretical value (148 mA h g^{-1}). This discharge capacity may only correspond to that of the first potential plateaus. In such a case, we may observe the first discharge plateaus. There are two reasons for the low capacity compared with the theoretical value. One is a low utilization of $LiMn_2O_4$ in the composite electrode system. Because voids were observed in the composite electrode system (Fig. 8.13), some parts of $LiMn_2O_4$ were isolated electrically from the current collector. This resulted in a lowering of the utilization of $LiMn_2O_4$. Another is the presence of TiO_2 as an impurity in the composite electrode. TiO_2 detected in the composite electrode may have increased the electrical resistance of the electrode. Consequently, the discharge capacity was decreased. By increasing the filling ratio of $LiMn_2O_4$ in the pore and decreasing the amount of impurity in the electrode, the capacity was improved. The composite electrode system showed good cycle stability up to three cycles and a coulombic efficiency of 99 % at the third cycle. If the morphology of the composite electrode changed significantly during the charge–discharge cycle, the capacity fade must be observed by

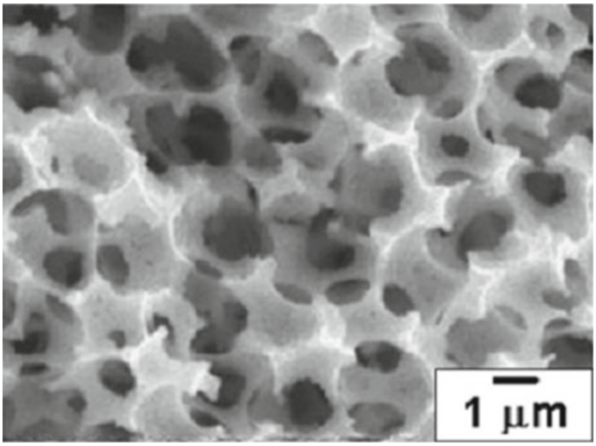

Fig. 8.15 Cross-sectional SEM image of 3DOM LLT

a lowering of the $LiMn_2O_4$ utilization because of the elimination of $LiMn_2O_4$ from LATP or the breaking down of the 3DOM structure by an expansion of $LiMn_2O_4$. From the fact that a remarkable capacity fade is not observed within three cycles (Fig. 8.14), it can be said that the morphology of the composite electrode system does not change significantly.

8.1.4 $LiMn_2O_4$: 3DOM LLT Composite Electrode

LLT has a perovskite structure and has also been thought to be a promising solid electrolyte due to its high Li-ion conductivity (approximately 10^{-3} S cm^{-1}) [19]. 3DOM LLT was prepared by the suspension filtration method combined with the sol–gel method. PS beads suspended in water were filtered and interconnected by heat treatment at 110 °C for 1 h. The precursor sol for LLT was injected into the voids of the PS template using vacuum impregnation and converted to gel under vacuum at room temperature. After gelation, the composite of ordered PS and precursor gel for LLT was calcined at 450 °C for 1 h to remove PS beads and at 1,000 °C for 1 h to crystallize LLT. Following heat treatment, a crystallized porous LLT membrane was obtained. A cross-sectional SEM image of 3DOM LLT before impregnation of active material is shown in Fig. 8.15. The macropore size was around 2 μm, which was smaller than that of the PS beads used as the template (3 μm), indicating that the shrinkage of the 3DOM LLT took place during heat treatment. An interconnecting window was observed on the entire LLT membrane. To estimate the ionic conductivity of the 3DOM LLT, a silver paste was used to obtain electrical contact from the sample. The ionic conductivity of the 3DOM LLT was estimated by AC impedance measurement, and the conductivity was around

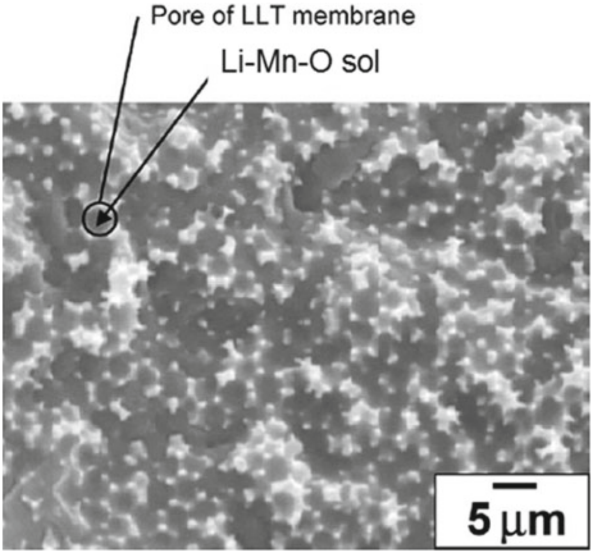

Fig. 8.16 Cross-sectional SEM image of 3DOM LLT after filling with Li-Mn-O gel

2.1×10^{-4} S cm^{-1}, which was lower than the reported value (>10^{-3} S cm^{-1}) [19], because of defects in the 3DOM-LLT, which broke down part of the ion-conduction network. The pores of the pores LLT were filled with $LiMn_2O_4$ by a solvent substitution method. At first, the pores of the 3DOM LLT were filled with 0.02 mol dm^{-3} sodium dodecyl sulfate (SDS) solution. The 3DOM LLT filled with SDS solution was immersed in the precursor sol for $LiMn_2O_4$-containing lithium acetate and manganese acetate to inject the sol into the pores of the 3DOM LLT. The SDS solution in the macropores was replaced with Li-Mn-O sol during immersion. Following immersion, the 3DOM LLT membrane was lifted up from the sol solution, and the sol involved in the LLT porous membrane was converted into gel at 60 °C. The LLT-gel composite was calcined at 450 °C. Since the gel contained a large amount of solvent and organic compounds, voids remained as a result of evaporation of the solvent and decomposition of organic species during the heat treatment. To increase the filling ratio of active material in the pores of the 3DOM solid electrolyte, injection of the sol and the following heat treatment was repeated four times. Finally, the composite was calcined at 700 °C for 10 h. Figure 8.16 shows a cross-sectional SEM image of 3DOM LLT following injection and gelation of the sol. In Fig. 8.16, the bright area with a circular shape corresponds to 3DOM LLT, and the gray area represents the gel impregnated into the pores of the LLT membrane. It can be seen that the pores of the 3DOM LLT are almost completely filled up with the gel. Figure 8.17a, b shows SEM images of the composite electrode between 3DOM LLT and $LiMn_2O_4$ after the first and fourth sol injections and the following heat treatment at 450 and 700 °C, respectively. By comparing the SEM image of the composite electrode system with that of the 3DOM LLT (Fig. 8.15), it was found that $LiMn_2O_4$ was

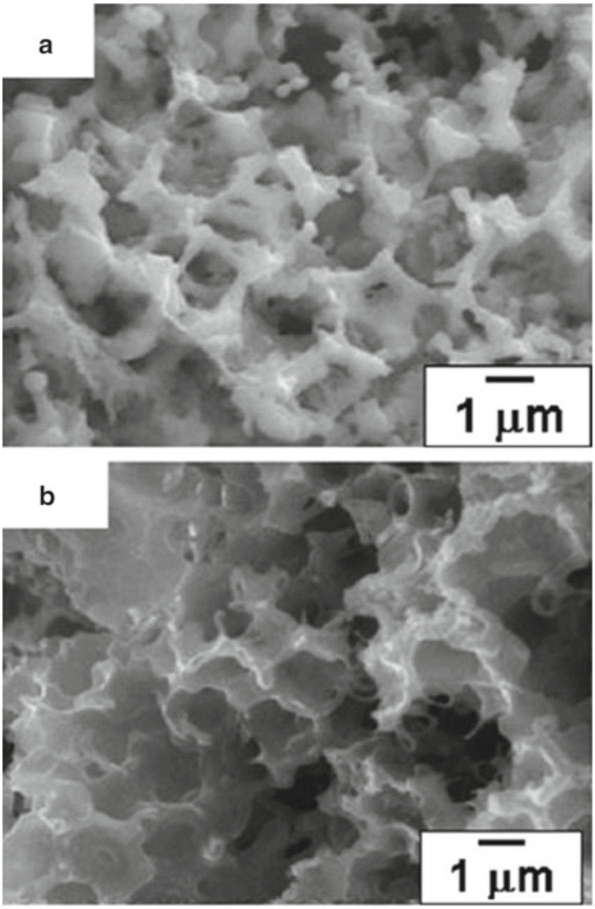

Fig. 8.17 Cross-sectional SEM image of composite electrode system of 3DOM LLT and $LiMn_2O_4$ after (**a**) first and (**b**) fourth injections

injected into the pores of the 3DOM LLT. Although the 3DOM LLT was filled up with the Li-Mn-O gel with SDS pretreatment, as shown in Fig. 8.16, voids were still observed in the composite electrode following heat treatment at 450 °C. This was due to a large amount of solvent contained in the Li-Mn-O gel injected into the pores of the 3DOM LLT. A decrease in the remaining voids in the composite following impregnation of the Li-Mn-O sol was observed four times, as shown in Fig. 8.17b.

Figure 8.18 shows the charge–discharge curves of all-solid-state cells with a composite electrode system between 3DOM LLT and $LiMn_2O_4$. The potential plateaus due to redox reactions of $Mn^{3+/4+}$ in $LiMn_2O_4$ were observed around 4.0 V. The result indicates that Li deintercalation/intercalation from/into $LiMn_2O_4$ take

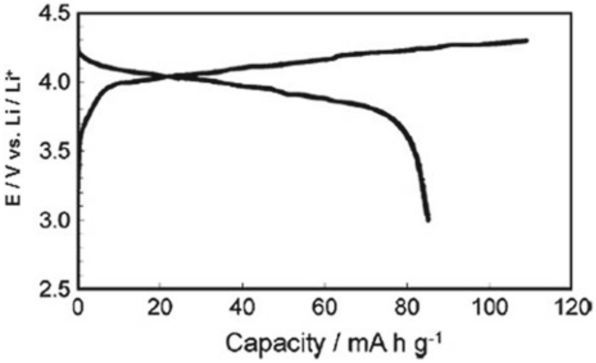

Fig. 8.18 Charge and discharge curves of composite electrode system of 3DOM LLT and $LiMn_2O_4$

place at the interface of the $LiMn_2O_4$–LLT solid electrolyte. The first discharge capacity was 83 mAh g^{-1}, which was lower than the theoretical value (148 mA h g^{-1}). However, the volumetric capacity of the LLT–$LiMn_2O_4$ composite exhibited a relatively high capacity, 220 mA h cm^{-3}, which was better than the volumetric capacity of a $LiMn_2O_4$ electrode used in a Li-ion battery with liquid electrolyte.

8.2 Summary

Some applications of a 3DOM structure to electrodes for lithium-ion batteries were described. A 3DOM anode and a 3DOM solid electrolyte-active material composite electrode showed good charge and discharge behavior due to the large contact area between electrode and electrolyte. It is expected that fabrication of high-performance Li-ion batteries will be achieved by application of the 3DOM structure.

References

1. S.-W. Woo, K. Dokko, K. Kanamura, Preparation and characterization of three dimensionally ordered macroporous $Li_4Ti_5O_{12}$ anode for lithium batteries. Electrochim. Acta **53**, 79–82 (2007)
2. T. Ohzuku, A. Ueda, N. Yamamoto, Zero-strain insertion material of $Li[Li_{1/3}Ti_{1/3}]O_4$ for rechargeable lithium cells. J. Electrochem. Soc. **142**, 1431 (1995)
3. S. Scharner, W. Weppner, P. Schmid-Beurmann, Evidence of two-phase formation upon lithium insertion into the $Li_{1.33}Ti_{1.67}O_4$ spinel. J. Electrochem. Soc. **146**, 857 (1999)
4. K. Kanamura, T. Umegaki, H. Naito, Z. Takehara, T. Yao, Structural and electrochemical characteristics of $Li_{4/3}Ti_{5/3}O_4$ as an anode material for rechargeable lithium batteries. J. Appl. Electrochem. **31**, 73–78 (2001)
5. Y.H. Rho, K. Kanamura, Li^+-ion diffusion in $LiCoO_2$ thin film prepared by the poly(vinylpyrrolidone) sole-gel method. J. Electrochem. Soc. **151**, A1406–A1411 (2004)

6. Y.Li. Jiang, J.G. Duh, M.H. Yang, D.T. Shieh, Electroless-plated tin compounds on carbonaceous mixture as anode for lithium-ion battery. J. Power Sources. **193**, 810–815 (2009).
7. H. Mukaibo, T. Momma, M. Mohamedi, T. Osaka, Structural and morphological modifications of a nanosized 62 atom percent Sn-Ni thin film anode during reaction with anode. J. Electrochem. Soc. **152**, A560–A565 (2005)
8. J. Hassoun, S. Panero, B. Scrosati, Electroplated Ni-Sn intermetallic electrodes for advanced lithium ion batteries. J. Power Sources. **160**, 1336–1341 (2006)
9. C.J. Wen, R.A. Huggins, Thermodynamic study of the tin-lithium system. J. Electrochem. Soc. **128**, 1181–1187 (1981)
10. J. Wang, I.D. Raistrick, R.A. Huggins, J.O. Besenhard, Electrochem. Solid-State Lett. **2**, 161 (1999)
11. F. Robert, P.-E. Lippens, J. Oliver-Fourcade, J.-C. Jumas, F. Gillot, M. Morcrette, J.-M. Tarascon, Mossbauer spectra as a “fingerprint” in tin-lithium compounds: Applications to Li-ion batteries. J. Solid State Chem. **180**, 339–348 (2007)
12. H. Mukaibo, T. Sumi, T. Yokoshima, T. Momma, T. Osaka, Electrodeposited Sn-Ni alloy film as a high capacity anode material for lithium-ion secondary batteries. Electrochem. Solid-State Lett. **6**, A218–A220 (2003)
13. A. Ulus, Y. Rosenberg, L. Burstein, E. Peled, Tin-alloy graphite composite anode for lithium ion batteries. J. Electrochem. Soc. **149**, A635–A643 (2002)
14. M. Stjerndahl, H. Bryngelsson, T. Gustafsson, J. Vaughey, M.M. Thackeray, K. Edstrom, Surface chemistry of intermettalic AlSb-anodes for Li-ion batteries. Electrochmica. Acta. **52**, 4947–4955 (2007)
15. H. Bryngelsson, M. Stjerndahl, T. Gustafsson, K. Edstrom, How dynamic is SEI? J. Power Sources **174**, 970–975 (2007)
16. K. Hoshina, K. Dokko, K. Kanamura, Investigation on electrochemical interface between $Li_4Ti_5O_{12}$ and $Li_{1-x}Al_xTi_{2-x}(PO_4)_3$ NASICON-type solid electrolyte. J. Electrochem. Soc. **152**, A2138–A2142 (2005)
17. X. Xu, Z. Wen, J. Wu, X. Yang, Preparation and electrical properties of NASICON-type structured $Li_{1.4}Al_{0.4}Ti_{1.6}(PO_4)_3$ glass-ceramics by the citric acid-assisted sol–gel method. Solid State Ion. **178**, 29–34 (2007)
18. M. Cretin, P. Fabry, Comparative study of lithium ion conductors in the system $Li_{1+x}Al_xA_{2-x}$IV(PO4)3 AIV = Ti or Ge and $0 < x < 0.7$ for use as Li^+ sensitive membranes. J. Eur. Ceram Soc. **19**, 2931–2940 (1999)
19. Y. Inaguma, C. Liquan, M. Itoh, T. Nakamura, T. Uchida, H. Ikuta, M. Wakihara, High ionic conductivity in lithium lanthanum titanate. Solid State Commun. **86**, 689–693 (1993)

Chapter 9
Direct Current Methods for Battery Evaluation

Masaaki Hirayama and Ryoji Kanno

9.1 Electrode and Battery Preparation

9.1.1 Handling

Nano-sized particles of lithium-containing materials are highly reactive in ambient air due to their high surface area. Generally, the surfaces of lithium intercalation electrodes are covered with lithium carbonate and lithium hydroxide via reactions between lithium in the electrode and moisture and carbon dioxide in the atmosphere [1–6]. For example, a small amount of lithium is spontaneously deintercalated from $LiFePO_4$ nanoparticles upon air exposure, leading to a capacity loss for the first charging [7]. The surface phase formation could cause severe degradation in electrode properties of nano-sized particles. Hence, the preparation of nano-sized electrodes and cell assembly should be carried out in an inert atmosphere.

9.1.2 Mixing with Conductive Additive and Binder

Conductive additives, such as carbon materials, are widely applied for nano-sized electrodes, especially for active materials with low electronic/ionic conductivity. Conductive additives improve surface electronic conductivity, leading to high a charge/discharge capacity and high rate characteristics of the electrodes. The nano-composite electrode is simply obtained by mixing together nanoparticles of the

---

M. Hirayama (✉) • R. Kanno
Department of Electronic Chemistry, Interdisciplinary Graduate School of Science
and Engineering, Tokyo Institute of Technology, 4259 Nagatsuta-cho,
Midori-ku, Yokohama 226-8502, Japan
e-mail: hirayama@echem.titech.ac.jp; kanno@echem.titech.ac.jp

T. Osaka and Z. Ogumi (eds.), *Nanoscale Technology for Advanced Lithium Batteries*,
Nanostructure Science and Technology 182, DOI 10.1007/978-1-4614-8675-6_9,

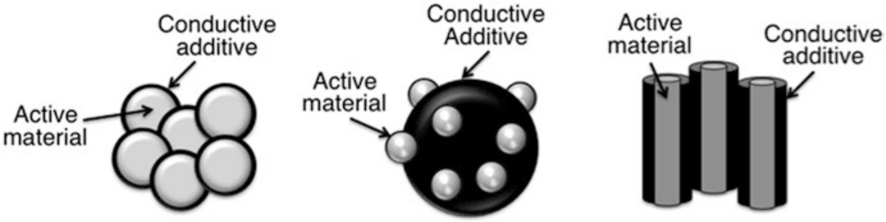

Fig. 9.1 Schematic drawings of various types of nanocomposite electrodes

active material, the conductive additive, and a polymeric binder such as polyvinylidene difluoride. However, the nanoparticles easily aggregate during the mixing process. The aggregated nanoparticles decrease contact points between the active material and the conductive additive. To prevent aggregation of the nanoparticles and achieve close contact with the conductive additive, the nanocomposite electrode is directly synthesized from a mixture of starting materials of the active component and the source of the conductive additive. In the synthesis process, the conductive additive acts to inhibit an increase in particle size. Figure 9.1 shows various types of composite electrodes that have been reported to achieve close contact between nanoparticles and conductive additives.

Coated electrodes are generally used for electrochemical tests of lithium batteries. The active material including the conductive additive, carbon material and binder material were thoroughly mixed by grinding, and made into a slurry by adding a polar organic solvent such as 1-methyl-2-pyrrolidinone (NMP) The slurry was spread on a metal foil and vacuum dried. The aluminum and copper foils were used as positive and negative electrodes, respectively.

9.1.3 Cell Configuration

The electrochemical cell used for nano-sized electrodes has the same configuration as that used for micro-sized electrodes. Although a cell consists of a cathode, an anode, and an electrolyte, various types of cell configurations are proposed for different purposes. A standard single cell to evaluate battery performance is a coin-type cell with a two-electrode configuration, as shown in Fig. 9.2. The coin-type cell consists of a working electrode of the active material and a counter electrode of metallic lithium in a half-cell configuration. Cell voltages are usually given with respect to the metallic lithium electrode (Li/Li^+). Since the metallic lithium electrode exhibits no change in the electrochemical potential, the charge and discharge curves of the half-cell provide information for the change in the electrochemical potential of the working electrode. The counter electrode serves as a reference electrode as well. A separator is used to avoid electrical contact between the working and counter electrodes. Appropriate species of separators and

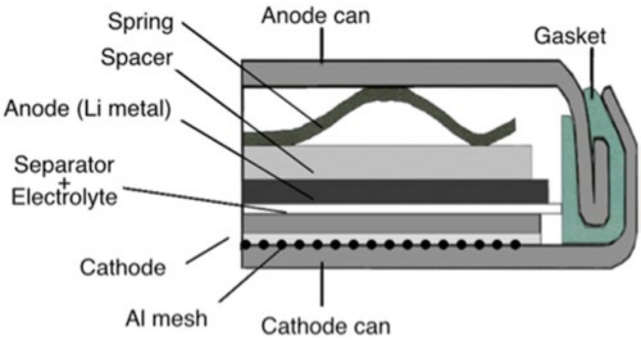

Fig. 9.2 Schematic diagram of standard coin-type cell

electrolytes should be chosen to optimize the battery performance. The cell should be assembled inside a glove box, under an inert gas atmosphere with as little content of O_2 and H_2O as possible. After completing the cell assembly, the cell is often left inside the glove box in order to make sure the electrodes are completely soaked with the electrolyte.

A half-cell using metallic lithium as a counter electrode is commonly used to evaluate the performance of working electrodes. However, practical lithium batteries do not contain metallic lithium due to safety considerations. Therefore, to investigate battery performance for practical use, the cell needs to contain a practical counter electrode such as graphite or $Li_4Ti_5O_{12}$ or metallic Si anodes for positive electrodes.

9.2 Calculation of Cell Capacity

Galvanostatic cycling is the most popular method to evaluate battery performance. A constant current, i (mA), is applied to the cell, and the potential is monitored as a function of time, t (h). The quantity of charge per hour, Q (C), is given by

$$Q = it \tag{9.1}$$

The total amount of charge passed per unit mass of electrode material, called the weight capacity density, C_w in Ah kg^{-1}, during complete discharge (or charge) is given by

$$C_w = it / 3.6m \tag{9.2}$$

where m is the mass of the electrode material in kilograms. Data from galvanostatic measurements are often displayed as cell voltage V as a function of C_w. The cyclability of the material is usually presented as the total charge or discharge capacity as a function of the cycle number.

The weight energy density, E_w (Wh kg^{-1}), and weight power density, P_w (W kg^{-1}), are used to evaluate the power characteristics of batteries. The weight energy density and the weight power density are given by

$$E_w = C_w V_{ave} \tag{9.3}$$

$$P_w = E_w / t \tag{9.4}$$

9.3 Charge/Discharge Test

9.3.1 Constant Current Mode

Charge/discharge cycling under a constant current (CC) is usually used for preliminary evaluation of the cell capacity of lithium-ion batteries. The test is conducted using a charge/discharge apparatus consisting of a potentiostat/galvanostat unit and a personal computer with appropriate controlling software. Figure 9.3 shows a schematic representation of the voltage and current changes for the CC mode. During the charge process, the cell voltage changes with the application of a constant current flow until the voltage reaches specified cutoff voltages.

Figure 9.4 shows the charge discharge curves of a cell with a $LiCoO_2$ cathode, a Li metal anode, and an organic electrolyte (ethylene carbonate/diethyl carbonate = 3:7 with 1 M $LiPF_6$). The cell voltage increases with the deintercalation of lithium ions from the $LiCoO_2$ lattice during the charging process. The charging process finishes when the voltage reaches 4.2 V, which is the upper cutoff voltage. During the discharging process, the cell voltage decreases with the intercalation of lithium ions into the $LiCoO_2$ lattice. The discharge process completes when the voltage reaches 2.5 V, the lower cutoff voltage. The crystal structure of $LiCoO_2$ changes with the Li^+ ion composition. The discharge capacity is approximately 140 mAh g^{-1}, attributed to the lithium (de)intercalation between $LiCoO_2$ and $Li_{0.5}CoO_2$. The structural change shows high reversibility in this composition region.

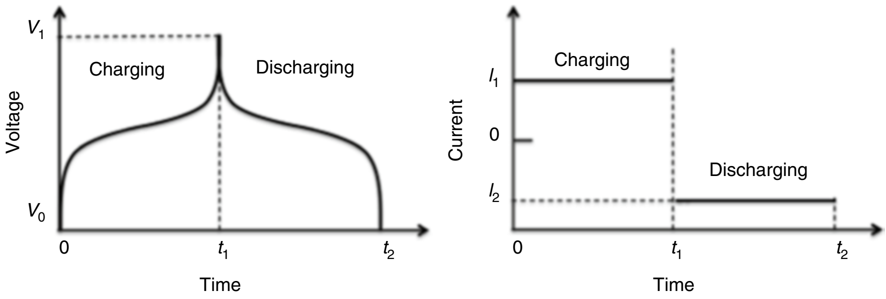

Fig. 9.3 Schematic representation of voltage and current changes for CC mode

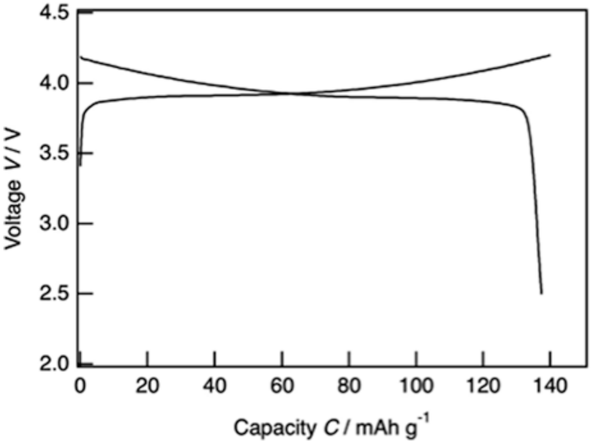

Fig. 9.4 Charge discharge curves of a cell with a $LiCoO_2$ cathode and a Li metal anode between 4.2 and 2.5 V at 25 °C. The cell was charged and discharged under a CC mode. The charge/discharge rate was 1/10 C (27 mA g^{-1})

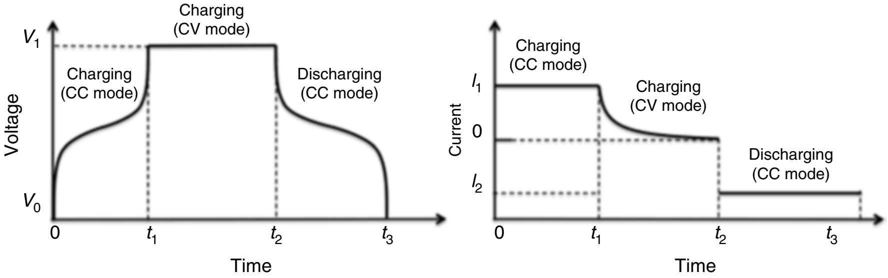

Fig. 9.5 Schematic representation of voltage and current changes for CC/CV charging and CC discharging

9.3.2 Constant Current and Constant Voltage Mode

Lithium batteries are vulnerable to damage if the upper voltage limit is exceeded in the charging process. Special precautions are needed to ensure that the battery is fully charged while at the same time is not being overcharged. Therefore, the charging method typically is switched to a constant voltage (CV) method before the cell voltage reaches its upper limit. The preferred charge algorithm for lithium batteries is a CC and CV algorithm, shown in Fig. 9.5. During the initial part of the charging, a constant current is carried into the cell until the battery voltage rises to a specific value (called the float voltage). Once the float voltage is reached (t_1), the output voltage of the charger is maintained at the float value (CV mode) until the charge current decreases to a fixed, low value. Once the low current is reached, the charger

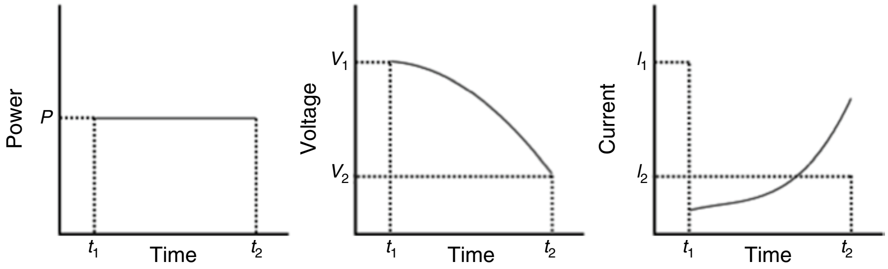

Fig. 9.6 Schematic representation of power, voltage, and current changes at constant power discharging

is turned off (t_2). Lithium batteries are usually not trickle-charged after charge termination. Maintaining a low current after charge termination can actually damage some types of lithium battery. In practical lithium batteries, a trickle charge is often used to restore charge to deeply depleted cells.

9.3.3 Constant Resistance Mode

The constant resistance mode simulates a standard resistive load by providing a current drain proportional to the voltage. The discharge current decreases as the battery voltage drops, and the power decreases as the square of the battery voltage. Under this mode of discharge, in order to assure that the required power is available at the end of the discharge voltage, the current and power during the earlier part of the discharge start higher than the minimum required. The battery discharges at a high current, draining its ampere-hour capacity rapidly and excessively, which will result in a shorter discharge time.

9.3.4 Constant Power Mode

The constant power mode was designed to study the discharging properties of cells that successively produce a constant power. The constant power is controlled by holding the power, $P = VI$, to a constant value. In the constant power mode, the current is lowest at the beginning of the discharge and increases as the voltage drops in order to maintain a constant-power output at the level required by the equipment, as shown in Fig. 9.6. The average current is lowest under this mode of discharge, and, hence, the longest discharge time is obtained. As the voltage decreases near the end of discharging, the current increases to maintain constant power. This mode is commonly used for Ragone plot representations [8]. Batteries are classified in this representation according to their power and energy properties.

9.3.5 Cycle Life Test

The cycle life is one of the key cell performance parameters and gives an indication of the expected working lifetime of a cell. In charge/discharge cycling, the electrochemical reaction is accompanied by a slow deterioration of the materials in the cell that will be almost imperceptible to the user. This deterioration may be the result of unavoidable, unwanted chemical actions in the cell or due to crystal or dendrite growth, thereby altering the morphology of the particles making up the electrodes. Both of these events may have the effect of reducing the volume of the active chemicals in the cell, and hence its capacity, or of increasing the cell's internal impedance. The cycle life also depends on the temperature, both operating and storage.

9.3.6 Rate Capability Experiment

The rate capability experiment is a useful technique to assess the electrochemical performance of an electrode and its active material. It measures the amount of charge stored within an electrode under various experimental conditions with increasing cycle numbers. The experiments can be controlled in different ways. For example, the charge or discharge of the electrode can have a potentiostatic step, including the voltage being held constant until the current falls below a certain limit. In contrast, while the voltage is not controlled in a galvanostatic step, the current can be defined. The specific current, i_m, is often expressed as ampere per gram, with mass relative to the amount of active material. Alternatively, the specific current can be expressed in terms of a C-rate, which is the theoretical amount of charge that can be extracted from a given material within 1 h. The discharge curves for a lithium-ion battery show that the effective capacity of the cell is reduced if the cell is discharged at very high rates (or conversely increased with low discharge rates).

9.3.7 Charge/Discharge Performance of Nano-Sized Electrodes

Nano-sized electrodes exhibit larger charge/discharge capacities and better rate characteristics than micro-sized electrodes. Various interpretations of these advantages have been established in terms of both the bulk and surface properties [9–16]: (1) shorter path lengths for electronic and lithium-ion transport enhance reaction rates in the bulk region, (2) different strains, ionic distributions, and crystallinities in the bulk region lead to fast lithium diffusion, (3) high contact area at the electrode/electrolyte increases the frequency of interfacial reactions, and (4) different thermodynamic energy at the near-surface region changes the reaction potential and increases the capacity. Currently, most electrodes for lithium batteries are prepared

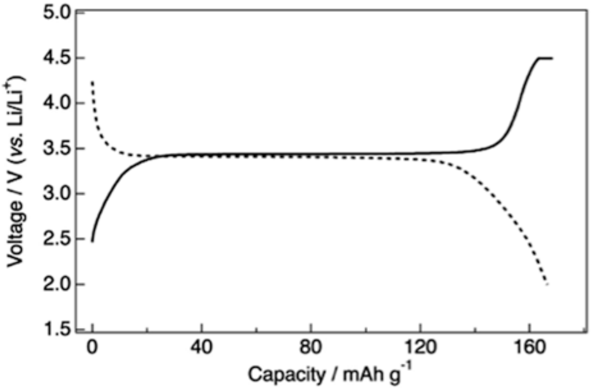

Fig. 9.7 Charge discharge curves for a cell with a 40-nm $LiFePO_4$/C composite electrode between 4.5 and 2.0 V at 25 °C. The cell was charged under a CC/CV mode and discharged under a CC mode. The charge/discharge rate was 1/20 °C

in the form of nanoparticles, and their charge/discharge performance has been investigated.

A successful example of nanosizing is the $LiFePO_4$ cathode material, which has intrinsically low electronic and ionic conductivities. Therefore, the electrochemical reaction of micro-sized $LiFePO_4$ is slow and restricted in its extent. Nanosizing and coating of conductive carbon enhance the electronic and ionic conductivities of $LiFePO_4$ electrodes, yielding larger charge/discharge capacities and better rate characteristics than micro-sized $LiFePO_4$ [9, 10, 15, 16]. Figure 9.7 shows the charge/discharge curves of a cell with a 40-nm $LiFePO_4$/C composite electrode between 4.5 and 2.0 V at 25 °C. The cell was charged under a CC/CV mode and was discharged under a CC mode. The reversible capacity of 166 mAh g^{-1} is almost equal to the theoretical capacity of $LiFePO_4$ (170 mAh g^{-1}). A flat charge/discharge profile over a large composition range at 3.4 V indicates that the two-phase redox reaction proceeds via a first-order transition between $Li_{1-\alpha}FePO_4$ and $Li_{\beta}FePO_4$. Nano-sized $LiFePO_4$ exhibits a wider range of the solid solution than micro-sized $LiFePO_4$.

A rate capability experiment was conducted for 80-nm $LiFePO_4$ nanoparticles. A $LiFePO_4$/C nanocomposite electrode was used as the cathode in a nonaqueous lithium cell. The cell was discharged under various rates including 1/20 °C, 1/10 °C, 1/5 °C, 1/2 °C, 1 °C, 5 °C, 10 °C, 20 °C, and 50 °C, with 1 °C being proportional to 170 mA g^{-1}, which is the theoretical amount of discharge inserted into $Li_{1-x}FePO_4$ for $x=0$. Figure 9.8 shows the discharge curves and the specific discharge capacities for different discharge rates. Although the performance of the material decreases as the C-rate increases, the $LiFePO_4$/C nanocomposite electrode delivered a discharge capacity of over 100 mAh g^{-1} under an extremely high rate operation at 50 °C. Recent studies have proposed that the wider solid-solution range compared to the micro-sized $LiFePO_4$ is responsible for the enhanced rate of lithium intercalation [9, 17].

Nano-sized electrodes often exhibit a higher discharging capacity than micro-sized electrodes. Figure 9.9 shows the charge/discharge curves of nano-sized

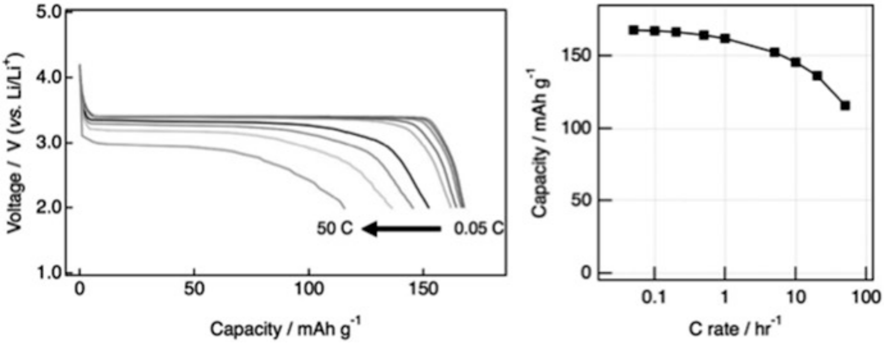

Fig. 9.8 Rate capability experiment for 80 nm $LiFePO_4$ nanoparticles. 1 °C is equivalent to 170 mA g^{-1}

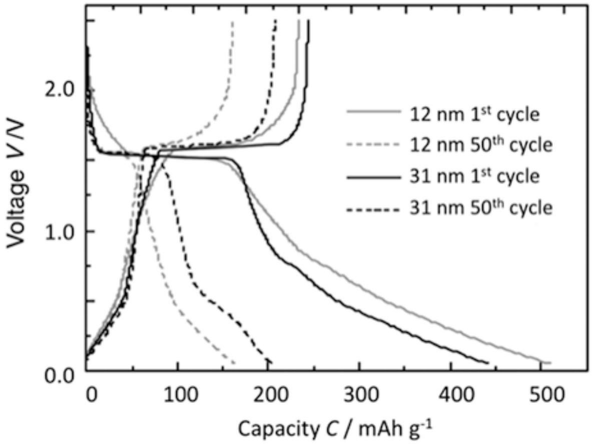

Fig. 9.9 First and 50th charge/discharge curves of 12- and 31-nm $Li_4Ti_5O_{12}$ crystallites at a charge rate of 17.5 mAh g^{-1} (C/10) between 2.5 and 0.05 V vs. Li/Li^+ (Data taken from [14])

$Li_4Ti_5O_{12}$, a promising anode material for lithium batteries. In the initial cycle, nano-sized $Li_4Ti_5O_{12}$ exhibited a higher capacity than micro-sized $Li_4Ti_5O_{12}$ particles (approximately 175 mAh g^{-1}; $Li_4Ti_5O_{12}+3Li+ +3e^- \rightarrow Li_7Ti_5O_{12}$). A crystal structure in the surface region of $Li_4Ti_5O_{12}$ different from that in the bulk region due to the distribution of different redox potentials at the surface has been proposed as excess lithium storage in nano-sized $Li_4Ti_5O_{12}$. However, the capacity of nano-sized $Li_4Ti_5O_{12}$ surprisingly drops upon further cycling. This deterioration behavior is often observed for nano-sized electrodes because the large surface area enhances side reactions of the electrolyte species such as decomposition of the electrolyte, formation of a surface interfacial layer, and dissolution of electrode species.

Nanosizing can activate the electrochemical reactivity of electrode materials with low activity. Layered rock-salt-type $LiFeO_2$ was expected to be an alternative

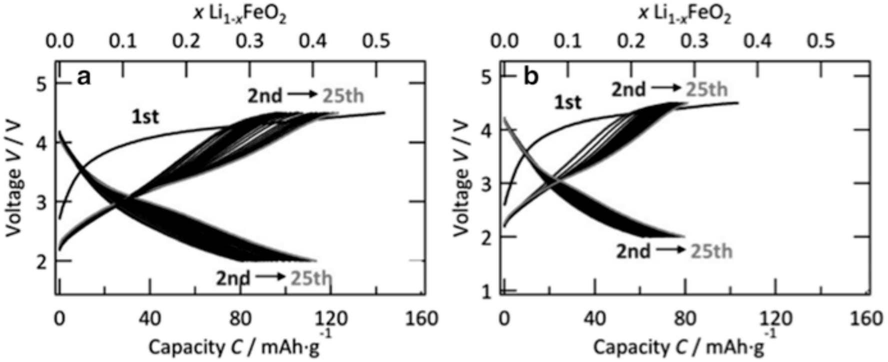

Fig. 9.10 Charge/discharge curves of $LiFeO_2$ nanoparticles with particle size of (**a**) 40 nm and (**b**) 400 nm. The current density was 10 mA g^{-1} (1/28 °C). The cutoff voltages were 4.5 and 2.0 V (Data taken from [16])

to the $LiCoO_2$ cathode used in practical cathodes because of its low cost and non-toxicity. However, the $LiFeO_2$ micro-sized particles provided only a low electrochemical capacity of 8 mAh g^{-1} due to the difficulty in the oxidation of Fe^{3+} to Fe^{4+} [18]. In contrast, $LiFeO_2$ nanoparticles show higher electrochemical activity with higher charge/discharge capacities than micro-sized electrodes [16, 19]. Figure 9.10 shows the charge/discharge curves of $LiFeO_2$ nanoparticles. The $LiFeO_2$ nanoparticles exhibited a discharge capacity of over 100 mAh g^{-1}. Whereas a plateau around 4 V was observed during the first charge process, it disappeared in the second charge process. Furthermore, a new plateau gradually appeared around 3 V during electrochemical cycling. These changes in charge/discharge curves suggest a phase transition in the $LiFeO_2$ nanoparticles during the first charge process and following cycles. The average voltage of the discharge curve increased from 2.83 V for the first discharge to 2.95 V for the 25th discharge.

9.4 Cyclic Voltammetry

Cyclic voltammetry is a potentiodynamic electrochemical measurement technique for initial electrochemical studies to evaluate the reaction potentials and reversibility of a redox system and is very useful for obtaining information about fairly complicated electrode reactions. Cyclic voltammetry also provides data on the kinetics of heterogeneous electrotransfer reactions [20].

In a cyclic voltammetry experiment, the voltage of a working electrode vs. a reference electrode is swept using a potentiostat. The voltage linearly increases in a linear sweep vs. time for the working electrode cycled against a counter electrode. An example of a linear sweep with a scan rate of 1 mV s^{-1} is shown in Fig. 9.11a, wherein a voltaic cell is cycled between a potential of 3.0 and 4.5 V vs. Li/Li^+. The current response of the cell is plotted as a cyclic voltammogram.

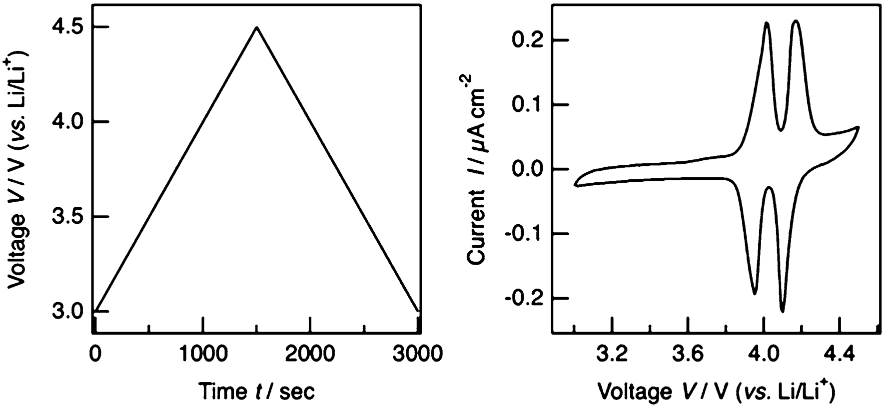

Fig. 9.11 Cyclic voltammetry measurements of 33-nm-thick $LiMn_2O_4$ thin film between 3.0 and 4.5 V with a scan rate of 1 mV s^{-1}. (**a**) Voltage changes during measurement. (**b**) Cyclic voltammogram

As an example, a 30-nm-thick $LiMn_2O_4$ thin film was prepared as a working electrode and arranged into a voltaic cell with lithium metal acting simultaneously as the counter and reference electrode. The cell was cycled between 3.3 and 4.5 V vs. Li/Li^+ at 1 mV s^{-1}. The resulting Cyclic voltammogram is seen in Fig. 9.11b.

The Cyclic voltammogram provides information on the redox reactions of the $LiMn_2O_4$ electrode: two pairs of redox peaks at approximately 4.00 and 4.15 V are clearly observed, indicating two stages of lithium-ion deintercalation and intercalation [21, 22]. The first oxidation peak at 4.0 V is attributed to the removal of one-half Li^+ in the $LiMn_2O_4$ lattice:

$$\mathrm{LiMn_2O_4 \rightarrow Li_{0.5}Mn_2O_4 + 1/2\,Li^+ + 1/2\,e^-} \tag{9.5}$$

The second oxidation peak at 4.2 V is attributed to the removal of the remaining Li^+ from the lattice:

$$\mathrm{Li_{0.5}Mn_2O_4 \rightarrow 2MnO_2 + 1/2\,Li^+ + 1/2\,e^-} \tag{9.6}$$

The reactions in Eqs. 9.5 and 9.6 are detected by Cyclic voltammogram experiments in Fig. 9.11b. The peak positions are not located at the thermodynamic potential due to the overpotentials that occur. Factors contributing to the overpotentials in this heterogeneous system include the electrolyte resistance, the resistance between the current collector and active material, the charge-transfer resistance, and the diffusion processes. Generally, a lower scan rate causes the peaks to occur at positions closer to the thermodynamic potentials of the system, whereas a higher scan rate increases the overpotentials.

Note that the shape of the Cyclic voltammogram for composite electrodes is often affected by the conductive addictive and binder present. The use of thin-film and single-particle electrodes with no additives is a way to evaluate the intrinsic properties of active materials.

9.5 Open-Circuit Voltage Measurement

Open-circuit voltage (OCV) measurement is used to evaluate the actual redox potential, excluding the internal resistance, in lithium batteries. The cell is charged or discharged with a constant current for a while, then the current is stopped and the cell is left in the open-circuit state until the magnitude of the change in the voltage diminishes with time before it is charged or discharged again. By repeating this process, OCV curves are obtained.

9.6 Galvanostatic and Potentiostatic Intermittent Titration Technique

Galvanostatic intermittent titration (GITT) and potentiostatic intermittent titration (PITT) are performed to determine the redox potentials and the kinetics of diffusion of lithium ions in active electrodes. Both GITT and PITT are based on the same assumption of Fick's law [23, 24].

The GITT method corresponds to performing successive charge increments by applying a constant current from a galvanostat as a function of time, then switching to open circuit to determine the corresponding equilibrium potential. The time dependence of the potential when the current is switched on and off (chronopotentiometry) can provide information on the kinetics of the process. Assuming one-dimensional diffusion in a solid solution (not a two-phase coexisting reaction), the ion diffusion coefficient is explained using Fick's law through the following equation:

$$D_{\mathrm{GITT}} = \frac{4}{\pi}\left(\frac{IV_M}{z_A FS}\right)^2 \left[\left(\frac{dE(x)}{dx}\right) \Big/ \left(\frac{dE(t)}{d\sqrt{t}}\right)\right]^2 \left(t \ll L^2 / D_{\mathrm{GITT}}\right) \tag{9.7}$$

where L is the characteristic length of the electrode material, F is the Faraday constant, Z_A is the charge number of the active material, S is the current applied, and V_M is the molar volume of the electrode material. The value of $dE(t)/dt^{1/2}$ is obtained from a plot of the voltage vs. the square root of the time during a constant current pulse, and dE(x)/dx is obtained by plotting the equilibrium voltage for each composition of active material after a current pulse. Ohmic potential drop, double layer charging, charge-transfer kinetics, and phase transformation are excluded in this calculation.

The PITT method corresponds to applying, using a potentiostat, a potential equal to the initial equilibrium potential to the electrode. Then, a small voltage step is applied to the cell, and the resulting current (chronoamperometric response) is measured as a function of time. Switching to open circuit makes it possible to record the equilibrium potential, which will be as close to the previously applied potential as the final current was negligible at the cutoff. The diffusion coefficient of ions in solid-solution electrodes can be estimated based on Fick's law using the following equation with the same assumptions as those made for GITT:

$$D_{\mathrm{PITT}} = -\frac{d\ln I(t)}{dt}\frac{4L^2}{\pi}\left(t \gg L^2 / D_{\mathrm{PITT}}\right) \tag{9.8}$$

Here, L is the characteristic length of the electrode material and $I(t)$ is the current measured during the constant voltage step.

Diffusion coefficient values in electrode materials for batteries are usually in a range of 10^{-8}–10^{-12} cm^2 s^{-1}. With a diffusion coefficient of 10^{-10} cm^2 s^{-1}, it takes hours to be close to equilibrium in a grain of material with a 20-μm diameter after a change in the surface concentration related to the potential step.

For active materials operated with a two-phase reaction, lithium ions are transported through both movement of an interphase boundary and ionic diffusion. The moving-boundary model has been proposed by taking into account the effect of phase transformation and assuming equilibrium conditions at the interphase boundary [25–28].

References

1. K. Matsumoto, R. Kuzuo, K. Takeya, A. Yamanaka, Effects of CO2 in air on Li deintercalation from $LiNi_{1-x-y}Co_xAl_yO_2$. J. Power. Sources **81–82**, 558–561 (1999)
2. R. Moshtev, P. Zlatilova, S. Vasilev, I. Bakalova, A. Kozawa, Synthesis, XRD characterization and electrochemical performance of overlithiated LiNiO2. J. Power. Sources **81–82**, 434–441 (1999)
3. D. Aurbach, K. Gamolsky, B. Markovsky, G. Salitra, Y. Gofer, U. Heider, R. Oesten, M. Schmidt, The study of surface phenomena related to electrochemical lithium intercalation into $LiMO_y$ host materials (M = Ni, Mn). J. Electrochem. Soc. **147**, 1322–1331 (2000)
4. M. Hirayama, K. Sakamoto, T. Hiraide, D. Mori, A. Yamada, R. Kanno, N. Sonoyama, K. Tamura, J. Mizuki, Characterization of electrode/electrolyte interface using in situ X-ray reflectometry and $LiNi_{0.8}Co_{0.2}O_2$ epitaxial film electrode synthesized by pulsed laser deposition method. Electrochim. Acta **53**, 871–881 (2007)
5. M. Hirayama, N. Sonoyama, T. Abe, M. Minoura, M. Ito, D. Mori, A. Yamada, R. Kanno, T. Terashima, M. Takano, K. Tamura, J. Mizuki, Characterization of electrode/electrolyte interface for lithium batteries using in situ synchrotron X-ray reflectometry – A new experimental technique for $LiCoO_2$ model electrode. J. Power. Sources **168**, 493–500 (2007)
6. M. Hirayama, N. Sonoyama, M. Ito, M. Minoura, D. Mori, A. Yamada, K. Tamura, J. Mizuki, R. Kanno, Characterization of electrode/electrolyte interface with X-ray reflectometry and epitaxial-film $LiMn_2O_4$ electrode. J. Electrochem. Soc. **154**, A1065–A1072 (2007)
7. J.F. Martin, A. Yamada, G. Kobayashi, S.I. Nishimura, R. Kanno, D. Guyomard, N. Dupre, Air exposure effect on $LiFePO_4$. Electrochem. Solid State Lett. **11**, A12–A16 (2008)
8. T. Christen, M.W. Carlen, Theory of Ragone plots. J. Power. Sources **91**, 210–216 (2000)
9. A. Yamada, H. Koizumi, S.-I. Nishimura, N. Sonoyama, R. Kanno, M. Yonemura, T. Nakamura, Y. Kobayashi, Room-temperature miscibility gap in Li_xFePO_4. Nat. Mater. **5**, 357–360 (2006)
10. P. Gibot, M. Casas-Cabanas, L. Laffont, S. Levasseur, P. Carlach, S. Hamelet, J.M. Tarascon, C. Masquelier, Room-temperature single-phase Li insertion/extraction in nanoscale $LixFePO_4$. Nat. Mater. **7**, 741–747 (2008)

11. H. Chen, X. Qiu, W. Zhu, P. Hagenmuller, Synthesis and high rate properties of nanoparticled lithium cobalt oxides as the cathode material for lithium-ion battery. Electrochem. Commun. **4**, 488–491 (2002)
12. M. Wagemaker, W.J.H. Borghols, F.M. Mulder, Large impact of particle size on insertion reactions. A case for anatase Li_xTiO_2. J. Am. Chem. Soc. **129**, 4323–4327 (2007)
13. W.J.H. Borghols, M. Wagemaker, U. Lafont, E.M. Kelder, F.M. Mulder, Impact of nanosizing on lithiated rutile TiO_2. Chem. Mater. **20**, 2949–2955 (2008)
14. W.J.H. Borghols, M. Wagemaker, U. Lafont, E.M. Kelder, F.M. Mulder, Size effects in the $Li_{4+x}Ti_5O_{12}$ spinel. J. Am. Chem. Soc. **131**, 17786–17792 (2009)
15. A. Yamada, S.C. Chung, K. Hinokuma, Optimized LiFePO4 for lithium battery cathodes. J. Electrochem. Soc. **148**, A224–A229 (2001)
16. M. Hirayama, H. Tomita, K. Kubota, R. Kanno, Structure and electrode reactions of layered rocksalt $LiFeO_2$ nanoparticles for lithium battery cathode. J. Power Sources. **196**, 6809–6814 (2011)
17. N. Meethong, H.Y.S. Huang, S.A. Speakman, W.C. Carter, Y.M. Chiang, Strain accommodation during phase transformations in olivine-based Cathodes as a materials selection criterion for high-power rechargeable batteries. Adv. Func. Mater **17**, 1115–1123 (2007)
18. K. Ado, M. Tabuchi, H. Kobayashi, H. Kageyama, O. Nakamura, Y. Inaba, R. Kanno, M. Takagi, Y. Takeda, Preparation of $LiFeO_2$ with alpha-$NaFeO_2$-type structure using a mixed-alkaline hydrothermal method. J. Electrochem. Soc. **144**, L177–L180 (1997)
19. M. Hirayama, H. Tomita, K. Kubota, H. Ido, R. Kanno, Synthesis and electrochemical properties of nanosized $LiFeO_2$ particles with a layered rocksalt structure for lithium batteries. Mater. Res. Bull **47**, 79–84 (2012)
20. J. Heinze, Cyclic voltammetry – "electrochemical spectroscopy". New Anal. Methods 25, Ang. Chem. Int. Ed. **23**, 831–847 (1984)
21. J.M. Tarascon, D. Guyomard, G.L. Baker, An update of the Li metal-free rechargeable battery based on $Li_{1+x}Mn_2O_4$ cathodes and carbon anodes. J. Power. Sources **44**, 689–700 (1993)
22. M. Winter, J.O. Besenhard, M.E. Spahr, P. Novák, Insertion electrode materials for rechargeable lithium batteries. Adv. Mater. **10**, 725–763 (1998)
23. W. Weppner, R.A. Huggins, Determination of the kinetic parameters of mixed-conducting electrodes and application to the system Li_3Sb. J. Electrochem. Soc. **124**, 1569–1578 (1977)
24. C.J. Wen, B.A. Boukamp, R.A. Huggins, W. Weppner, Thermodynamic and mass transport properties of "LiAl". J. Electrochem. Soc. **126**, 2258–2266 (1979)
25. A. Funabiki, M. Inaba, T. Abe, Z. Ogumi, Stage transformation of lithium-graphite intercalation compounds caused by electrochemical lithium intercalation. J. Electrochem. Soc. **146**, 2443–2448 (1999)
26. M.D. Levi, D. Aurbach, Frumkin intercalation isotherm, a tool for the description of lithium insertion into host materials: A review. Electrochim. Acta **45**, 167–185 (1999)
27. E. Markevich, M.D. Levi, D. Aurbach, Comparison between potentiostatic and galvanostatic intermittent titration techniques for determination of chemical diffusion coefficients in ion-insertion electrodes. J. Electroanal. Chem. **580**, 231–237 (2005)
28. Y. Zhu, C. Wang, Galvanostatic intermittent titration technique for phase-transformation electrodes. J. Phys. Chem. C **114**, 2830–2841 (2010)

Chapter 10
Characterization of Neighbor Atoms

Yuki Orikasa, Titus Masese, Hajime Arai, Yoshiharu Uchimoto, and Zempachi Ogumi

10.1 Introduction

X-ray absorption spectroscopy (XAS) is powerful tool to investigate electronic or local structural change during a charge/discharge process in the electrode materials of Li-ion batteries. X-ray absorption fine structure (XAFS) spectroscopy is a well-established technique for structural investigations of samples in the solid state. XAFS can be divided into two components: absorption edge-spectrum, also referred to as near-edge X-ray absorption near-edge structure (XANES), and extended X-ray absorption fine structure (EXAFS). The edge spectra result from X-ray-induced transitions of the core electron (e.g., a 1*s* electron for a *K*-edge) to unoccupied levels and are thus very sensitive to electronic structure. The EXAFS results from the scattering of an ejected core electron by neighboring atoms and is used to probe the local structure within a material. In the following sections, we will describe the physical principles of XAFS at a sufficiently basic level so that scientists working in the field of electrochemistry get to know some applications of the XAFS technique in battery research.

Y. Orikasa (✉) • T. Masese • Y. Uchimoto
Graduate School of Human and Environmental Studies, Kyoto University,
Yoshida-nihonmatsu-cho, Sakyo-ku, Kyoto 606-8501, Japan
e-mail: orikasa.yuuki.2a@kyoto-u.ac.jp; uchimoto.yoshiharu.2n@kyoto-u.ac.jp

H. Arai • Z. Ogumi
Society-Academia Collaboration for Innovation, Kyoto University,
Gokasho, Uji 611-0011, Japan
e-mail: h-arai@saci.kyoto-u.ac.jp; ogumi@scl.kyoto-u.ac.jp

T. Osaka and Z. Ogumi (eds.), *Nanoscale Technology for Advanced Lithium Batteries*,
Nanostructure Science and Technology 182, DOI 10.1007/978-1-4614-8675-6_10,

10.2 Principles of XAFS Spectroscopy

When a beam of X-ray photons passes through a material, the incident intensity *I* will be decreased by an amount determined by the absorption characteristics of the material being irradiated. For a path length *dt* of the radiation through the material the decrease *dI* is given by

$$dI = -\mu\left(E\right) Idt \tag{10.1}$$

with the linear absorption coefficient $\mu(E)$ being a function of the photon energy. Integrating Eq. (10.1) over the total thickness *t* yields Beer–Lambert's law:

$$I = I_0 e^{-\mu(E)t} \tag{10.2}$$

X-ray absorption spectroscopy exhibits a generally smoothly decreasing intensity to higher energy. When the energy of the incoming photons is large enough to excite an electron from a deeper core level to a vacant excited state or to the continuum (e.g., after the absorption edge), a sharp rise in the absorption intensity appears. This sharp rise is denoted as the threshold energy or absorption edge.

At the absorption edge, E_{edge}, the kinetic energy of the electron (E_k) is defined to be equal to E_0, often referred to as the zero-point energy or inner potential. For any energy above this, the kinetic energy of the photoelectron is given by

$$E_k = h\nu - E_{binding} \tag{10.3}$$

Quantum mechanically the outgoing photoelectron can be represented as a spherical wave with wavelength λ (recall Debroglie's equation) defined as

$$\lambda = 2\pi / k$$

and

$$k = \left\{\left(8\pi^2 m / h^2\right)\left(h\nu + E_o - E_{edge}\right)\right\}^{1/2} \tag{10.4}$$

with *k* as the wave vector, *m* the electron mass, and *h* Planck's constant.

The linear absorption coefficient $\mu(E)$ is proportional to the transition probability of the photoelectric event. According to Fermi's golden rule, the transition probability is (within the dipole approximation) a function of the initial-state and final-state wave functions [1]:

$$\mu\left(E\right) = C \parallel \psi_f \parallel \text{Œ} \parallel \psi_i \parallel^2 \delta\left(E_f - E_{edge} - h\nu\right) \tag{10.5}$$

Here ê is the electric field polarization vector of the photon and *r* the coordinate vector of the electron. The dipole approximation is only valid when the wavelength of the photons is larger than the size of the absorbing atom. The final-state wave function ψ_f consists of two main parts, namely, the outgoing electron wave and a backscattered electron wave:

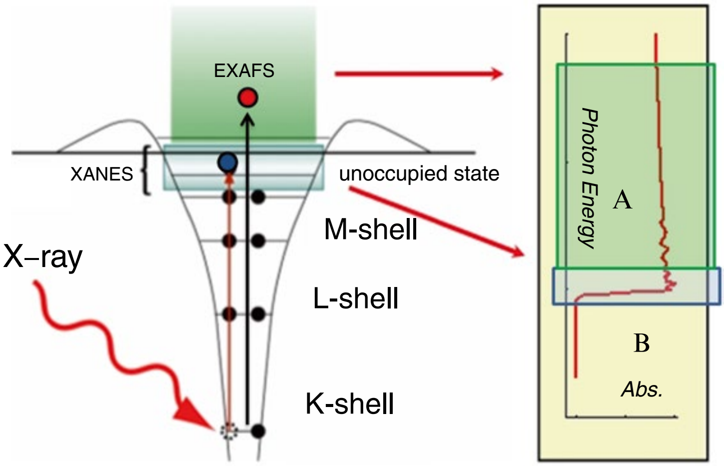

Fig. 10.1 Schematic illustration of photoelectric effect in terms of excitation of different energy levels

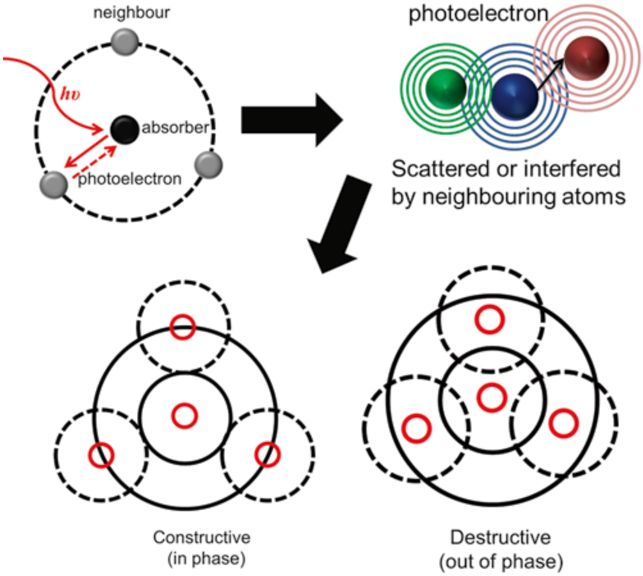

Fig. 10.2 Illustration of neighboring shells of atoms about absorber (*top*) and constructive (*in phase*) or destructive (*out of phase*) interference between outgoing photoelectron wave and the neighboring atoms backscattered off this wave (*bottom*)

$$\psi_f = \psi_{outgoing} + \psi_{backscattered} \tag{10.6}$$

Interference between these two final-state wave functions causes the observed fine structure in X-ray absorption spectra.

Figure 10.1 shows a schematic representation of the photoelectric effect, that is, the interaction of an X-ray photon with matter producing a photoelectron with a kinetic energy given by Eq. 10.3. Figure 10.2 clearly shows that the outgoing electron can be viewed as a spherical wave that scatters off neighboring atoms (e.g., electron density), producing a backscattered wave. The outgoing and backscattered waves interfere, causing an interference pattern varying between total construction (the two waves are fully in phase) or total destruction (the two waves are exactly out of phase). Since the path lengths of both waves define their final phase, it can be seen that the distance to the neighboring atoms determines the interference pattern. Equation 10.5 shows that the absorption coefficient is proportional to the transition probability defined by the matrix element.

Several authors have given derivations for the EXAFS theory [2–5]. The simplest theory is based on the single-scattering plane-wave approximation. In this approximation the electron wave is viewed as a plane wave, rather than a spherical wave, to simplify the mathematical derivation. The plane-wave approximation assumes that the atomic radii are much smaller than the interatomic distances and is valid only for higher k-values ($k > 3$ Å) [Eq. 10.4]. At lower k-values the curved wave, or spherical wave, theory must be used to give reasonable agreement with experiments.

Here only the equations obtained from the plane-wave approximation will be given. In the single-scattering event, the electron is assumed to be scattered only once before it returns to the absorber atom. This simplification is sufficient to describe and analyze the EXAFS signals in most experimental data. The χ function can be given as a summation over all interference patterns (sine waves) scattered off of all neighboring atoms:

$$\chi(k) = \sum_i \chi_i(k) \tag{10.7}$$

$$\chi_i(k) = A_i(k)\sin\left(2kR_i + \delta_i(k)\right) \tag{10.8}$$

$$A_i(k) = N_i\left|f_i(k,\pi)\right|\exp\left(-\left(2\sigma_i^2k^2 + R_i/\lambda\right)\right)/kR_i^2 \tag{10.9}$$

where k is the wave number of the photon, R_i the distance between the absorber and the scattered atom, $f(k,\pi)$ the backscattering amplitude (which is element specific), λ the mean free path, δ the phase shift, N the coordination number, and σ the Debye–Waller factor (local distortion factor).

10.3 Electronic and Local Structural Changes in Li_2FeSiO_4 Nanoparticles

As a case example, let us see how the XAFS technique has been employed to study electronic and local structural changes in Li_2FeSiO_4 – a promising high-capacity cathode material for next-generation lithium-ion batteries. XAFS spectroscopic measurements were performed in order to investigate the structural changes that occur in

Fig. 10.3 (**a**) Charge and discharge profiles of phase-pure Li_2FeSiO_4 recorded at C/20 rate and (**b**) cyclability data at room temperature

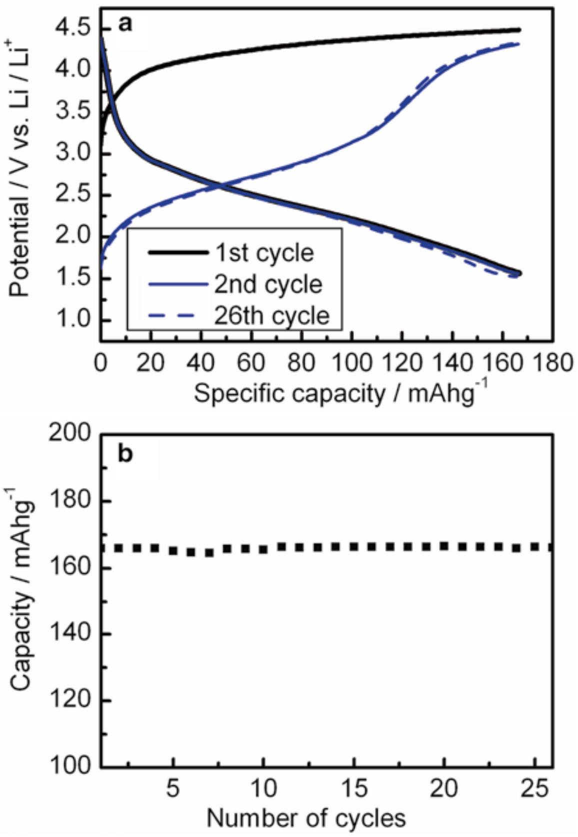

Li_2FeSiO_4 upon lithium insertion/extraction during initial cycling. The electrochemical redox process occurring in Li_2FeSiO_4 during cycling is as shown below:

$$\mathrm{Li_2}\mathbf{Fe}^{2+}\mathrm{Si}O_4 \leftrightarrow \mathrm{Li}\mathbf{Fe}^{3+}\mathrm{Si}O_4 + \mathrm{Li}^+ + e^-$$

Looking at the galvanostatic measurements shown in Fig. 10.3a, the initial discharge profile and subsequent charge–discharge cycle curves are quite similar, explicitly implying there are no major structural changes occurring after the first charging process. It is interesting to note that the initial charge profile is different from subsequent charge curves. This phenomenon has been ascribed to structural rearrangements occurring during initial cycling [6]. Therefore, a focus on structural transformations occurring only during initial cycling is sufficient to obtain a succinct overview of the Li^+ insertion/extraction mechanism in this material. Essential to the further elucidation of the mechanisms (particularly the shift in initial potential plateau) occurring in Li_2FeSiO_4 is indeed a better understanding of the changes in the electronic and local structural characteristics of this material during initial cycling.

10.3.1 X-ray Absorption Measurements

Reference compounds [$Fe_3(PO_4)_2 \cdot 8H_2O$, Fe_2O_3, and pristine Li_2FeSiO_4] were prepared. Powders were intimately mixed with boron nitride powders and pressed into pellets with a total absorption thickness of $\Delta \mu t = 1.0$ at the Fe *K*-edge. The X-ray absorption spectra of the Li_2FeSiO_4 samples and the reference compounds were measured in the energy region of the Fe *K*-edge at room temperature in transmission mode at the beamline of the SPring-8 synchrotron radiation facility (BL14B2) in Hyogo, Japan. The intensity of the X-ray beam was measured by ionization chambers.

In all the experiments, the apposite energy calibration and the absolute energy reproducibility of the measured spectra were established. For XANES analysis, in situ measurements were performed using a laminated electrochemical cell comprising three electrodes (working electrode, Li counter electrode, and Li reference electrode) and optimized to minimize the thickness of the electrolyte, which is highly absorbing at the Fe *K*-edge. For EXAFS analysis, ex situ measurements were carried out because high-quality oscillated data were needed. Charged/discharged electrodes with a nominal change in composition $\Delta x = 0.1$ in $Li_{2-x}FeSiO_4$ were removed from the cell in the glove box, carefully washed with dimethyl carbonate (DMC), and dried. The dried $Li_{2-x}FeSiO_4$ electrodes were sealed in laminated packets in an argon-filled glove box. Treatment of the raw X-ray absorption data was performed with the Athena package [7], allowing the alignment, normalization, and $\chi(k)$ extraction. The pre-edge energies were normalized for absorbance by fitting the spectral region with a victoreen function and subtracting this as background absorption. Quantitative analysis of Fe *K*-edge EXAFS spectra were performed with the Rigaku, Japan REX2000 program package [8]. The effective backscattering amplitude, f, and the total central atom phase shift, ϕ, were determined using the multiple-scattering theoretical calculation program code, FEFF8.20[9, 10]. A model incorporating a tentative spatial distribution of neighboring atoms, based on the unit cell parameters of the monoclinic Li_2FeSiO_4 crystal structure with $P2_1$ space group [11], was selected. The $\chi(k)$ function was fitted according to the equation

$$\chi(k) = \sum_i \frac{Nf(k,\pi)\exp\left(-2\sigma_i^2 k^2\right)\exp\left(-2R_i / \lambda_i\right)\sin[2kR_i + \phi_i(k)]}{kR_i^2}$$

where N is the number of neighboring atoms, R_i the atomic distance to the neighboring atom, σ^2 the Debye–Waller (DW) factor, and λ the mean free path. The k-weight used for the Fourier transformation fittings was 3 and they were weighted with a Hanning window.

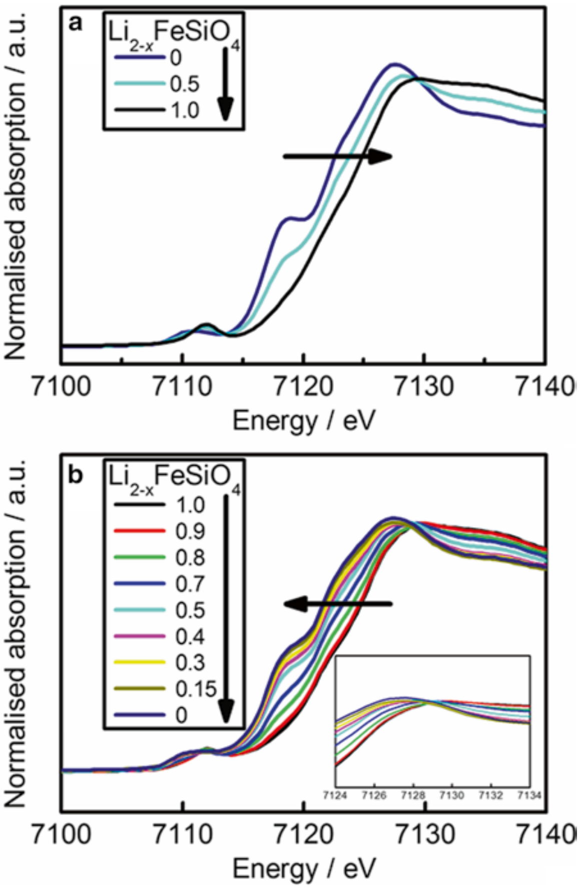

Fig. 10.4 Normalized Fe *K*-edge XANES spectra of $Li_{2-x}FeSiO_4$ electrode as a function of x during (**a**) initial charging and (**b**) initial discharging process

10.3.2 Electronic Structure (XANES)

Figure 10.4 shows the Fe *K*-edge XANES spectra during initial charge and discharge. The absorption edge shifts toward higher (lower) energies, which is evident during charging (discharging) due to the change in the valency state of Fe cations. To determine the Fe oxidation states during the cycling process, the XANES spectra at the Fe *K*-edge for γ-Fe_2O_3 and $Fe_3(PO_4)_2{\cdot}8H_2O$ were used. Caution was taken to use reference compounds with the same tetrahedral coordination of FeO_4 as Li_2FeSiO_4. In view of this, we used Fe_2O_3 and $Fe_3(PO_4)_2{\cdot}8H_2O$ to verify Fe^{2+} and Fe^{3+} valency states, respectively. The first inflection point of the absorption edge or the edge crest is generally chosen as a measurement of the oxidation state value of the absorbing element in samples and reference compounds. However, this approach has been proven to misestimate the actual oxidation states of Fe due to the possibility of both negative and positive interferences between atomic absorption with multiple-scattering contributions from distant neighbor atoms. In such cases, the shape

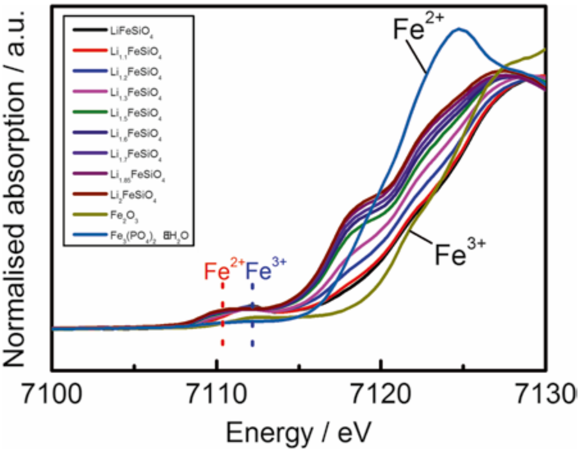

Fig. 10.5 XANES spectra comparisons of Li_2FeSiO_4 (pristine) and $LiFeSiO_4$ with reference compounds, verifying that the end-phase members are in the Fe^{2+} and Fe^{3+}, respectively

and energy positions of the pre-edge peak can be easily analyzed. XANES spectra comparisons of Li_2FeSiO_4 (pristine) and $LiFeSiO_4$ delithiated phase with reference compounds reveal the end-phase members to be in the Fe^{2+} and Fe^{3+} valency states, respectively (Fig. 10.5).

Looking closely at Fig. 10.4, it is also notable that every spectrum incorporates a weak peak (pre-edge) at 7,110–7,113 eV, which is known to be a sensitive indicator of the site symmetry about Fe ions [12]. The pre-edge peaks are, in principle, due to electronic transitions from the Fe 1*s* orbital to an empty molecular orbital with a Fe 3*d* character [13] and thus can be assigned to $1s \rightarrow 3d$ orbital transitions enhanced by hybridization of iron 3*d* with oxygen 2*p* orbitals. Furthermore, high-intensity peaks such as those observed in the range of 7,114 –7,126 eV arise from a significant mixing of 3*d* and 4*p* orbitals due to the noncentrosymmetricity of the Fe ion site geometry [14].

Isosbestic points (or points of common absorption) are common in spectroscopic data, provided that the stoichiometric changes of the species in the chemical reaction are all linearly interrelated [15]. In XAS spectra, the existence of such isosbestic points is the hallmark of two compounds in a mixture [16] and has been pointed out in the extraction/insertion of lithium ions in stellar $LiFePO_4$ polyanionic moieties [17], whereas the lack of these points is characteristic of monophasic behavior and has been experimentally observed in layered substituted oxides [18–21]. Inspection of the XANES spectra reveal an isosbestic point evident at around 7,129 eV in post-edge features, which in principle can heuristically represent a direct transformation from Li_2FeSiO_4 into $LiFeSiO_4$. In such cases, the application of a least-squares fit between initial and final phases can directly point to the fraction of initial-state and final-state materials at each step of the transformation [22]. The fitting XANES spectra are consistent with the experimental data, as shown in Fig. 10.6a. As is clear in Fig. 10.6b, linear combinations of the spectra for Li_2FeSiO_4 and $LiFeSiO_4$ phase members were obtained.

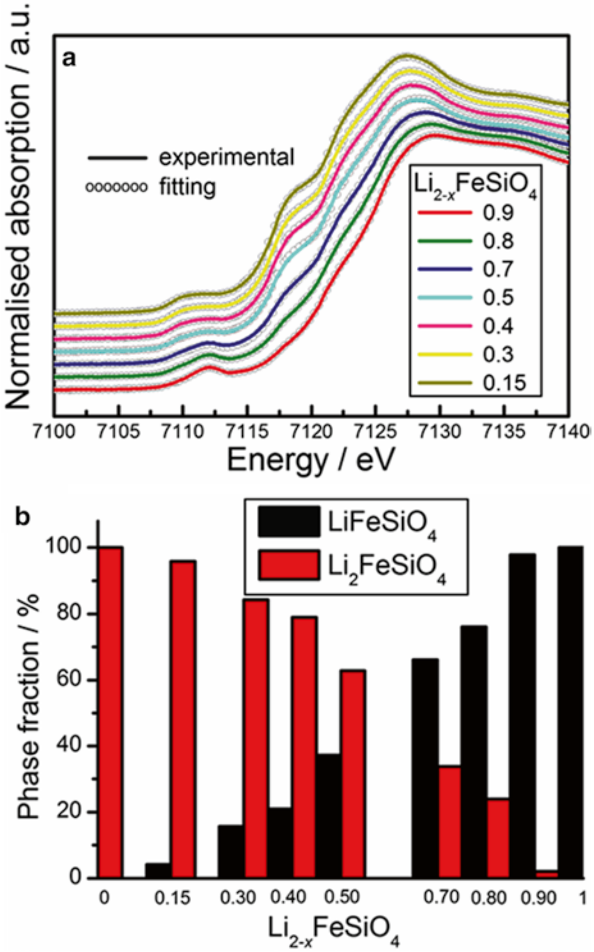

Fig. 10.6 (**a**) Normalized in situ Fe *K*-edge XANES spectra of $Li_{2-x}FeSiO_4$ electrode as a function of x during initial discharging process. (**b**) Variations of $LiFeSiO_4$ phase ratio in least-squares fit of the data shown in (**a**) as a function of x

10.3.3 Local Structure (EXAFS)

Short-range orders around Fe cations in $Li_{2-x}FeSiO_4$ during initial oxidation and reduction were directly probed by EXAFS analysis. A qualitative comparison of the spectra (Fig. 10.7) indicated that the initial cycling process was not completely reversible; the local order of the structure around the Fe atoms after one cycle is not the same as in the as-prepared sample (i.e., Li_2FeSiO_4). However, no significant differences were observed in the local environment of Fe in the initial delithiated state ($LiFeSiO_4$) compared to that of the subsequent cycle. The apparent irreversibility in the local structural environment of Fe can be ascribed to the structural

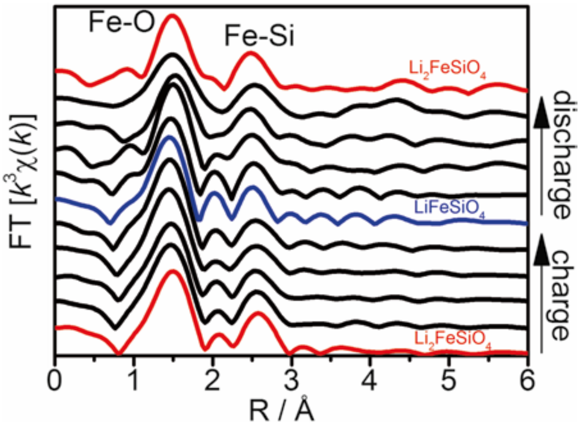

Fig. 10.7 Fourier transform magnitude comparison of pristine sample before and after initial cycling

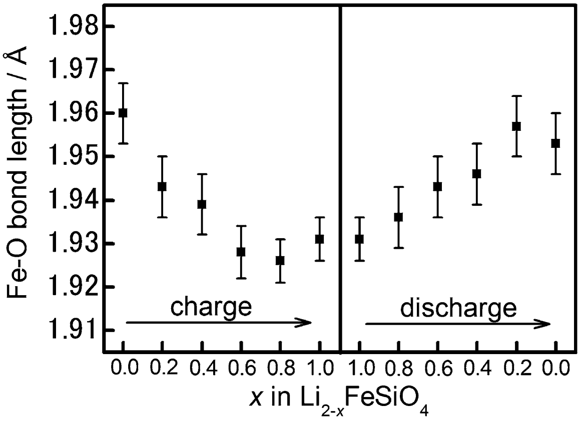

Fig. 10.8 Variations in mean Fe-O bond lengths as a function of x in $Li_{2-x}FeSiO_4$ during initial charging and discharging process

rearrangements toward a more stable structure during initial cycling of this material, as reported in the literature [23].

Seminal works regarding XAFS analysis of Li_2FeSiO_4 carried out by Dominko and coworkers [24], however, revealed no changes in the local structure around Fe atoms during initial cycling of this material. The reason for the disparity is that, as previously mentioned, the material synthesized by Dominko et al. contained a considerable amount of impurities, notably Fe_3C, which should have influenced the Fe *K*-edge XAS spectra. It is also notable that their material could only reversibly extract/insert approximately 0.7 Li^+. Electrochemical measurements of the material that was synthesized revealed a reversible extraction/insertion of 1 Li^+, and thus our results reflect the innate local structural changes that occur upon one Li^+ insertion and extraction in Li_2FeSiO_4.

With such valuable information in hand, we were motivated to examine the interatomic distances in order to investigate the very concise and detailed variation in the local structures around Fe upon cycling. Since the contribution of Li atoms in the

EXAFS signal was very weak, we focused on the structural variation around Fe atoms. Figure 10.8 shows the variations of Fe-O mean bond lengths in $Li_{2-x}FeSiO_4$ during initial cycling. A progressive diminution in the average Fe-O bond lengths with delithiation is due to the so-called rehybridization shift [25], which occurs in Fe ligand bonds at high levels of oxidation in order to diminish the effect of the change in valency of Fe ions. The interaction between Fe and O atoms arises (presumably) from the hybridization of Fe-3*d* and O-2*p* orbitals [26]. There were, however, hardly any discernible changes in the Fe-Si average bond lengths as compared to the observed changes in the average Fe-O bond lengths during the entire electrochemical process. Such perturbations made us aware of distortions that probably occur in this material upon initial cycling.

Single-phase Li_2FeSiO_4 nanoparticles show excellent cyclability at room temperature with a capacity of one Li^+ extraction and insertion. Fe *K*-edge XANES and EXAFS spectra provide conclusive evidence of irreversible changes occurring in the local environment (short-range order) of iron in pure-phase Li_2FeSiO_4, which can be correlated to the shift in the potential plateau during initial cycling. Further, Fe *K*-edge XANES spectra of $Li_{2-x}FeSiO_4$ reveal the presence of isosbestic points, suggesting that the Li^+ insertion and extraction in single-phase Li_2FeSiO_4 proceeds via a two-phase (biphasic) reaction.

10.4 Summary

We briefly introduced the principle of X-ray absorption fine structure (XAFS) and discussed how this technique could be employed to clarify the reaction mechanism of the charge/discharge process of Li_2FeSiO_4. Using an in situ or *in operando* XAS measurement technique, we can measure the electronic and local structural changes in electrode active materials and reveal the charge–discharge mechanism.

References

1. J.E. Muller, J.W. Wilkins, Phys. Rev. B **29**, 4331 (1984)
2. P.A. Lee, J.B. Pendry, Phys. Rev. B **11**, 2795 (1975)
3. S.J. Gurman, R.F. Pettifer, Phil. Mag.B. **40,** 345 (1979)
4. D.E. Sayers, E.A. Stern, F.W. Lytle, Phys. Rev. Lett. **27**, 1204 (1971)
5. B.K. Teo, *EXAFS: Basic Principles and Data-analysis* (Springer, New York, 1986)
6. A. Nyten, S. Kamali, L. Haggstrom, T. Gustafsson, J.O. Thomas, J. Mater. Chem. **16**, 2266 (2006)
7. B. Ravel, M. Newville, J. Synchrot. Radiat. **12**, 537–541 (2005)
8. T. Taguchi, T. Ozawa, H. Yashiro, Phys. Scr. **205**, T115 (2005)
9. J.J. Rehr, R.C. Albers, Rev. Mod. Phys. **72**, 621 (2000)
10. S.I. Zabinsky, J.J. Rehr, A. Ankudinov, R.C. Albers, M.J. Eller, J. Phys. Rev. B **52**, 2995–3009 (1995)
11. S. Nishimura, S. Hayase, R. Kanno, M. Yashima, N. Nakayama, A. Yamada, J. Am. Chem. Soc. **130**, 13212 (2008)

12. R. Dominko, C. Sirisopanaporn, C. Masquelier, D. Hanzel, I. Arcon, M. Gaberscek, J. Electrochem. Soc. **157**(12), A1309–A1316 (2010)
13. S. Kim, I.T. Bae, M. Sandifer, P.N. Ross, R. Carr, J. Woicik, M.R. Antonio, D.A. Scherson, J. Am. Chem. Soc. **113**, 9063–9066 (1991)
14. J.–U. Rhode, A. Stubna, E.L. Bominaar, E. Munck, W. Nam, L. Que, Inorg. Chem. **45**, 6435–6445 (**2006**)
15. K. Nam, W. Yoon, K. Zaghib, K.Y. Chung, X. Yang, J. Power. Sources **11**, 2023–2026 (2009)
16. X. Wang, J.C. Hanson, A.I. Frenkel, J.Y. Kim, J.A. Rodriguez, J. Phys. Chem. B **108**, 13667–13673 (2004)
17. L. Laffont, C. Delacourt, P. Gibot, M. Yue Wu, P. Kooyman, C. Masquelier, J.M. Tarascon, Chem. Mater. **18**, 5520–5529 (2006)
18. S.W. Yoon, C.P. Grey, M. Balasubramanian, X.Q. Yang, J. McBreen, Chem. Mater. **15**, 3161 (2003)
19. G. Jain, J.C. Yang, M. Balasubramanian, J.J. Xu, Chem. Mater. **17**, 3850 (2005)
20. M. Balasubramanian, X. Sun, X.Q. Yang, J. McBreen, J. Electrochem. Soc. **147**(8), A2903 (2000)
21. I. Nakai, T. Nakagone, Electrochem. Solid-State Lett. **1**(6), 259 (1998)
22. A. Piovano, G. Agostini, A.I. Frenkel, T. Bertier, C. Prestipino, M. Ceretti, W. Paulus, C. Lamberti, J. Phys. Chem. C **115**, 1311–1322 (2011)
23. P. Larsson, R. Ahuja, A. Nyten, J.O. Thomas, Electrochem. Commun. **8**, 797–800 (2006)
24. R. Dominko, I. Arcon, A. Kodre, D. Hanzel, M. Gaberscek, J. Power. Sources **189**, 51 (2009)
25. F. Zhou, M. Cococcioni, C.A. Marianetti, D. Morgan, G. Ceder, J. Phys. Rev. B **70**, 235121 (2004)
26. J. McBreen, J. Solid State Electrochem. **1051–1061**, 13 (2009)

Chapter 11
Alternating Current Methods for Battery Evaluation

M. Itagaki

11.1 Introduction to Alternating Current Methods

Alternating current (AC) methods are powerful electrochemical measurement tools to evaluate the performance of batteries because the time constants in electrochemical signals can be discriminated without damage to the electrodes. An electrochemical impedance is determined by measuring the alternating current response to the alternating voltage imposed on the electrode/electrolyte interface. The electrode/electrolyte interface can be characterized by the interpretation of the electrochemical impedance spectrum. The AC method was recently called electrochemical impedance spectroscopy (EIS) because the impedance spectrum measured in a wide frequency range provides information concerning the detailed structure of the electrode/electrolyte interface. The typical interpretation of an impedance spectrum is explained using a simple equivalent circuit (Fig. 11.1). Figure 11.1a shows a conceptual scheme of an electrode contacted with an electrolyte. The anodic or cathodic reaction rate at the electrode/electrolyte interface has to do with the charge-transfer resistance R_{ct}. In addition, an electric double layer is formed at the interface, and the double-layer capacitance is represented by C_{dl}. Figure 11.1b describes an equivalent circuit involving R_{ct} in parallel with C_{dl}, which is in series with the electrolyte resistance R_{ele}.

M. Itagaki (✉)
Tokyo University of Science, 1-3 Kagurazaka, Shinjuku, Tokyo, Japan
e-mail: itagaki@rs.noda.tus.ac.jp

T. Osaka and Z. Ogumi (eds.), *Nanoscale Technology for Advanced Lithium Batteries*,
Nanostructure Science and Technology 182, DOI 10.1007/978-1-4614-8675-6_11,

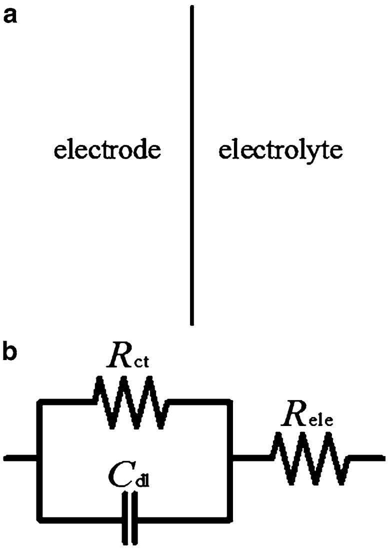

Fig. 11.1 Simple equivalent circuit for electrode/electrolyte interface. R_{ct}: charge-transfer resistance, C_{dl}: electric double-layer capacitance, R_{ele}: electrolyte resistance

11.2 Principle of AC Methods

11.2.1 Impedance Presented by Complex Number

The impedance Z is presented by the following complex number with real part Z' and imaginary part Z'':

$$Z = Z' - \mathrm{j}Z'' \tag{11.1}$$

The relation of Z' and Z'' on the complex plane is depicted in Fig. 11.2. The imaginary axis of the complex plane is usually represented by a minus value of the imaginary component because almost electrochemical impedance shows the capacitive behavior, and thus Z'' means a minus value of the imaginary part. The complex-plane plot of Z is called a Nyquist plot. The magnitude and phase shift of Z are represented as follows:

$$|Z| = \sqrt{(Z')^2 + (Z'')^2} \tag{11.2}$$

$$-\varphi = \arctan\left(\frac{Z''}{Z'}\right) \tag{11.3}$$

$$\theta = \frac{90}{\pi}\varphi \tag{11.4}$$

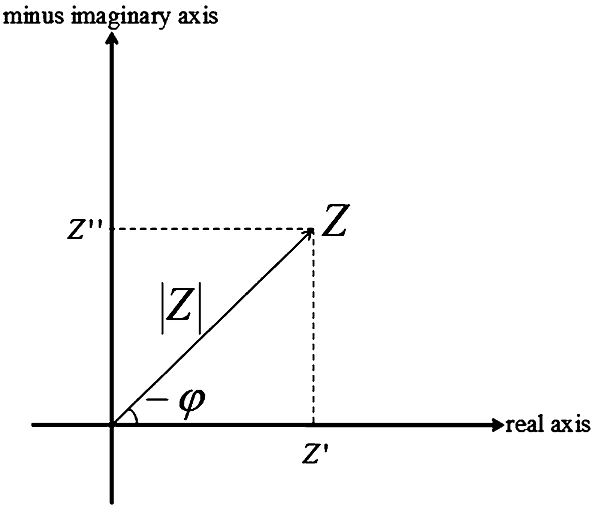

Fig. 11.2 Complex plane to represent impedance *Z* as a complex number

The angle of vector *Z* against the real axis corresponds to −φ (radian) or −θ (degrees) on the complex plane in Fig. 11.2. The magnitude and phase shift of *Z* are often displayed on a Bode plot, namely, plots of log|*Z*| vs. log*f* and θ (or φ) vs. log*f*.

11.2.2 Nyquist and Bode Plots Corresponding to a Simple Equivalent Circuit

The equivalent circuit in Fig. 11.1b gives the real and imaginary parts of *Z* as follows:

$$Z' = R_{ele} + \frac{R_{ct}}{1+\omega^2 R_{ct}^2 C_{dl}^2} \tag{11.5}$$

$$Z'' = \frac{\omega^2 R_{ct}^2 C_{dl}^2}{1+\omega^2 R_{ct}^2 C_{dl}^2} \tag{11.6}$$

The calculated results of the Nyquist plot, whose axes are Z' and Z'', are shown in Fig. 11.3a. The plots display the locus of a semicircle. The coordinates of the center are (0, $R_{\mathrm{ele}}+R_{\mathrm{ct}}/2$), and the radius is $R_{\mathrm{ct}}/2$. The locus takes R_{ele} and $R_{\mathrm{ele}}+R_{\mathrm{ct}}$ on the real axis as the high- and low-frequency limits, respectively. The frequency at the maximum of semicircle f_{max} has the relation $R_{\mathrm{ct}}C_{\mathrm{dl}} = 1/(2\pi f_{\mathrm{max}})$. The $R_{\mathrm{ct}}C_{\mathrm{dl}}$ has a unit of seconds and is called the time constant. Therefore, the locus in Fig. 11.3a is generally called a capacitive semicircle with time constant $R_{\mathrm{ct}}C_{\mathrm{dl}}$.

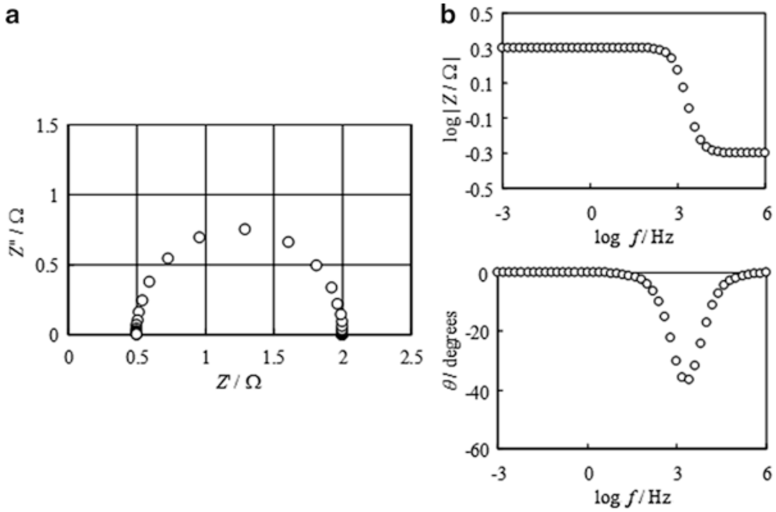

Fig. 11.3 Nyquist plot (**a**) and Bode plot (**b**) of impedance spectrum calculated by equivalent circuit in Fig. 11.1. $R_{ele} = 0.5\ \Omega$, $R_{ct} = 1.5\ \Omega$, and $C_{dl} = 10^{-4}$ F. The frequency range was from 100 to 1 MHz

In addition, Fig. 11.3b shows the Bode plots of Z corresponding to the equivalent circuit in Fig. 11.1b. The magnitude and phase shift of Z are calculated from Z' and Z'' by Eqs. 11.2, 11.3, and 11.4. Log$|Z|$ takes a constant value in the low-frequency range because $1/\omega C_{dl}$ is large and Z can be approximated to $R_{ele} + R_{ct}$, and θ is zero degrees in the low-frequency range. In the middle-frequency range, log$|Z|$ decreases with increases in log$f$ whose slope is -1 because $R_{ct} \gg 1/\omega C_{dl}$ and current flows in the C_{dl} branch. Log$|Z|$ takes log$|R_{ele} + R_{ct}|$, and θ is zero degrees in the high-frequency range.

11.3 Instruments for Impedance Measurements

11.3.1 Instruments to Measure Electrochemical Impedance

The spectrum of electrochemical impedance can be easily and precisely measured by the combination of a potentiostat and frequency response analyzer (FRA), though many experimental methods are reported to measure the electrochemical impedance. The scheme of the experimental setup is depicted in Fig. 11.4. The electrochemical cell is connected to the potentiostat, and the electrochemical control of the cell is carried out by the potentiostat. The electrochemical impedance is assessed by

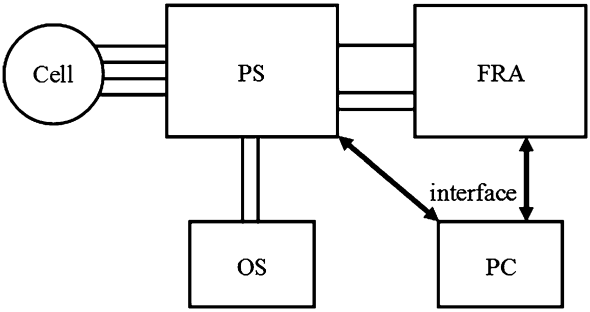

Fig. 11.4 Scheme of experimental setup for impedance measurement. FRA: frequency response analyzer, PS: potentiostat, PC: personal computer, OS: oscilloscope

the FRA connected to the potentiostat from input potential and output current signals. The simultaneous monitoring of input and output signals by oscilloscope is recommended, and the oscilloscope can be set by branching the output cables from the potentiostat to the FRA. The conditions of parasitic noise and linearity can be checked by the oscilloscope.

11.3.2 Potentiostat

The potentiostat has various ranges of controlling potential and measurable current depending on the model; thus the user must select the model for the application purpose. For example, evaluation of the biosensor requires a current range on the order of nA, and that of an energy device like a lithium-ion battery needs a relatively large current range on the order of mA to A. Generally, the potentiostat provides multiple channels of current range. The current is transformed into a voltage signal via resistor in the current follower in the potentiostat. The potentiostat has outputs in the form of voltage versus ground (common line) for both potential and current.

The response time is the most important specification for a potentiostat in the case of impedance measurements because the response time is concerned with the maximum value of the high-frequency limit of the impedance measurements. The potentiostat should output precise signals with minimal phase shift up to at least 10 kHz and preferably to 1 MHz. The instrument should have a high input impedance on the order of 10^{11}–10^{14} Ω for the potential measurement to minimize current drawn from the system during measurement. The sensitivity and accuracy of the instrument should be sufficient to detect a change of 1.0 mV.

11.3.3 Frequency Response Analyzer

The FRA has an AC generator to provide a suitable voltage signal with an arbitrary frequency and an analyzer to determine the impedance by current and voltage outputs from the potentiostat. The impedance spectrum can be determined automatically by scanning the frequency of the imposed signal. The measurable frequency range depends on the model of FRA. One model covers a wide frequency range from microhertz to megahertz. For reference, the high-frequency limit is influenced by the connected potentiostat, as mentioned earlier, and the measurement of low-frequency impedance requires a considerable amount of time.

11.4 Equivalent Circuits and the Impedance Spectra

11.4.1 Impedance Spectra of R, C, RC Series Circuit, and RC Parallel Circuit

In this section, the impedance spectra of the fundamental parameters *R* and *C* and their combination are explained in order to understand the fundamentals of impedance plots. Figure 11.5a shows the Nyquist and Bode plots of resistor *R*. The impedance of *R* is represented by the following simple equation: $Z=R$. The locus tends to one value of the real axis on the Nyquist plot. In addition, the magnitude |Z| and phase shift θ take a constant value and zero, respectively, against the

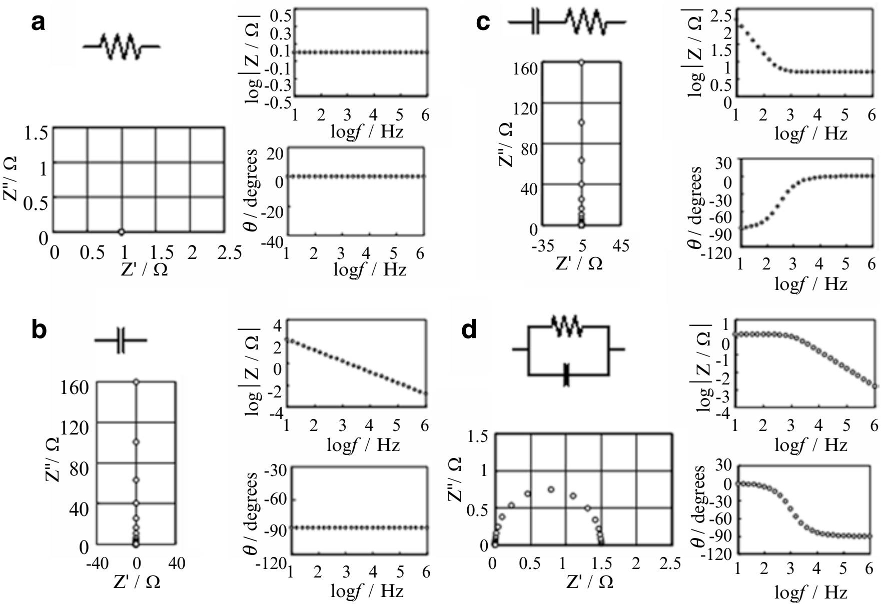

Fig. 11.5 Impedance spectra of simple equivalent circuits. (**a**) Resistor: $R=1\ \Omega$. (**b**) Capacitor: $C=10^{-4}$ F. (**c**) Series of resistor and capacitor: $R=1\ \Omega$ and $C=10^{-4}$ F. (**d**) *RC* parallel circuit: $R=1\ \Omega$ and $C=10^{-4}$ F

frequency change on the Bode plot. Figure 11.5b shows the Nyquist and Bode plots of capacitor C. The impedance of C is represented by the following equation: $Z = 1/j\omega C$. The locus is described on the imaginary axis and converges to the origin on the Nyquist plot at the high-frequency limit. On the Bode plot, the logarithmic of magnitude $\log|Z|$ decreases with increases in $\log f$, whose slope is −1 because of the relation $\log|Z| = -\log f - \log(2\pi C)$, and the phase shift θ is −90° in the whole frequency. Figure 11.5c shows the Nyquist and Bode plots of a series of R and C. The locus is described on a vertical line parallel to the imaginary axis and converges to the R of the real axis on the Nyquist plot at the high-frequency limit. On the Bode plot, $\log|Z|$ decreases with an increase in $\log f$, whose slope is −1 in the low-frequency range because $R \ll 1/\omega C$, and θ is −90° in the low-frequency range. In addition, $\log|Z|$ takes a constant value in the high-frequency range because $R \gg 1/\omega C$, and θ is zero degrees in the high-frequency range. Figure 11.5d shows the Bode plots of a RC parallel circuit. The locus describes a semicircle on the Nyquist plot. On the Bode plot, $\log|Z|$ takes a constant value in the low-frequency range because $R \ll 1/\omega C$ and current flows in the R branch, and θ is zero degrees in the low-frequency range. In addition, $\log|Z|$ decreases with increases in $\log f$ whose slope is −1 in the high-frequency range because $R \gg 1/\omega C$ and current flows in the C branch, and θ is −90° in the high-frequency range.

11.4.2 Impedance Spectra Presented by Constant Phase Element

The locus of the impedance spectrum often shows the capacitive loop as being depressed by a true semicircle. In this case, the curve fitting of the impedance spectrum can be carried out using an equivalent circuit involving a constant phase element (CPE). The impedance Z_{CPE} of the CPE is composed of CPE constant T and CPE exponent p as follows:

$$Z_{\mathrm{CPE}} = \frac{1}{(j\omega)^p T} \tag{11.7}$$

When the electrode shows a capacitive behavior, the p takes a value from 0 to 1. The absolute value $|Z_{\mathrm{CPE}}|$ and phase shift are presented from the transformation of Eq. 11.7 as follows:

$$|Z_{\mathrm{CPE}}| = \frac{1}{\omega^p T} \tag{11.8}$$

$$\mathrm{q} = -90p \text{ or } \mathrm{j} = -\frac{\mathrm{p}}{2}p \tag{11.9}$$

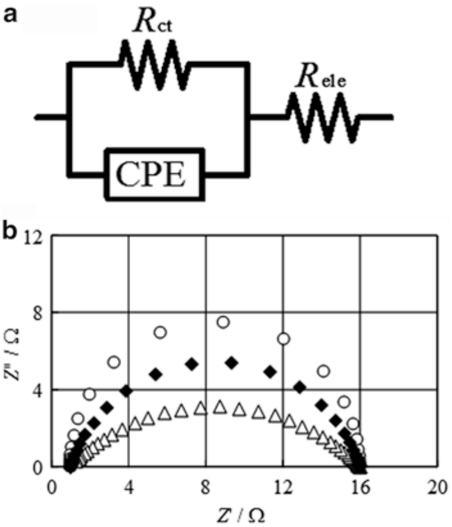

Fig. 11.6 (**a**) Equivalent circuit involving R_{ct} in parallel with CPE, which is in series with electrolyte resistance R_{ele}. (**b**) Nyquist plots of impedance calculated by this circuit. $R_{ele} = 1\ \Omega$, $R_{ct} = 15\ \Omega$, $T = 10^{-3}$ Fs^{p-1}, and $p = 1$(○), 0.8(◆) and 0.5(△). The frequency range was from 1 to 1 MHz

It can be understood from Eq. 11.9 that the phase shift takes a constant value depending on p. Therefore, this element is called a constant phase element.

Figure 11.6a shows an equivalent circuit involving R_{ct} in parallel with CPE, which is in series with the electrolyte resistance R_{ele}. CPE is arranged in an equivalent circuit as a kind of capacitor instead of an electric double-layer capacitance. Figure 11.6b shows the calculated results of impedance spectra with the equivalent circuit in Fig. 11.6a. The impedance spectrum describes a true semicircle when $p = 1$. In this case, Z_{CPE} is identical to the capacitive reactance by electric double-layer capacitance, assuming that $T = C_{dl}$. The impedance spectra describe a depressed loop when $p < 1$, and the distortion from a true semicircle becomes remarkable when the value of p decreases. Generally, the value of p decreases with increases in the heterogeneity of the electrode surface. The curve fitting can be carried out with the equivalent circuit shown in Fig. 11.6a for the experimental results of a depressed capacitive loop, and two resistances, R_{ele} and R_{ct}, can be obtained directly. The relation between the CPE constant T and the capacitance C will be discussed later in this section.

The impedance Z is expressed by the equivalent circuit in Fig. 11.6a as follows:

$$Z = R_{ele} + \frac{R_{ct}}{1 + (j\omega)^p T R_{ct}} \tag{11.10}$$

It is known that the impedance of the RC parallel circuit with the series of R_{ele} is represented by the following equation considering the distribution of the time constant. Equation 11.11 is generally called the Cole–Cole equation:

$$Z = R_{ele} + \frac{R_{ct}}{1 + (j\omega R_{ct} C)^p} \tag{11.11}$$

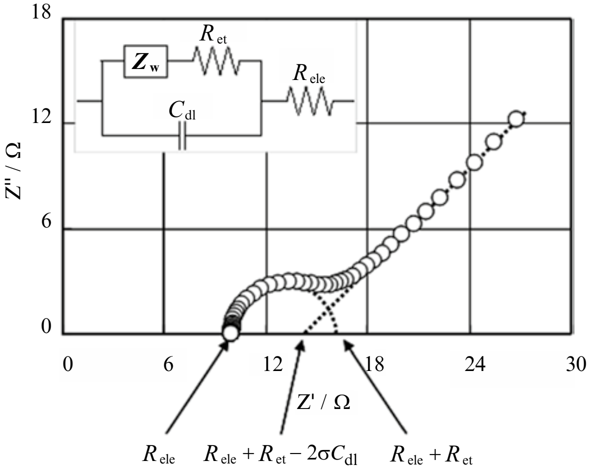

Fig. 11.7 Nyquist plot of impedance spectrum for electrode influenced by semi-infinite diffusion. $R_{ele} = 10\ \Omega$, $R_{ct} = 5\ \Omega$, $C_{dl} = 10^{-1}$ F, $A_r = 0.196$ cm^2, $T = 298$ K, $c^* = 10^{-4}$ mol/cm^3, and $D = 10^{-4}$ cm^2/s. The frequency range was from 1 to 1 MHz

The impedance describes a depressed semicircle on the Nyquist plane when $0 < p \leqq 1$, and its shape is in agreement with that calculated by Eq. 11.10 selecting the suitable parameters. Furthermore, the following relation can be obtained by comparing Eqs. 11.11 and 11.19, and the average capacitance C can be obtained by the following equation:

$$C = T^{1/p} R_{ct}^{(1-p)/p} \tag{11.12}$$

11.4.3 Diffusion Impedance

An electrochemical reaction involves various processes, namely, a charge transfer on the electrode and a mass transfer in the electrolyte solution. EIS enables the discrimination of their time constants by imposing a sinusoidal signal in a wide frequency range. Figure 11.7 shows the calculated results of the impedance spectrum for an electrode influenced by a semi-infinite diffusion process. The impedance describes a capacitive loop in the high-frequency range and a straight line with a slope of 45° in the low-frequency range. This straight line in the low-frequency range is called the Warburg impedance, Z_W, and is a special locus indicating the contribution of the semi-infinite diffusion process. Generally, a capacitive loop related to the charge-transfer resistance R_{ct} and the electric double-layer capacitance C_{dl} appears in the high-frequency range and the Warburg impedance appears in the low-frequency range because the time constant of the charge transfer is much smaller than that of the mass transfer in an electrolyte. The equivalent circuit to represent this locus is shown in the upper left of Fig. 11.7.

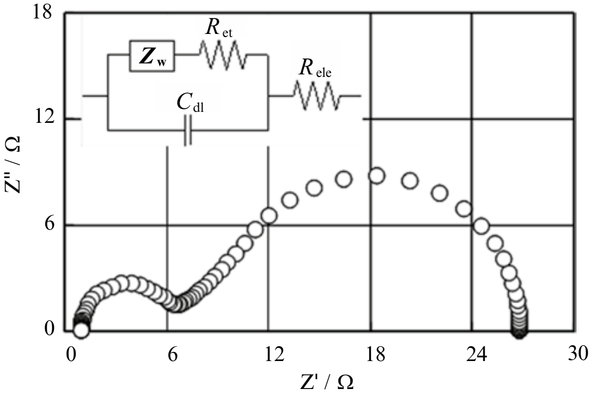

Fig. 11.8 Nyquist plot of impedance spectrum for the electrode influenced by finite diffusion. $R_{ele}=1\ \Omega$, $R_{ct}=5\ \Omega$, $C_{dl}=10^{-5}$ F, $A_r=0.196\ \text{cm}^2$, $T=298$ K, $c^*=10^{-5}\ \text{mol/cm}^3$, $D=6.5\times10^{-6}\ \text{cm}^2/\text{s}$, and $\boldsymbol{\delta}=0.001$ cm. The frequency range was from 1 to 1 MHz

The Z_W for a plane electrode with the redox reaction Ox + ne- = Red was derived as follows:

$$Z_W = \frac{(1-j)\sigma}{\sqrt{\omega}} \tag{11.13}$$

$$\sigma = \frac{RT}{\sqrt{2}n^2F^2A_r}\left(\frac{1}{D_O^{1/2}c_O}+\frac{1}{D_R^{1/2}c_R}\right) \tag{11.14}$$

In these equations, σ is the constant for the diffusion condition, D_O and D_R are diffusion coefficients for Ox and Red, respectively, c_O and c_R are bulk concentrations [mol cm^{-3}] of Ox and Red, respectively, and A_r is the surface area of the electrode. Equation 11.14 can be replaced by the following equation, neglecting the diffusion of the product from the electrode surface to the electrolyte bulk:

$$\sigma = \frac{RT}{\sqrt{2}n^2F^2A_r}\left(\frac{1}{D^{1/2}c^*}\right) \tag{11.15}$$

In Eq. 11.15, D and $c*$ are the diffusion coefficient and bulk concentration of the reactant, respectively.

When the electrode reaction is influenced by the finite diffusion with the thickness of diffusion layer δ, Z_W is expressed by the following equation:

$$Z_W = \frac{(1-j)\sigma}{\sqrt{\omega}}\tanh\left\{\delta\sqrt{\frac{j\omega}{D}}\right\} \tag{11.16}$$

If the two diffusion processes of Ox and Red must be considered in Eq. 11.16, the following assumption is necessary: $D_O=D_R=D$. The impedance spectrum calculated using Eqs. 11.16 and 11.15 is shown in Fig. 11.8. The capacitive loop related to the time constant $R_{ct}C_{dl}$ appears in the high-frequency range. The characteristic locus appears in the low-frequency range, that is, a straight line with a slope of 45° on the high-frequency side and convergence on the real axis at the low-frequency limit. Equation 11.16 is expressed by the following equation at the low-frequency limit ($\omega \to 0$):

$$Z_W = \sigma\delta\sqrt{\frac{2}{D}} \tag{11.17}$$

For reference, Eq. 11.16 can be approximated by Eq. 11.18 when the diffusion layer δ is very thick and the relation $\delta \to \infty\ s^{-1}$ is substituted into Eq. 11.16 because $\tanh\{\infty\} = 1$:

$$Z_W = \frac{(1-j)s}{\sqrt{w}} \text{ at } d \to \infty \tag{11.18}$$

Equation 11.18 is identical to Eq. 11.13, and finite diffusion with a thick diffusion layer can be considered as being semi-infinite in the case of impedance analysis.

11.4.4 Equivalent Circuit for Blocking Behavior

The electrode that shuts off the DC current is called the blocking electrode. A typical equivalent circuit for the blocking electrode is shown in Fig. 11.9a, and the series capacitance C_B is added to the equivalent circuit in Fig. 11.1. In this equivalent circuit, the electrode reaction presented by the charge-transfer resistance R_{ct} can occur, but the amount of charge cannot flow above the capacitance C_B when AC voltage is imposed on the electrode. Figure 11.9b shows a Nyquist plot of the impedance spectrum calculated using the equivalent circuit in Fig. 11.9a. The impedance shows that the capacitive loop appears in the high-frequency range and the vertical line parallel to the imaginary axis in the low-frequency range. The imaginary component of the low-frequency impedance can be approximated by $-1/\omega C_B$. In the evaluation of a battery, the value of C_B corresponds to the differential capacitance during the charge and discharge of active materials at an arbitrary equilibrium condition.

11.4.5 Equivalent Circuit with Two Time Constants

The capacitive loop is described on a Nyquist plot corresponding to the equivalent circuit of an RC parallel connection. And the frequency at the top of loop f_{max} is expressed by the following relation:

$$2\pi f_{max} = \frac{1}{RC} \tag{11.19}$$

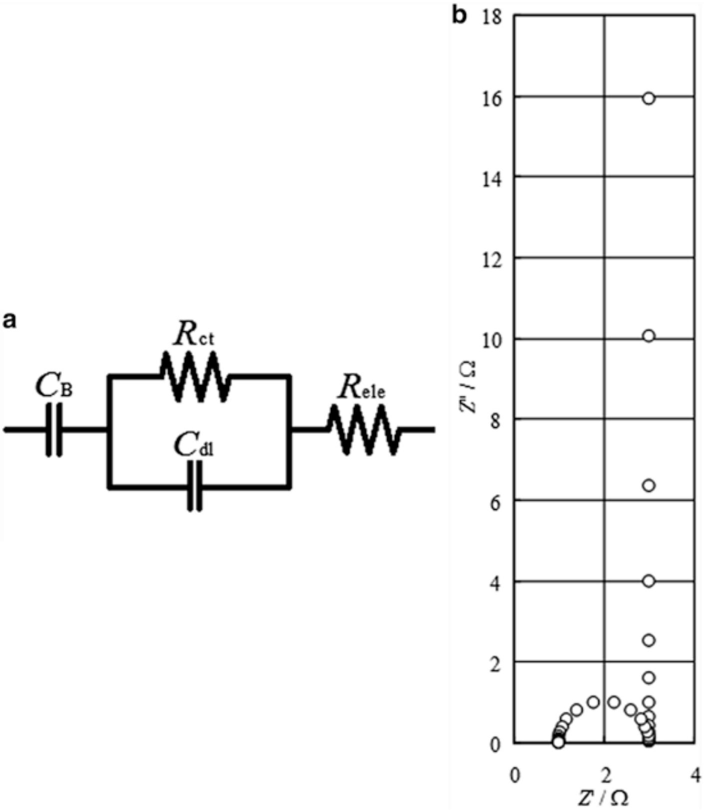

Fig. 11.9 (**a**) Equivalent circuit for blocking electrode. (**b**) Nyquist plots of impedance calculated by this circuit. $R_{ele} = 1\ \Omega$, $R_{ct} = 2\ \Omega$, $C_{dl} = 10^{-4}$ F, and $C_B = 1$ F. The frequency range was from 100 to 1 MHz

An equivalent circuit with two time constants is shown in Fig. 11.10a. Generally, each time constant originated at the parallel connection of the resistance and capacitance of the electrode/electrolyte interface or surface film on the electrode. A Nyquist plot of impedance with two time constants is shown in Fig. 11.10b. Two capacitive loops are observed. The capacitive loop in the low-frequency range relates to the time constant R_1C_1 because C_1 is much larger than C_2 in this context. On the other hand, the capacitive loop in the high-frequency range relates to the time constant R_2C_2. An almost double-digit difference is necessary between two time constants in order to discriminate two capacitive loops. Figure 11.10c shows a Bode plot of impedance with two time constants. The log$|Z|$ shows three plateaus: log R_{ele}, log ($R_{ele} + R_2$), and log ($R_{ele} + R_2 + R_1$), from high frequency to low frequency. The θ shows two minimum peaks.

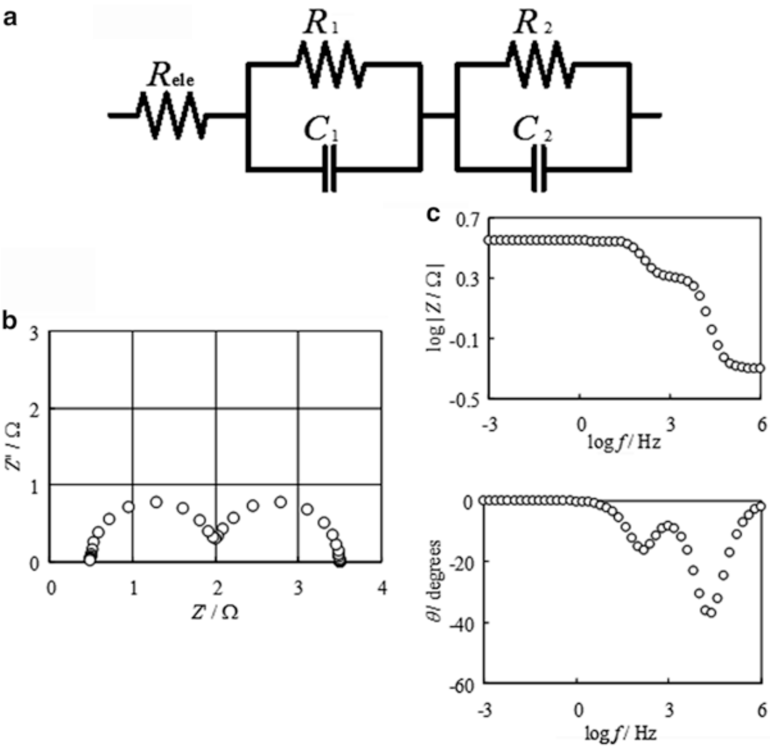

Fig. 11.10 (**a**) Equivalent circuit involving two parallel connections of *R* and *C*. (**b**) Nyquist plots of impedance calculated by this circuit. $R_{ele} = 0.5\ \Omega$, $R_1 = 1.5\ \Omega$, $C_1 = 10^{-3}$ F, $R_2 = 1.5\ \Omega$, and $C_2 = 10^{-5}$ F. The frequency range was from 1 to 1 MHz

11.5 Analyses of Lithium-Ion Rechargeable Batteries by AC Method

The charge-transfer resistance and electric double-layer capacitance can be obtained by the application of an AC method to the evaluations of electrode/electrolyte interfaces in lithium-ion rechargeable batteries [1–20]. The charge-transfer resistance is related to the reciprocal of the exchange current of the electrode at equilibrium. In addition, the electric double-layer capacitance gives information concerning the actual electrode surface area and the condition of the electric double layer. When a protective film is formed on the electrode, the time constant of the film can be extracted from the impedance spectrum measured in the wide frequency range. Laboratory experiments on electrode/electrolyte interfaces are divided into one on negative electrodes (anodes) [1–11] and ones on positive electrodes (cathodes) [12–20]. In this section, an example of impedance analysis on a negative electrode is introduced first.

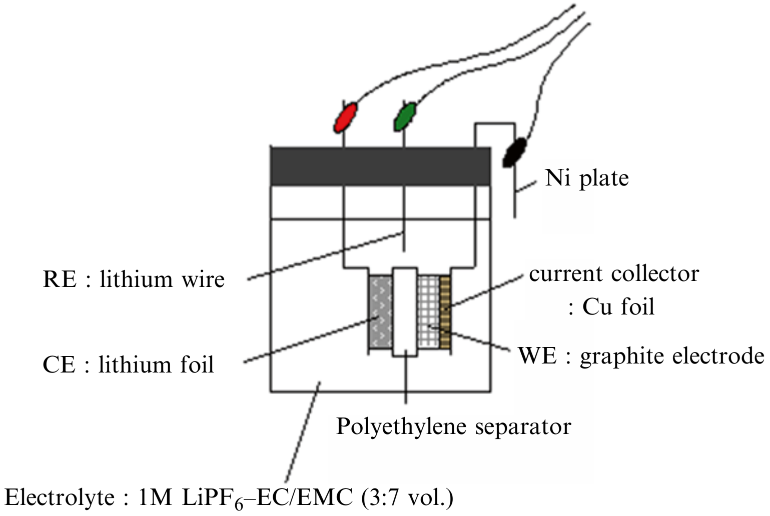

Fig. 11.11 Example of electrochemical cell to investigate reaction at electrolyte–graphite interface [8]

The typical electrochemical cell used for impedance measurements [8] is shown in Fig. 11.11. The graphite working electrode (WE) (1×0.4 cm^2) was prepared by bonding graphite powder onto a copper foil as a current collector. A lithium foil was used as the counter electrode (CE), and a lithium wire was used as the reference electrode (RE). A polyethylene (PE) filter as the separator was sandwiched between the WE and the CE. To prevent the deformation of the WE due to the volume change by electrolysis, the WE and CE were fixed with nickel plates.

It is well known that a stable film is formed on graphite electrodes (anodes) in ethylene carbonate (EC) electrolyte solutions. This film protects the electrolyte solution from its further decomposition and is a lithium-ion-conductive material. The film is formed by the decomposition of the electrolyte solution during the first cycle charge and is called solid electrolyte interphase (SEI). It is known that the SEI has a multilayer structure composed of inorganic components like LiF, Li_2O, and Li_2CO_3 and organic species (polymers) like $ROCO_2Li$. Figure 11.12 shows the potential–capacity curve of a graphite electrode in EC/EMC electrolyte solution containing 1 M $LiPF_6$ and the impedance spectra at room temperature (25 °C) in a dry argon atmosphere. During measurement of the charge–discharge curves at a DC current density of 0.2 mA cm^{-2}, the impedance spectra were measured successively by superimposing the small AC current on the DC current. The amplitude of the AC current made the AC component of the potential response smaller than 5 mV. The impedance measurement was carried out in a frequency range of 10 mHz to 10 kHz and started at a high frequency and moved toward low frequencies in the logarithmic scan. In this experiment, the impedance spectra were measured by in situ measurement using the potential–capacity curve, and details on in situ measurement can be

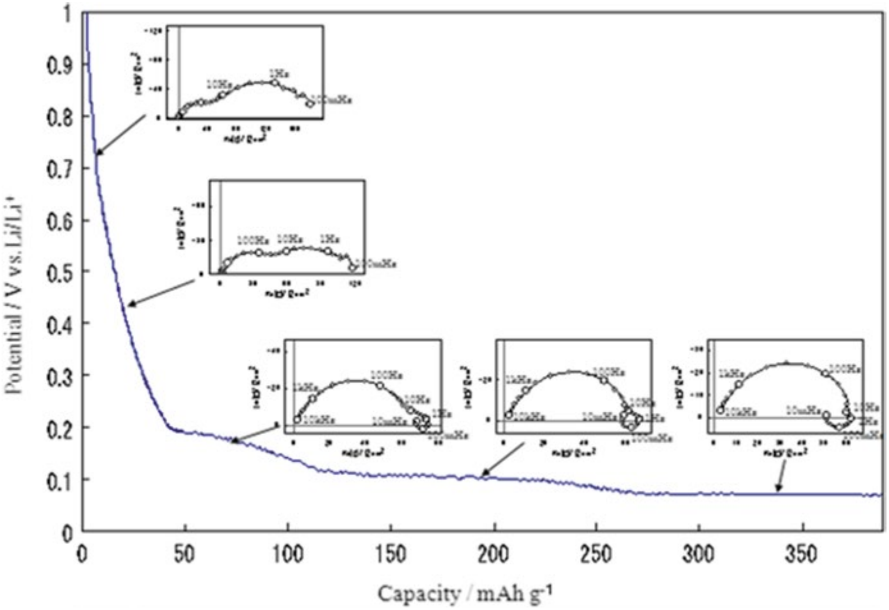

Fig. 11.12 Potential–capacity curve of graphite electrode in 1 M $LiPF_6$–EC/EMC (3:7 by volume) in first cycle charge and impedances at various states of charge. Current density: 0.2 mA cm^{-2} [8]

found in the literature [8, 9, 18]. Generally, the impedance spectrum is measured at steady state after waiting a sufficient amount of time to reduce the potential change after stopping the charge. The experimental setup consisted of a potentiostat (Hokuto Denko, HA501G) and a FRA (NF block, 5020) controlled by a personal computer (IBM ThinkPad A22m) through the GP-IB (General Purpose Interface Bus) interface. Lithium-ion intercalation occurred randomly in the graphite electrode in the early period of the charge in a potential region above 0.2 V, and the SEI film formation took place in this potential region. In Fig. 11.12, the impedance shows two capacitive loops in an early period of the first charge cycle. The high-frequency loop in the impedance spectrum is related to the time constant of lithium-ion permeation through the SEI film. The low-frequency loop is related to the time constant of the charge-transfer resistance and electrical double-layer capacitance on the graphite particle surface. With additional charges, the inductive loop appears in the low-frequency range. It is known that the inductive behavior generally originates from decreases in the reaction resistance by catalysts formed on the electrode. Since the intercalation of lithium ions could relate to the electrode resistance in the case of graphite electrodes, the electrochemical behavior of the intercalation site could be discussed on the basis of the inductive loop. Graphite is a typical layered substance that consists of hexagonal sheets of sp^2–carbon atoms (graphene layers). The graphene layers are weakly bonded together by van der Waals forces as an A·B·A·B··· stacking sequence along the c-axis. Lithium ions are intercalated between the graphene layers. The distance between graphene layers is expanded by the intercalation

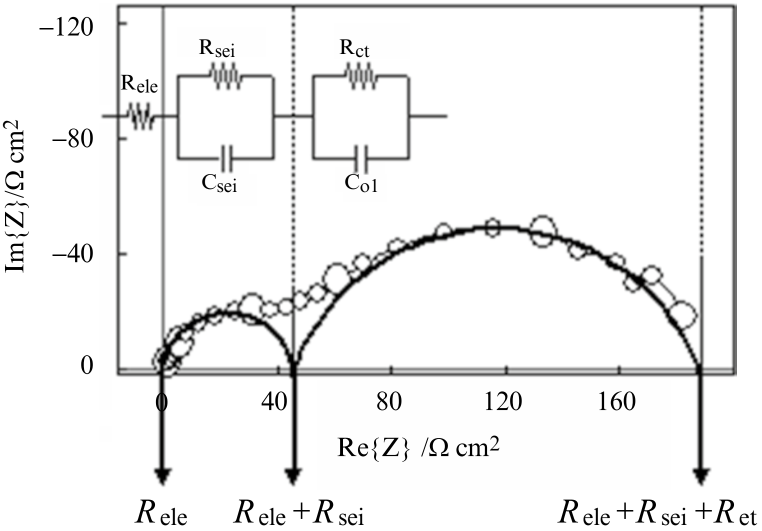

Fig. 11.13 Typical electrochemical impedance of graphite electrode in 1 M $LiPF_6$–EC/EMC(3:7 by volume) and equivalent circuit [8]

of the lithium ions into each interlayer, and the resistance of the intercalation of subsequent lithium ions diminishes. Therefore, it can be considered that the aforementioned inductive period yields an inductive loop in a Nyquist plot of the impedance. A typical impedance of graphite electrodes in 1 M $LiPF_6$–EC/EMC (3:7 by volume) and an equivalent circuit used to analyze the electrochemical process for the lithium-ion intercalation into the graphite electrode [8] are shown in Fig. 11.13. In Fig. 11.13, R_{ele} represents the electrolyte resistance, R_{sei} and C_{sei} are the resistance and capacitance of the SEI film, respectively, and R_{ct} and C_{dl} are the charge-transfer resistance and double-layer capacitance on the graphite particle surface, respectively.

The impedance spectrum of batteries involves information concerning the electrolyte and both positive and negative electrodes [21, 22]. The subsequent measurement of the impedance spectrum contributes to monitoring of the degradation of batteries. Osaka et al. [21] reported the equivalent circuit in Fig. 11.14 for commercial lithium-ion rechargeable batteries. This circuit was designed with several assumptions and considerations taking into account the structure of batteries. The impedance of the electrolyte/electrode interface is considered with the interfacial resistance and capacitance in parallel. The two Warburg impedances in parallel were designed with the assumption that the cathode consisted of two different particle sizes, resulting in two different diffusion paths. The reason for the mixture might be found in the fact that a mixture of different size particles for the cathode will increase the capacity with a decrease in resistance. Typical experimental results of the impedance spectra of commercial lithium-ion rechargeable batteries [21] are shown in Fig. 11.15. More than two capacitive loops are observed on the Nyquist plot. In addition, the apparent locus related to the Warburg impedance is

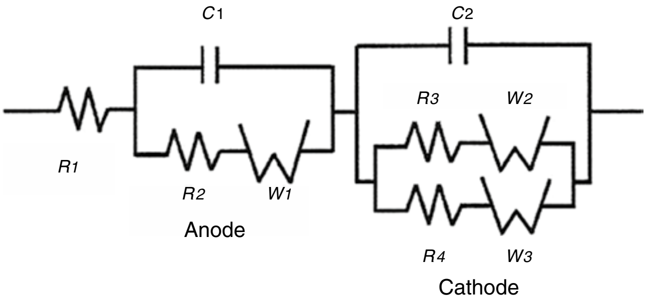

Fig. 11.14 Equivalent circuit for commercial lithium-ion rechargeable batteries. R_1: resistance of electrolyte and current collector, R_{2-4}: interfacial resistance, $C_{1,2}$: capacitance of electrode surface layer, W_{1-3}: Warburg impedance [21]

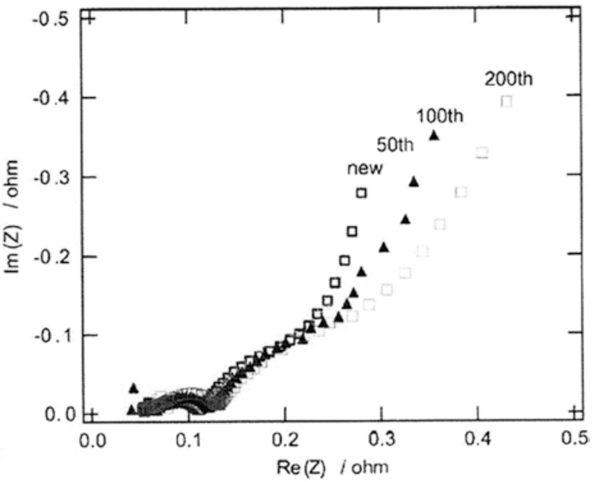

Fig. 11.15 Typical Nyquist plots of impedance of commercial lithium-ion rechargeable battery at cell voltage of 4.0 V. The measurements were repeated after the presented number of cycles. The frequency range was 0.2 mHz to 200 Hz [21]

observed in the low-frequency range. It can be seen that the imaginary value at a very low frequency increased with the cycle number. A very low-frequency impedance is related to the limiting capacitance, and a decrease in its value indicates that the amount of active materials has decreased, which could be caused by phase changes or dissolution. Figure 11.15 shows the fitted results of the impedance spectra in Fig. 11.14 with the equivalent circuit in Fig. 11.13. The interfacial resistance of the cathode increased with the cycle number, while that of the anode remained nearly constant. These results are interpreted assuming that the anode is rather stable after the formation of a SEI during the initial cycle, and the surface layer on the cathode grows due to the oxidizing power of Co(VI) in the charged state.

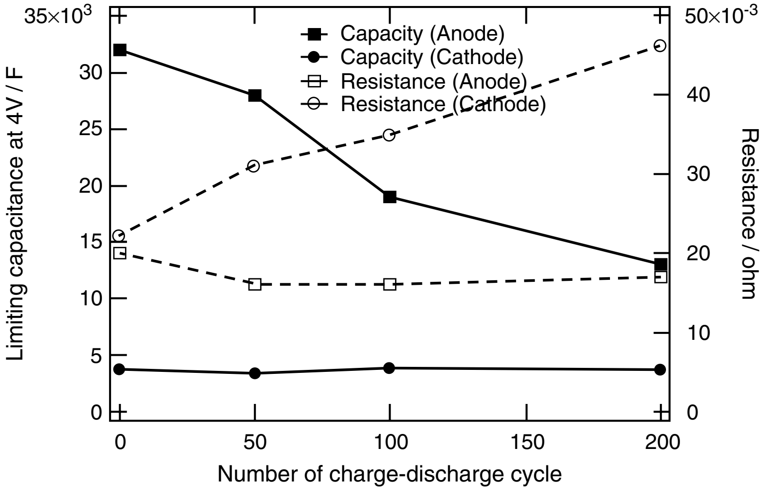

Fig. 11.16 Parameters obtained by fitting of impedance in Fig. 11.15 with number of cycles. *Right axis*: interfacial resistance; *left axis*: limiting capacitance [21]

For the limiting capacitance, only that of the anode decreased with the cycle number. It was reported that the capacity fade was attributed to the increase in the cathode resistance and decreases in the anode capacitance [21] (Fig. 11.16).

In this section, two examples of the application of an AC method were introduced. As mentioned earlier, detailed information on the electrode/electrolyte interface can be obtained by the AC method, and evaluations of electrode materials, electrolytes, and their interface should contribute to the further development of advanced electrodes for lithium-ion rechargeable batteries. In addition, the nondestructive inspection of batteries can be carried out by establishing a suitable equivalent circuit.

References

1. N. Takami, A. Satoh, M. Hara, T. Ohsaki, J. Electrochem. Soc. **142**, 371 (1995)
2. A. Funabiki, M. Inaba, Z. Ogumi, J. Power Sources **68**, 227 (1997)
3. S.S. Zhang, M.S. Ding, K. Xu, J. Allen, T.R. Jow, Electrochem. Solid-State Lett. **4**, A206 (2001)
4. C. Wang, A.J. Appleby, F.E. Little, Electrochim. Acta **46**, 1793 (2001)
5. J.Y. Song, H.H. Lee, Y.Y. Wang, C.C. Wan, J. Power Sources **111**, 255 (2002)
6. T. Abe, H. Fukuda, Y. Iriyama, Z. Ogumi, J. Electrochem. Soc. **151**, A1120 (2004)
7. T. Abe, K. Takeda, T. Fukutsuka, Y. Iriyama, Z. Ogumi, J. Electrochem. Soc. **151**, C694 (2004)
8. M. Itagaki, N. Kobari, S. Yotsuda, K. Watanabe, S. Kinoshita, M. Ue, J. Power Sources **135**, 255 (2004)
9. M. Itagaki, S. Yotsuda, N. Kobari, K. Watanabe, S. Kinoshita, M. Ue, Electrochim. Acta **51**, 1629 (2006)

10. S.S. Zhang, K. Xu, T.R. Jow, Electrochim. Acta **51**, 1636 (2006)
11. K. Ku, J. Electrochem. Soc. **154**, A162 (2007)
12. Z. Lu, M.D. Levi, G. Salitra, Y. Gofer, E. Levi, D. Aurbach, J. Electroanal. Chem. **491**, 211 (2000)
13. J.S. Gnanaraj, Y.S. Cohen, M.D. Levi, D. Aurbach, J. Electroanal. Chem. **516**, 89 (2001)
14. K. Dokko, M. Mohamedi, Y. fujita, T. Itoh, M. Nishizawa, M. Umeda and I. Uchida, J. Electrochem. Soc. 148 ,A422 (2001)
15. M. Takahashi, Shin-ichi Tobishima, K. Takei and Y. Sakurai, Solid State Ionics 148, 283 (2002)
16. A.-K. Hjelm, G. Lindbergh, Electrochim. Acta **47**, 1747 (2002)
17. S.S. Zhang, K. Xu, T.R. Jow, Electrochem. Solid-State Lett. **5**, A92 (2002)
18. M. Itagaki, N. Kobari, S. Yotsuda, K. Watanabe, S. Kinoshita, M. Ue, J. Power Sources **148**, 78 (2005)
19. H. Miyashiro, A. Yamanaka, M. Tabuchi, S. Seki, M. Nakayama, Y. Ohno, Y. Kobayashi, Y. Mita, A. Usami, M. Wakihara, J. Electrochem. Soc. **153**, A348 (2006)
20. M. Gaberscek, J. Moskon, B. Erjavec, R. Dominko, J. Jamnik, Electrochem. Solid-State Lett. **11**, A170 (2008)
21. T. Osaka, S. Nakade, M. Rajamaki, T. Momma, J. Power Sources **119–121**, 929 (2003)
22. S. Seki, T. Kobayashi, N. Serizawa, Y. Kobayashi, K. Takei, H. Miyashiro, K. Hayamizu, S. Tsuzuki, T. Mitsugi, Y. Umebayashi, M. Watanabe, J. Power Sources **195**, 6207 (2010)

Chapter 12
Nuclear Magnetic Resonance Study of Lithium-Ion Batteries

Miwa Murakami, Yoshiki Iwai, and Junichi Kawamura

12.1 Introduction to Nuclear Magnetic Resonance Spectroscopy for Lithium-Ion Batteries

Nuclear magnetic resonance (NMR), which has been widely used for the structural analysis of organic compounds [1], can also be applied to investigate the organic electrolytes of lithium-ion (Li) batteries and product materials produced by charge and discharge cycling. Such an investigation has been made possible by recent technological advances. One advance is the development of high-power and stable superconducting magnets and digital technology for high-frequency circuits, which can improve the sensitivity of NMR signals. With the improved sensitivity, NMR of a nuclear spin with very low sensitivity, which was previously undetectable, has now been observed [2].

A second advance is the development of high-resolution NMR techniques for solid materials. Since many materials in a Li battery are amorphous solids or powder solids, the resolution is generally low due to so-called powder broadening, mostly attributable to chemical-shift anisotropy, except for a mobile atom/ion/molecule whose linewidth is motionally narrowed. An example of motional narrowing is ^{7}Li signals of lithium ions in carbon materials used as anodes. Most NMR signals of solid materials are, however, broad, and a technique called magic-angle spinning (MAS) is applied to remove the powder broadening. In Sect. 12.2, NMR studies of cathode and anode materials without or with MAS are discussed. Further, two

---

M. Murakami (✉)
Office of Society-Academia Collaboration for Innovation,
Kyoto University, Gokasho, Uji, Kyoto 611-0011, Japan
e-mail: m-murakami@saci.kyoto-u.ac.jp

Y. Iwai • J. Kawamura
Institute of Multidisciplinary Research for Advanced Materials,
Tohoku University, Katahira 2-1-1, Aobaku, Sendai 980-8577, Japan
e-mail: iy@mail.tagen.tohoku.ac.jp; kawajun@tagen.tohoku.ac.jp

T. Osaka and Z. Ogumi (eds.), *Nanoscale Technology for Advanced Lithium Batteries*,
Nanostructure Science and Technology 182, DOI 10.1007/978-1-4614-8675-6_12,

advanced NMR techniques – two-dimensional (2D) NMR and the double-resonance method – are introduced.

A third advance has been made in magnetic resonance imaging (MRI), which is used in medical science. Nowadays, with new imaging techniques and a high-power and accurate pulse-shaped magnetic-field gradient, MRI can now be used in the investigation of materials. NMR microscopy using MRI techniques can be applied to obtain microscopic images of the distribution of nuclear spins, such as ^{7}Li in Li batteries (Sect. 12.3). The magnetic-field-gradient technique can also be used to measure the diffusion coefficients of Li ions, which is one of the important applications of NMR in Li batteries and is also touched upon in Sect. 12.3.

12.2 Nuclear Magnetic Resonance in Cathode and Anode Materials

In this chapter, we first deal with ^{7}Li NMR studies of lithium inserted into carbon anode materials (Sect. 12.2.1). The observed resolution of ^{7}Li NMR is good enough to distinguish intercalated lithium, lithium dissolved in electrolyte, and metallic lithium, even without spinning the sample (MAS). Various types of intercalated lithium have been identified for different carbon systems. The high resolution obtained for a static sample then prompted the development of in situ NMR (Sect. 12.2.2), that is, observation of the insertion/extraction process was made possible using a special electrochemical cell and a NMR probe. In Sect. 12.2.3, we discuss the effects and limitations of MAS, which is an indispensable technique to observe high-resolution NMR of solid material, through its application to Li batteries. A number of studies examining the high resolution achieved by MAS have already been concisely reviewed by Grey et al. [3–5]. Hence, in this chapter, we describe the application of advanced techniques applied concurrently with MAS, namely, 2D NMR and double resonance (Sect. 12.2.4).

12.2.1 Lithium Inserted into Carbon Anode Materials

The first application of NMR to the examination of the microstructure of an electrode material may be the work of Conard and Estrade on lithium-intercalated graphite (LiC_6) in 1977 [6]. They observed ^{7}Li NMR spectra of LiC_6 over a wide temperature range (from 200 up to 460 K), and the observed signal was attributed to Li^+ ions intercalated between graphite layers. In this work, one can appreciate several aspects of ^{7}Li NMR of lithiated carbons as summarized in what follows.

The chemical shift of a ^{7}Li species is ascribed to several electrostatic effects, such as the diamagnetic/paramagnetic shielding and the shift due to conducting electrons (the Knight shift). The small Knight shift (approximately 40 ppm) compared to that for lithium metal (ca. 265 ppm) [7] was attributed to the low metallic character of lithium in this intercalation compound, which suggests the π orbitals of graphite are necessary intermediates in the bonding of lithium atoms. Further, this signal was attributed to Li^+ ions intercalated between graphite layers where the conduction electron density associated with graphene planes is supplied by the Li 2s electrons [7].

The linewidth and the lineshape are attributed to the distribution of the local structure of the ^7Li species. For example, the static linewidth of the central transition (approximately 4.0 kHz) was thought to be compatible with lithium ions lying in planes with six nearest lithium neighbors at a distance of 4.3 Å. Because conductivity and molecular motion, such as the diffusive motion of a lithium ion, depend on temperature, the signal position (the Knight shift) and the lineshape/linewidth depend on temperature. In fact, Conard and Estrada deduced from the temperature dependence of the linewidth that a mobility of lithium appears around 280 K, as in metallic lithium, with a correlation time around 10^{-5} s. Note that this work used a static sample, and narrowing of the linewidth may be expected if one applies MAS.

As the spin quantum number ($I=3/2$) of ^7Li is larger than 1, its NMR is also affected by the quadrupolar interaction. Since the quadrupolar broadening is smaller for the central transition between the spin states of −1/2 and 1/2 than those for the satellite transitions between 3/2 and 1/2 or −3/2 and −1/2, one usually observes a narrower central transition associated with two satellite transitions appearing as sidebands of the central transition separated by the quadrupolar coupling in Hertz. The quadrupolar broadening would also depend on temperature if motion exists because molecular motion generally alters the electric field gradient around ^7Li, which determines the size of the quadrupolar interaction.

Graphite intercalation compounds at various “stages” identified by X-ray diffraction [8] are called 4, 3, diluted 2, 2, and 1, which correspond to LiC_{36}, LiC_{27}, LiC_{18}, LiC_{12}, and LiC_6, respectively. Some of the corresponding ^7Li signals were reported by Zaghib et al. [7]. It was reported that the Knight shifts for each stage are 2.2, 6.8, 10, 43.9, and 41.4 ppm and the quadrupolar coupling constants (e^2qQ/h) are 37, 37.5, 39.5, 34, and 46 kHz.

Figure 12.1 is a typical example of a ^7Li NMR spectrum of lithium in graphite (Fig. 12.1a) and carbon/carbon composite electrodes (Fig. 12.1b) [9]. The sharp/strong signals at around 0 ppm are ^7Li ions in electrolyte solution (0 ppm is 1 M LiCl in H_2O). Intercalated ^7Li in graphite appears at 42 ppm (LiC_6, LiC_{12}) with its satellite transitions at 120 ppm and −40 ppm. The signal at 13 ppm was ascribed to LiC_{18}, LiC_{27}, and LiC_{36} in graphite. In the carbon/carbon composite, ^7Li of an initial intercalation in the graphitelike coating of the fibers appears at 18 ppm. ^7Li inserted into the carbon core appears at 104 ppm, for which a significant shift/linewidth change was observed during a galvanostatic cycle [9]. A broad ^7Li NMR signal was also found for fully doped lithium in hard carbon at approximately 80–120 ppm [10–16] at room temperature, while Tatsumi et al. reported that at 143 K the ^7Li signal of Li-doped nongraphitizable carbon splits into two peaks at 18 and 192 ppm [10]. The 192 ppm signal was ascribed to quasi-metallic lithium forming a lithium cluster in the pore of the hard-carbon structure. The 18 ppm peak was attributed to lithium ions intercalated into graphene layers and the lithium ions existing on the

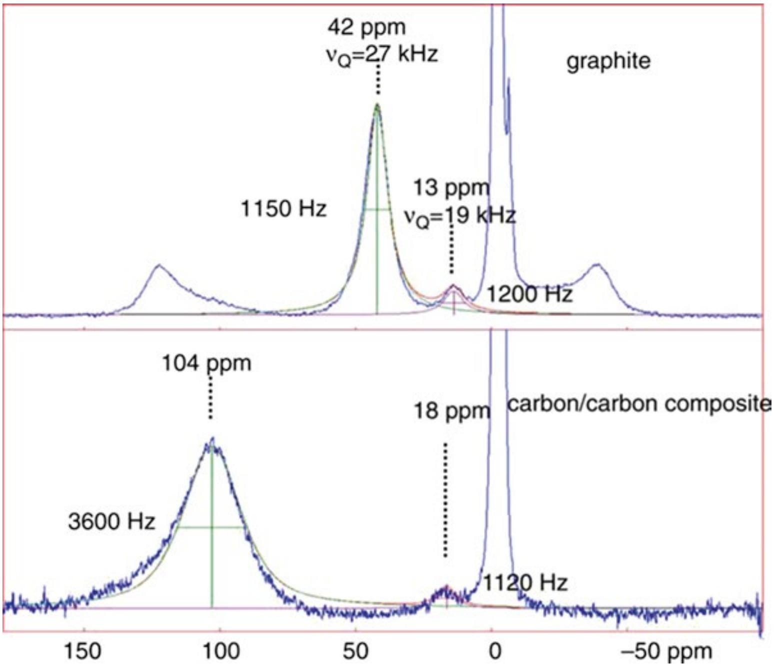

Fig. 12.1 Shifts and linewidth for carbon/carbon composite electrode when fully inserted by lithium [9] (Reprinted from Journal of Physics and Chemistry of Solids, 67, Letellier M, Chevallier F, Béguin F, In situ Li NMR during lithium electrochemical insertion into graphite and a carbon/carbon composite, 1228–1232, Copyright (2006), with permission from Elsevier)

edge of the carbon. Letellier et al. also reported in a carbon fiber that the signal of intercalated lithium appeared at 18 ppm, while that of quasi-metallic lithium appeared at 18–110 ppm [17]. The variation in the chemical shift can be ascribed to the Knight shift due to the interaction between lithium and free electrons. These works clearly show that the ^{7}Li chemical shift of lithium in a carbon system varies not only with the different stages but also with the type of carbon (hard carbon, graphite, or a nanotube), the quantity of lithium, and temperature.

12.2.2 *In Situ Nuclear Magnetic Resonance of Lithium Insertion into Carbon Anode Materials*

As shown previously, various lithium species intercalated in an anode can be distinguished by their chemical shifts. Therefore, the structural changes in an anode during charge/discharge can be studied by observing the spectral changes in ^{7}Li NMR sequentially at suitable time intervals. Since ex situ NMR after the destruction of a cell would modify the material and the observation [14], in situ NMR without

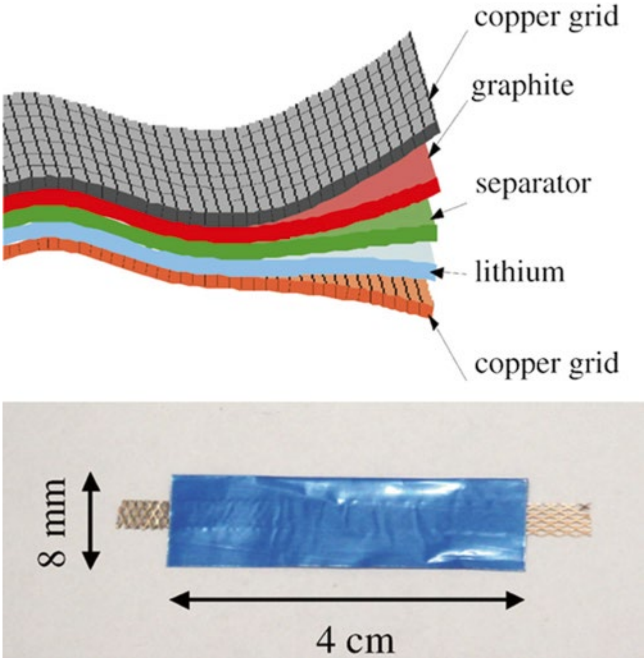

Fig. 12.2 Laminate cell used for in situ NMR [19] (Reprinted from Carbon, 45, Letellier M, Chevallier F, Morcrette M, In situ ^{7}Li nuclear magnetic resonance observation of the electrochemical intercalation of lithium in graphite; 1st cycle. 1025–1034, Copyright (2007), with permission from Elsevier)

destroying the cell is desirable. In fact, several groups reported in situ NMR for the study of the charge/discharge process [9, 17–23].

The first in situ NMR experiments of batteries were performed by Rathke et al. [18]. A special electrochemical cell and a NMR detector using a toroid cavity was developed to investigate the reversible electrochemical process (insertion/extraction) of lithium ions in graphitic carbon. They showed that lithium speciation could be followed continuously throughout multiple charge/discharge cycles.

Since a toroid cavity requires a special cell design, the researchers' method was difficult to combine with a standard battery cell. Letellier et al. adopted a so-called laminated cell (Fig. 12.2) [19] for the NMR sample to examine the insertion reaction of lithium in disordered carbon and graphite anodes by ^{7}Li NMR. They developed a NMR probe with a coil that could accommodate the flat laminated cell and two electrodes to apply electrostatic voltages for charge/discharge.

Figure 12.3 plots the 100 ^{7}Li spectra observed during the three first charge/discharge cycles [17]. In this experiment, lithium insertion/extraction (charge/discharge) was done stepwise with each NMR observation. Clearly the observed shift change at 0–104 ppm is synchronous with the Li insertion/extraction, showing that in situ observation can done to study the change in the stage of intercalation.

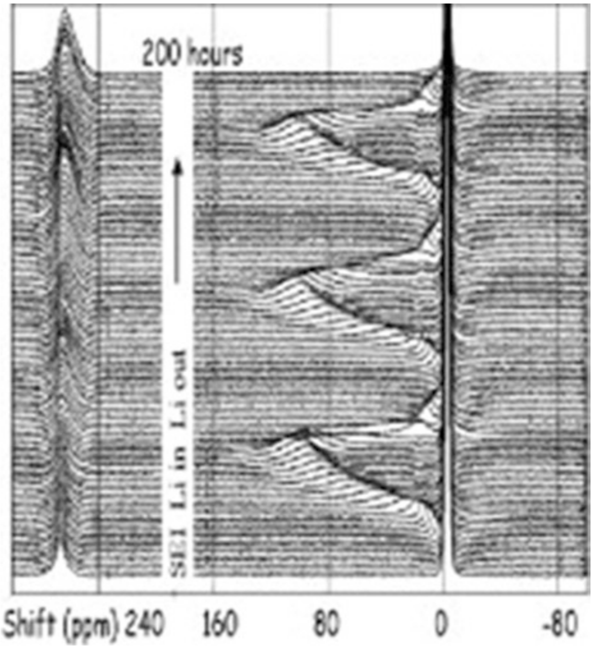

Fig. 12.3 100 ^{7}Li spectra of first three electrochemical cycles [17] (Reprinted from Journal of Physics and Chemistry of Solids 65 Letellier M, Chevallier F, Béguin F, Frackowiak E, Rouzaud J-N, The first in situ ^{7}Li NMR study of the reversible lithium insertion mechanism in disorganised carbons, 245–251. Copyright (2004), with permission from Elsevier)

Note that this signal corresponds to the ^{7}Li in graphite at 42 ppm in Fig. 12.1a, and the signal at 230–260 ppm in Fig. 12.3 was assigned to metallic lithium.

An explanation of the spectra obtained by in situ NMR is thus straightforward, and several in situ experiments using ^{7}Li and ^{6}Li NMR were done to study the charge/discharge process of lithium in various carbon materials [9, 17–23]. Recently, Grey et al. reported changes in the ^{7}Li NMR spectrum with lithium insertion into a silicon cathode [22]. They also reported the use of in situ NMR spectroscopy to provide time-resolved, quantitative information about the nature of metallic lithium deposited on lithium-metal electrodes [23].

12.2.3 Application of Magic-Angle Spinning and Its Limitations

In the preceding discussion, we found that the resolution of ^{7}Li NMR of lithium inserted into carbon anode materials is good without applying MAS. The higher resolution is apparently achieved by motional averaging of several anisotropic spin

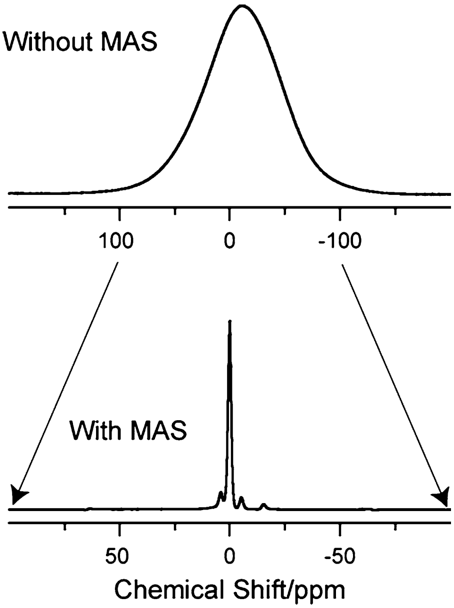

Fig. 12.4 ^{7}Li NMR spectra of $LiCoO_2$ without and with MAS

interactions. Since such averaging does not occur in most solid materials, MAS is indispensable to obtain high-resolution NMR. Figure 12.4 compares the ^{7}Li MAS spectra of $LiCoO_2$ without and with MAS. For the spectrum without MAS (the static sample), the existence of the small signals observed under MAS around the main signal cannot be realized from the observed characterless broad lineshape.

The application of MAS to electrode materials started around 1995. One of the first works may be the one by Sato et al. in 1994 [24]. They applied ^{7}Li MAS NMR for a disordered carbon material, prepared by heat treatment of polyphenylene, in which lithium was stored electrochemically, and suggested the existence of Li_2 covalent molecules in the carbon material. For cathode materials, in 1995, Marichal et al. reported ^{6}Li and ^{7}Li MAS spectra of $LiNi_{1-y}$ Co_yO_2, which are sensitive to hyperfine coupling with both the nearest and next nearest nickel neighbors [25]. A large number of studies using MAS appeared in subsequent years and are reviewed in the literature [3–5]. Although most MAS studies are of ^{6}Li and ^{7}Li in cathode materials, several studies use other nuclear spins: ^{2}H (Li_2MnO_3) [26, 27], ^{19}F ($Li(Ni_{0.425}Mn_{0.425}Co_{0.15})O_2$) [28], ^{29}Si (Si cathode) [22], ^{31}P ($LiFePO_4$, $LiMnPO_4$) [29], ^{51}V ($Li_{1+x}V_3O_8$) [30], and ^{59}Co (Li_xCoO_2) [31, 32]. Most of the aforementioned studies observed MAS NMR of one of the skeletal nuclei in each cathode material, except for the ^{2}H NMR by Paik et al. They used ^{2}H MAS NMR to study H^+/Li^+ ion exchange at specific lithium sites during acid leaching. As exemplified by these studies, MAS is useful in studying cathode materials; however, some limitations/problems can also be appreciated, which will be discussed in what follows.

There are certain requirements and limitations on MAS's ability to remove linewidth due to various anisotropic spin interactions. The most stringent limitation of the application of MAS to Li batteries may be the finite spinning speed in the removal of paramagnetic broadening. A paramagnetic state of nuclei such as Co or Ni often occurs in a cathode material that brings severe line broadening (paramagnetic broadening) to the NMR signal of a nuclear spin close to the paramagnetic center. At the same time, a shift of the resonance line (paramagnetic shift) occurs. These paramagnetic effects were first explored in detail by Grey et al. [5, 33] and have been observed in many cathode materials.

In principle, MAS can remove paramagnetic broadening if the MAS spinning speed in Hertz is larger than the paramagnetic broadening. At present, the highest spinning speed commercially available is around 80 kHz, and most of the experiments reported use a spinning speed of a few tens of kilohertz. On the other hand, it is not rare to find paramagnetic broadening of more than a few hundred kilohertz. Hence, in many paramagnetic cathode materials, the MAS spinning speed is not fast enough to remove the paramagnetic broadening and a large number of spinning sidebands do appear, which makes it difficult to identify the central peaks and to determine the number of structurally different sites. Because the size of paramagnetism depends on the strength of the static magnetic field (B_0), a smaller B_0 may be desirable for a paramagnetic material; however, the resolution and sensitivity become worse for smaller B_0.

For spins with a half-integer I, for example, $I=3/2$ for ^{7}Li, the first-order quadrupolar interaction does not affect to its central transition ($1/2 <-> -1/2$). However, the central transition is affected in the second order and the second-order quadrupolar powder shape, whose size is inversely proportional to B_0, appears. The line broadening due to the quadrupolar interaction in most cases reduces the resolution, and identification of each site becomes difficult. Hence for higher resolution, removal of the quadrupolar lineshape is desirable. The other limitation of MAS is that it cannot remove the so-called second-order quadrupolar powder lineshape. Hence, to reduce the broadening due to the second-order quadrupolar lineshape, a larger B_0 is desirable. On the other hand, since a quadrupolar interaction is an interaction between the quadrupolar moment of a nucleus and the electric field gradient around the nucleus, its size depends on the local symmetry of the nucleus and can thus be a useful observable to discuss the local structure.

For spins with an integer spin quantum number ($I=3$ for ^{6}Li and $I=1$ for ^{2}H), there is no central transition and all NMR transition are affected by the first-order quadrupolar interaction. Similar to the paramagnetic broadening, MAS can remove the effect of the first-order quadrupolar interaction if the speed of MAS in Hertz is larger than the size of the first-order quadrupolar interaction. If the speed is lower, then one observes many spinning sidebands.

Even with these reservations, MAS is still a useful and indispensable technique for the study of cathode materials. In what follows, we describe the application of 2D NMR and double-resonance techniques under MAS to investigate cathode materials.

12.2.4 Advanced Techniques Applied Under Magic-Angle Spinning

As was shown, a high-resolution 1D spectrum obtained using MAS is useful to identify different sites in electrode materials. Lithium exchange among these sites is a fundamental and crucial property of the electrode material to conduct lithium ions through a crystal. By applying 2D exchange NMR, observation of Li exchange among the different sites becomes possible and thus gives an unambiguous and direct answer to the question of whether or not lithium is hopping between two different sites and on what time scale. When the exchange of lithium occurs between sites with different chemical shifts, i.e., crystallographically different sites, the exchange can be observed directly as cross peaks in a 2D exchange spectrum whose intensities are analyzed as a function of time and temperature. The data allow the extraction of three types of information. First is the pathway of Li diffusion in crystal by examining the cross-peak pattern. Second is the time scale on which the Li hops from one site to another, and third is the atomic site occupancies as a function of temperature, which yields in an Arrhenius analysis the activation energy of the hopping process.

Verhoeven et al. applied 2D exchange NMR of ^{7}Li in $Li[Mn_{1.96}Li_{0.04}]O_4$ under MAS [34]. They showed that a millisecond time scale exchange of lithium starts around 285 K between two different sites in a unit cell (the 8a and 16c site, Fig. 12.5a). At 380 K, it was shown that lithium starts to hop between more than two sites (Fig. 12.5b, c). Activation energies of around 0.5 eV and jump rates are derived, which are consistent with those determined macroscopically. Similar application of 2D exchange NMR to the dynamics of lithium has been done for various cathode materials such as $Li_{4+x}Ti_5O_{12}$ [35], $Li_3V_2(PO_4)_3$ [36], $LiMn_2O_4$ [37], $Li_4V(PO_4)_2F_2$ [38], $Li_3Fe_2(PO_4)_3$ [39]. In these studies, the researchers adopted an exchange time that is an integer multiple of the spinning cycle time (rotor-synchronized exchange NMR [40]). The rotor synchronization was necessary to avoid rotor-induced cross peaks among the spinning sidebands, which make it difficult to examine lithium-exchange-induced cross peaks.

These studies show that 2D exchange NMR is a powerful technique to study lithium exchange in a cathode material. Its application, however, requires at least two resolved signals for different sites and a time scale for exchange that is shorter than the spin–lattice relaxation time. In the next Sect. 12.3, we describe the diffusion measurement of Li ions in (dense) solution using the field-gradient technique. As the diffusion is slow in solids, such diffusion measurements using the field gradient is difficult for a solid cathode material.

Another promising NMR technique is double resonance, which makes it possible to examine the distance proximities between two different nuclear spins. Recently, Murakami et al. applied ^{7}Li/^{19}F double-resonance NMR to examine LiF formed at the surface layer of a $LiCoO_2$ electrode during charge–discharge cycles [41]. They observed ^{7}Li and ^{19}F signals using ^{19}F to ^{7}Li and ^{7}Li to ^{19}F cross polarization (CP), respectively, whose chemical shifts are consistent with those of pure LiF. As was

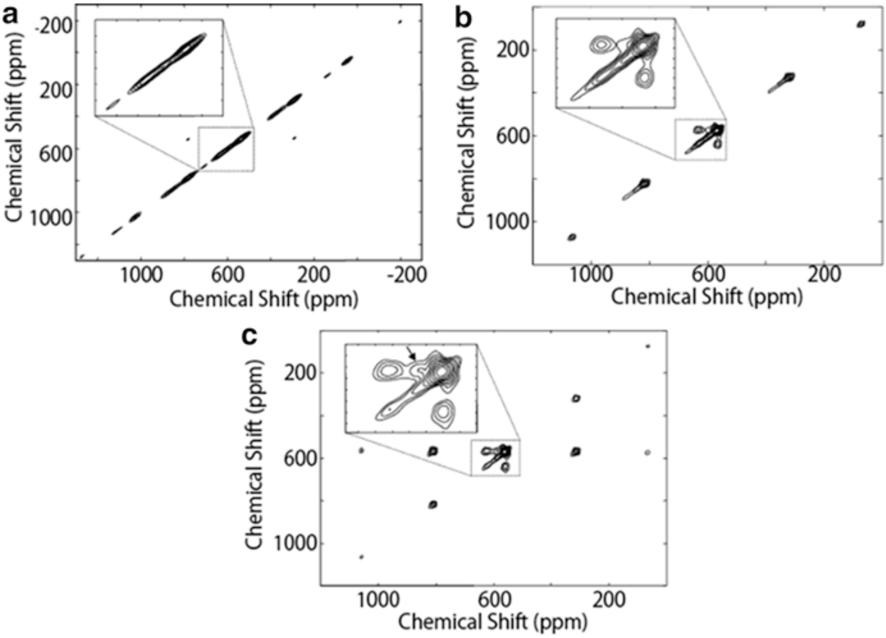

Fig. 12.5 Two-dimensional MAS NMR spectra of $Li[Mn_{1.96}Li_{0.04}]O_4$ (**a**) at 285 K with exchange time of 5 ms, (**b**) at 380 K and 5 ms, and (**c**) 10 ms [34]. Several spinning sidebands appeared (spinning speed: 28 kHz = ca. 241 ppm). *Arrow*: cross peak between two sites 8*a* and 16*d* (Reprinted with permission from Verhoeven et al., Phys Rev Lett 86, 4314–4317, 2001. Copyright (2001) by American Physical Society)

shown earlier, the apparent chemical shifts may not be unequivocal fingerprints of LiF because one may have a Knight shift, a paramagnetic shift, and an isotropic second-order quadrupolar shift. Hence, the researchers further studied the magnetization-transfer curves during ^{7}Li/^{19}F CP to examine the ^{7}Li-^{19}F distance and indicated that the observed CP signals were of LiF in the $LiCoO_2$ electrode.

12.3 Diffusion Measurement and In Situ Nuclear Magnetic Resonance Micro Imaging for Lithium-Ion Batteries

In Sect. 12.3.1, we will introduce two typical studies of diffusion measurement using the pulsed-field-gradient technique with a focus on Hayamizu's work. One is a standard analysis of diffusion coefficients and the second is a new in situ measurement that combines diffusion measurement with an external electric field. A triaxial magnetic gradient makes it possible to obtain a three-dimensional NMR image of ^{7}Li distribution in a material, which is described in Sect. 12.3.2. Recent advanced imaging techniques are introduced in Sect. 12.3.3.

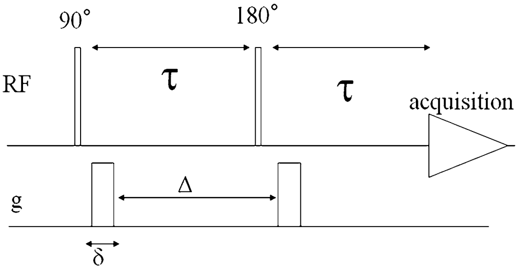

Fig. 12.6 A conventional pulse sequence called the pulse-gradient spin-echo (PGSE) method, which is used for diffusion measurement

12.3.1 Diffusion Measurement

The pulsed-field-gradient spin-echo (PGSE) sequence (Fig. 12.6) is an established method for diffusion measurement by NMR. Many diffusion coefficients in electrolytes for Li batteries have been investigated by Hayamizu and coworkers [42–45]. The first example is the study of lithium bis(trifluoromethanesulfonyl)amide, whose trivial name is $LiN(SO_2CF3)_2$ (abbreviated LiTFSA), in various solvents [43]. The solvents are those commonly used for Li batteries, such as, for example, PC (propylene carbonate), EC (ethylene carbonate), DMC (dimethyl carbonane), and DME (1,2-dimethoxyethane). The researchers measured the self-diffusion coefficients of solvent (D_{solvent}), lithium ions (D_{Li}), and fluorine ions that are included in counter anions (D_{anion}). In all the electrolytes, the three diffusion coefficients showed the following relation:

$$D_{solvent} > D_{anion} > D_{Li}, \tag{12.1}$$

which is contradictory to the size of each bare molecular or ionic radius calculated by $D = kT/(c\pi\eta r)$. This result was ascribed to the solvation effect, that is, cation and anion are surrounded by solvents; they diffuse with an environmental solvent.

Hayamizu et al. then adopted a simple experimental parameter that estimates the degree of solvation effect:

$$R_{ion} = \frac{D_{solv}}{D_{ion}} = \frac{r_s^{ion}}{r_s^{solv}}, \tag{12.2}$$

where r_s^{solv} and r_s^{ion} are the effective radii of solvent and ions (ion = Li or TFSI) [45]. This R_{ion} value is a ratio of the diffusion radius with reference to a solvent. For PC and EC solvents, its R_{Li} is around 2, suggesting that lithium ion diffuses in association with two solvent molecules on average. In contrast, R_{anion} is around 1.4, which is smaller than R_{Li}. This means the solvation effect for TFSA is less than that for lithium ions.

An estimation of the transport number is also possible; it was measured by the electrochemical method. The transport number for cations is given by

$$t_+ = D_{Li} / \left(D_{Li} + D_{anion} \right). \tag{12.3}$$

The transport number obtained from the diffusion measurement falls between 0.35 and 0.50 for PC, EC, DMC, and DME. From these values we can discuss the degree of dissociation and ion-pair formation. The R_{ion} and transport number t_+, which are easily determined by a PGSE experiment, provide microscopic information of electrolytes in Li batteries.

Recently, a new technique was developed that is useful for understanding ionic motion in electric fields. The new technique combines diffusion measurement and electrochemistry by applying a DC voltage to an electrolyte during diffusion measurement. An electric field induces motion for cations and anions, which move in opposite directions due to their opposite charges (the electrophoretic effect). The induced flow is observed as a phase shift of the NMR signal in the PGSE pulse sequence, leading to attenuation of the signal intensity given by

$$\cos\left(\gamma g v \delta \Delta \right), \tag{12.4}$$

where v is a drift velocity induced by an electric field [46]. This technique allows us to determine the individual drift velocity for lithium ions and counter anions.

Hayamizu et al. demonstrated PGSE NMR under a constant electric field (Fig. 12.7), which they referred to as ENMR (electrophoretic NMR), by using a homemade NMR cell equipped with Li/Li electrodes [46]. A propylene carbonate (PC) solution doped with 0.5 M $\mathrm{LiN(SO_2CF_3)_2}$ (LiTFSI) was used for the measurement.

Signal attenuation was observed by applying DC voltage, and the researchers calculated the drift velocity as a function of applied voltage V and its duration time t_{DC} applied in advance to the application of the PGSE sequence. The drift velocity of the lithium ions was around 2.5×10^{-9} m/s at $V = 3.0$ and $t_{\mathrm{DC}} = 0.4$ s. In contrast, the drift velocity of TFSI anions is one-tenth smaller than that of lithium ions. The large deviation shows that the acceleration of diffusion of lithium ions by DC voltage is much larger than that of TFSI. It is interesting to note that this is in contrast to that obtained without DC voltage, where diffusion coefficient of TFSI is larger than lithium ion ($D_{\mathrm{TFSI}} > D_{\mathrm{Li}}$). This information is quite important for understanding lithium ion motion during the charge and discharge process for Li batteries.

This technique is still rather new, and interpretations of acquired data are not well defined. Moreover, there remain some unresolved problems, such as the poor reproducibility and surface effect of lithium electrodes. However, we do believe that this technique occupies an important position for analyzing lithium-ion motion in electrolytes.

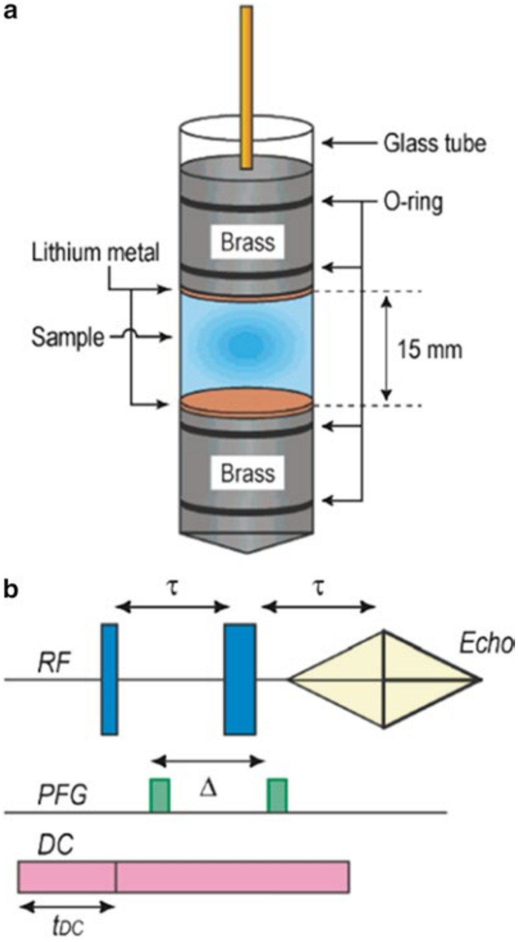

Fig. 12.7 Schematic cell design for diffusion measurement with DC voltage (**a**) and pulse sequence used for ENMR measurement (Reprinted with permission from Hayamizu K, Seki S, Miyashiro H, Kobayashi Y, J Phys Chem B 110:22302–22305. Copyright (2006) American Chemical Society)

12.3.2 In Situ Nuclear Magnetic Resonance Imaging for Lithium Batteries

NMR imaging is a combination of conventional NMR and a triaxial magnetic gradient probe with power amplifiers for gradient pulses, which is synchronized with other NMR pulses to produce magnetic gradients along an intended direction and intensity.

The first in situ NMR imaging, combined with electrochemistry, was done for polymer electrolyte membranes in fuel cells. Several researchers reported a visualization of a proton (^{1}H) in Nafion membranes that has been used widely in fuel cells in low-temperature operations [47–50]. For example, visualizations of macroscopic

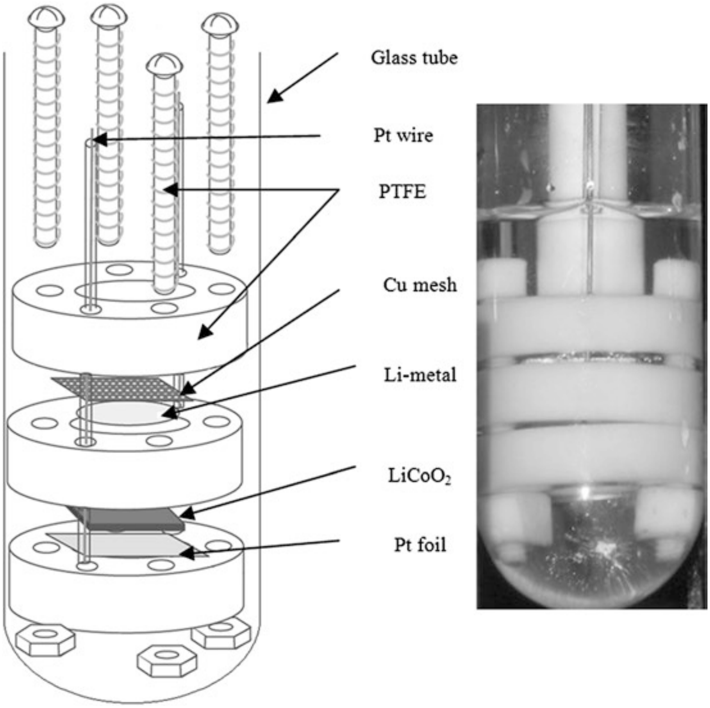

Fig. 12.8 Schematic design (*left*) and picture (*right*) of lithium-ion battery for in situ NMR imaging for batteries. *Right-hand side* picture is filled with liquid electrolyte $LiClO_4$/PC

proton motion by means of mutual diffusion between water and deuterium, change in water content during fuel cell operation, electrophoretic motion of protons and water by application of an electric field, and inversion have been studied [47].

Recently, there is a demand for a nondestructive visualization method in Li batteries during electrochemical cycling to understand the degradation mechanisms and improve battery safety. A well-known technique to see through batteries is X-ray and neutron tomography; however, NMR imaging is also suitable because it is quite sensitive to protons that are included in the electrolytes of Li batteries. In addition, with current high-sensitivity and high-resolution NMR machines, it is possible to detect the spatial distribution of lithium ions from ^{7}Li NMR signals. However, the radio frequency that is used in NMR measurement is less transmissive through the exterior metal packing of commercial batteries, which requires the appropriate design of model Li batteries and imaging techniques. A similar requirement has been applied to the special cells used in the in situ experiments described in Sect. 12.2.2. In what follows, we will present several NMR images of ^{1}H and ^{7}Li for model Li batteries obtained in our laboratory to evaluate the possibilities and limitations of this approach.

Figure 12.8 shows a model Li battery developed for NMR imaging. For better transmission of radio-frequency wave and magnetic gradients applied by a gradient

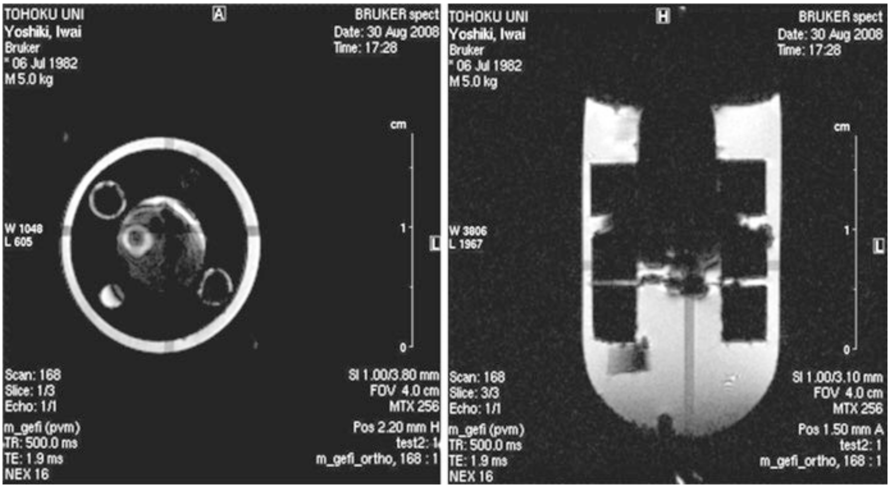

Fig. 12.9 Example of ^{1}H NMR imaging for model lithium-ion battery. *Left-hand side*: *x-y* cross section; *right-hand side*: *x-z* cross section

probe, the cell contains as much nonmagnetic material as possible, for example, a glass tube (φ 18 mm) as the container, Polytetrafluoroethylene (PTFE) as the separator, and fixing. The model cell was located in the NMR imaging probe. The resonance frequency of ^{1}H is 400 MHz and that of ^{7}Li is 155 MHz. A pulse sequence for NMR imaging is based on the spin-echo method Multi Slice Multi Echo (MSME), which is installed in measurement software (ParaVision) made by Bruker Biospin co.

Figure 12.9 shows typical ^{1}H NMR images for Li batteries. The left-hand side is an x-y cross section and the right-hand side is an x-z cross section. The white parts correspond to electrolyte. A small bubble is observed in this picture. If the electrolyte in the model battery is placed in contact with lithium metal for a long time, reductive decomposition leads to polymerization. This process involves gelification of the electrolyte and gas formations (Fig. 12.10).

Figure 12.11 shows an example of in situ NMR imaging. The cathode and anode materials are $LiCoO_2$ and lithium metal, respectively. The degradation process becomes a very slow one if one imposes certain conditions; however, a long acquisition time induces an inhomogeneous distribution of electrolyte in the bottom part of the model cell. In addition, intensity enhancement was observed for areas located close to the $LiCoO_2$ cathode material. The same phenomenon was also observed for the $LiMn_2O_4$ cathode material (not shown). These increases in intensity imply that the effect should be ascribable to paramagnetism of the cathode material, which produces an extra magnetic field to distort the applied magnetic-field gradient. Further detailed analysis is omitted in this chapter.

The preceding examples are of ^{1}H NMR imaging; however, if NMR imaging could detect lithium ions themselves, that would be more powerful and informative as it would allow us to visualize the diffusion, migration, and reaction of mobile

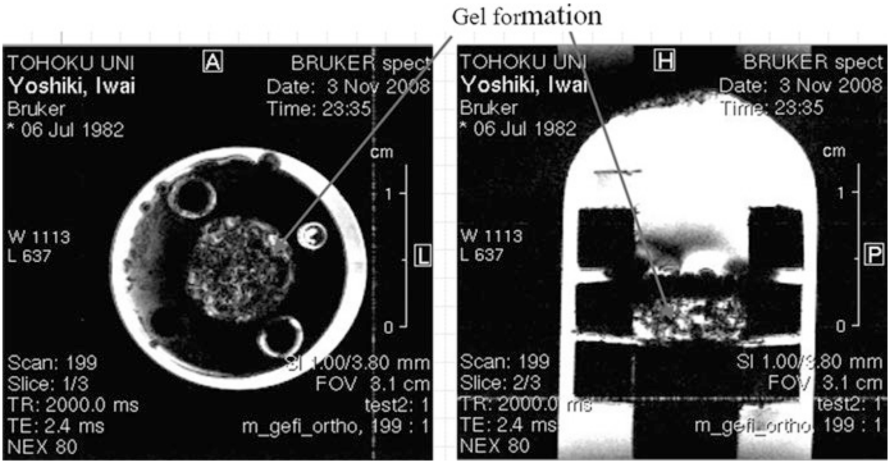

Fig. 12.10 Example of ^{1}H NMR imaging for model lithium-ion battery after 2 months. *Left-hand side*: *x-y* cross section; *right-hand side*: *x-z* cross section

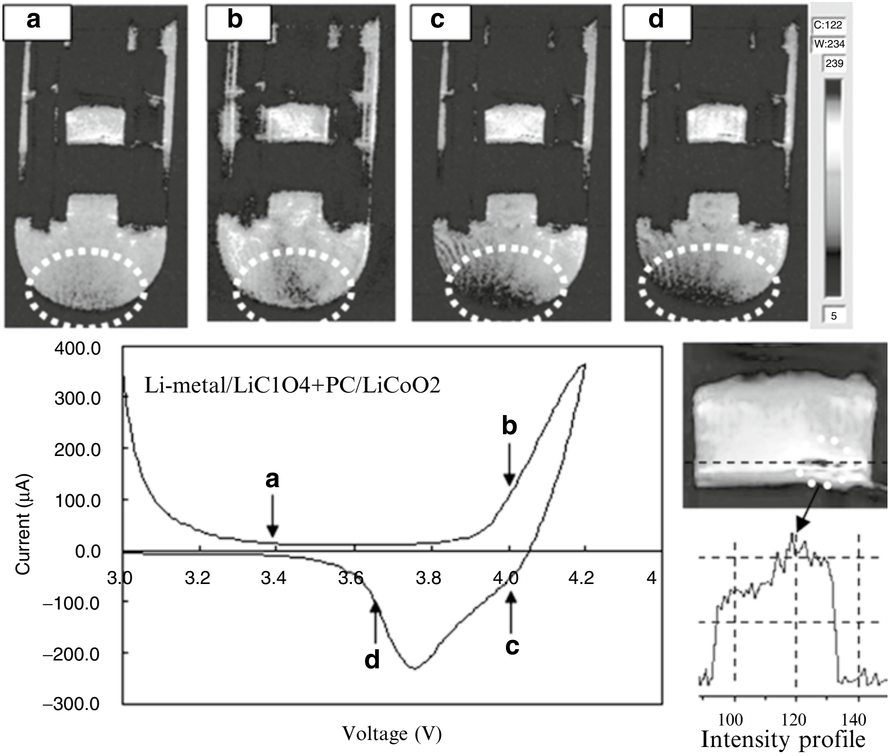

Fig. 12.11 In situ ^{1}H NMR imaging for model lithium-ion battery

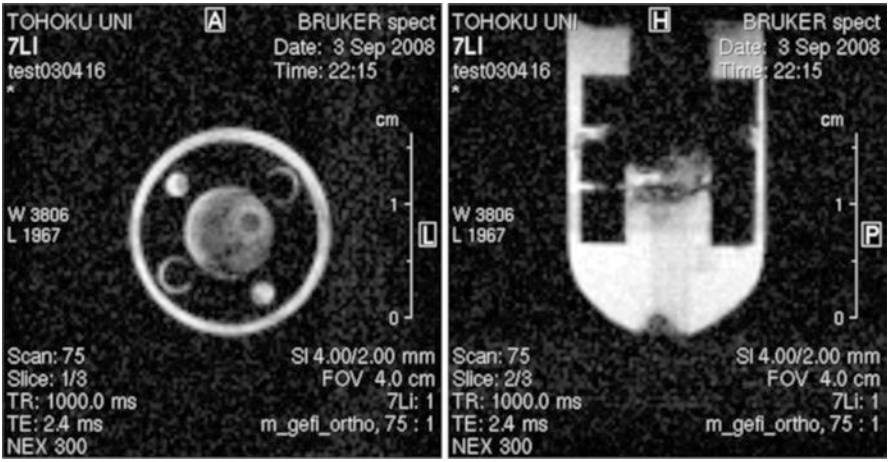

Fig. 12.12 ^{7}Li NMR imaging for model lithium-ion battery. *Left-hand side*: *x-y* cross section; *right-hand side*: *x-z* cross section

lithium ions in electrodes. To the best of our knowledge, the first application of ^{7}Li NMR imaging for Li batteries was first reported by Soderegger et al. in 1992 [51]. They measured the distribution of lithium ions in a polymer electrolyte [$PEO_8(LiClO_4)$] and investigated how a heat treatment of polymer electrolyte affects ^{7}Li NMR images. They discovered that a heated spot shows low intensity, which reflects a difference in the relaxation time. The researchers tried to monitor the behavior of electrolytes in the charging and recharging cycles of batteries. Although the observed ^{7}Li imaging shows low spatial resolution, this is an epoch-making study of Li batteries. After many trials and errors, ^{7}Li NMR images have become detectable in practical use while to produce a clear image compared with the acquisition time of ^{1}H. Figure 12.12 shows a ^{7}Li NMR image taken in our laboratory. It takes over several hours to detect the image at a spatial resolution of 300 mm (128 × 128 pixels).

To evaluate a NMR image, one must take the so-called skin depth into account. The skin depth is the depth to which the applied NMR pulse penetrates. For a non-metal material, the NMR pulse can penetrate the entire sample, but for a metallic material, the pulse is screened. The degree of screening effect of an electromagnetic wave by free electrons in metal is determined by the effective resistance of the conductor, which increases with the frequency of the current because much of the conductor carries little current. The skin depth is given by

$$\delta = \sqrt{\frac{2}{\mu \omega \sigma}}, \tag{12.5}$$

where μ, ω and σ are the absolute magnetic permeability of the conductor, angular frequency of the electromagnetic wave, and resistivity of the conductor, respectively. The skin depth in most normal metal ranges from 1 to 10 mm at $\omega = 2\pi \times 500$ MHz.

This indicates that a NMR pulse does not reach a sample if it is covered with thick metal (>10 mm), thereby leading to no "image" of the inside of the metal.

To be honest, the spatial resolution achieved in the present imaging experiment is not enough to be called a NMR microscope. The resolution of NMR imaging depends on the intensity of the magnetic gradient and its duration. A simple estimation of the resolution of NMR imaging, Δ, is described as

$$\Delta = 2\pi / \left(\gamma g t\right), \tag{12.6}$$

where γ, g, and t are the gyromagnetic ratio, the gradient constant, and the duration, respectively. This formula indicates that if one wants to increase the resolution, a strong gradient constant and long applied time are necessary. A commercially available gradient probe produces a maximum gradient constant of around 0.5 [T/m], and the applied time is around 10 ms, which is restricted by the relaxation time T_2. In the case of ^{1}H ($\gamma = 2.68 \cdot 10^8$ [rad/(s·T)]), the resolution is $\Delta \sim 5 \cdot 10^{-6}$ [m] at best. This is micrometer resolution. A much higher gradient may be possible theoretically, and one could cut out a much smaller volume from the sample. However, this would reduce the intensity of the NMR signal because the NMR intensity is inversely proportional to the detection volume. Suppose one could reduce the spatial resolution by half, that is, from 5 to 2.5 μm; the NMR intensity for each volume would become 1/8, thus leading to a much longer NMR machine time. Furthermore, intense magnetic gradients cause side effects, such as noise and eddy currents, which induce a reduction of the signal-to-noise ratio and unwanted artifacts in the NMR imaging.

12.3.3 New Approach to Overcoming Conventional Nuclear Magnetic Resonance Imaging

Finally, we would like to introduce two new imaging approaches to overcoming the aforementioned drawbacks. The first example is a study by Gerald et al., at Argonne National Laboratory [52]. They demonstrated a sophisticated technique of imaging inside of a battery to obtain one axial projection image of a lithium ion. To avoid the skin-depth problem, they developed a coin-type cell for Li batteries, which works as a NMR resonator equipped with wires to produce an alternative magnetic gradient inside the cell. The cell is inserted into a toroid cavity imager. Using an imaging technique in a rotating frame, the researchers detected the NMR intensity of ^{7}Li. This technique has a spatial resolution of around 1 mm. The researchers measured the lithium dendrites that had been created on the hard carbon electrode during the charge–discharge cycle (Fig. 12.13).

Another approach was introduced by Ruger et al. in an IBM group [53, 54]; the approach applies scanning microscope techniques with an ultrasensitive cantilever. This technique is called magnetic resonance force microscopy (MRFM), and it achieved nanometer resolution. Figure 12.14 shows a basic setup of MRFM. The entire experiment is conducted in a static field. In the field, a sample is on a cantilever tip. The radio freqency (RF) coil shown in Fig. 12.14 produces a radio freqency

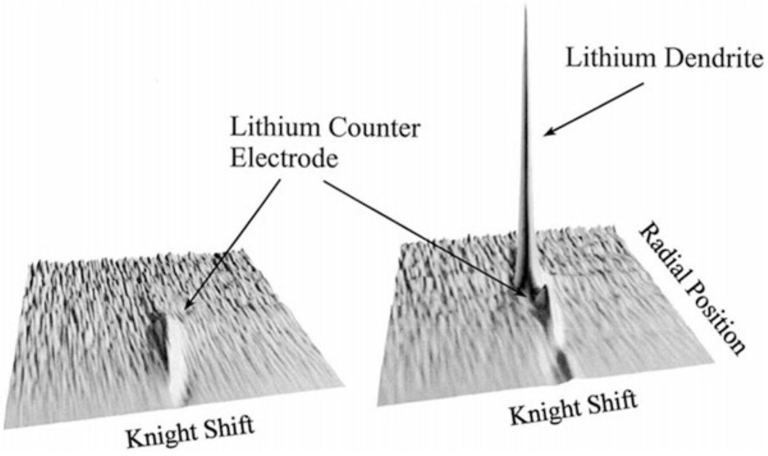

Fig. 12.13 ^{7}Li NMR images of counter electrode and lithium dendrites in lithium-ion battery, before (**a**) and after (**b**) passing current through battery cell (Reprinted from Journal of Power Sources, 89, Gerald II RE, Johnson CS, Rathke JW, Klingler RJ, Sandí G, Scanlon LG, 7Li NMR study of intercalated lithium in curved carbon lattices, 237. Copyright (2000), with permission from Elsevier)

Fig. 12.14 Basic setup and components of MRFM experiment (Reprinted from Nature Nanotechnology 2:301–306. Copyright (2007), with permission from Macmillan)

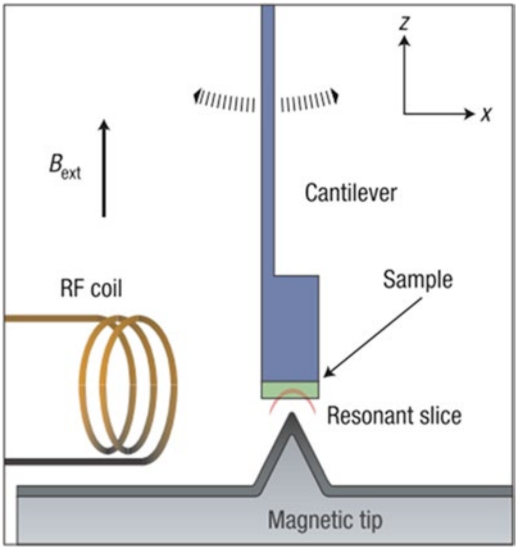

to rotate a nuclear spin. A magnet tip located near the sample produces a magnetic gradient. This gradient affects the nuclear spin in the sample to generate a tiny force that can be measured by the cantilever frequency shift.

Only resonance condition is

$$|B_{tip}(r) + B_{ext}| = \omega_{RF} / \gamma. \tag{12.7}$$

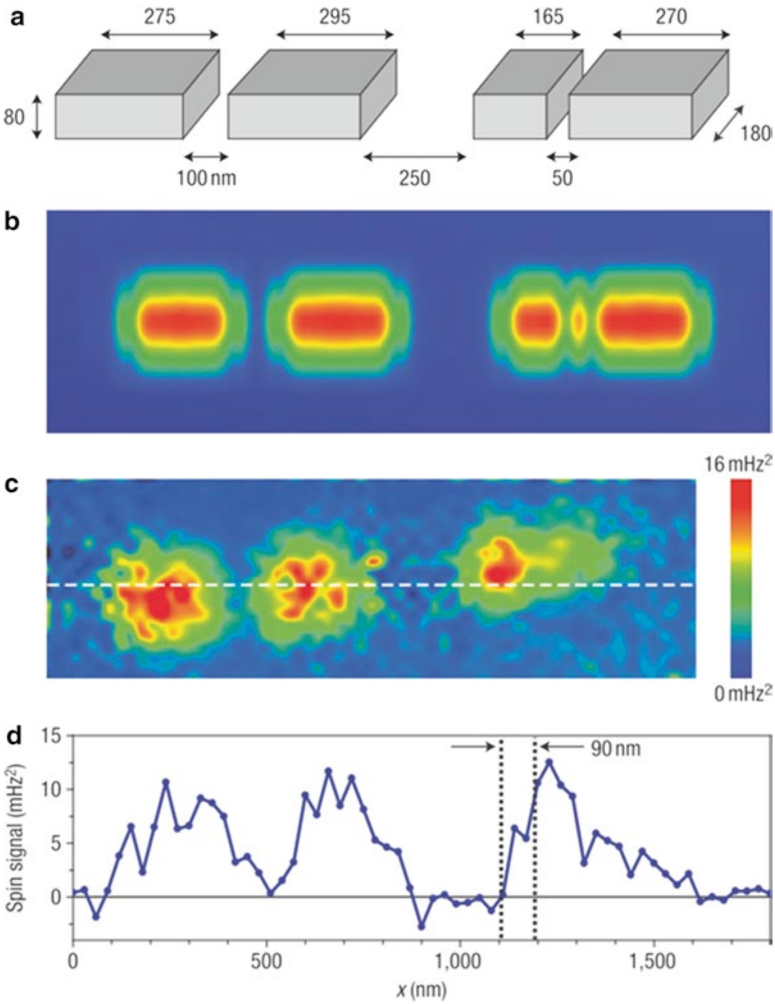

Fig. 12.15 Experimental results and simulation showing two-dimensional imaging of ^{19}F nuclei. (**a**) Schematic of CaF_2 structure used for imaging test object. (**b**) Simulated image of ^{19}F distribution. (**c**) Experimental result. (**d**) Line scan along *dotted line* in Fig. 12.15c (Reprinted from Nature Nanotechnology 2:301–306. Copyright (2007), with permission from Macmillan)

Under the situation the freqnency of the cantilever is modulated by a force between nuclear spins and the gradient field.

The stronger the magnetic gradient produced by the magnet tip B_{tip}, the finer the resolution (nanometer scale) achieved [19]. The researchers applied this technique to CaF_2 on a cantilever and obtained two-dimensional image of a ^{19}F distribution~ with a resolution of 90 nm (Fig. 12.15). Most recently, the same IBM group has been improved the spatial resolution; they visualized a three-dimensional reconstruction of a virus particle at a resolution of 4 nm.

This technique has not yet been applied to Li batteries; however, in the near future, it will be useful tool to invesitigate electrochemical systems, including Li batteries. The nano-scale spatial resolution and the ability of chemical identification will solve a longstanding issue: the composition and structure of solid electrolyte interfaces (SEIs).

References

1. E. Pretsch, P. Bühlmann, M. Badertscher, *Structure Determination of Organic Compounds: Tables of Spectral Data* (Springer, New York, 2009)
2. K.J.D. MacKenzie, M.E. Smith, *Multinuclear Solid-State NMR of Inorganic Materials* (Elsevier, New York, 2002)
3. C.P. Grey, S.G. Greenbaum, Nuclear magnetic resonance studies of lithium-ion battery materials. MRS Bull. **27**, 613–618 (2002)
4. C.P. Grey, Y.J. Lee, Lithium MAS NMR studies of cathode materials for lithium-ion batteries. Solid State Sci. **5**, 883–894 (2003)
5. C.P. Grey, N. Dupr, NMR studies of cathode materials for lithium-ion rechargeable batteries. Chem. Rev. **104**, 4493–4512 (2004)
6. J. Conard, H. Estrade, Résonancemagnétiquenucléaire du lithium interstitieldans le graphite. Mater. Sci. Eng. **31**, 173–176 (1977)
7. K. Zaghib, K. Tatsumi, Y. Sawada, S. Higuchi, H. Abe, T. Ohsaki, ^{7}Li-NMR of well-graphitized vapor-grown carbon fibers and natural graphite negative electrodes of rechargeable lithium-ion batteries. J. Electrochem. Soc. **146**, 2784–2793 (1999)
8. H. Zabel, S.A. Solin (eds.), *Graphite Intercalation Compounds I and II* (Springer, Berlin, 1990/1992)
9. M. Letellier, F. Chevallier, F. Béguin, In situ ^{7}Li NMR during lithium electrochemical insertion into graphite and a carbon/carbon composite. J. Phys. Chem. Solids **67**, 1228–1232 (2006)
10. K. Tatsumi, J. Conard, M. Nakahara, S. Menu, P. Lauginie, Y. Sawada, Z. Ogumi, ^{7}Li NMR studies on a lithiated non-graphitizable carbon fibre at lowtemperatures. Chem. Commun. 687–688 (1997)
11. K. Tatsumi, T. Kawamura, S. Higuchi, T. Hosotubo, H. Nakajima, Y. Sawada, Anode characteristics of non-graphitizable carbon fibers for rechargeable lithium-ion batteries. J. Power Sources **68**, 263–266 (1997)
12. K. Tatsumi, J. Conard, M. Nakahara, S. Menu, P. Lauginie, Y. Sawada, Z. Ogumi, Low temperature ^{7}Li-NMR investigations on lithium inserted into carbon anodes for rechargeable lithium-ion cells. J. Power Sources **81–82**, 397–400 (1999)
13. S. Wang, H. Matsui, H. Tamamura, Y. Matsumura, T. Yamabe, Mechanism of lithium insertion into disordered carbon. Phys. Rev. **B58**, 8163–8165 (1998)
14. K. Guérin, M. Ménétrier, A. Février-Bouvier, S. Flandrois, B. Simon, P. Biensan, A Li NMR study of a hard carbon for lithium–ion rechargeable batteries. Solid State Ion. **127**, 187–198 (2000)
15. S. Yamazaki, T. Hashimoto, T. Iriyama, Y. Mori, H. Shiroki, N. Tamura, Study of the states of Li doped in carbons as an anode of LiB by ^{7}Li NMR spectroscopy. J. Mol. Struct. **441**, 165–171 (1998)
16. S. Gautier, F. Leroux, E. Frackowiak, A.M. Faugére, J.-N. Rouzaud, F. Béguin, Influence of the pyrolysis conditions on the nature of lithium inserted in hard carbons. J. Phys. Chem. **A105**, 5794–5800 (2001)
17. M. Letellier, F. Chevallier, F. Béguin, E. Frackowiak, J.-N. Rouzaud, The first in situ ^{7}Li NMR study of the reversible lithium insertion mechanism in disorganised carbons. J. Phys. Chem. Solid **65**, 245–251 (2004)

18. R.E. Gerald II, J. Sanchez, C.S. Johnson, R.J. Klingler, J.W. Rathke, In situ nuclear magnetic resonance investigations of lithium ions in carbon electrode materials using a novel detector. J. Phys. Condens. Mater. **13**, 8269–8285 (2001)
19. M. Letellier, F. Chevallier, M. Morcrette, In situ ^{7}Li nuclear magnetic resonance observation of the electrochemical intercalation of lithium in graphite; 1st cycle. Carbon **45**, 1025–1034 (2007)
20. M. Letellier, F. Chevallier, C. Clinard, E. Frackowiak, J.N. Rouzaud, F. Béguin, M. Morcrette, J.M. Tarascon, The first in situ ^{7}Li nuclear magnetic resonance study of lithium insertion in hard-carbon anode materials for Li-ion batteries. J. Chem. Phys. **118**, 6038–6045 (2003)
21. F. Chevallier, M. Letellier, M. Morcrette, J.M. Tarascon, E. Frackowiak, J.N. Rouzaud, F. Beguin, In situ ^{7}Li nuclear magnetic resonance observation of reversible lithium insertion into disordered carbons. Electrochem. Solid State Lett. **6**, A225–A228 (2003)
22. B. Key, R. Bhattacharyya, M. Morcrette, V. Seznéc, J.M. Tarascon, C.P. Grey, Real-time NMR investigations of structural changes in silicon electrodes for lithium-ion batteries. J. Am. Chem. Soc. **131**, 9239–9249 (2009)
23. R. Bhattacharyya, B. Key, H.L. Chen, A.S. Best, A.F. Hollenkamp, C.P. Grey, In situ NMR observation of the formation of metallic lithium microstructures in lithium batteries. Nat. Mater. **9**, 504–510 (2010)
24. K. Sato, M. Noguchi, A. Demachi, N. Oki, M. Endo, A mechanism of lithium storage in disordered carbons. Science **264**, 556–558 (1994)
25. C. Marichal, J. Hirschinger, P. Granger, M. Ménétrier, A. Rougier, C. Delmas, ^{6}Li and ^{7}Li NMR in the $LiNi_{1-y}Co_yO_2$solid solution ($0 \leq y \leq 1$). Inorg. Chem. **34**, 1773–1778 (1995)
26. Y. Paik, C.P. Gray, C.S. Johnson, J.-S. Kim, M.M. Thackeray, Lithium and deuterium NMR studies of acid-leached layered lithium manganese oxides. Chem. Mater. **14**, 5109–5115 (2002)
27. Y. Paik, W. Bowden, T. Richards, C.P. Grey, The effect of heat-treatment on electrolytic manganese dioxide: A ^{2}H and ^{6}Li magic angle spinning NMR study. J. Electrochem. Soc. **152**, A1539–A1547 (2005)
28. M. Ménétrier, J. Bains, L. Croguennec, A. Flambard, E. Bekaert, C. Jordy, P. Biensan, C. Delmas, NMR evidence of LiF coating rather than fluorine substitution in $Li(Ni_{0.425}Mn_{0.425}Co_{0.15})O_2$. J. SolidState Chem. **181**, 3303–3307 (2008)
29. M.C. Tucker, M.M. Doeff, T.J. Richardson, R. Finones, J.A. Reimer, E.J. Cairns, ^{7}Li and ^{31}P magic angle spinning nuclear magnetic resonance of $LiFePO_4$-type materials. Electrochem. Solid State Lett. **5**, A95–A98 (2002)
30. N. Dupré, J. Gaubicher, D. Guyomard, C.P. Grey, ^{7}Li and ^{51}V MAS NMR study of the electrochemical behavior of $Li_{1+x}V_3O_8$. Chem. Mater. **16**, 2725–2733 (2004)
31. R. Siegel, C.D. HirschingerJ, S. Matar, M. Ménétrier, C. Delmas et al., ^{59}Co and ^{6,7}Li MAS NMR in polytypes O2 and O3 of $LiCoO_2$. J. Phys. Chem. B **105**, 4166–4174 (2001)
32. M.P.J. Peeters, M.J. van Bommel, P.M.C.N. Wolde, H.A.M. van Hal, W.C. Keur, A.P.M. Kentgens, A ^{6}Li, ^{7}Li and ^{59}Co MAS NMR study of rock salt type Li_xCoO_2 ($0.48 \leq x \leq 1.05$). Solid State Ion. **112**, 41–52 (1998)
33. Y.J. Lee, F. Wang, C.P. Grey, ^{6}Li and ^{7}Li MAS NMR studies of lithium manganate cathode materials. J. Am. Chem. Soc. **120**, 12601–12613 (1998)
34. V.W.J. Verhoeven, I.M. de Schepper, G. Nachtegaal, A.P.M. Kentgens, E.M. Kelder, J. Schoonman, F.M. Mulder, Lithium dynamics in $LiMn_2O_4$ probed directly by two-dimensional ^{7}Li NMR. Phys. Rev. Lett. **86**, 4314–4317 (2001)
35. M. Wagemaker, E.R.H. van Eck, A.P.M. Kentgens, F.M. Mulder, Li-ion diffusion in the equilibrium nanomorphology of spinel $Li_{4+x}Ti_5O_{12}$. J. Phys. Chem. B **113**, 224–230 (2009)
36. L.S. Cahill, R.P. Chapman, J.F. Britten, G.R. Goward, ^{7}Li NMR and two-dimensional exchange study of lithium dynamics in monoclinic $Li_3V_2(PO_4)_3$. J. Phys. Chem. B **110**, 7171–7177 (2006)
37. L.S. Cahill, R.P. Chapman, C.W. Kirby, G.R. Goward, The challenge of paramagnetism in two-dimensional ^{6,7}Li exchange NMR. Appl Magn Reson **32**, 565–581 (2007)
38. L.S. Cahill, Y. Iriyama, L.F. Nazar, G.R. Goward, Synthesis of $Li_4V(PO_4)_2F_2$ and ^{6,7}Li NMR studies of its lithium ion dynamics. J. Mater. Chem. **20**, 4340–4346 (2010)

39. L.J.M. Davis, I. Heinmaa, G.R. Goward, Study of lithium dynamics in monoclinic $Li_3Fe_2(PO_4)_3$ using ^{6}Li VT and 2D Exchange MAS NMR Spectroscopy. Chem. Mater. **22**, 769–775 (2010)
40. K. Schmidt-Rohr, H.W. Spiess, *Multidimensional Solid-State NMR and Polymers* (Academic, London, 1994)
41. M. Murakami, H. Yamashige, H. Arai, O.Z. UchimotoY, Direct evidence of LiF formation at electrode/electrolyte interface by ^{7}Li and ^{19}F double-resonance solid-state NMR Spectroscopy. Electrochem. Solid State Lett. **14**, A134–A137 (2011)
42. K. Hayamizu, Y. Aihara, S. Arai, W.S. Price, Diffusion, conductivity and DSC studies of a polymer gel electrolyte composed of cross-linked PEO, g-butyrolactone and $LiBF_6$. Solid State Ion. **107**, 1–12 (1998)
43. K. Hayamizu, Y. Aihara, S. Arai, Pulse-gradient spin-echo 1H, 7Li, and 19F NMR diffusion and ionic conductivity measurements of 14 organic electrolytes containing LiN(SO2CF3)2. J. Phys. Chem. B **103**, 519–524 (1999)
44. K. Hayamizu, Y. Aihara, S. Arai, W.S. Price, Self-diffusion coefficients of lithium, anion, polymer, and solvent in polymer gel electrolytes measured using ^{7}Li, ^{19}F, and ^{1}H pulsed-gradient spin-echo NMR. Electrochim. Acta **45**, 1313–1319 (2000)
45. K. Hayamizu, Ion and solvent diffusion and ion conduction of PC-DEC and PC-DME binary solvent electrolytes of $LiN(SO_2CF_3)_2$. Electrochim. Acta **49**, 3397–3402 (2004)
46. K. Hayamizu, S. Seki, H. Miyashiro, Y. Kobayashi, Direct in situ observation of dynamic transport for electrolyte components by NMR combined with electrochemical measurements. J. Phys. Chem. B **110**, 22302–22305 (2006)
47. J. Kawamura, K. Hattori, T. Hongo, R. Asayama, N. Kuwata, T. Hattori, J. Mizusaki, Microscopic states of water and methanol in Nafion membrane observed by NMR micro imaging. Solid State Ion. **176**, 2451–2456 (2005)
48. Y. Iwai, J. Kawamura, Observation of electrophoretic nuclear magnetic resonance imaging in polymer electrolyte. J. Phys. Soc. Jpn. Suppl. **A79**, 160–162 (2010)
49. W.F. Kirk, S.H. Bergens, R.E. Wasylishen, The use of 1H NMR microscopy to study proton-exchange membrane fuel cells. Chem. Phys. Chem. **7**, 67–75 (2005)
50. K. Teranishi, S. Tsushima, S. Hirai, Analysis of water transport in PEFCs by magnetic resonance imaging measurement. J. Electrochem. Soc. **153**, A664–A668 (2006)
51. M. Sonderegger, J. Roos, C. Kugler, M. Mali, D. Brinkmann, NMR imaging of Li-7 in a PEO(8)(LiClO4) film. Solid State Ion. **53**, 849–852 (1992)
52. R.E. Gerald II, C.S. Johnson, J.W. Rathke, R.J. Klingler, G. Sandí, L.G. Scanlon, ^{7}Li NMR study of intercalated lithium in curved carbon lattices. J Power Sources **89**, 237–243 (2000)
53. H.J. Mamin, M. Poggio, C.L. Degen, D. Rugar, Nuclear magnetic resonance imaging with 90-nm resolution. Nat. Nanotechnol. **2**, 301–306 (2007)
54. C.L. Degen, M. Poggio, H.J. Mamin, C.T. Rettner, D. Rugar, Nanoscale magnetic resonance imaging. Proc. Natl. Acad. Sci. U. S. A. **106**, 1313–1317 (2009)

Chapter 13
Nano Aspect of Vibration Spectra Methods in Lithium-Ion Batteries

C.M. Julien and A. Mauger

Abbreviations

BWF	Breit–Wigner–Fano
C-$LiFePO_4$	Carbon-coated $LiFePO_4$
FTIR	Fourier Transform Infrared
FWHM	Full Width at Half Maximum
HRTEM	High-Resolution Transmission Electron Microscopy
IR	Infrared
LFP	Lithium Iron Phosphate
LP	$LiFePO_4$
PPP	Polyparaphenylene
RS	Raman Scattering
SSR	Solid-State Reaction
TEM	Transmission Electron Microscopy
XRD	X-Ray Diffraction

C.M. Julien (✉)
Université Pierre et Marie Curie – Paris 6, Physicochimie des Electrolytes,
Coloïdes et Systèmes Analytiques (PECSA), Bat. F74, 4 place Jussieu,
75005 Paris, France
e-mail: christian.julien@upmc.fr

A. Mauger
Université Pierre et Marie Curie – Paris 6, Institut de Minéralogie
et Physique de la Matière Condensée (IMPMC),
Tour 23, 4 place Jussieu, 75005 Paris, France
e-mail: alain.mauger@impmc.jussieu.fr

T. Osaka and Z. Ogumi (eds.), *Nanoscale Technology for Advanced Lithium Batteries*,
Nanostructure Science and Technology 182, DOI 10.1007/978-1-4614-8675-6_13,

13.1 Introduction

Lithium-ion technology has opened a wide research field both in material physics and chemistry to achieve a class of materials for high-voltage cells. At present, lithium-ion battery technology seems to have the potential to satisfy all requirements of high-energy, high-power applications and to meet low cost demands. However, there remain several key materials issues, such as structural stability over several hundred cycles, which need to be resolved. In the area of positive electrode materials, extensive investigations on the requirements of optimum-ideal electrode systems have shown that layered oxides, spinels, and polyphosphates are the most promising systems with great potential for structural improvements for a long cycle life [1, 2].

One of the prospective solutions for the preparation of electrodes with high energy density is the choice of nanocomposite materials. Among the intrinsic properties of intercalation, the geometric design of the insertion-compound electrode is crucial. An important strategy in the design and optimization of the electrode is the use of smaller intercalation compound particles. Nanocomposite materials may give a high electrode–electrolyte interfacial area, coupled with short diffusion distance within the electrodes. They have a uniform electric field and a smaller change in the volume-to-surface-area ratio upon lithiation or delithiation.

The characterization of the new materials and the ultimate goal of correlating structural characteristics with physical and chemical properties demand the use of a broad range of techniques that could provide the information to establish the desired correlations. Vibrational spectroscopy is one of the most powerful techniques available for materials characterization [3]. As local probes, Raman scattering (RS) and Fourier transform infrared (FTIR) spectroscopy are useful tools when X-ray diffraction is ineffective for amorphous substances. The vibrational spectrum of a molecule, as observed in both infrared (IR) absorption and Raman studies, is the direct manifestation of forces arising from the mutual interactions of electrons and nuclei. By vibrational spectroscopy is meant the determination of the energy levels of various fundamental modes of vibration occurring in the molecules or complex ions of interest. Thus, from the observed mode frequencies we can glean information about the force constants, which hopefully can then be correlated with electronic structure and bonding theories. As a first approximation, the spectra consist of a superposition of the components of all local entities present in the same material, in contrast to diffraction data, which give a weighted average of similar interplanar spacing. As a general rule, the frequencies and relative intensities of the bands are sensitive to coordination geometry and oxidation states. Thus, the spectra are less affected by the grain size or the degree of the long-range order of the lattice.

However, it should be noted that Raman spectroscopy is essentially a probe to examine the surface of compounds that strongly absorb visible light, which is the case for all electrode materials used in Li-ion batteries, e.g., carbons, silicon, transition-metal oxides, and olivines, while IR spectroscopy is a tool used to examine the entire volume of particles. Although it is important to mention that RS and FTIR are complementary techniques in terms of selection rules, Raman spectroscopy investigates the phonons at the Brillouin-zone center ($\boldsymbol{q}=0$), while FTIR spectroscopy probes the entire Brillouin zone ($0<\boldsymbol{q}<2\pi/\boldsymbol{a}$). One of the sensitive cases is the lattice dynamics of the layered transition-metal oxides LiMO$_2$ where the Li-cage mode is only allowed in IR, so that only this technique is able to probe the local structure of the Li$_x$$MO_2$ electrode during cycles of charge–discharge.

The purpose of this chapter is to study the lattice dynamics of several insertion compounds used as electrodes in advanced lithium-ion batteries, especially nanomaterials for high-power-density application. Negative and positive electrodes having various crystal chemistries are presented. Section 13.2 presents the principle of RS for nano-objects at the elementary level. Since numerous textbooks address the theoretical aspects and instrumentation as well, no attempt has been made to cover any sophisticated aspects. Section 13.3 reports on the vibrational features of anode materials; carbonaceous and silicon nanoparticles are examined. The properties of (nanometer thick) carbon coating are reported in Sect. 13.4. The Raman spectra of the various oxides, including lamellar and spinel, are presented in Sect. 13.5. Section 13.6 is devoted to the intrinsic vibrational modes of nano-sized LiFePO$_4$ olivine structures. Finally, in Sect. 13.7, we report the properties of delithiated LiFePO$_4$ and the reactivity of this material when exposed to water.

13.2 General Considerations on Lattice Dynamics of Nanoparticles

It is well established that a frequency shift of the Raman spectrum can result from various effects. Tensile and compressive stresses affect the Raman line by a red shift and a blue shift, respectively. A downshift is also observed in the case of thin slabs or nanoparticles [4]. For a perfect single crystal of infinite size, lattice vibrations (phonons) are well-defined plane waves, and each of them has a well-defined wavevector $\boldsymbol{q}$. Only phonons near the center of the Brillouin zone are observed by Raman spectroscopy ($|\boldsymbol{q}|=\omega/c\approx 0$) because the frequency of the excitation light c is much greater than the frequency of phonons (Fig. 13.1a). For a nanoparticle of size L assumed to be spherical, the vibration is confined in the volume of the crystallite. As a consequence, the wavevector spectrum of the phonon is broadened and takes a finite width on the order of $2\pi/L$ around the zone center (Fig. 13.1b). This effect leads to asymmetric broadening and a frequency shift of the observed phonon through a relaxation of the $\boldsymbol{q}=0$ selection rule.

13.2.1 Vibrational Modes of a Sphere

The vibrational modes of a free sphere, i.e., an isolated spherical particle of homogeneous material, are divided into two classes: torsional modes and spheroidal

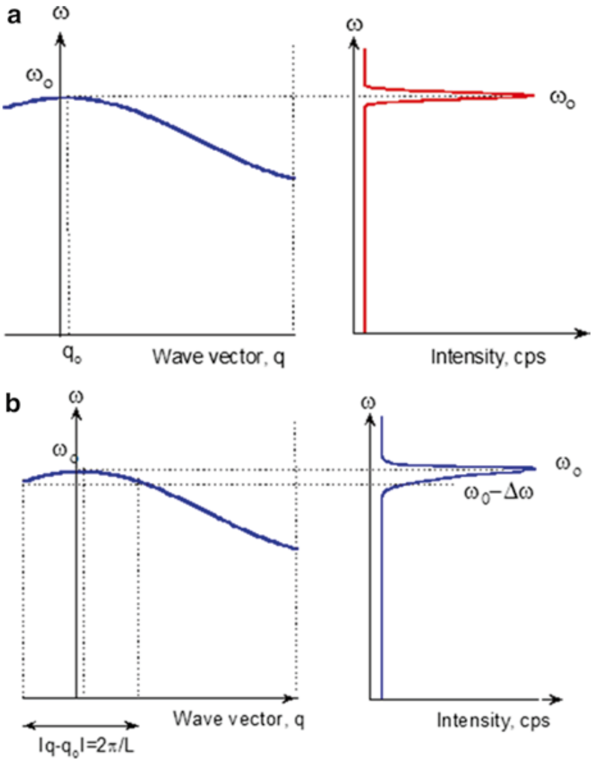

Fig. 13.1 Dispersion curves and Raman responses for (**a**) single crystal and (**b**) nanoparticle

modes (Fig. 13.2). Within these two classes, the vibrations are identified by two numbers, namely the principal quantum number n and the quantum number j associated to the length of the total angular momentum. The boundary conditions of the free sphere are defined by a stress tensor that is null at the surface. Tamura et al. have described a theory that takes into account the effect of contact of each spherical small particle with a rigid matrix using an elastic body approximation [5]. Consideration of both vector fields and a scalar field yields the proper vibrational modes. The eigenfrequencies of the elastic vibrations are derived by considering the circumstances surrounding a small particle: the matrix effect, surface relaxation effect, local clamping effect, and shape effect.

For a spherical particle, the Raman selection rules allow only the observation of $j=0$ and $j=2$ modes. Duval [6] demonstrated that torsional modes cannot be observed by Raman spectroscopy. Consequently, only the spheroidal modes $n=1$, $j=0$ and $n=1, j=2$ are observable by Raman spectroscopy. The mode $j=0$ is Raman active within the parallel polarization but forbidden in perpendicular polarization. The mode $j=2$ is Raman active in both polarizations.

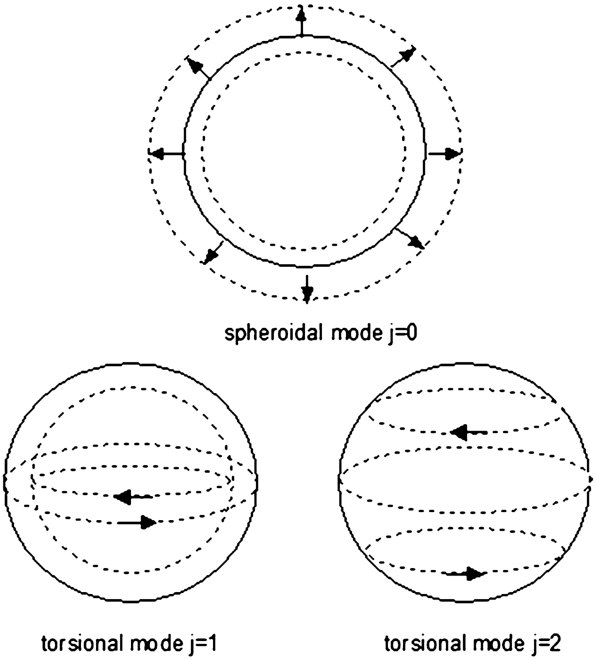

Fig. 13.2 Vibrational modes of free sphere

13.2.2 Ritcher's Theory

About 25 years ago, asymmetric one-phonon Raman bands were first observed in small particles. The Gaussian phonon confinement model was proposed in [7]. Let us briefly discuss this model. The RS intensity $I(\omega, L)$ for a particle of diameter L at photon frequency shift ω with respect to the laser frequency is [4, 8, 9].

$$I(\omega,d) = I_0 \int_0^1 2\pi q dq \frac{|C(q)|^2}{[\omega - \omega_0(q,T)]^2 + (\Gamma(T)/2)^2}. \tag{13.1}$$

We use a spherical Brillouin zone and consider the phonon dispersion curve to be isotropic. For a spherical nanoparticle, the Gaussian weighting function is

$$|C(0,q)|^2 = C_0 \exp\left\{-\frac{1}{2}\left(\frac{qL}{a_0}\right)^2\right\}, \tag{13.2}$$

where a_0 is the lattice constant of the crystal. Equation 13.1 is then a sum of weighted Lorentzian contributions to the Raman band from each bulk phonon of wavevector $\boldsymbol{q}$. Note that both the phonon frequency $\omega_0(q)$ and the phonon lifetime $1/\Gamma$ in Eq. 13.1

Table 13.1 Cation–oxygen internuclear distance r_{M-O} for cation coordination numbers 4–12

	$r_{M\text{-}O}$ (Å)				
Cation	4	6	8	10	12
Li	1.99	2.16	2.32	–	–
Na	2.39	2.42	2.58	–	–
K	2.77	2.78	2.91	2.99	3.04

are given an explicit temperature (*T*) dependence. This will be shown to be important later, when we shall consider inhomogeneous laser heating.

So far, we have considered only bulk vibration modes, but surface modes also contribute, especially when the particles are small, since the surface-over-volume ratio becomes larger. Vibrational surface modes are responsible for very-low-frequency Raman bands, which have been observed and investigated as a function of the size of spherical spinel microcrystallites in a nucleated cordierite glass [10]. The frequency of the maximum of intensity of these Raman bands is proportional to the inverse diameter of the particles.

13.2.3 Lattice Dynamics

All the materials used as active elements of positive electrodes for Li-ion batteries contain oxygen in their chemical formula. The cation–oxygen distance r_{M-O} and the reduced mass of vibration μ depend on the specific coordination geometry. The values of ionic radii were tabulated by Shannon and are used to calculate the cation–oxygen distance, $r_{M-O}=r_M+r_O$, where r_M is the cation radius and $r_O=1.40$Å. The results (Table 13.1) show an increase in r_{M-O} upon increasing the coordination number and are in good agreement with those obtained from crystallographic studies.

The reduced mass of cation vibrations should now be determined. In general, the reduced mass is given by $\mu=G_{ij}^{-1}$, where G_{ij} is the appropriate element of the symmetry-factored *G* matrix in the Wilson's matrix approach. *G* matrix elements have been determined for different point-group symmetries, and thus the reduced mass for tetrahedral (μ_4), octahedral (μ_6), and cubic (μ_8) symmetries can be obtained:

$$\mu_4=\frac{3m_Cm_A}{3m_C+4m_A}, \tag{13.3}$$

$$\mu_6=\frac{m_Cm_A}{m_C+2m_A}, \tag{13.4}$$

$$\mu_8=\frac{3m_Cm_A}{3m_C+8m_A}, \tag{13.5}$$

where m_C and m_A are the mass of cation and oxygen, respectively. Equations 13.3,13.4, and 13.5 has been employed by Exarhos et al. [11] to calculate the reduced mass of cation vibrations in alkali-metal and alkaline-earth metaphosphate glasses.

From the expression of the vibrational frequency of the symmetrical stretching mode, the vibrational force constant, F, is given by

$$F = 4\pi^2 c^2 \mu \nu^2, \tag{13.6}$$

where c is the light velocity and ν the wavenumber.

The cation vibration frequencies and their compositional dependence, obtained from IR measurements, have been used to elucidate the role of the alkali-metal cation on the LiMO$_2$ structure [12]. The dependence of the cation motion frequency on the symmetry and size of the anionic network site has been studied using a simplified type of the Born–Mayer potential to describe the cation-network interactions. Assuming then that each alkali-metal cation is surrounded by six nearest oxygen neighbors arranged in an octahedral type of configuration, it was shown that the following expression holds for the square of the cation motion wavenumber ν:

$$\nu^2 = \left(\frac{\alpha}{48\pi^2 c^2 \varepsilon_0} \right) \frac{q_C q_A}{\mu r_{M-O}^3} \tag{13.7}$$

where q_C and q_A are the charge of the cation and anionic sites, respectively, μ is the reduced mass of vibration, and $r_{M\text{-}O}$ is the equilibrium cation–oxygen distance. The various constants involved are as follows: ε_0 is the permittivity of the free space and α is a pseudo-Madelung constant. The Madelung constant depending on the site symmetry is $\alpha = 1.638$ for the zinc blend structure ($N = 4$), $\alpha = 1.747$ for the sodium chloride structure ($N = 6$), and $\alpha = 1.762$ for the cesium chloride structure ($N = 8$). Thus, with the value $\alpha = 1.747$ appropriate to the octahedral environment in Eq. 13.7, the force constant in Eq. 13.6 can be related to the average M-O bond length by the relation

$$F = \frac{17}{r_{M-O}^3}, \tag{13.8}$$

with F expressed in N/cm and r_{M-O} in Å.

13.2.4 Curve Fitting

A classic fitting procedure of Raman spectra was done using the GRAM/386 software from Thermo Galactic Corporation (Salem, New Hamshire, USA). The curve fitting is based on the original algorithm of nonlinear peak fitting described by Marquardt and known as the Levenberg-Marquardt algorithm [13]. The curve fitting of complex band profiles, although one might expect this to be a well-known procedure, often does not seem to be applied in an appropriate, i.e. scientifically justifiable, way. Most strikingly, the calculation is done assuming a linear baseline for the

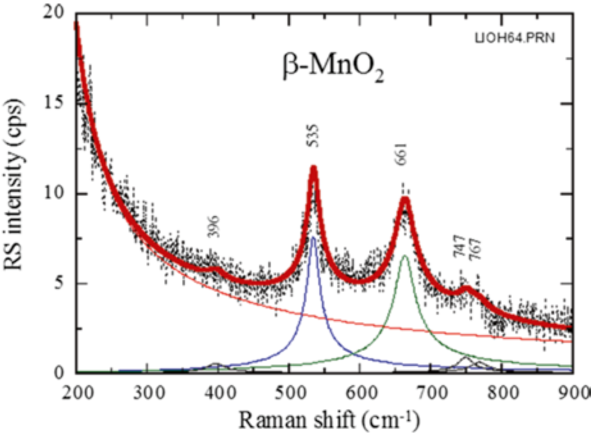

Fig. 13.3 Fitting of Raman spectrum of β-MnO$_2$ using Lorentzian-shape bands. *Thin red line*: baseline; *thick red line*: fit of data with Lorentzian profiles reported in other colors

spectra and assuming that all the Raman lines introduced in the fit have a mixed Gauss–Lorentz line shape of the form

$$S(\nu) = \alpha G(\nu) + (1-\alpha) L(\nu). \tag{13.9}$$

To appreciate this, let us start the line profile of an individual Raman band that is Lorentzian in nature, with the Lorentz line profile given by

$$L(\nu) = \mathrm{L}_0 \frac{\nu_L^2}{(\nu-\nu_0)^2 + \nu_L^2}. \tag{13.10}$$

There may be Gaussian line broadening due to instrumental effects or to sample characteristics. The Gaussian line profile is given by

$$G(\nu) = G_0 \exp\left[-\left(\frac{\nu-\nu_0}{w_G}\right)^2\right]. \tag{13.11}$$

Broadening with a Gaussian line profile implies that one must multiply the Lorentzian profile by a Gaussian profile, leading to a so-called Voigt profile, which is a convolution of a Gaussian and a Lorentzian profile [14].

As an example, we present the curve fitting of Raman bands for the MnO$_2$ sample (Fig. 13.3). It is accomplished by selection of the spectral range 200–900 cm^{-1}. After determination of the baseline (nonlinear in this case), the individual Raman band was synthesized using the Lorentzian line profile, the broadening of which is due to sample characteristics, i.e., disordered structure. The vibration modes corresponding to the five bands detected in the spectrum have been identified [15].

13.3 Vibrational Features of Nanoparticles: Anode Materials

13.3.1 Nanocarbons

Raman spectroscopy is a sensitive method for identifying different forms of carbon [16–19] and characterizing structural perfection and ordering in carbon, graphite, and carbon fibers [20–23]. It is also a nondestructive technique for monitoring stress and strain in graphite and carbon fibers [21, 23] and carbon-containing SiC fibers produced by polymer precursors [24].

The Raman spectrum is characterized by two bands: the D-band, and the G-band at higher frequency, as it can be seen in Figure 13.4. The position, width, and intensity of both carbon bands are sensitive to the disorder in the carbon structure. Any difference in the Raman band shape of both carbon bands reflects changes in the microstructure of carbon. It is therefore important to know the curve-fitting procedures used when comparing band positions and bandwidths. Since the carbon Raman bands from the carbon coating are overlapping and rather broad, the determination of band position and bandwidth could be affected by the curve-fitting procedure used, such as the number of bands chosen and particular function used to fit the band. Due to the asymmetrical nature of the G-band with tails toward lower wavenumbers, it is often necessary to add more bands to best fit the whole spectrum. The carbon spectrum has been fit in several ways: a Lorentzian for the D-band and two Gaussians at approximately 1,500 and 1,600 cm^{-1} for the asymmetrical G-band [25], while others [16, 17] have tried a Lorentzian fit for the D-band and an asymmetrical Breit–Wigner–Fano (BWF) fit for the G-band. The BWF profile is defined as

$$I(\omega) = I_0 \frac{\left[1+(\omega-\omega_{BWF})/q\Gamma\right]^2}{1+[\omega-\omega_{BWF})/q\Gamma]^2}, \tag{13.12}$$

where 1/q is a parameter that measures the phonon-plasmon coupling, i.e. the interaction between the phonon and the collective excitations of the electron gas in a metal, and Γ is the damping factor. This profile is thus justified only in the case of the highly conductive form of carbon, i.e., graphite [26], but not in the case of a carbon deposit on particles used as active elements of electrodes, which is ill-crystallized or amorphous coke, a variety of carbon that is less conductive than graphite [27], as will be seen in Sect. 13.4. In the present study we have chosen to fit the D- and G-bands separately using a Lorentzian function on a linear sloping baseline, consistent with previous studies [21, 28]. It has been shown that the D-band grows in intensity with increasing disorder or decreasing crystal size, while the ratio of its intensity to that of the G-band, I_D/I_G, is inversely proportional to the average in-plane crystallite size (L_α) for disordered graphite in the range $2 < L_a < 300$nm [18, 29]. I_D/I_G can be expressed as follows:

$$\frac{I_D}{I_G} = \frac{C(\lambda)}{L_\alpha}, \tag{13.13}$$

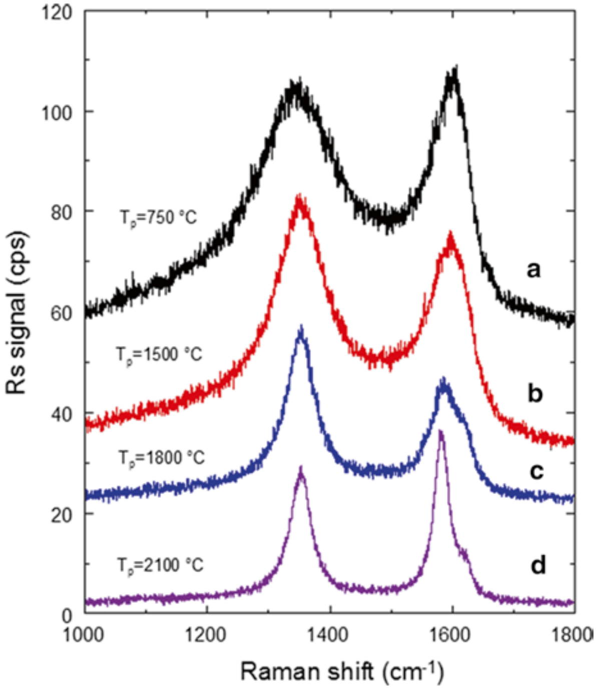

Fig. 13.4 Raman spectra of carbon synthesized at various pyrolysis temperatures, T_p, showing the shape evolution of the D- and G-bands

where $C(k)$ is 4.4 nm for incident laser wavelengths of 488 and 514 nm [29] and 5.8 nm for an incident laser of 633 nm [28]. Figure 13.4 displays the Raman spectra of carbon synthesized at various pyrolysis temperatures, T_p, showing the shape evolution of the D- and G-bands. The intensity ratio of the spectrum of carbon synthesized at $T_p = 750$ °C indicates that the carbon has a typical crystal size of approximately 10 nm. This is consistent with other microstructural investigations such as transmission electron microscopy (TEM) [30].

13.3.2 Nanosilicon

Silicon is a promising candidate for negative electrodes in lithium-ion batteries due to its large theoretical energy density of approximately 4,200 mAh/g, ten times higher than graphite (372 mAh/g), and relatively low working potential (approximately 0.5 V vs. Li/Li$^+$). However, the pulverization of silicon caused by volume expansion with lithium-ion insertion results in rapid capacity fading with cycling. A number of different nanophase forms of silicon show promise in addressing this problem, including

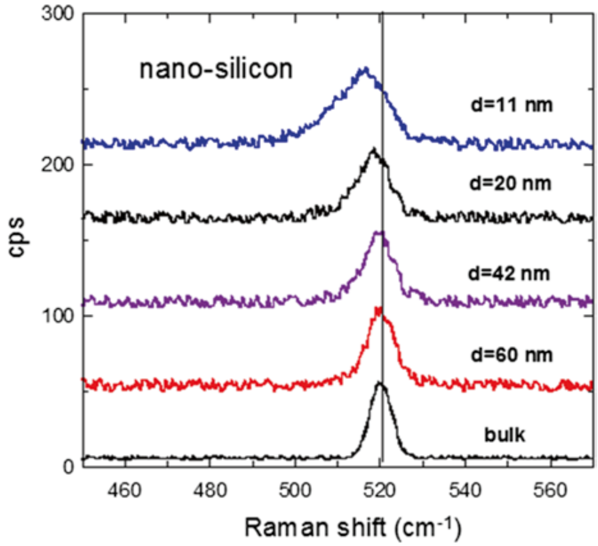

Fig. 13.5 Experimental micro-Raman scattering spectra of Si nanoparticles recorded using laser line $\lambda_0 = 514.5$ nm. The evolution of the first-order 520 cm^{-1} Raman peak of the nanoparticles is compared with the spectrum of bulk Si<001>

nanocrystals, nanocomposites with either carbon or other phases inactive to lithium, nanoporous materials [31], nanowires [32], bundled Si nanotubes, and thin films.

Figure 13.5 shows the micro-Raman experiments of Si nanoparticles. The line shape of the 520 cm^{-1} one-phonon band is presented as a function of the particle size. As expected, comparison of the Raman spectrum of bulk silicon single-crystal with those of nanoparticles leads to a small downshift of the silicon Raman peak at approximately 520 cm^{-1} and asymmetric broadening toward lower wavenumbers. Thus, phonon confinement is observed in the case of silicon nanoparticles [33]. We can explain the complex changes using Richter's model. The phonon quantum confinement effect causing relaxation of the Raman selection rule $\boldsymbol{q} = 0$ allows participation of phonons away from the Brillouin-zone center, i.e., at the U point. Note that the quantum confinement effect is observable effectively only for structures with at least one of the three main dimensions smaller than approximately 20 nm [34, 35]. When Si nanoparticles formed in the present study were large in diameter ($L \geq 40$ nm), no significant downshift could be observed. It is also clear (Fig. 13.5) that an $L = 42$ nm nanoparticle exhibits a very weak signature of phonon confinement, i.e., the line shape is almost Lorentzian. Finally, the one-phonon Raman peaks broadened and little asymmetry is observed at 517 cm^{-1} full width at half maximum (FWHM) of 12 cm^{-1} for nanoparticles 11 nm in diameter. Further, the first-order Raman intensity has a similar magnitude compared to that of bulk silicon, as shown in Fig. 13.5.

13.4 Carbon Deposit onto Particles

Since the discovery of Goodenough's group [36], the phospho-olivine $LiFePO_4$ (LFP) is considered as a potential positive electrode material for lithium-ion batteries, but its low electrical conductivity requires the deposit of a conductive layer (carbonaceous film) on the surface of the particles. This was achieved for the first time by Armand'group [37] by mixing LFP powders with sugar solution. The aim of this section is to characterize the carbon thin film surrounding electrode particles, i.e., the coating deposited at the surface of $LiFePO_4$ samples, in order to investigate the effect of carbon on the structural and electrochemical properties of $LiFePO_4$ [38].

The main difference between Raman spectra becomes apparent at larger wave numbers than those of the Raman peaks associated to the vibrations of $LiFePO_4$. Two broad lines at 1,345 and 1,583 cm^{-1} are evidenced in the carbon-coated sample only, as can be seen in Fig. 13.6. These broad lines are a fingerprint of amorphous carbon films. Since they constitute protective optical or tribological coatings [39], a tremendous amount of work has been devoted to amorphous carbon films deposited by a wide variety of methods; this work is reviewed and referenced; see for instance Kostecki et al. [40]. These different methods affect both local bonding and

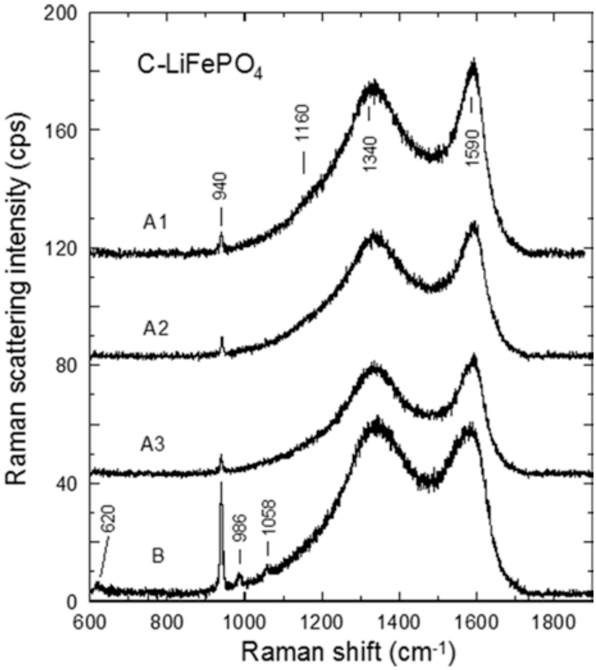

Fig. 13.6 Raman spectrum of carbon-coated $LiFePO_4$ sample, recorded using 514.5 nm laser line. Symmetric stretching mode of $(PO_4)^{3-}$ anions is observed at 940 cm^{-1}

intermediate-range order, so that they lead to a wide variety of films, including amorphous diamond, hydrogenated "diamondlike" carbon, and plasma polymers [41]. All these films have in common the existence of these two broad lines in the Raman spectra, derived from the corresponding features in the spectrum of graphite. The structure at 1,583 cm^{-1} mainly corresponds to the G-line associated to the Raman-active, E_{2g}-zone-center mode of crystalline graphite. The structure at 1,345 cm^{-1} mainly corresponds to the D-line associated to the disorder-allowed, zone-edge modes of graphite. The exact position of the structures in amorphous films depends on the probe laser wavelength [42–45], so that a quantitative comparison of spectra in the literature is possible only between experiments using the same wavelength. Tamor and Vassell [44] compared the Raman spectra of nearly 100 amorphous carbon films obtained with the same probe laser wavelength (argon line) as the one we have chosen. We have also paid attention to the fact that all the other Raman spectra to which we refer hereunder for direct comparison, including those obtained for carbon-coated LiFePO$_4$, were also measured with this probe laser wavelength [27].

First of all, we note that the Raman spectra of hydrogen-free carbon films can be distinguished from those of hydrogenated films by an additional broad feature centered at 600 cm^{-1} [44]. Since this structure never exists in hydrogenated carbon and always exists in hydrogen-free films, this criterion is considered to be robust [45]. In the present case, this structure is not observed. Therefore, the carbon is hydrogenated, which is actually not surprising since the preparation process involved different organic additives. As we shall see, however, the amount of hydrogen is only small. Second, the spectrum is characteristic of amorphous conductive carbon, meaning that the carbon atoms are essentially three-coordinated and bound by sp^2 type hybrid orbitals, in opposition to diamondlike carbon [46]. This result was actually expected since graphitic carbon is the only carbon type that can be conductive, and the carbon coating was found to be efficient at increasing the electrical conductivity in our material. We report subsequently a more complete analysis of the D- and G-bands since they have been recognized as predictive of both structural and physical properties [45]. In particular, a comprehensive study to relate the D- and G-features in the Raman spectrum to the structure of disordered graphitic films has been reported [18], while the relation to physical properties was given by Yoshikawa et al. [45].

The analysis of the D- and G-lines in such films is always done by fitting the Raman curves in the region from 1,000 to 2,000 cm^{-1} with Gaussians:

$$I(\omega) = \sum_i \Psi_i \exp\left[-4\ln(2)\left(\frac{\omega-\omega_i}{\Gamma_i}\right)^2\right] \tag{13.14}$$

where ψ_i is the intensity of the ith mode of frequency ω_i and phonon lifetime Γ_i. The number of Gaussians varies from two to four (Sect. 13.2). In our case, we found that the deconvolution of Raman spectra with two Gaussians (one for the D-line, one for the G-line) did not give good results, and four Gaussians were necessary to account

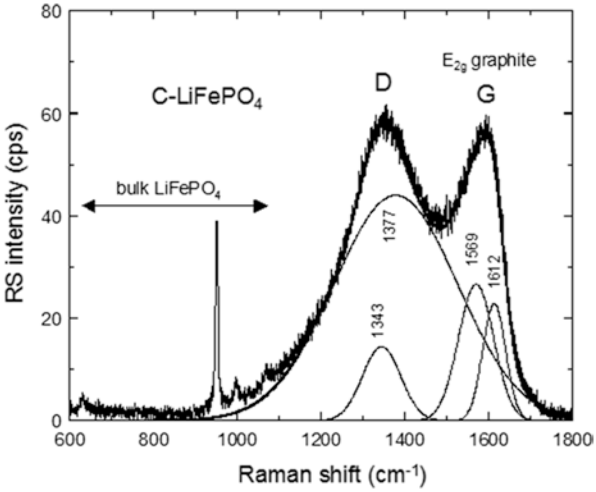

Fig. 13.7 Fit (*thick line*) showing deconvolution of Raman spectrum by Gaussians (*thin lines*, identified by their position) of the *D* and *G* carbon structures of the Raman spectrum of the carbon-coated LiFePO$_4$ sample

Table 13.2 Parameters of four Gaussians that fit G- and D-lines of Raman spectra for C-LiFePO$_4$ samples

		D-band				G-Band			
		Mode ν_1		Mode ν_2		Mode ν_3		Mode ν_4	
Sample	Particle size (μm)	ω(cm)$^{-1}$	FWHM	ω (cm)$^{-1}$	FWHM	ω (cm)$^{-1}$	Fwhm	ω (cm)$^{-1}$	FWHM
A1	3	1,328.9	97.4	1,350.2	347.4	1,571.8	115.0	1,594.1	54.6
A2	7	1,338.9	131.2	1,310.6	345.6	1,539.0	168.5	1,592.2	64.3
A3	15	1,332.5	100.1	1,350.6	346.9	1,571.8	119.6	1,595.5	56.0
B	10	1,343.7	107.4	1,377.7	347.6	1,569.4	99.4	1,612.7	64.6

for the Raman spectra. The result of this fit is shown in Fig. 13.7, and values are summarized in Table 13.2. The Gaussians are centered at 1,344, 1,378, 1,569, and 1,612 cm^{-1}. These lines compare well with the corresponding lines at 1,344, 1,367, 1,591, and 1,622 cm^{-1}, respectively, found using the same fitting procedure for pyrolyzed photoresists [40] and have, then, the same origin. The band at 1,569 cm^{-1} can be assigned to the E_g mode of graphite, while the very broad dominant band centered at 1,378 cm^{-1}, which extends over the entire spectral range of carbon vibrations, is the disorder-induced peak characteristic of highly defective graphite [47]. If only two Gaussians are used in the fitting procedure, then those are the only structures identified. Among the two extra structures identified in the fit of the spectra by four Gaussians, the band at 1,612 cm^{-1} is typical for severely disordered carbonaceous materials [46, 48]. The origin of the other line at 1,344 cm^{-1} is more questionable. Such a line has been observed in the Raman spectra of polyparaphenylene (PPP)-based carbon prepared at low heat-treatment temperatures below 750 °C [49]. For this PPP-based carbon, this line was attributed to a quinoidlike interring stretching mode due to a contraction in the interring bond length as the PPP chains are converted into graphitic ribbons, or to a “bridging” of the aromatic rings along the chain by more than one C-C bond [49]. The initial idea that this line was related somehow to the nature of the initial polymer derived from the fact that it is not observed in PPP-based carbon films heated at higher temperatures ($T > 750$ °C), which suggests the reminiscence of some PPP domains at lower temperature. However, the fact that the same peak is observed in carbon films prepared by pyrolyzed photoresists [40] and now in our C-$LiFePO_4$ shows that it is not related to the existence of PPP and should be related to some aromatic rings preferentially formed, irrespective of the original polymer, in the course of the conversion of the carbon into disordered conductive carbon. The fact that the original polymer is unimportant is also evidenced by the fact that the peak has been observed in many pyrolyzed photoresists, irrespective of the pyrolysis temperature, which could be as high as 1,000 °C [40].

Let us now analyze the other parameter of interest for characterizing a carbon film, namely, the intensity of the Raman lines. The ratios of the Raman intensities, defined as the integral of the Gaussians in Fig. 13.7, are $I_{1343.7}/I_{1377} = 0.102$ and $I_{1569}/I_{1612} = 1.789$. If we compare these intensities with the values determined for pyrolyzed photoresists, we find that the carbon coating of $LiFePO_4$ has the Raman spectrum of a carbon film deposited on silicon wafers by spin coating and then pyrolyzed at a temperature in the range 800–860 °C. The remarkable result is that our carbon film in the present case was obtained by heating at 700 °C only. This temperature difference is critical for the electrical conductivity of the carbon film since the sheet resistance of a pyrolyzed carbon sheet is highly resistive when the carbon film is prepared at a pyrolysis temperature of $T_p = 700$ °C; the resistivity decreases dramatically for higher pyrolysis temperatures to reach a sheet resistivity of 10 Ω per square at $T_p = 1{,}000$ °C. We can then expect, on the basis of the Raman spectra, that the conductivity of the carbon in the carbon-coated $LiFePO_4$ will be comparable to that of the carbon deposited by pyrolysis at 850 °C, which means reasonably good. This explains the successful increase in the electrical conductivity that has been reported in the literature for carbon-coated $LiFePO_4$. Incidentally, it shows that if the efficiency of the carbon-coating process in $LiFePO_4$ had not been improved with respect to the pyrolysis technique, the result would have been a total failure because it is not possible to heat $LiFePO_4$ above 800 °C without damaging the material, resulting in the growth of inclusions of various chemical compositions mentioned earlier in this work.

The width of the G-line at 1,569 cm^{-1} is 99.3 cm^{-1}, which is characteristic of hydrogen-free (a-C) carbon layers and markedly larger than the width of this line in hydrogenated amorphous carbon (a-C:H) [45]. This gives evidence that, although some hydrogen is in the carbon deposited on $LiFePO_4$ for the reason already mentioned, the H/C ratio is very small. This is actually consistent with the fact that the dramatic increase in the electrical conductivity after pyrolysis at temperatures above 700 °C is due to a decrease in the H/C ratio [40]. Since the Raman spectrum is that of pyrolyzed carbon obtained at a significantly higher temperature of 800–860 °C, the H/C ratio must be small indeed. For the same reason, we expect the hardness of the carbon deposit to be comparable to that of a-C films. However, the carbon films investigated in the literature are thick, so that the hardness is an intrinsic property that does not depend on the substrate. We have already noticed that the average thickness of the deposit is 3 nm. This thickness is not large enough to guarantee that the adherence on the $LiFePO_4$ particles will not quantitatively affect the hardness of the a-C film since the strain interactions are long range, but it is large enough to insure that the order of magnitude of the hardness is unaffected. Although the hardness of the a-C:H films increases from 0 up to 20 GPa when the G-line width increases from 50 to 80 cm^{-1}, the hardness of an a-C film with a G-line width of 100 cm^{-1} is right in the middle, namely, 10 GPa [45]. This hardness can be qualified as small. For instance, a hardness up to 80 GPa has been reported for diamond-like i-C carbon films. The small hardness of the carbon deposited on the $LiFePO_4$ is actually expected, especially as the substrate on which the carbon is deposited is not flat, as in the case of silicon wafers, but is the bent surface of nanoparticles. We can even consider that this a-C structure chosen by the carbon is an example of self-adaptation to allow for an adhesion on such a surface, which would be impossible with a strong hardness.

The D/G intensity ratio is used in the literature to determine the size of the graphite particles in polycrystallite carbon [49]. Some extension has often been made to use the same relation to determine the correlation length of the graphitic order. This is, however, a confusion that has already been outlined [46]. The D/G intensity ratio gives the size of particles in the absence of any disorder and should not be confused with the loss of long-range order in amorphous materials. In disordered carbon, information on the disorder is provided by the optical gap, according to the Robertson and O’Reilly law, which allows for an estimate of the number of carbon rings inside a local cluster [50]. In particular, the simultaneous study of both the optical gaps and the Raman D/G ratio has revealed contradictions that show that the D/G intensity ratio is determined by factors other than the graphitic cluster size in amorphous carbon [43, 51, 52]. This point is sometimes missed, and we can find recent analyses on C-$LiFePO_4$ that postulate that a decreasing D/G intensity ratio is related to carbon disorder. In this same analysis, it is postulated that a decreasing D/G intensity also means a decreasing sp^3/sp^2 ratio. This is not justified either, and it is not possible to evaluate the content of sp^2 and sp^3 coordinated carbon in a material that is dominantly graphitic. This is because the intrinsic Raman intensity of the graphite spectrum is 50 times that of the diamond spectrum. Therefore, Raman spectroscopy is a sensitive tool that can be used to detect residual sp^2 bonds in diamond, but it does not provide a reliable test of the presence of sp^3 bonds in a dominantly graphitic carbon [46]. In the carbon-coated samples investigated in this work, we did not investigate the optical gaps, but we note that the width (not the intensity) of the Raman lines is related to the degree of carbon disorder, which shows that in the present case, the carbon is amorphous. We do not know the sp^3/sp^2

ratio, but we know that the amount of sp^3 is small. In addition, this is always the case for disordered carbon. Even in diamondlike carbon films, the percentage of tetrahedral carbon is small [40]. In the present case, however, the percentage should be even smaller than in most cases because the positions of the D- and G-lines are quite close to those of graphite.

The bending of a graphite sheet is expected to induce some sp^3 character in the sp^2 bonds, which are planar. Therefore, the small amount of sp^3 gives evidence that the bending is small, i.e., that the radius of curvature is large at the scale of the bond length. This is consistent with the Raman spectra, which show that carbon coats secondary particles and does not penetrate into $LiFePO_4$ particles.

Analysis of the Raman spectrum yielded an insight into the electrical conductivity of the carbon layer, with the result that a sintering temperature of 750 °C was sufficient to obtain a carbon layer with a good electrical conductivity. The next question for industrial applications is whether it is possible to decrease the sintering temperature without damaging this conductivity since heating costs money. Unfortunately, we have found that a decrease in this temperature below 700 °C results in a dramatic change in the Raman spectrum, which is the signature of carbon that has become insulating [53]. This result is not surprising since we have shown that it is already very lucky that a conducting carbon coat could be obtained at temperatures as small as 700 °C. Other precursors of the carbon coating have been explored [54]. So far, however, they have not made possible a decrease in the sintering temperature.

This conclusion has consequences when the hydrothermal route is chosen to prepare the samples. With this route, the synthesis of $LiFePO_4$ can be performed at much lower temperatures, namely, 175 °C [55–57]. However, the need for an electrical contact between the particles allows a choice between two procedures only. In one of them, C-$LiFePO_4$ is made in one step at a low temperature. In that case, one must use conductive carbon nanotubes in addition to the precursors of $LiFePO_4$ to obtain the appropriate electrical contact between the particles via the conductive nanotubes [55]. The other procedure is to make the $LiFePO_4$ first by a hydrothermal process and then to reheat the particles at 700–750 °C in the presence of the carbon precursor. Because the price of carbon nanotubes is very high, the first process is for use in the laboratory only.

13.5 Raman Features of Nano-Sized Particles: Cathode Materials

13.5.1 $LiNi_{1-y}Co_yO_2$ Mixed Phases

The $LiMO_2$ oxides (M = Ni, Cr, Co) adopt the α-$NaFeO_2$-type layered structure that belongs to the crystallographic $R\overline{3}m$ space group with the corresponding spectroscopic D_{3d}^5 space group. This structure derives from the NaCl structure, with a

Table 13.3 Factor group analysis for LiMO$_2$ structure (space group D_{3d}^5)

Atom	Wyckoff position	Site group	Irreducible representation
M	3a	D_{3d}	$A_{2u} \oplus E_u$
Li$_{\text{octa}}$	3b	D_{3d}	$A_{2u} \oplus E_u$
O	6c	C_{2h}	$A_{1g} \oplus E_g \oplus A_{2u} \oplus E_u$
Total			$A_{1g} \oplus E_g \oplus 3A_{2u} \oplus 3E_u$
Acoustic			$A_{2u} \oplus E_u$
Raman			$A_{1g} \oplus E_g$
Infrared			$2A_{2u} \oplus 2E_u$

stacking of Li ions between adjacent MO$_2$ slabs. The individual coordination octahedra are face sharing. They show a higher operating voltage than conventional 3-V systems; a relationship between the level of operating voltage of transition metal oxides and their d-electron character has been recognized. The M cations are located in octahedral 3a (000) sites, and oxygen anions are in a cubic close packing, occupying the 6c (00z, 00z) sites. Li cations reside at Wyckoff 3b (001/2) sites. The transition metals and lithium ions occupy the alternating (111) planes. The site symmetry for D_{3d}^5 contains both the IR- and Raman-active modes given by [58]

$$\mathbf{2D}_{3d}, C_{3v}(2), \mathbf{2C}_{2h}(\mathbf{3}), (6), C_s(6), C_1(12), \qquad (13.15)$$

where each site-group symbol is preceded by an integer indicating the number of distinct sites of each symmetry and is followed by the multiplicity in parentheses. The boldface type corresponds to a Wickoff position with the lowest eigensymmetry. By factor group analysis, one obtains an irreducible representation (Table 13.3).

Thus, LiMO$_2$ compounds exhibit A_{1g} and E_g modes, which are Raman active. Only the oxygen atoms vibrate in these modes, i.e., they correspond mainly to vibrations of oxygen cages. In the A_{1g} mode, the two oxygen atoms vibrate in the opposite direction parallel to the c-axis of LiMO$_2$, while they vibrate alternately in the opposite directions parallel to the Li and transition-metal planes in the E_g mode. As a general rule in a layered rock-salt structure, the high-frequency Raman band is assigned to the A_{1g} mode, while the low-frequency one is of the E_g species. Replacing Co with Ni does not change the space group. This was confirmed by the presence of the two Raman bands (A_{1g} and E_g modes) of the LiNi$_{1-y}$Co$_y$O$_2$ samples, although the intensities of these peaks are functions of composition and disorder in the cation sublattice.

The four IR-active modes $2A_{2u} \oplus 2E_u$ correspond to the stretching and bending modes of the intralayer chemical bonds MO$_6$ plus one species assigned to the Li-cage mode. This latter vibration occurs in the spectral range 240–280 cm^{-1}. Thus, only FTIR spectroscopy is a tool for investigating the local environment of Li$^+$ cations.

The FTIR absorption spectra of LiNi$_{1-y}$Co$_y$O$_2$ powders (Fig. 13.8) display the predominance of the stretching modes and the IR resonant frequency of LiO$_6$

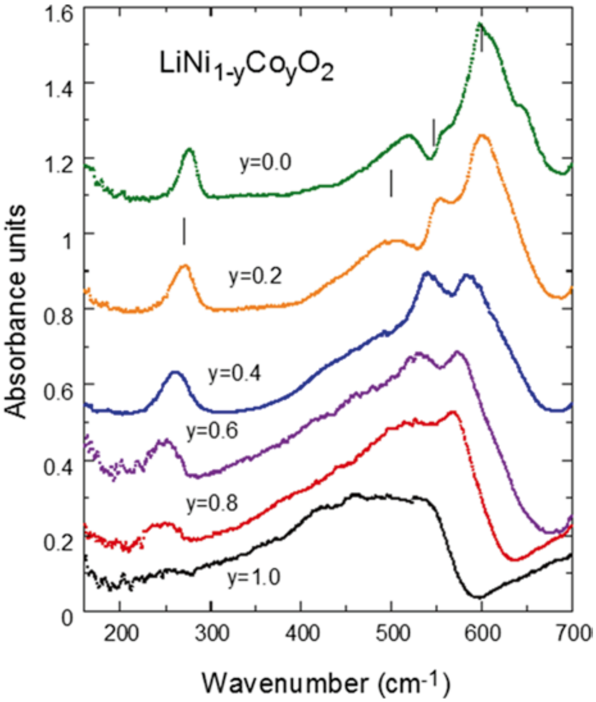

Fig. 13.8 FTIR absorption spectra of $LiNi_{1-y}Co_yO_2$ powders synthesized by sol–gel method

octahedra located between 269 and 234 cm^{-1}. The changes in the vibrational frequencies are well related to those observed by X-ray diffraction [59]. Information on the oxide structure, especially on the distribution of the transition metal in the (Ni, Co)O_2 slabs, is also obtained from the shape of FTIR spectra owing to the predominance of the stretching modes of (Co, Ni)O_6 octahedra at around 500–600 cm^{-1}.

The frequency shift of both the stretching and bending modes as a function of the cobalt substitution is due to the cationic disorder in the $(Ni_{1-y}Co_y)O_2$ slabs. The frequency shift of the LiO_6 mode has two origins: (1) the slight expansion of the interslab distance with increasing temperature and (2) the small mixing of Li-O stretching and O-M-O bending motion present in the low-wavenumber peak. Figure 13.9 shows the variation of the frequencies of the high-wavenumber IR modes with the Co content in $LiNi_{1-y}Co_yO_2$ oxides. One distinguishes a quasi-linear variation with y, which is the result of the one-mode behavior of the $LiNi_{1-y}Co_yO_2$ solid solution system. The evolution of the ν7-IR band due to the Li-O stretching mode shows the characteristic one-mode behavior with a slight deviation toward a low wavenumber for Ni-rich samples. This effect is attributed to the cationic mixing that appears for a high content of Ni substitution (y > 0.3).

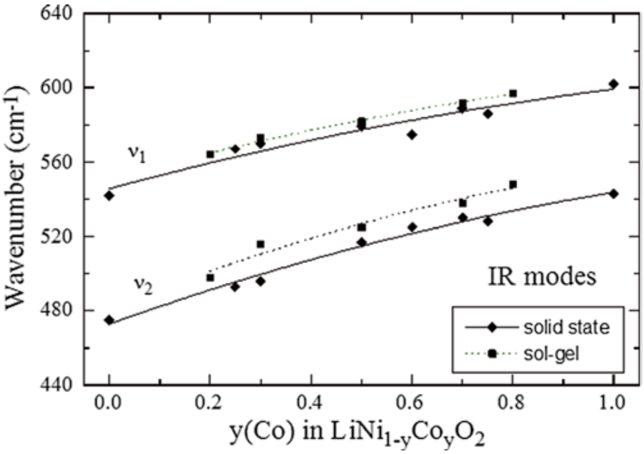

Fig. 13.9 Evolution of IR-mode frequencies as a function of composition in layered $LiCoO_2$-LiNiO2 solid solution

13.5.2 The Case of Al-Doped $LiCoO_2$

It has been shown that *sp*-elements such as aluminum are interesting dopants of $LiCoO_2$ cathode materials. Their principal role is in structural stabilization because the ionic radii of Al^{3+} and Co^{3+} in the octahedral coordination are very close. The fixed valence +3 of Al might also prevent the overcharge of $LiCoO_2$//Li cells [60, 61]. In addition, Myung et al. [62] have shown that $LiCo_{1-x}Al_xO_2$ electrodes present a lower initial discharge capacity, while the open-circuit voltage and chemical diffusion coefficient are enhanced with increasing Al content.

$LiCo_{0.95}Al_{0.05}O_2$ powders synthesized by the wet-chemical method assisted by succinic acid are particles with a hexagonal form. They are submicron sized in diameter with a homogeneous size distribution. The synthesis method used causes the powder sample to have high porosity and high specific surface area. As the doping amount of Al increases, we observe modifications of the Raman spectra; the particle size becomes smaller with better grain distribution (Fig. 13.10).

The marked decrease in the particle size of Al-doped oxides is then unequivocally correlated with the kinetics of grain formation using a wet-chemical synthesis assisted by succinic acid. Different possibilities can be considered: (1) conditions under which hydrolysis and condensation of the precursor species take place in a weak acidic medium (pH≈4.5), (2) fast kinetics of grain formation with the use of succinic acid, (3) limiting effect of Al for the growth of particles, (4) strong exothermic reaction during nitrate decomposition around 250 °C, and (5) effect due to the Al environment during reaction in solution. The homogeneous cation mixing of Li + Co + Al and Li in the initial emulsion favors the tendency of the grains to be small. Since electrochemical lithium intercalation and deintercalation are in general limited by the rate of diffusion, the aforementioned features are important since a smaller grain size enhances the lithium-ion mobility in the particles by reducing the ion diffusion pathway.

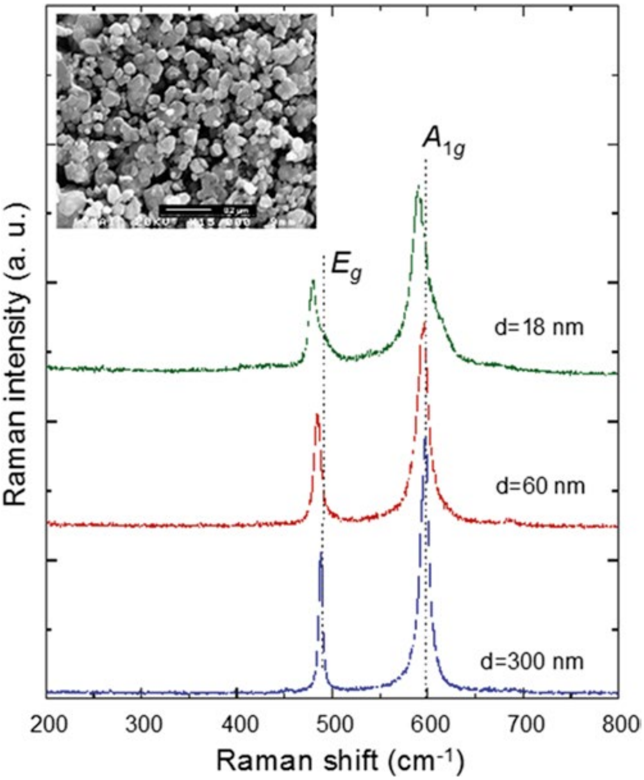

Fig. 13.10 Raman scattering spectra of $LiCo_{0.95}Al_{0.05}O_5$ nanoparticles

13.5.3 The Case of $LiNi_{1/3}Mn_{1/3}Co_{1/3}O_2$

Since the first report on the electrochemical properties of $LiNi_{1/3}Mn_{1/3}Co_{1/3}O_2$ (LNMCO) by Ohzuku's group in 2001, this material is now widely studied as an alternative 4-V material to replace $LiCoO_2$ for use in the next generation of Li batteries [63, 64]. In this section we investigate a series of $LiNi_{1/3}Mn_{1/3}Co_{1/3}O_2$ samples synthesized by the wet-chemical method assisted by tartaric acid as a chelating agent. Various acid-to-metal-ion ratios R were used to investigate the effect of this parameter on physical and electrochemical properties. We found that $LiNi_{1/3}Mn_{1/3}Co_{1/3}O_2$ sintered at 900 °C for 15 h with an acid-to-metal-ion ratio of $R = 2$ was the optimum condition for this synthesis. For this optimized sample, only 1.3 % of nickel ions occupied the 3*b* Wyckoff site of the lithium-ion sublattice. The electrochemical cell delivered an initial discharge capacity of 172 mAh/g in a cutoff voltage of 2.8–4.4 V, with a coulombic efficiency of 93.4 % [65].

LNMCO compounds have the same α-$NaFeO_2$ structure, $R\bar{3}m$ space group, and spectroscopic D_{3d}^{5} symmetry as the other materials already mentioned in this section, so the vibrational modes associated to each transition-metal ion are decomposed as

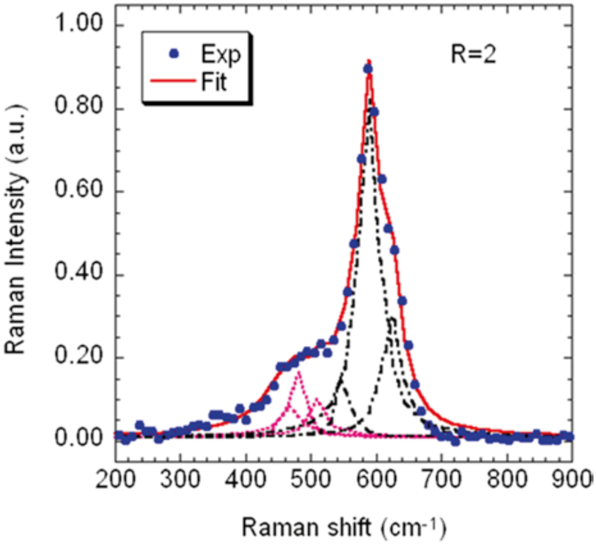

Fig. 13.11 Raman scattering spectra of LNMCO, $R=2$ sample. The decomposition of the peaks is shown as the *dotted and dashed* lines. The *thick line* over the raw data is the best fit obtained by decomposition of both the A_{1g} and E_g structures in three Lorentzian bands (*dotted and dashed curves*) corresponding to the vibrations of the three metal ions with the oxygen

shown in Table 13.3. Since the compounds have three different transition-metal cations, we expect $3A_{1g}$ and $3E_g$ Raman-active modes that overlap to give rise to the two broad A_{1g} and E_g structures shown in Fig. 13.11. The best fit to the Raman spectra have then been achieved, starting from a prescribed set of three individual bands of Lorentzian shape for the overlapping A_{1g} band profile and the same for the E_g band profile. Taking the $R=2$ sample as an example (Fig. 13.10), the E_g bands are centered at 467, 483, and 510 cm^{-1}, and the A_{1g} bands are centered at 547, 591, and 625 cm^{-1} for $M=$Ni, Co, and Mn, respectively. These positions compare well with the corresponding bands of $LiNiO_2$, $LiCoO_2$, and λ-$LiMn_2O_4$, respectively [3]. On the other hand, after normalization, the band intensity (integral of the Lorentzian individual band) of the Ni-O and O-Ni-O vibrations (ν_1 and ν_4, respectively) are smaller in the $R=4$ sample than in the $R=2$ sample. This feature is due to the fact that Ni(3*b*) cannot participate in the A_{1g} and E_g modes, and it gives evidence of the higher cation mixing between Li^+ and Ni^{2+} in the $R=4$ case. Note also that the widths of these ν_1 and ν_4 vibrations are larger in the $R=4$ case, which means that the lifetime of these phonons is shorter. This is further evidence of the larger Ni cationic disorder in this sample, in agreement with the structural analysis [65].

Fig. 13.12 Raman scattering spectra of Mn_3O_4 as a function of particle size

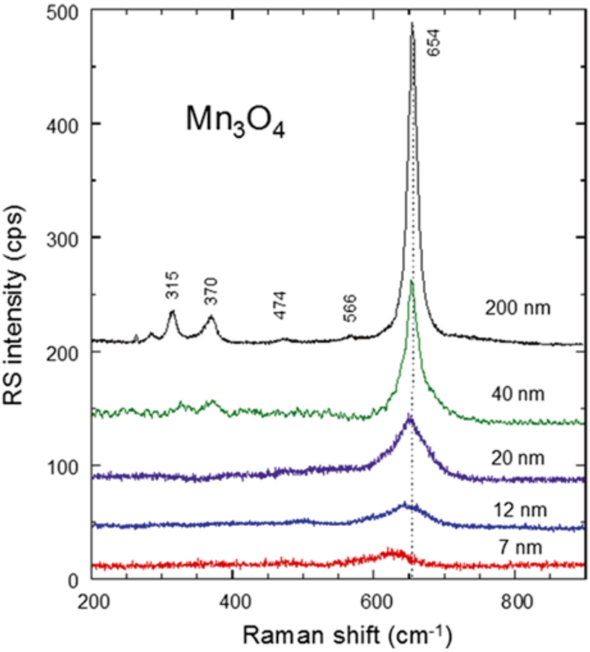

13.5.4 The Case of Mn_3O_4

Nanoparticles of hausmannite Mn_3O_4 with dimensions $7 \leq L \leq 200$ nm were synthesized by several methods. Folch et al. [66] reported a new approach to the synthesis and organization of Mn_3O_4 nanoparticles using the thermolysis of the magnetic cluster $[Mn_{12}O_{12}(C_2H_5COO)_{16}(H_2O)_3]$ linked to mesoporous silica functionalized with –COOH groups. A facile room-temperature synthesis was developed to prepare colloidal Mn_3O_4 nanoparticles (5–25 nm) by an ultrasonic-assisted method in the absence of any additional nucleation and surfactant [67]. Mn_3O_4 nanowires with diameters of 30–60 nm and lengths of up to more than 100 μm were synthesized by decomposing the precursor $MnCO_3$ nanoparticles in NaCl flux [68]. In this study, we adopted the sol–gel method using an aqueous solution 0.01 *M* $MnCl_2 \cdot 4H_2O$ mixed with an appropriate amount of ammonium chloride NH_4Cl. The pH value of the solution was adjusted with ammonia $NH_3 \cdot H_2O$ to 8.0 (Amdouni and Julien [69]).

The Raman spectra of the Mn_3O_4 nanoparticles prepared at 120 °C are shown in Fig. 13.12. The intense peak at 654 cm^{-1} and the two weak peaks at 370 and 315 cm^{-1} are in good agreement with the literature values for hausmannite [70]. The strong peak at 654 cm^{-1} in the Raman spectrum is characteristic of all spinel structures, such as Fe_3O_4 and $LiMn_2O_4$. This peak is assigned to the A_{1g} mode, which corresponds to the *M*-O (Mn–O here) breathing vibration. The results indicate that the Raman peak is asymmetric; it is broadened and red-shifted by 16 cm^{-1} compared

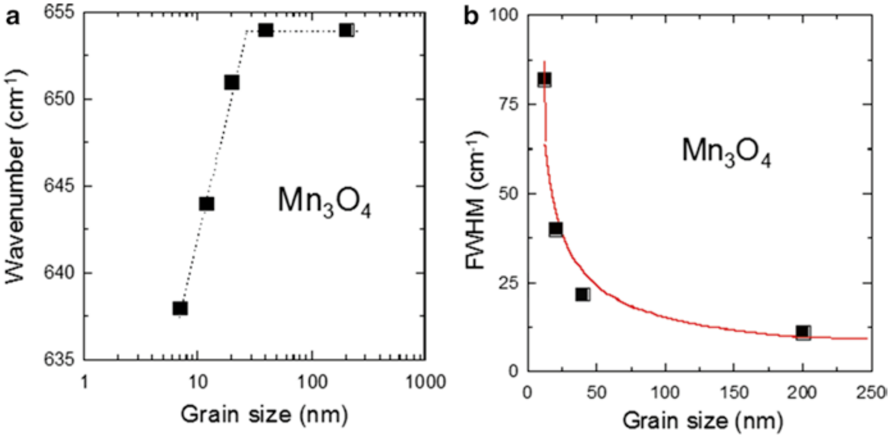

Fig. 13.13 Grain-size effects on frequency position (**a**) and full width at half maximum (**b**) of A_{1g} Raman-allowed mode of Mn_3O_4

with that of bulk Mn_3O_4 crystals. A rational explanation for the red shift and broadening of the Raman peak is discussed in detail according to the phonon confinement model [4]. Figures 13.13a, b show clearly that a blue shift and band broadening appear gradually for the Raman peaks of the nano-sized Mn_3O_4 when the mean size of the particles is reduced from 200 to 7 nm. However, as observed for silicon, the phonon confinement occurs only for particles smaller than 40 nm. The plot in Fig. 13.13a verifies the exponential dependence of the phonon shift on particle size.

13.6 Intrinsic Vibrational Modes of Nano-Sized $LiFePO_4$

The structural properties of microcrystalline $LiFePO_4$ prepared by hydrothermal synthesis were analyzed by FTIR and Raman spectroscopy. $LiFePO_4$ was prepared from $FePO_4(H_2O)_2$ and Li_2CO_3. The stoichiometric amount of precursors was thoroughly mixed together in isopropanol. After drying, the blend was heated at 700 °C in a reducing atmosphere. The high resolution transmission electron microscope (HRTEM) images of LFP materials showed polydispersed primary particles with a mean size of $\approx$90 nm, which is larger, by a factor of 3, than the average size of the monocrystallite grains deduced from the application of Scherrer's law on the XRD pattern. Therefore, the primary particles are polycrystallites of $LiFePO_4$ made of a few (three on average) monocrystallites of LFP. The carbon layer appears to be amorphous in nature.

13.6.1 Lattice Dynamics of Phospho-Olivine

A group theoretical analysis was carried out for the olivine-like structure, and Table 13.4 summarizes the details of the type and activity of the normal modes of a

Table 13.4 Factor group analysis for Li*M*PO$_4$ phospho-olivine structure (space group D_{2h}^{16})

	Number of modes						
Species	Li	*M*	P		PO$_4^{3-}$		Spectral activity
D_{2h}	C_i	C_s^{xz}	C_s^{xz}	N$_{\text{libr}}$	C_s^{xz}	Total	
A$_g$	–	2	2	1	6	11	α_{xx}, α_{yy}, α_{zz}
B$_{1g}$	–	1	1	2	3	7	α_{xy}
B$_{2g}$	–	2	2	1	6	11	α_{xz}
B$_{3g}$	–	1	1	2	3	7	α_{yz}
A$_u$	3	1	1	2	3	10	Inactive
B$_{1u}$	3	2	2	1	6	14	E//z
B$_{2u}$	3	1	1	2	3	10	E//y
B$_{3u}$	3	2	2	1	6	14	E//x

Acoustic modes $1B_{1u}+1B_{2u}+1B_{3u}$

Optical active modes $11A_g+7B_{1g}+11B_{2g}+7B_{3g}+13B_{1u}+9B_{2u}+13B_{3u}$

Li*M*PO$_4$ lattice. Olivine belongs to the spectroscopic group D_{2h}^{16}; the primitive cell is centrosymmetric with four formula units in the cell. Li, *M*, and P atoms are distributed at the 4*a*, 4*c*, and 4*c* positions (Wyckoff notation), respectively. Subtracting the three acoustic modes from the total number of vibrations ($N_{tot}=3n=84$), the optical modes are represented by

$$\Gamma = 11\text{A}_\text{g} + 7\text{B}_{1\text{g}} + 11\text{B}_{2\text{g}} + 7\text{B}_{3\text{g}} + 13\text{B}_{1\text{u}} + 9\text{B}_{2\text{u}} + 13\text{B}_{3\text{u}}, \qquad (13.16)$$

in which even (gerade) species are Raman-active and odd (ungerade) species are IR-active modes. This treatment was carried out by assuming the separation of the vibrations into internal $(PO_4)^{3-}$ and external (lattice) modes, the validity of this approximation being supported by the previous results [71, 72]. One interesting point is evidenced by the correlation method (Table 13.4): there is no Raman-active species in the irreducible representation related to the Li atoms located on 4*a* sites (C_i symmetry). In other words, the Li atoms are not allowed to move during Raman-active vibrations. This relates to the fact that these atoms are located on inversion centers of the crystal cell.

13.6.2 FTIR Spectroscopy

The FTIR features of LiFePO$_4$ were reported in earlier works [72, 73]. The FTIR spectrum of the LiFePO$_4$ nanopowders ($L=90$ nm) is shown in Fig. 13.14. As the structure of phospho-olivine is built from LiO$_6$ and FeO$_6$ octahedra linked to $(PO_4)^{3-}$ polyanions, the local cationic arrangement can be discussed with the aid of factor group analysis and a molecular vibration model [74]. It can be seen from Table 13.4 that the internal vibrations of LiFePO$_4$ can be derived from the fundamental

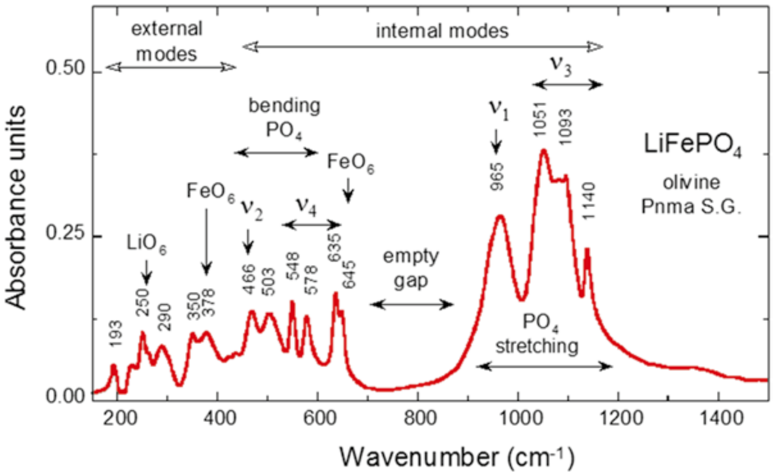

Fig. 13.14 FTIR spectrum of $LiFePO_4$

$(PO_4)^{3-}$ modes ν_1–ν_4, and that the stretching and bending mode regions are well separated from each other. As expected, the vibrational spectrum is dominated by the fundamental vibrations of the PO_4^{3-} polyanions, which are split into many components due to the correlation effect induced by the coupling of PO_4^{3-} with Fe-O units in the structure.

In the region of the internal modes of the phosphate anion, the high-wavenumber region 945–1,139 cm^{-1} corresponds to the stretching modes of the $(PO_4)^{3-}$ units. They involve symmetric and antisymmetric modes of the P-O bonds, at frequencies closely related to those of the free molecule, which explains why the frequencies of theses modes are the same in both samples. We identify the symmetric stretching mode at $\nu_1 = 946$ cm^{-1} and the triplets ν_3 in the regions 1,009–1,085 cm^{-1}. The low-wavenumber region 372–647 cm^{-1} corresponds to the bending modes (ν_2 and ν_4), the doublet ν_2 at 415–464 cm^{-1} and the multiplet ν_4 at 580–637 cm^{-1} involving O-P-O symmetric and antisymmetric modes, respectively. The vibrational mode implying Li^+ ions also occurs in this spectral domain. In particular, the line at 230 cm^{-1} corresponds to this same cage mode of the lithium ions that undergo translation vibrations inside the cage formed by the six nearest-neighbor oxygen atoms [75]. Note the empty gap between the stretching and bending modes, which reflects the well-crystallized and impurity-free material.

However, the modes in the carbon-free sample are significantly broader than those in the carbon-coated sample [76]. This broadening gives evidence of a decrease in the lifetime of the phonons, which reveals the existence of defects breaking the periodicity of the lattice sites. Different reasons can be invoked. First, the carbon precursor is an organic compound, and the hydrogen in it is a reducing agent that prevents the formation of impurities of Fe^{3+}-based materials, in particular γ-Fe_2O_3 impurities that have been detected by magnetic measurements. However, this

Fig. 13.15 Raman spectrum of $LiFePO_4$

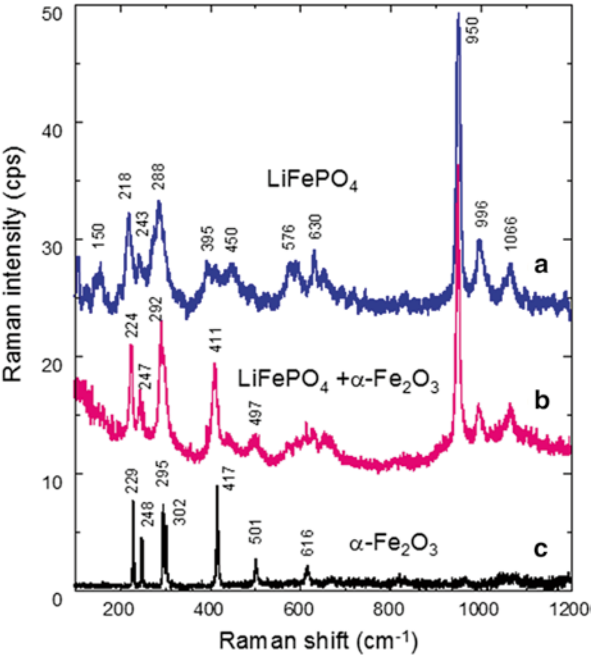

impurity, when formed, is expected to be located at the surface of the particles, not in the bulk. The broadening of the FTIR bands may be the result of poor crystallization, and indeed, it has been observed in amorphous $LiFePO_4$ [77], but we are concerned here with well-crystallized samples, as verified by X-ray diffraction (XRD) analysis. In this case, the reason should be a surface effect. TEM images show that a surface layer of particles not coated with carbon is severely disordered over a thickness of a few nanometers. A side effect of carbon coating is to reduce the structural disorder of this surface layer, resulting in the shrinking of the FTIR bands [78].

13.6.3 Raman Spectroscopy

The surface properties of the $LiFePO_4$ particles have been explored by micro-Raman experiments. Figure 13.15 displays the Raman spectra recorded with an incident-light wavelength of 515 nm of (1) carbon-free (uncoated) powders, (2) $LiFePO_4$ with few thousand parts per million of α-Fe_2O_3 as impurity, and (3) α-Fe_2O_3 powders. According to the absorption coefficient of $LiFePO_4$, the penetration depth with Raman spectroscopy is approximately 40 nm [79]. In the wavenumber range 100–1,100 cm^{-1} part of the spectrum displays lines characteristic of $LiFePO_4$ due to Raman-allowed modes (Table 13.4). The peak positions reported in Fig. 13.15a,b in this range are within a few per centimeter, the same as those reported by Burma and

Frech [73], and we refer to this prior work for their assignment. The largest difference is for the line at 395 cm^{-1}, which is reported at 410 cm^{-1} by Burma and Frech [73]. This line is associated to the PO_4 bending modes ν_2, ν_4, which are strongly coupled. However, we can consider this difference as significant since all the other lines associated to PO_4 have the same position. This is the case in particular for the lines at 620, 940, 986, and 1,058 cm^{-1} associated to the ν_4, ν_1, ν_3, and ν_2 intramolecular stretching modes of PO_4, respectively. The only difference in this range of wavenumbers is a shift of the Raman lines by approximately 10 cm^{-1} toward lower frequencies in the carbon-coated sample. This shift of the Raman lines is in contrast to the absence of any shift of the FTIR lines, which gives evidence that it is a surface effect. This shift of the Raman lines is attributable to the increase of the bonding length in the first layers of $LiFePO_4$ particles near the interface, taking its origin in the strain induced by the adhesion of the parasitic film.

For samples with a different mode of preparation, the presence of impurities such as α-Fe_2O_3 is clearly observed (Fig. 13.15b). Because the laser light probes the skin of particles a few nanometers deep, α-Fe_2O_3 are located at the surface; thus the net Raman spectrum is the superposition of two contributions, $LiFePO_4$ and α-Fe_2O_3. However, a careful examination is required because the Fe-O vibrations occur in the same spectral region, below 650 cm^{-1}. If some amorphous layer grows on the surface of particles, it could be responsible for a screening of the signal from $LiFePO_4$, so that only a weak band at 942 cm^{-1} associated to PO_4 groups could still be detected [80]. Again, such a screening is not expected for the reasons mentioned earlier, i.e., careful synthesis in reducing atmosphere and it is not observed in the present case.

A remarkable aspect of the Raman spectrum of phospho-olivine is the fact that both bending vibrations (ν_2 and ν_4) show a reverse behavior, although usually the symmetric bending is expected to have a higher intensity. The most noticeable feature in vibrational patterns is the highest frequencies of the ν_4 modes for the cobalt phase $LiCoPO_4$. The strong covalent bonds within the $(PO_4)^{3-}$ complex of $LiCoPO_4$ explains the difference between redox energies.

13.6.4 Local Structure and Redox Energy

The strongly condensed framework of lithium phosphates presents different physical and spectroscopic properties according to the various polyanionic environments. The phospho-olivine structure is built from LiO_6 and FeO_6 octahedra linked to $(PO_4)^{3-}$polyanions, whereas FeO_6 octahedra share no edges with other polyhedra in a Nasicon-like structure. The internal electrostatic field changes when the structure changes [from orthorhombic $LiFePO_4$ to monoclinic $Li_3Fe_2(PO_4)_3$, for instance], whereas the covalence of the Fe-O bond differs with the degree of covalence in the P-O bond. Electrochemical results show that the Fe^{3+}/Fe^{2+} level lies lower in the ordered olivine structure than in the Nasicon-like framework, giving a higher voltage vs. lithium [81].

Fig. 13.16 Experimental relationship between covalency bonding factor obtained from FTIR data and cell voltage for lithium metal phosphates including $LiCoPO_4$, $LiFePO_4$, $LiMnPO_4$, $LiFeP_2O_7$, and $Li_3Fe_2(PO_4)_3$

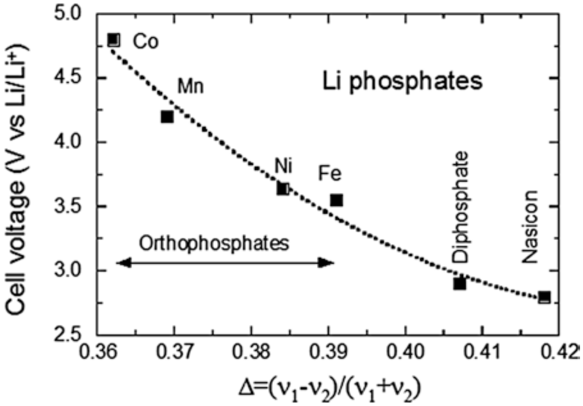

The energy of a given redox couple varies from one material to another depending on two main factors: (1) the electrostatic field at the cation position and (2) the covalent contribution to the cation-anion bonding. The study of both factors can be properly accomplished on oxides formed by MO_6 octahedra (M = transition metal cation) linked by tetrahedral polyanions $(PO_4)^{3-}$.

Investigations of framework structures built with polyphosphate anions have shown that the choice of the transition metal M has a significant effect on the cell voltage because it is primarily dependent on the redox couple of the metal atom present in the structure [82]. The use of polyanions has demonstrated a lowering of the M^{3+}/M^{2+} redox energy to useful levels in lithium cells. Polarization of the electrons of the O^{2-} ions into strong covalent bonding within the $(PO_4)^{3-}$ polyanion reduces the covalent bonding to the metal ion, which lowers its redox energy. The stronger the covalent bonding within the polyanion, the higher the voltage vs. lithium displayed by the positive electrode.

Since vibrational spectra are sensitive to the covalency of the phosphate group, it is worth studying the relationship between the relative energy levels and the covalency bonding in host structures having $(PO_4)^{3-}$ and $(P_2O_7)^{4-}$ anions. The useful estimate of a covalency strength is a parameter, Δ, defined by the relationship [83]

$$\Delta = \frac{\nu_1 - \nu_2}{\nu_1 + \nu_2}, \tag{13.17}$$

where ν_1 and ν_2 are the internal mode wavenumbers of the phosphate anion.

Figure 13.16 shows the empirical relationship between the covalency bonding factor and cell voltage for several lithium metal phosphates, including $LiCoPO_4$, $LiFePO_4$, $LiMnPO_4$, $LiFeP_2O_7$, and $Li_3Fe_2(PO_4)_3$ [84]. Among the compounds with an olivinelike structure, the cell voltages vs. Li/Li^+ are 3.55 V for $LiFePO_4$ and 4.75 V for $LiCoPO_4$. The cell voltage for $LiMnPO_4$ has been reported to be 4.1 V vs. lithium [85]. On the other hand, a cell voltage of 2.9 V is measured for the diphosphate $LiFeP_2O_7$ and 2.8 V for a Nasicon-like framework.

13.7 Vibrational Features of Delithiated Electrodes

To illustrate the vibrational response of a material upon delithiation, we have chosen olivine material, which turns from triphylite $LiFePO_4$ into heterosite $FePO_4$ during the charge of the battery according to the delithiation process [36]

$$LiFePO_4 \rightleftarrows (1-x)LiFePO_4 + xFePO_4 + xLi^+ + xe^-, \qquad (13.18)$$

and not Li_xFePO_4 solid solutions at the temperature of interest. In this section, we present the FTIR and RS investigation of this system.

13.7.1 *FTIR of Delithiated $LiFePO_4$*

The FTIR spectra of the three samples ($x=0$, 0.5, and 1) are reported in Fig. 13.17. The IR spectra of $LiFePO_4$ have been already reported and analyzed [73, 75, 86]. The spectrum of the $x=1$ sample is in agreement with these earlier results. The FTIR spectrum has also been reported in delithiated samples [87]. Incidentally, the notation used in this prior work is Li_xFePO_4 to designate partially delithiated samples, but this should be read as $xLiFePO_4+(1-x)FePO_4$ as in the present work since the samples are biphased just like our own $x=0.5$ sample. The juxtaposition of the spectra helps in the assignment of the vibrations. The basic feature is that, upon delithiation, the frequencies of the vibrations show only a small shift (by a few per centimeter) due to the change in the lattice parameters, and also, below 600 cm^{-1}, due to the change in the iron valence state. Such is the case for the external mode, or lattice vibrations, which occur below 400 cm^{-1}. If we try to follow up the shift of

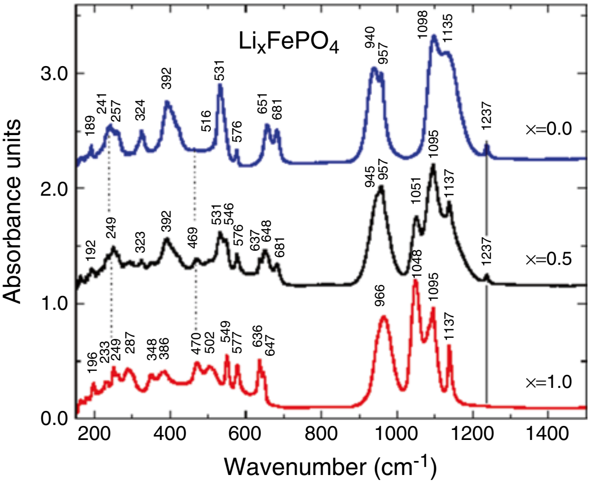

Fig. 13.17 Fourier transform infrared spectra of three samples defined by their concentration *x* in lithium. *Continuous vertical lines*: position of band that exists only in $FePO_4$; *broken vertical lines*: bands that exist only in $LiFePO_4$

the mode frequencies, we can make a correspondence of the wavenumbers of the lines from $x=1$ to $x=0$: 386→392, 348→324, 287→257, 249→241, 196→189 cm^{-1}. This confirms that these modes are primarily translation and vibration motions of the $(PO_4)^{3-}$ oxo-anions and translation motions of the Fe^{2-} ions. However, there is an extra line at 233 cm^{-1} in the $x=0$ samples only, and thus it is associated to the vibration of the lithium ion, i.e., the vibration of Li in its octahedral cage. To identify this mode, we note that the isotopic ^{6}Li–^{7}Li substitution in lithiated dioxides of transition metals has proven that the far-IR peak between 200 and 300 cm^{-1} is characteristic of an asymmetric stretching vibration of LiO_6 [88]. In particular, this mode in the same O_h configuration has been observed at 260 cm^{-1} in $LiCoO_2$ and 240 cm^{-1} in $LiNiO_2$ [89]. The line at 233 cm^{-1} in our samples with $x=0$, only shifted by a few per centimeter with respect to $LiNiO_2$, corresponds to this same cage mode of the lithium ions, namely, translation vibrations of Li inside the cage formed by the six nearest-neighbor oxygen atoms. Above 400 cm^{-1}, the modes are the external modes associated to the intramolecular vibrations of the PO_4 and FeO_6 units. In the FeO_6 spectral range of vibrations, two modes at 636 and 647 cm^{-1} ($x=1$) are shifted to 651 and 681 cm^{-1} ($x=0$) upon delithiation. In the intermediate range of 400–600 cm^{-1}, we can assume that the modes at 577, 549, and 502 cm^{-1} ($x=1$) are shifted to 576, 531, and 516 cm^{-1} and correspond to the bending modes (ν_2–ν_4) of the $(PO_4)^{3-}$ oxo-anions. On the other hand, we are left with an extra line at 470 cm^{-1} in the $x=0$ samples, which means that this line, also assumed to be a (ν_2–ν_4) mode, involves lithium-ion motion. In contrast, an extra line is clearly evidenced at 1,237 cm^{-1} in $FePO_4$, which does not exist in $LiFePO_4$. This extra line is also present in the FTIR spectra of $FePO_4$ in prior works [67, 78]. If we try to identify this mode with phosphate-ion complexes, we first note that such complexes as $(P_2O_7)^{4-}$ and $(P_3O_{10})^{5-}$ do not exist in our material since these ions would give rise to vibration modes in the spectral gap 700–900 cm^{-1}, where no modes are detected. On the other hand, we can make the hypothesis that this mode is linked to a vibration mode of PO_3. Indeed, lantern units present in the Nasicon phase give rise to IR bands in the range 1,150–1,250 cm^{-1}, which are attributed to the stretching vibration modes of terminal PO_3 units and are a fingerprint of the $Li_3Fe_2\,(PO_4)_3$ FTIR spectrum [15]. The same vibration mode has also been observed in $R(PO_3)_3$ This is [90] metaphosphates with R=Ga, In, Y, Sm, Gd, and Dy in the range 1,230–1,280 cm^{-1} [90].

13.7.2 Raman Scattering of Delithiated $LiFePO_4$

The Raman spectrum of both $LiFePO_4$ and $FePO_4$ are well known and distinct [91], so that Raman spectroscopy has been used to determine the structural composition of the surface layer at different stages x of the delithiation process, with the aim of distinguishing between a solid solution Li_xFePO_4 and the two-phase system $x\text{LiFePO}_4+(1\text{-}x)\text{FePO}_4$. This study was conducted using 100-nm-sized particles [92] for $x=0.5$ and particles for which the size was unfortunately not mentioned [93]. In both cases, however, the results were the same. They are illustrated in Fig. 13.18, showing the Raman spectrum of the 100-nm particles at $x=0.5$, together with that of

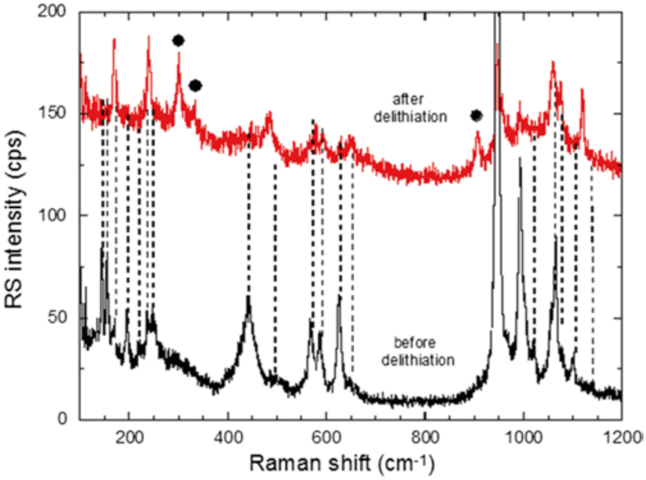

Fig. 13.18 Raman scattering spectra of $LiFePO_4$ and chemically delithiated phase $0.5(LiFePO_4+FePO_4)$. *Dashed lines*: Raman peaks characteristic of $LiFePO_4$ phase; *dots*: peaks characteristic of $FePO_4$ phase

the $LiFePO_4$ sample for comparison. For clarity, vertical broken lines were added to mark the Raman lines of $LiFePO_4$, together with their assignment. The Raman spectrum of $FePO_4$ is mainly characterized by lines also marked in Fig. 13.17, which were selected because they are located at wavenumbers where there are no Raman lines of $LiFePO_4$ in their vicinity. Those are the two lines at 306 and 338 cm^{-1}, both located in the gap between the T-vibration mode at 238 cm^{-1} and the ν_2 mode at 442 cm^{-1} of LFP, and the line at 911 cm^{-1} in the spectral gap between the $A_g(\nu_4)$ and $A_g(\nu_1)$ modes of $LiFePO_4$. Therefore, we find that the Raman spectrum of the $x=0.5$ sample is simply the juxtaposition of the Raman spectra of the two end members, showing that the region probed by Raman spectroscopy, i.e., the several-nanometer-thick shell of the particles is a two-phase system. This result was one argument among others [92] invalidating the core-shell model. It corroborates the idea of the mosaic model, according to which Li-insertion/extraction occurs from many nucleation sites at the surface so that both phases coexist in the shell. This does not mean, however, that the particle is homogeneous at a mesoscopic scale, i.e., that the composition x is the same in the shell and in the core region. In particular, the shell composition cannot be determined from the ratio of the intensities of Raman lines associated to the end members because the absorption of the particles varies with the composition. However, the Raman spectrum shows that the surface region, just like the core region, is biphased.

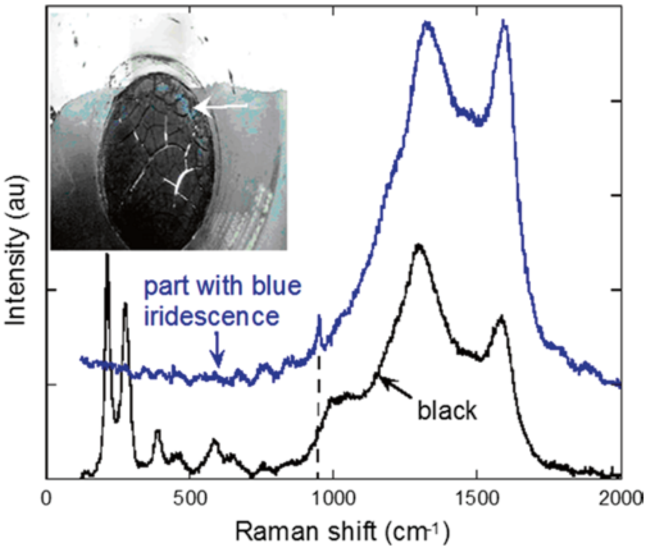

Fig. 13.19 Raman spectrum of deposit shown in Fig. 13.10 for SSR $LiFePO_4$ sample. *Black*: black part; *blue*: part that shows blue iridescence. The spectrum of uncoated $LiFePO_4$ is shown for comparison. *Vertical broken line*: position of stretching mode of PO_4 units

13.7.3 Reactivity of $LiFePO_4$ Nanoparticles with Water

The effects of the exposure of carbon-coated $LiFePO_4$ particles to H_2O have been investigated. Upon immersion in water, part of the product floats while the main part sinks. Both the floating and the sinking parts have been analyzed by optical spectroscopy (FTIR, RS) [94]. $LiFePO_4$ particles were synthesized by solid-state reaction (SSR).

The deposit after evaporation of the water in which the samples were immersed is shown in the insert of Fig. 13.19. In this experiment, the floating part was removed before the solution was dried out so that the deposit was made part of the sample that had sunk, plus part of the material that was dissolved in the water. The color of this deposit is almost black with blue iridescence in some areas for the SSR sample. Note, however, that the reaction of $LiFePO_4$ with H_2O is necessarily the same in both cases. The only differences between the two samples are the distribution size and the carbon deposit. In both samples, however, we are dealing with particles that are larger than 100 nm. No quantum effect on the electronic structure is expected for such large particles. The particles can then be considered big enough so that the size is not the pertinent parameter. The difference observed in Fig. 13.19 must then come from the carbon. Since we have shown that part of the carbon floats while another part has sunk when the samples are immersed in water, part of the carbon can also be in the intermediate position, i.e., in suspension in the water. The presence of such carbon particles in suspension in the solution is evidenced by the turbidity of the colored solution in which the SSR sample was immersed. Upon drying, this carbon in suspension will deposit at the bottom of the container, forming a black crust. This is in essence the origin of the black color of the deposit in the case of the SSR sample. The blue iridescence is also observed at the surface of iron after phosphatation invoked earlier, in which case it is attributed to the diffraction of light on the ultrathin layer. The same effect is presumably the cause of the iridescence observed here. The consequence is that the product decanted by evaporation of the solution in this case is mainly the LiOH, in addition to the iron compounds mentioned earlier. Of course, one cannot preclude the existence of, for example, Li_3PO_4 in small quantities since it is not soluble in water, or Li_2CO_3. Indeed, LiOH and Li_2CO_3 are white minerals and give this color to the residue.

Further support of this analysis is provided by RS spectroscopy, which is a remarkable tool for demonstrating the presence of carbon, due to the two characteristic Raman bands in the 1,200–1,700 cm^-1 spectral range. The Raman spectra of the black/blue deposits were measured using a He-Ne laser beam as excitation source (wavelength 632.8 nm). The result is illustrated in Fig. 13.19 for the black/blue part of the deposit of SSR. The spectrum of uncoated $LiFePO_4$ particles is also reported for comparison. While the intrinsic spectrum of $LiFePO_4$ is dominated by the peak at 960 cm^{-1} associated to the stretching mode of the PO_4 unit, the Raman spectrum of the part that shows blue iridescence is dominated by the two bands characteristic of the carbon. The structure centered at 960 cm^{-1}, however, is distinct, so that this part of the material also contains phosphate. The Raman spectrum of the black part that does not show blue iridescence shows again the dominant bands characteristic of carbon, but on the other hand, it does not show any structure at 960 cm^{-1}, which confirms that the blue iridescence is linked to the presence of phosphate and a phosphatation effect. However, three additional structures can be seen at lower frequencies at 398, 263, 219 cm^{-1} that are characteristic of lithium hydroxide monohydrate $LiOH \bullet H_2O$ [95]. A broad band can be seen in the vicinity of 1,070 cm^{-1}, which is also detected in the part with blue iridescence. This broad line has also been detected in the Raman spectrum of molten LiOH and is attributed to the vibration of a CO_3 molecular unit [95], which confirms the presence of Li_2CO_3 in addition to the lithium hydroxide.

Of course, the bands associated to the carbon are absent from the Raman spectrum of the white part of the white deposit for the SSR sample, and the spectrum (not shown here) does not display spectral features in the 1,200–1,700 cm^{-1} spectral range.

Although FTIR spectroscopy is in principle a useful tool for probing the local composition of the surface layer because the vibrations of the molecular units of the $LiFePO_4$ lattice are responsible for absorption bands in the spectrum even when the material is disordered [57], in the present case, we could not detect significant variations upon immersion in water. For sinking particles, the spectrum remains unchanged after 1 h in the water.

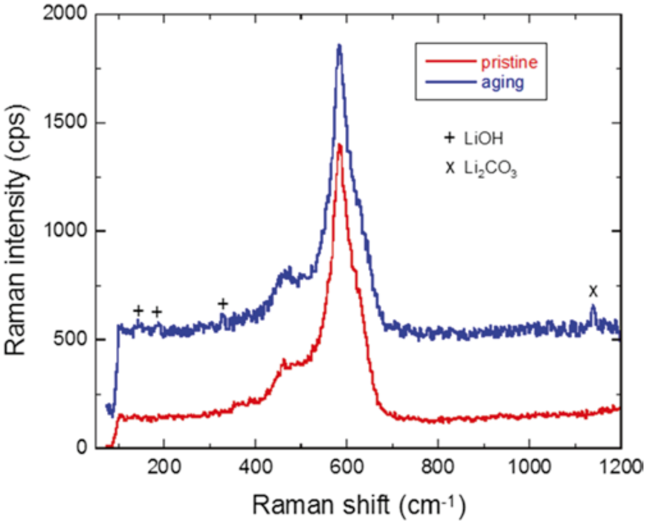

Fig. 13.20 Raman spectra of $LiNi_{1/3}Mn_{1/3}Co_{1/3}O_2$ in pristine state (*lower curve*) and after exposure to ambient atmosphere for 24 h (*upper curve*). + = LiOH, x = lithium carbonate

13.7.4 Reactivity of Lamellar Compounds with Water

We have shown (Fig. 13.11) the Raman spectrum of pristine $LiNi_{1/3}Mn_{1/3}Co_{1/3}O_2$ [96]. Upon exposure to ambient atmosphere for 1 day, the Raman spectrum of $LiNi_{1/3}Mn_{1/3}Co_{1/3}O_2$ (Fig. 13.20) shows three additional bands (marked "+") that are characteristic of LiOH and another band (marked "x") characteristic of a CO_3 molecular unit, which shows the presence of Li_2CO_3 in addition to lithium hydroxide, just as in the case of $LiFePO_4$ [96]. We thus recover the general trend in intercalation compounds, whether or not they are lamellar, according to which the reaction of lithium with H_2O at the surface results in the delithiation of the surface layer, the lithium involved in the process forming LiOH and Li_2CO_3 at the surface.

In their work on $LiVO_2$, Manthiram and Goodenough [97] were the first to show the migration of lithium ions to the surface on exposing the layered oxides to moisture, and the consequent formation of Li_2CO_3. The presence of lithium carbonate on the surfaces of active cathode materials such as $LiNiO_2$ and its analogs $LiNi_{1\text{-}x\text{-}y}Co_xAl_yO_2$ has long been noted. The difference between olivines and lamellar compounds is only in the thickness of the delithiated layer. It is difficult to measure quantitatively this parameter by Raman spectroscopy. However, this can be done by other means, in particular by analysis of the magnetic measurements. The delithiated layer is approximately 5 nm thick in the case of $LiFePO_4$, but 10 nm thick in the case of $LiNi_{1/3}Mn_{1/3}Co_{1/3}O_2$ and other lamellar compounds [98]. Therefore, lamellar compounds are more sensitive to humidity than olivine compounds. Due to the degradation of the electrochemical properties by these chemical reactions with water at the surface, the powders must be stored in a dry chamber.

References

1. C.M. Julien, Local environment in 4-volt cathode materials for Li-ion batteries. C.M. Julien and Z. Stoynov editors. NATO-ASI Series **3–85**, 309–326 (2000)
2. C.M. Julien, Lithium intercalation compounds, charge transfer and related properties. Mater. Sci. Eng. R **40**, 47–102 (2003)
3. C.M. Julien, Local cationic environment in lithium nickel-cobalt oxides used as cathode materials for lithium batteries. Solid State Ion. **136–137**, 887–896 (2000)
4. I.H. Campbell, P.M. Fauchet, The effects of microcrystal size and shape on the phonon Raman spectra of crystalline semiconductors. Solid State Commun. **58**, 739–741 (1986)
5. A. Tamura, K. Higeta, T. Ichinokawa, Lattice vibrations and specific heat of a small particle. J. Phys. C **15**, 4975–4992 (1983)
6. E. Duval, Far-infrared and Raman vibrational transitions of a solid sphere: selection rules. Phys. Rev. B **46**, 5795–5797 (1992)
7. H. Richter, Z.P. Wang, Y. Ley, The one phonon Raman spectrum in microcrystalline silicon. Solid State Commun. **39**, 625–629 (1981)
8. K.W. Adu, H.R. Gutierrez, U.J. Kim, G.U. Sumanasekera, P.C. Eklund, Confined phonons in Si nanowires. Nano Lett. **5**, 409–414 (2005)
9. K.W. Adu, H.R. Gutierrez, P.C. Eklund, Inhomogeneous laser heating and phonon confinement in silicon nanowires: a micro-Raman scattering study. Phys. Rev. B **73**, 155333 (2006)
10. E. Duval, A. Boukenter, B. Champagnon, Vibration eigenmodes and size of microcrystallites in glass: observation by very-low-frequency Raman scattering. Phys. Rev. Lett. **56**, 2052–2055 (1986)
11. G.J. Exarhos, P.J. Miller, W.M. Risen, Interionic vibrations and glass transitions in ionic oxide metaphosphate glasses. J. Chem. Phys. **60**, 4145–4155 (1974)
12. P. Tarte, J. Preudhomme, ^{6}Li-^{7}Li isotopic shifts in the infrared spectrum of inorganic lithium compounds – II: rhombohedral $LiXO_2$ compounds. Spectrochim. Acta A **26**, 747 (1970)
13. D.W. Marquardt, An algorithm for least-squares estimation of nonlinear parameters. SIAM J. Appl. Math. **11**, 431–441 (1963)
14. R. Meier, On art and science in curve-fitting vibrational spectra. Vibrat. Spectr. **39**, 266–269 (2005)
15. C. Julien, M. Massot, C. Poinsignon, Lattive vibrations of manganese oxides: Part 1. Periodic structures. Spectrochim. Acta Part A **60**, 689–700 (2004)
16. A.C. Ferrari, J. Robertson, Interpretation of Raman spectra of disordered and amorphous carbon. Phys Rev. B **61**, 14095–14107 (2000)
17. A.C. Ferrari, J. Robertson, Resonant Raman spectroscopy of disordered, amorphous and diamondlike carbon. Phys. Rev. B **64**, 075414 (2001)
18. D.S. Knight, W.B. White, Characterization of diamond films by Raman spectroscopy. J. Mater. Res. **4**, 385–393 (1989)
19. I. Pocsik, M. Hundhausen, M. Koos, L. Ley, Origin of the D peak in the Raman spectrum of microcrystalline graphite. J. Non-Cryst. Solids **227–230**, 1083–1086 (1998)
20. C. Chien, G. Dresselhaus, M. Endo, Raman studies of benzene-derived graphite fibers. Phys. Rev. B **26**, 5867–5877 (1982)
21. Y. Huang, R.J. Young, Effect of fibre microstructure upon the modulus of PAN- and pitch-based carbon. Carbon **33**, 97–107 (1995)
22. I.M. Robinson, M. Zakikhani, R.J. Day, R.J. Young, Strain dependence of the Raman frequencies for different types of carbon fibres. J. Mater. Sci. Lett. **6**, 1212–1214 (1987)

23. H. Sakata, G. Dresselhaus, M.S. Dresselhaus, M. Endo, Effect of uniaxial stress on the Raman spectra of graghite fibers. J. Appl. Phys. **63**, 2769–2772 (1988)
24. R.J. Young, A. Broadbridge, S.L. So, Analysis of SiC fibres and composites using Raman microscopy. J. Microsc. **196**, 257–265 (1999)
25. G. Gouadec, S. Karlin, P. Colomban, Raman extensometry study of NLM2020 and Hi-nicalon SiC fibres. Compos. B Eng. **29**, 245–245 (1998)
26. M. Paillet, P. Ponchara, A. Zahab, J.-L. Sauvajol, Vanishng of the Breit-Wiger-Fano component in indivudual single-wall carbon nanotubes. Phys. Rev. Lett. **94**, 237401–237405 (2005)
27. C.M. Julien, K. Zaghib, A. Mauger, M. Massot, A. Ait-Salah, M. Selmane, F. Gendron, Characterization of the carbon-coating onto $LiFePO_4$ particles used in lithium batteries. J. Appl. Phys. **100**, 63511 (2006)
28. Y. Ward, R.J. Young, R.A. Shatweel, Determination of residual stresses in SiC monofilament reinforced metal-matrix composites using Raman spectroscopy. Compos. A **33**, 1409–1416 (2002)
29. F. Tuinstra, J.L. Koenig, Raman spectrum of graphite. J. Chem. Phys. **53**, 1126–1130 (1970)
30. K. Zaghib, A. Mauger, F. Gendron, C.M. Julien, Surface effects on the physical and electrochemical properties of thin $LiFePO_4$ particles. Chem. Mater. **20**, 462–469 (2008)
31. I. Gregora, B. Chapagnon, A. Halimaoi, Raman investigation of light emitting porous silicon layers: estimate of characteristic crystalline dimensions. J. Appl. Phys. **75**, 3034–3039 (1994)
32. B.B. Li, D.P. Ju, S.L. Zhang, Raman spectral study of silicon nanowires. Phys Rev B **59**, 1645–1648 (1999)
33. K.W. Adu, Q. Xiong, H.R. Gutierrez, G. Chen, P.C. Eklund, Raman scattering as a probe of phonon confinement and surface optical modes in semiconducting nanowires. Appl. Phys. A **85**, 287–297 (2006)
34. S. Piscanec, M. Contoro, A.C. Ferrari, J.A. Zapien, Y. Lifshitz, S.T. Lee, S.H. Hoffman, J. Robertson, Raman spectroscopy of silicon nanowires. Phys Rev B **68**, 241312 (2003)
35. C. Li, G. Fang, S. Sheng, Z. Chen, J. Wang, S. Ma, X. Zhao, Raman spectroscopy and field electron emission properties of aligned silicon nanowire arrays. Physica E **30**, 169–173 (2005)
36. A.K. Padhi, K.S. Nanjundaswamy, J.B. Goodenough, Phospho-olivines as positive electrode materials for rechargeable lithium batteries. J. Electrochem. Soc. **144**, 1188–1194 (1997)
37. N. Ravet, Y. Chouinard, J.F. Magnan, S. Besner, M. Gauthier, M. Armand, Electroactivity of natural and synthetic triphylite. J. Power Sources **97**, 503 (2001)
38. C.M. Julien, A. Ait-Salah, F. Gendron, J.F. Morhange, A. Mauger, C.V. Ramana, Microstructure of $LiXPO_4$ (X=Ni, Co, Mn) prepared by solid-state chemical reaction. Scripta Mater. **55**, 1179 (2006)
39. Y. Hu, M. M. Doeff, R. Kostecki, R. Finones, Electrochemical Performance of Sol-Gel Synthesized LiFePO4 in Lithium Batteries. J. Electrochem. Soc. **151**, A1279–A1285 (2004)
40. R. Kostecki, B. Schnyder, D. Alliata, X. Song, K. Kinoshita, R. Kötz, Surface studies of carbon films from pyrolyzed photoresist. Thin Solid Films **396**, 36–43 (2001)
41. M.W. Geis, M.A. Tamor, Diamond and diamondlike carbon, in *The Encyclopedia of Applied Physics*, ed. by G.L. Trigg, vol. 5 (VCH, New York, 1993)
42. J. Robertson, Properties of diamond-like carbon. Surf. Coatings Technol. **50**, 185–188 (1992)
43. M. Ramsteiner, J. Wagner, C. Wild, P. Koidl, Raman scattering from extremely thin hard amorphous carbon films. J. Appl. Phys. **62**, 729–730 (1987)
44. M.A. Tamor, W.C. Vassell, Raman fingerprinting of amorphous carbon films. J. Appl. Phys. **76**, 3823–3830 (1994)
45. M. Yoshikawa, G. Katagani, H. Ishida, A. Ishitami, T. Akamatsu, Resonant Raman scattering of diamondlike amorphous carbon films. Appl. Phys. Lett. **52**, 1639–1641 (1988)
46. N. Wada, P.J. Gaczi, S.A. Solin, Diamond-like 3-fold coordinated amorphous carbon. J. Non-Cryst. Solids **35–36**, 543–548 (1980)
47. P. Lespade, A. Marchand, M. Couzi, F. Cruege, Caractérisation de matériaux carbonés par microspectrometry Raman. Carbon **22**, 375–385 (1984)

48. M.S. Dresselhaus, G. Dresselhaus, in *Light Scattering in Solids III, Topics in Applied Physics*, ed. by M. Cardona, G. Gunterhodt, vol. 51 (Springer, Berlin, 1982)
49. M. Nakamizo, K. Tamai, Raman spectra of the oxidized and polished surfaces of carbon. Carbon **22**, 197–198 (1984)
50. M.J. Matthews, X.X. Bi, M.S. Dresselhaus, M. Endo, T. Takahashi, Raman spectra of polyparaphenylene-based carbon prepared at low heat-treatment temperatures. Appl. Phys. Lett. **68**, 1078–1080 (1996)
51. J. Robertson, E.P. O'Reilly, Electronic and atomic structure of amorphous carbon. Phys. Rev. B **35**, 2946–2957 (1987)
52. M.A. Tamor, J.A. Haire, C.H. Wu, K.C. Hass, Correlation of the optical gaps and Raman spectra of hydrogenated amorphous carbon films. Appl. Phys. Lett. **54**, 123–125 (1989)
53. M. Massot, K. Zaghib, A. Mauger, F. Gendron, C.M. Julien, Solid State Ionics-2006, edited by E. Traversa, T.R. Armstrong, C. Masquelier, Y. Sadaoka, 0972-AA13-7 (2006)
54. M. Doeff, M.Y. Hu, F. McLarnon, R. Kostecki, Effect of surface carbon structure on the electrochemical performance of $LiFePO_4$. Electrochem. Solid State Lett. **6**, A207–A209 (2003)
55. J. Chen, M.S. Whittingham, Hydrothermal synthesis of lithium iron phosphate. Electrochem. Commun. **8**, 855–858 (2006)
56. K. Dokko, S. Koizumi, K. Kanamura, Electrochemical reactivity of $LiFePO_4$ prepared by hydrothermal method. Chem. Lett. **35**, 338–339 (2006)
57. S. Yang, P.Y. Zavajil, M.S. Whittingham, Hydrothermal synthesis of lithium iron phosphate cathodes. Electrochem. Commun. **3**, 505–508 (2001)
58. C. Julien, M. Massot, in *Proceedings of the Int. Workshop Advanced Techniques for Energy Sources Investigation and Testing*, Sofia, Bulgaria, edited by Z. Stoynov and D. Vladikova, p. L3-1 (2004)
59. C. Julien, C. Letranchant, S. Rangan, M. Lemal, S. Ziolkiewicz, S. Castro-Garcia, L. El-Farh, M. Benkaddour, Layered $LiNi_{0.5}Co_{0.5}O_2$ cathode materials grown by soft-chemistry via various solution methods. Mater. Sci. Eng. B **76**, 145 (2000)
60. A. Castro-Couceiro, S. Castro-Garcia, M.A. Senaris-Rodriguez, F. Soulette, C. Julien, Effect of the aluminium doping on the microstructure and morphology of $LiNi_{0.5}Co_{0.5}O_2$ oxides. Ionics **8**, 192–200 (2002)
61. C. Julien, M.A. Camacho-Lopez, M. Lemal, S. Ziolkiewicz, $LiCo_{1-y}M_yO_2$ positive electrodes for rechargeable lithium batteries. I. aluminium doped materials. Mater. Sci. Eng. B **95**, 6–13 (2002)
62. S.-T. Myung, N. Kumagai, S. Komaba, H.-T. Chung, Effects of Al doping on the microstructure of $LiCoO_2$ cathode materials. Solid State Ion. **139**, 47–56 (2001)
63. Y. Koyama, N. Yabuuchi, I. Tanaka, H. Adachiand, T. Ohzuku, Solid-state chemistry and electrochemistry of $LiCo_{1/3}Ni_{1/3}Mn_{1/3}O_2$ for advanced lithium-ion batteries. J. Electrochem. Soc. **151**, A1545–A1551 (2004)
64. T. Ohzuku, Y. Makimura, Layred lithium insertion material $LiCo_{1/3}Ni_{1/3}Mn_{1/3}O_2$ for lithium-ion batteries. Chem. Lett. **30**, 642–643 (2001)
65. X. Zhang, A. Mauger, Qilu, H. Groult, L. Perrigaud, F. Gendron, C.M. Julien, Synthesis and characterization of $LiNi_{1/3}Mn_{1/3}Co_{1/3}O_2$ by wet-chemical method. Electrochim. Acta **55**, 6440–6449 (2010)
66. B. Folch, J. Larionova, Y. Guari, C. Guérin, A. Mehdi, C. Reyé, Formation of Mn_3O_4 nanoparticles from the cluster $[Mn_{12}O_{12}(C_2H_5COO)_{16}(H_2O)_3]$ anchored to hybrid mesoporius silica. J. Mater. Chem. **14**, 2703–2711 (2004)
67. S. Lei, K. Tang, Z. Fang, J. Sheng, One-step synthesis of colloidal Mn_3O_4 and γ-Fe_2O_3 nanoparticles at room temperature. J. Nanopart. Res. **9**, 833–840 (2006)
68. W. Wenzhong, A. Ling, Synthesis and optical properties of Mn_3O_4 nanowires by decomposing $MnCO_3$ nanoparticles in flux. Crystal Growth Design **8**, 358–362 (2008)
69. N. Amdouni, C.M. Julien, unpublished data (2005)
70. M.C. Bernard, A.H.L. Goff, B.V. Thi, Electrochromic reactions in manganese oxides. J. Electrochem. Soc. **140**, 3065–3070 (1993)

71. M.T. Paques-Ledent, P. Tarte, Vibrational studies of olivine-type compounds. I. The i.r. and Raman spectra of the isotopic species of Mg_2SiO_4. Spectrochim. Acta Part A **29**, 1007–1016 (1973)
72. M.T. Paques-Ledent, P. Tarte, Vibrational studies of olivine-type compounds. II. Orthophosphates, -arsenates and -vanadates $A^IB^{II}X^VO_4$. Spectrochim. Acta Part A **30**, 673–689 (1974)
73. C.M. Burma, R.J. Frech, Raman and FTIR spectroscopic study of Li_xFePO_4 ($0 \leq x \leq 1$). J. Electrochem. Soc. **151**, A1032–A1038 (2004)
74. W.G. Fateley, F.R. Dollish, N.T. McDevitt, F.F. Bentley, *Infrared and Raman Selection Rules for Molecular and Lattice Vibrations: the Correlation Method* (Wiley, New York, 1972)
75. A. Ait-Salah, J. Dodd, A. Mauger, R. Yazami, F. Gendron, C.M. Julien, Structural and magnetic properties of $LiFePO_4$ and lithium extraction effects. Z. Anorg. Allg. Chem. **632**, 1598–1605 (2006)
76. A. Ait-Salah, A. Mauger, K. Zaghib, J.B. Goodenough, N. Ravet, M. Gauthier, F. Gendron, C.M. Julien, Reduction Fe^{3+} of impurities in $LiFePO_4$ from pyrolysis of organic precursor used for carbon deposition. J. Electrochem. Soc. **153**, A1692–A1701 (2006)
77. P. Joziak, J.E. Garbarczyk, M. Wasiucionek, I. Gorzkowska, F. Gendron, A. Mauger, C.M. Julien, DTA, FTIR and impedance spectroscopy studies on lithium-iron-phosphate glasses with olivine-like local structure. Solid State Ion. **179**, 46 (2008)
78. K. Zaghib, P. Charest, M. Dontigy, A. Guerfi, M. Lagacé, A. Mauger, M. Kopek, C.M. Julien, From molten ingot to nanoparticles with high-rate performance in Li-ion batteries. J. Power Sources **195**, 8280–8288 (2010)
79. K. Zaghib, A. Mauger, J.B. Goodenough, F. Gendron, C.M. Julien, Electronic, optical and magnetic properties of $LiFePO_4$: small magnetic polaron effects. Chem. Mater. **19**, 3740–3747 (2007)
80. A. Hezel, S.D. Ross, The vibrational spectra of some divalent metal pyrophosphates. Spectrochim. Acta A **23**, 1583–1589 (1967)
81. S.-C. Yin, H. Grondey, P. Strobel, M. Anne, L.F. Nazar, Electrochemical properties: structure relationships in monoclinic $Li_{3-y}V_2(PO_4)_3$. J. Am. Chem. Soc. **125**, 10402–10411 (2003)
82. K.S. Nanjundaswamy, A.K. Padhi, J.B. Goodenough, S. Okada, H. Ohtsuka, H. Arai, J. Yamaki, Synthesis, redox potential evaluation and electrochemical characteristics of NASICON-related-3D framework compounds. Solid State Ion. **92**, 1–10 (1996)
83. A. Rulmont, R. Cahay, M. Liegeois, P. Tarte, New crystalline and glassy phases in the pseudobinary system $K_4P_2O_7$-$PB_2P_2O_7$. Eur. J. Solid Inorg. Chem. **28**, 1021–1034 (1991)
84. A. Ait-Salah, P. Jozwiak, J. Garbarczyk, K. Benkhouja, K. Zaghib, F. Gendron, C.M. Julien, Local structure and redox energies of lithium phosphates with olivine- and Nasicon-like structures. J. Power Sources **140**, 370375 (2005)
85. G. Li, H. Azuma, M. Tohda, $LiMnPO_4$ as the cathode for lithium batteries. Electrochem. Solid-State Lett. **5**, A135–A137 (2002)
86. A. Ait-Salah, K. Zaghib, A. Mauger, F. Gendron, C.M. Julien, Magnetic studies of the carbothermal effect on $LiFePO_4$. Phys. Status Sol. (a) **203**, R1–R3 (2006)
87. C.M. Burma, R.J. Frech, Vibrational igation of structurally-related $LiFePO_4$, $NaFePO_4$ and $FePO_4$ compounds. Spectrochim. Acta A **65**, 44–50 (2006)
88. P. Tarte, Identification of Li-O bands in the infrared spectra of simple lithium compounds containing LiO_4 tetrahedra. Spectrochim. Acta Part A **20**, 238–240 (1964)
89. C.M. Julien, M. Massot, Spectroscopic studies of the local structure in positive electrodes for lithium batteries. Phys. Chem. Chem. Phys. **4**, 4226–4235 (2002)
90. D. Ilieva, D. Koacheva, C. Petkov, G. Bogachev, *J. Raman Spectrosc.* **32**, 893–899 (2001)
91. W. Paraguassu, P.T.C. Freire, V. Lemos, S.M. Lala, L.A. Montoro, J.M. Rosolen, Phonon calculation on olivine-like $LiMPO_4$ (M = Ni, Co, Fe) and Raman scattering of the iron-containing compound. J. Raman Spectrosc. **36**, 213–220 (2005)
92. C.V. Ramana, A. Mauger, F. Gendron, C.M. Julien, K. Zaghib, Study of the Li-insertion/extraction process in $LiFePO_4/FePO_4$. J. Power Sources **187**, 555–564 (2009)

93. Y. Hu, M.M. Doeff, R. Kostecki, R. Finones, Electrochemical performance of sol–gel synthesized $LiFePO_4$ in lithium batteries. J. Electrochem. Soc. **151**, A1279–A1285 (2004)
94. K. Zaghib, A. Guerfi, P. Charest, M. Dontigny, J.F. Labrecque, K. Kopec, A. Mauger, F. Gendron, C.M. Julien, Aging of $LiFePO_4$ upon exposure to H_2O. J. Power Sources **185**, 698–710 (2008)
95. S. Okazaki, N. Ohtori, I. Okada, Raman spectroscopic study on the vibrational and rotational relaxation of OH^-ions in molten LiOH. J. Chem. Phys. **91**, 5587–5592 (1989)
96. X. Zhang, W.J. Jiang, X.P. Zhu, A. Mauger, Q. Lu, C.M. Julien, Aging of $LiNi_{1/3}Mn_{1/3}Co_{1/3}O_2$ cathode material upon exposure to H_2O. J. Power Sources 196 (2011) 5102
97. A. Manthiram, J.B. Goodenough, Refinement of the critical V–V separation for spontaneous magnetism in oxides. Canadian J. Phys. **65**, 1309–1317 (1987)
98. G.V. Zhuang, G. Chen, J. Shim, X. Song, P.N. Ross, T.J. Richardson, Li_2CO_3 in $LiNi_{0.8}Co_{0.15}Al_{0.05}O_2$ cathodes and its effects on capacity and power. J. Power Sources **134**, 293–297 (2004)

Chapter 14
Nano Aspects of Metal–Air Batteries

Hajime Arai and Takayuki Doi

14.1 General Features and Principles

A metal–air battery is composed of a metal electrode and an air electrode as negative and positive electrodes, respectively [1]. The active material of the positive electrode is oxygen supplied from the ambient air, and therefore, being different from general batteries as shown in Fig. 14.1a, the interior space of the metal–air battery can be mostly occupied by the negative metal electrode, as shown in Fig. 14.1b. This special feature of the metal–air battery results in a particularly large capacity and, hence, the high energy density of the battery. The specific and volumetric energy densities of a practical primary zinc–air battery are more than 500 Wh kg^{-1} and 1,000 Wh L^{-1}, respectively. Oxygen is an ideal active material for a positive electrode because it is lightweight and is free of any restrictions with respect to resource, cost, and environmental problems. This makes the metal–air battery promising as the next-generation battery system. The selection of the negative electrode material is a key factor in realizing successful secondary metal–air battery systems. Promising candidates for metal electrode materials with strong reducing powers and large capacities are base metals such as zinc, iron, lithium, aluminum, and magnesium.

The general chemical equations of a discharge reaction in an aqueous (alkaline) metal–air battery, with a metal M negative electrode of valence *n*, are as follows:

$$\text{Positive electrode: } O_2 + 2H_2O + 4e^- \rightarrow 4OH^- \tag{14.1}$$

$$\text{Negative electrode: } M + nOH^- \rightarrow MO_{n/2} + n/2H_2O + ne^- \tag{14.2}$$

$$\text{Total: } M + n/4O_2 \rightarrow MO_{n/2} \tag{14.3}$$

H. Arai (✉) • T. Doi
Office of Society-Academia Collaboration for Innovation, Center for Advanced Science and Innovation, Kyoto University, Gokasho, Uji 611-0011, Japan
e-mail: h-arai@saci.kyoto-u.ac.jp; doi@saci.kyoto-u.ac.jp

T. Osaka and Z. Ogumi (eds.), *Nanoscale Technology for Advanced Lithium Batteries*, Nanostructure Science and Technology 182, DOI 10.1007/978-1-4614-8675-6_14,

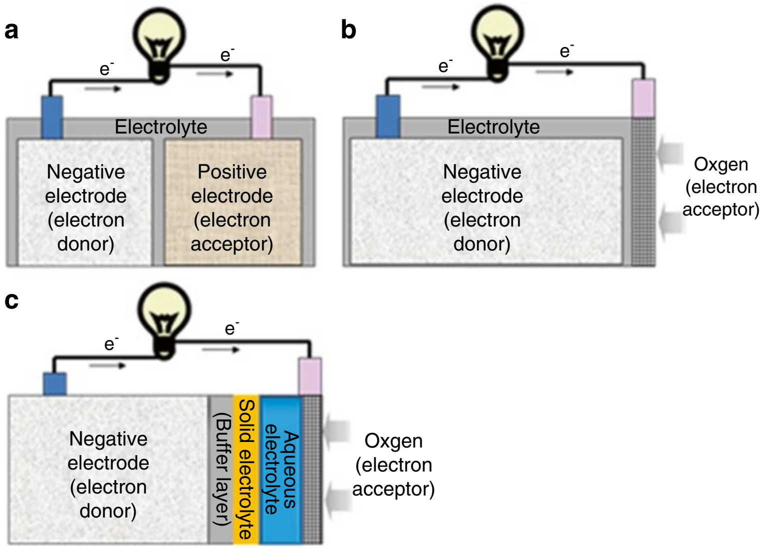

Fig. 14.1 Discharging reactions of general batteries (**a**), metal–air batteries (**b**), and aqueous metal–air batteries with active metals (**c**)

When the discharge product of the metal M is a hydroxide, reactions (14.2) and (14.3) are replaced as follows and water is consumed during the discharge process:

$$\text{Negative electrode:}\quad M + nOH^- \rightarrow M(OH)_n + ne^- \tag{14.4}$$

$$\text{Total:}\ M + n/4O_2 + n/2H_2O \rightarrow M(OH)_n \tag{14.5}$$

Reactions (14.1) and (14.2) are replaced by reactions (14.6) and (14.7) in a non-aqueous system with an oxide as the discharge product:

$$\text{Positive electrode:}\quad O_2 + 4e^- \rightarrow 2O^{2-} \tag{14.6}$$

$$\text{Negative electrode:}\quad M \rightarrow M^{n+} + ne^- \tag{14.7}$$

The total reaction is the same as reaction (14.3). When the discharge product is peroxide, reactions (14.6) and (14.3) are replaced as follows with a half electron transfer of reaction (14.3):

$$\text{Positive electrode:}\quad O_2 + 2e^- \rightarrow O_2^{\ 2-} \tag{14.8}$$

$$\text{Total:}\ M + n/2O_2 \rightarrow MO_n\left(=1/2M_2O_{2n}\right) \tag{14.9}$$

The selection of the electrolyte for the metal–air battery greatly depends on the reactivity, namely, the reducing power, of the metal used as the negative electrode. Zinc and iron are used in aqueous alkaline electrolyte (typically KOH) solutions because their stability is acceptable. An acidic solution cannot be applied to the electrolyte due to the high activity of the hydrogen evolution that accompanies metal dissolution. Aluminum and magnesium, with much higher activities than zinc and iron, are unstable in aqueous media and are used in reserve-type batteries where the negative electrodes are immersed in electrolyte (typically NaCl or KOH) solutions only when used for discharging. Lithium, one of the most base metals, is used in nonaqueous media, including organic electrolytes, polymer electrolytes, and ionic liquids. Lithium is metastable in these nonaqueous media and can be electrically recharged. Aluminum and magnesium could also be used in these nonaqueous media. A recent trial includes a combination of the lithium negative electrode in nonaqueous media and the air electrode in aqueous media separated by a lithium-conductive solid electrolyte, as shown in Fig.14.1c.

The general issues to be resolved for metal–air batteries include their limited power due to the limited oxygen supply at the air electrode, self-discharge of the negative electrode reacting with electrolyte or oxygen leaking through the electrolyte, degradation of the battery components by CO_2 and H_2O coming through the air electrode, and thermal management due to the exothermic reaction in the discharge process, i.e., metal oxide formation. For electrically rechargeable types of batteries, reversibility and stability of the metal and air electrodes should be additionally addressed. In mechanically rechargeable types of batteries, the discharge products are not charged in the battery but are regenerated in other separate electrolysis cells, and therefore problems associated with the charging process can be eliminated. This off-site regeneration process also has the advantages of a simple battery configuration used only for discharging, which is similar to fuel cells, and quick charging by replacement of the used negative electrodes with the regenerated ones, like refueling at a gas station, though regeneration infrastructures are necessary would be necessary. Zinc and aluminum have emerged as the candidates for negative electrode materials in mechanical rechargeable air batteries.

In this chapter, a general overview of air electrodes will be given in the next section, followed by three sections on aqueous systems, lithium systems in nonaqueous media, and lithium systems in aqueous media. Nano- or micro- technologies used in the electrodes and electrolytes are featured.

14.2 General Overview of Air Electrodes

The air electrode in a metal–air battery functions as an air inlet and an oxygen reduction reaction (ORR) electrode during the discharging process, which is close to that for fuel cells. To ensure a fast and uniform supply of air and to prevent the electrolyte from leaking, a hydrophobic gas diffusion layer is necessary inside the air inlet. The gas diffusion layer generally consists of a carbon substrate with a

Fig. 14.2 Oxygen reduction reaction schemes of air electrodes in aqueous (**a**) and nonaqueous lithium (**b**) media

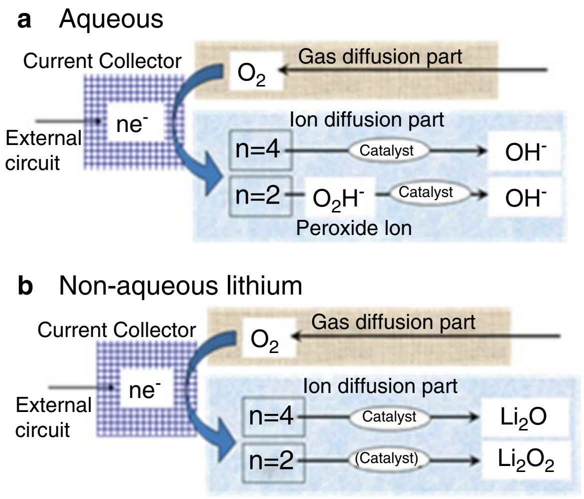

fluorocarbon polymer binder. A catalyst is necessary to ensure that the air electrode has sufficient activity. Figure 14.2 shows ORR schemes of air electrodes in aqueous and nonaqueous lithium media. Air electrodes used in aqueous media have a hydrophilic reaction layer where the catalyst is loaded on the catalyst substrate [2]. In nonaqueous media systems, the catalyst could be loaded directly on the gas diffusion layer. The nature of the catalyst and the substrate greatly affects both the activity and the stability of the air electrode. A conductive and oxidation resistive material, typically nickel, is used as the current collector.

The ORR in nonaqueous media often proceeds in a two-electron step, shown in reaction (14.8), rather than a four-electron step, as in reaction (14.6). The four-electron ORR in aqueous media shown in reaction (14.1) is also generally slow and occurs only in the presence of a special catalyst such as platinum. The ORR in aqueous media often proceeds in a two-electron electrochemical step, as shown in reaction (14.10), followed by a chemical disproportionation reaction, shown in reaction (14.11).:

$$\text{Electrochemical:} \quad O_2 + H_2O + 2e^- \rightarrow O_2H^- + OH^- \tag{14.10}$$

$$\text{Chemical:} \quad O_2H^- \rightarrow OH^- + 1/2O_2 \tag{14.11}$$

The total reaction of the air electrode for reactions (14.10) accompanied by (14.11) is apparently the same as for reaction (14.1). In this case, the catalyst in the air electrode functions in the disproportionation reaction shown in reaction (14.11). The electrochemical two-electron ORR causes a discharge voltage that is lower than the theoretically expected value, with a loss of more than 0.3 V.

The polarization of the air electrode is influenced by the activity of the catalyst and oxygen diffusion characteristics of the electrode at low and high current densities, respectively [3]. The typical air electrode catalysts are oxides and noble metals.

Manganese dioxides and a variety of perovskite-type oxides have been proposed. Some perovskite-type oxides are stable and active for oxygen evolution reactions (OERs). Platinum is expensive but an excellent ORR catalyst and can be used in nonaqueous systems, though it causes hydrogen evolution in aqueous media when dissolved in an electrolyte and reaches the negative electrode. Silver and gold are also good ORR catalysts. The dispersion of the catalyst is an important factor in obtaining high activity because it enables the formation of long triple-phase boundaries, where gas, liquid (electrolyte), and solid (catalyst) phases coexist. Nanotechnology could be a key factor in the production of highly dispersed catalyst particles with a large surface area and long triple-phase boundaries.

There has been serious difficulty in developing electrically rechargeable metal–air batteries due to the poor reversibility of the oxygen electrode. The activity of a bifunctional electrode, used for both ORR and OER, is still insufficient, and the stability, particularly of the carbon substrate, suffers from high electrode potential during OER. Some kinds of nanostructured carbon materials with limited surface areas are oxidation resistant and could offer high stability during the OER process. Oxides and metal foam materials with high surface areas are also candidates as stable substrates. Mechanically rechargeable types of batteries are advantageous in terms of avoiding the difficulty at both air and metal electrodes. The use of the third electrode used exclusively for the OER [4] is also an option for developing an electrically rechargeable metal–air battery.

14.3 Nanotechnology Used in Aqueous Systems

The high activity and stability of both negative and positive electrodes are necessary to realize secondary metal–air batteries. The rechargeability of metal and air electrodes is largely responsible for the activity and stability, and therefore attempts to enhance the rechargeability are the main topics in this field. In this section, nanotechnology used in this field is highlighted.

14.3.1 Negative Electrode

Zinc and iron can be deposited in an aqueous system, and the system can be electrically charged in the battery if it is equipped with a bifunctional air electrode. The rechargeability of zinc and iron electrodes is insufficient and should be improved for practical use. Aluminum and magnesium are used in mechanically rechargeable batteries and reserve batteries, and utilization improvement is most important in these materials. Some of the techniques shown below are not directly related to metal–air battery systems, but they can be applied to metal–air batteries mostly without any modification.

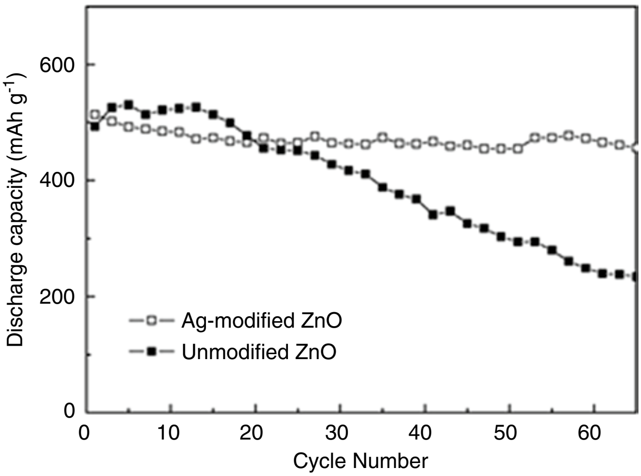

Fig. 14.3 Electrochemical cycle behavior of Ni/Zn cells with Ag-modified ZnO and unmodified ZnO anodes (Reprinted from Wu JZ, Tu JP, Yuan YF, Wang XL, Zhang L, Li RL, Zhang J, Ag-modification improving the electrochemical performance of ZnO anode for Ni/Zn secondary batteries, p. 626, Copyright (2009) with permission from Elsevier)

14.3.1.1 Zinc

The discharge product of zinc is a soluble $Zn(OH)_4^{2-}$ ion, and it finally condenses into ZnO. Due to the formation of $Zn(OH)_4^{2-}$, zinc electrodes suffer from problematic electrode shape changes and dendrite-shaped metallic zinc formation, leading to the internal short-circuiting of the battery. The general methods for restricting the solubility of $Zn(OH)_4^{2-}$ species include calcium complex formation [5] and KF dissolution into the electrolyte [6]. Pasted zinc electrodes with large surface areas are useful for decreasing the actual current density and for preventing zinc dendrite formation [7].

Zinc species dissolution can be restricted by adding nano-sized silver particles to the ZnO, leading to improved cycle performance [8] (Fig. 14.3). It has been shown that nano-sized calcium zincate powder prepared by the coprecipitation method exhibits cycle performance better than that prepared by the ball-milling method because of its large pore volume and high surface area [9].

Zinc dendrite formation and morphology changes can be suppressed using ZnO nanoplate particles prepared by the hydrothermal synthesis method with a thickness of approximately 50 nm [10]. It has been suggested that the nanoplate particles grow in parallel to the plate direction, as shown in Fig. 14.4, leading to the suppression of the dendrite growth of the metallic zinc. Rayon-type separators suppressing zinc dendrite growth propagation and microporous separators with uniform mass distribution (limited shape changes) are combined with improved cell setups and charging techniques, leading to the enhanced rechargeability of the zinc electrode [11].

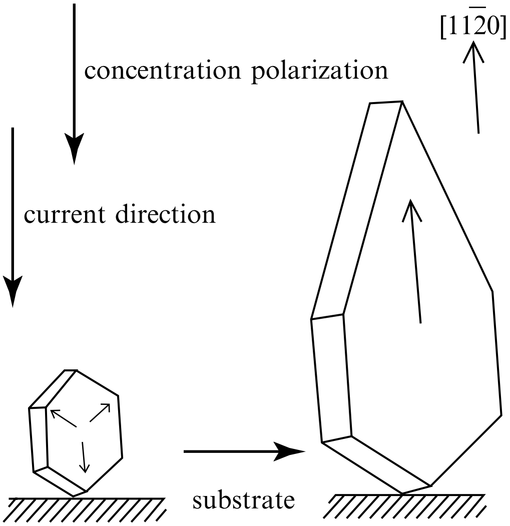

Fig. 14.4 Mechanism of suppressant effect of platelike ZnO, which stands erect with respect to the substrate on a growth of zinc dendrite (Reprinted from J. Power Sources 179, Ma M, Tu JP, Yuan YF, Wang XL, Li KF, Mao F. Zeng ZY, Electrochemical performance of ZnO nanoplates as anode materials for Ni/Zn secondary batteries, p. 399, Copyright (2008) with permission from Elsevier)

14.3.1.2 Iron

Iron has small electrochemical equivalents, 0.29 and 0.19 mg C^{-1} for divalent and trivalent iron, respectively, which is smaller than the 0.34 mg C^{-1} for zinc; hence, high discharge capacities are expected. In addition, iron electrodes show negative working potentials in concentrated alkaline aqueous solution, as shown in Fig. 14.5 [12]. Discharge reactions, i.e., anodic reactions of iron, proceed at around 0.9 and 0.7 V vs. Hg/HgO, whereas the corresponding charge reactions take place at very negative potentials. During charging, a hydrogen evolution reaction also occurs in parallel with the reduction of oxidized iron species to iron due to the low hydrogen overpotential, which leads to self-discharge reactions in the charged state [13]. Thus, the charge and discharge reactions of an iron electrode in alkaline aqueous solution are not highly reversible, which is a major drawback of iron electrodes. Plausible charge and discharge reactions are shown in Fig. 14.5, while various possible reactions of iron electrodes have been suggested [14]. Iron is thermodynamically unstable in aqueous solution and hence is prone to corrode to form oxidized iron species such as $Fe(OH)_2$, FeOOH, and Fe_3O_4; iron is passivated [15]. In addition, considerable experimental evidence suggests the presence of soluble intermediate species such as FeO_2^- and $HFeO_2^2$; iron electrodes are discharged and charged through dissolution/deposition processes [16]. These facts indicate that the charge and discharge reactions of an iron electrode are highly influenced by the electron conductivities of the oxidized iron species and solubility of the intermediate species.

The use of nano-sized particles of iron compounds makes it possible to shorten the conductive paths of the electrons within them, resulting in the apparent high conductivity of electrons. In addition, nano-sized particles possess a large specific surface area and, hence, present a relatively large reactive area on their surface.

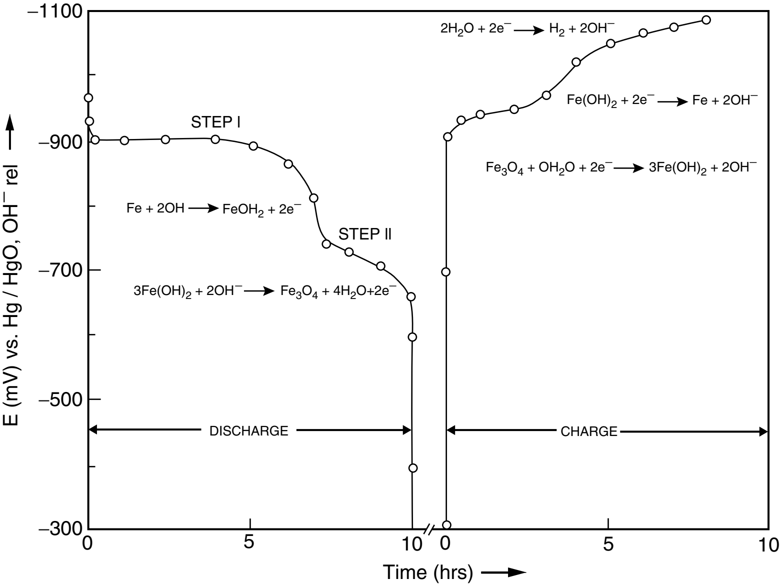

Fig. 14.5 Typical charge and discharge curves of an iron electrode in 6 M KOH aqueous solution (Reprinted from J. Power Sources 34, Vijayamohanan K, Balasubramanian TS, Shukla AK, Rechargeable alkaline iron electrodes, p.274, Copyright (1991) with permission from Elsevier)

Therefore, the charge-transfer resistances at the interface between the electrode and electrolyte are expected to be small. In recent years, nano-sized iron oxides supported on nano-sized carbonaceous materials have been reported to improve the charge and discharge performance [17]. Of these, nano-sized Fe_2O_3 particles 50 nm in size deposited inside carbon nanotubes (CNTs), as shown in Fig. 14.6a, exhibit high reversible capacities over repeated charge and discharge cycles [18]. However, when oxidized CNTs with a relatively large number of pores on their surfaces are used, the discharge capacities decrease more rapidly with increasing cycles, as shown in Fig. 14.6b. This is likely because part of the soluble intermediate species in the vicinity of the interface diffuses away into the bulk of the electrolyte solution through pores of the CNTs. These results suggest that the cycle performance of an iron electrode could be enhanced by confining the diffusion of the soluble intermediate species to nanoscale interfacial regions.

14.3.1.3 Aluminum and Magnesium

Metals with high reducing powers such as aluminum and magnesium are attractive negative electrodes and could offer high cell voltages, but they react with aqueous electrolyte solutions even in a neutral condition, such as a brine (NaCl) electrolyte, or in alkaline media. A passivation film formed on the metal surface can retard undesirable side reactions (hydrogen evolution and metal dissolution), but still the material can only be used electrochemically before the metal is chemically

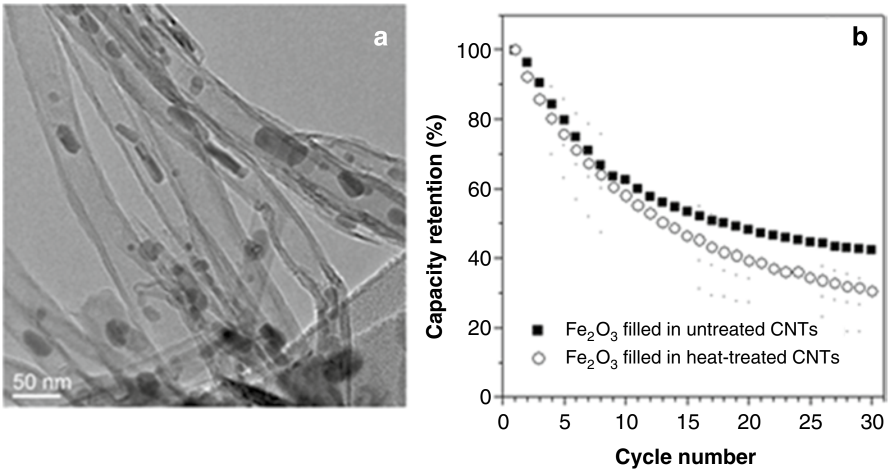

Fig. 14.6 Transmission electron microscopy image of as-prepared Fe_2O_3 deposited in carbon nanotubes (**a**) and variation of discharge capacity retention with cycle number of Fe_2O_3 deposited in untreated and heat-treated carbon nanotubes (**b**) (Reprinted from J. Power Sources 178, Hang BT, Hayashi H, Yoon SH, Okada S, Yamaki J, Fe_2O_3-filled carbon nanotubes as a negative electrode for an Fe–air battery, p. 395, Copyright (2008) with permission from Elsevier)

oxidized. Therefore, inhibiting unfavorable corrosion is the key factor in realizing high electrical utilization of these metals. Nanoparticles with good electrical contacts with the current collector but with less reactivity are desirable.

It has been reported that aluminum nanorods prepared by vapor deposition, 1–2 mm long and 30–90 nm in diameter, show a capacity of 460 mAh g^{-1} when combined with an air electrode and a 4 mol dm^{-3} KOH ethanol electrolyte, which is twice as large as that of commercial aluminum powder (240 mAh g^{-1}) with particle sizes of 5–30 mm, as shown in Fig. 14.7 [19]. This improved but insufficient utilization of only 15 % and low operating voltage (1.3 V vs. theoretical 2.7 V) should be further enhanced. Magnesium nanopowder with a sea-urchin-like structure has been reported to offer high electrochemical activity [20]. This material is also prepared by the vapor deposition method and has a high specific surface area of 130 m^2 g^{-1}. When tested in a mixed aqueous solution of $Mg(NO_3)_2$ and $NaNO_2$, the magnesium–air battery shows a high utilization of around 50 %, though the average operating voltage is low at 0.9 V.

14.3.2 Positive Electrode

14.3.2.1 Substrate

The catalyst substrate in air electrodes offers a surface area for electrochemical and chemical reactions and electrical conductivity. In bifunctional air electrodes, the stability is as important as the activity in restricting the corrosion of the substrate,

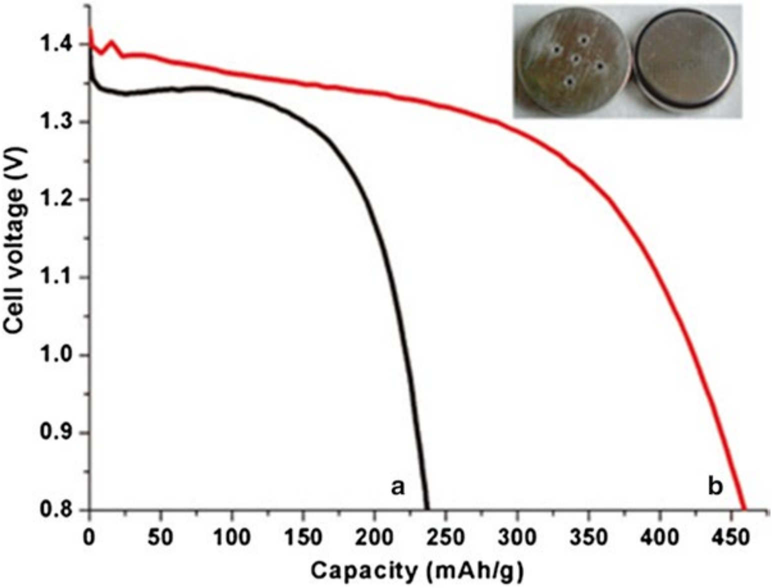

Fig. 14.7 Typical discharge curves of Al/air batteries made from (**a**) commercial Al powders and (**b**) as-prepared Al nanorods at a constant current density of 0.7 mA cm^{-2}. The *inset* shows laboratory-made Al–air batteries (Reprinted with permission from *Chem. Mater.*, **19**, 5814 (2007). Copyright 2007 American Chemical Society)

particularly in the OER process. In general, carbon materials with a large surface area are prone to be easily corroded, but the corrosion can be suppressed with the addition of proper catalysts [3]. The stability of graphitized carbon materials is acceptable [21]. Some trials have been conducted to use substrate materials other than carbon, such as nitrides [22] and pyrochlore-type oxides [23], but such research is still limited due to these oxides' low surface area and insufficient conductivity. CNTs have a high surface area and high electrical conductivity, and their chemical stability is considered to be high. These properties make CNTs promising as substrates for air electrodes.

Many techniques to load catalysts on CNTs have been employed. For example, a silver/MnO_2–CNT composite can be produced when an aqueous solution of silver permanganate containing CNTs is reduced with hydrazine [24]. The high conductivity of CNTs leads to good discharge performance of a zinc–air battery with this composite as the air electrode, as shown in Fig. 14.8. The wettability of CNT materials can be improved using a polymer-assisted technique, enabling good dispersion of the CNTs in an aqueous media for catalyst loading [25]. A $MnSO_4$ solution containing CNTs and the polymer is oxidized to form a nano-MnO_2/CNT composite with good ORR activity. It has been shown with a rotating ring-disk electrode measurement that the four-electron ORR pathway predominates with this electrode. Being similar to CNTs, graphene sheets with MnO_2 nanoparticle catalysts also exhibit activity in ORRs with an electron transfer number of nearly 4 [26].

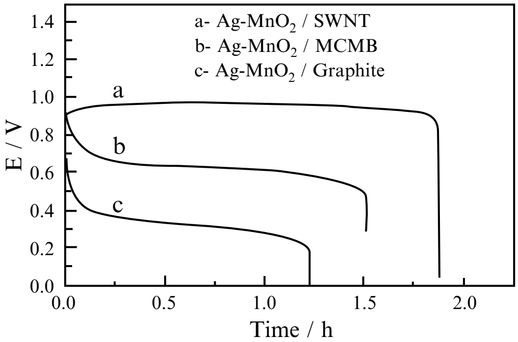

Fig. 14.8 Typical discharge curves of zinc–air cells using catalysts supported on different carbon materials at 94.2 mA constant discharge current. SWNT and MCMB denote single-walled carbon nanotubes and mesocarbon microbeads, respectively (Reprinted from Carbon 42, Zhang GQ, Zhang XG, Wang YG, A new air electrode based on carbon nanotubes and Ag-MnO$_2$ for metal air electrochemical cells, p. 3101, Copyright (2004) with permission from Elsevier)

Another method to use CNTs as the conductive substrate is to grow CNTs around the catalyst particles. CNTs can be grown around nano-sized $La_{0.6}Ca_{0.4}CoO_3$ particles by means of acetylene decomposition to finally enclose the metal oxide particle, as shown in Fig. 14.9, and the composite can function as a bifunctional air electrode [27]. Similarly, multiwalled CNTs are grown on a perovskite oxide catalyst, $La_{0.6}Sr_{0.4}CoO_3$, in a fluidized bed with chemical vapor deposition in an argon atmosphere using acetylene as carbon source [28]. The CNT growth at temperatures lower than 675 °C is necessary to prevent the perovskite catalyst from reducing. Figure 14.10 shows the good ORR activity of a CNT/perovskite catalyst composite because of the porous nature of the CNTs, which allows for a high dispersion of the catalyst.

A challenging trial is to use a conductive is to use a conductive perovskite oxide as catalyst support. A nano-sized $LaMnO_3$ catalyst prepared by a reverse-micelle method (see subsequent discussion) is loaded on a $LaNiO_3$ support of 200-nm-size particles prepared by a reverse homogeneous precipitation method, resulting in an active and highly stable bifunctional air electrode [29]. The catalytic performance can be improved by enhancing the surface area of the $LaNiO_3$ support, which is currently limited to around 10 m^2 g^{-1}.

14.3.2.2 Catalyst

A catalyst is an indispensable component in air electrodes in practical metal–air batteries. It is believed that the ORR in the four-electron pathway in reaction (14.1) proceeds only with the presence of the catalyst. Although the ORR in the two-electron pathway in reaction (14.10) can take place on the carbon substrate with

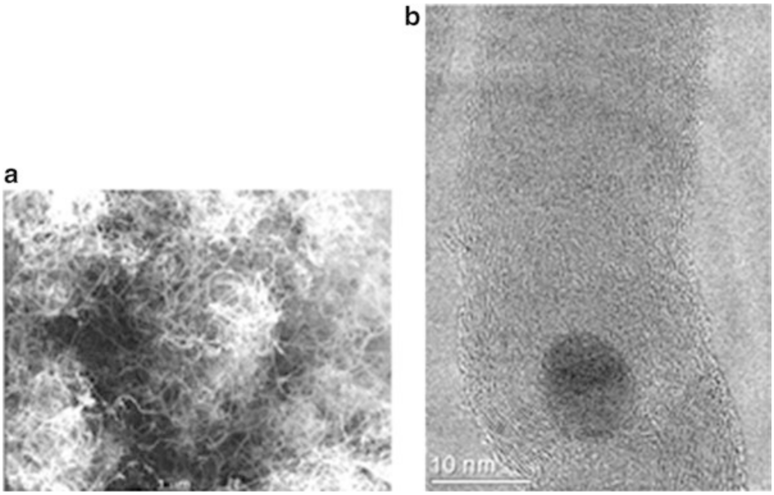

Fig. 14.9 (**a**) Scanning electron microscopy and (**b**) high-resolution transmission electron microscopy images of multiwalled carbon nanotubes/perovskite nanocomposite material. Carbon nanotubes enclose the metal oxide particles (Reprinted with permission from *Chem. Mater.*, **14**, 1804 (2002). Copyright 2002 American Chemical Society)

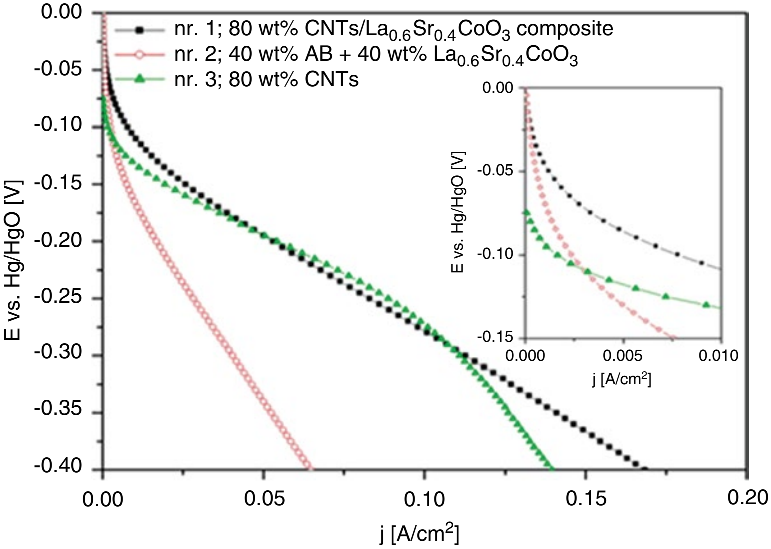

Fig. 14.10 Steady-state current-potential curves of electrodes (Reprinted from Diam. Relat. Mater. 18, Thiele D, Colmenarejo EL, Grobety B, Zuettel A, Synthesis of carbon nanotubes on $La_{0.6}Sr_{0.4}CoO_3$ as substrate, p. 36, Copyright (2009) with permission from Elsevier)

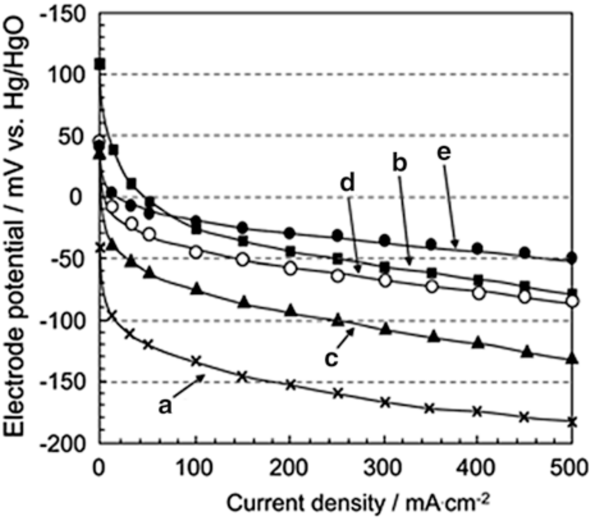

Fig. 14.11 Oxygen reduction activities of (**a**) carbon without electrocatalysts, (**b**) carbon-supported Pt nanoparticles (27.7 mass %), (**c**) carbon-supported $LaMnO_3$ obtained using conventional method [mechanical mixture of $LaMnO_3$ (50 mass %) and carbon], (**d**) carbon-supported $LaMnO_3$ (30 mass %), and (**e**) carbon-supported $La_{0.4}Ca_{0.6}Mn_{0.9}Fe_{0.1}O_3$ (30 mass %) obtained by reverse-micelle method (Reproduced with permission from *Electrochem. Solid-State Lett.*, **14**, A68 (2011). Copyright 2011, The Electrochemical Society)

acceptable kinetics, the decomposition of thus formed peroxide ions occurs mainly on the catalyst. The catalyst active for the OER is necessary to prevent the carbon support from undergoing serious oxidation during the OER process. Some perovskite oxides such as $La_{0.6}Ca_{0.4}CoO_3$ are known to have good activity and stability for both ORR and OER [30]. Catalysts suitable only for ORR are still worth studying when considering applications to mechanically rechargeable systems. Nano-sized catalysts widely dispersed on a substrate are attractive because of their apparent high surface area for oxygen absorption/desorption, the charge-transfer reaction, and the catalytic reactions.

A perovskite oxide catalyst finely dispersed on a substrate can be obtained by a reverse-micelle (RM) method, in which RM dispersion solutions of metal nitrates and hydroxide ions are separately prepared and mixed. Nano-sized $LaMnO_3$ [31] and its substituted compounds [32] thus obtained show ORR activity as high as platinum catalysts, as shown in Fig. 14.11. Similarly, $LiMnO_{3+\delta}$ particles 10 nm in size dispersed on carbon material are obtained by supporting a colloidal dispersion of the precursor of the target material on carbon in a liquid phase followed by high-temperature heating in a nitrogen atmosphere [33]. This method, called reverse homogeneous precipitation, can offer resultant electrodes with high activity in the ORR. Nano-sized, 50-nm $La_{0.6}Ca_{0.4}CoO_3$ particles are obtained with a reverse microemulsion process using a metal nitrate solution containing an oil phase and a surfactant [27].

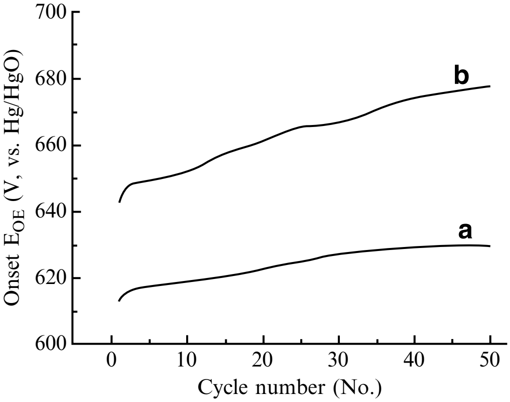

Fig. 14.12 Cycle tests of air electrodes loaded with 25 wt% (**a**) $La_{0.59}Ca_{0.41}CoO_3$ nanotube and (**b**) $La_{0.60}Ca_{0.41}Co_{0.99}O_3$ nanoparticle as electrocatalyst [34] (Reproduced with permission from *J. Electrochem. Soc.*, **152**, A2071 (2005). Copyright 2005, The Electrochemical Society)

A unique $La_{0.59}Ca_{0.41}CoO_3$ nanotube material is obtained by the thermal decomposition of its precursor within alumina membranes [34]. The length and diameter of the nanotubes are, respectively, 50 μm and 200 nm, with a surface area of 20 m^2/g. Air electrodes with nanotubes as catalysts exhibit better stability in the OER process than those with the corresponding nanoparticles, as shown in Fig. 14.12.

A nanoporous amorphous manganese oxide obtained by reducing a permanganate salt with organic compounds shows high catalytic activity for the two-electron ORR shown in reaction (14.10), thanks to its high defect concentration [35]. A nanostructured hollandite-type manganese dioxide shows ORR catalytic activity better than lambda-MnO_2 when mixed with mesocarbon microbeads and used as the air electrode in zinc–air batteries [36].

An interesting report on the ORR activity of silver catalysts demonstrates that the electron transfer numbers for large (174 nm) and small (4 nm) silver particles are, respectively, 4 and 3, indicating that silver nanoparticles are catalytically active for both reactions (14.1) and (14.10), particularly at high current regions [37]. Single-walled CNTs decorated with 3- to 5-nm sized silver particles show promising properties as ORR electrodes with high conductivity [38]. Figure 14.13 clearly shows the particle-size effect.

Nanocrystalline spinel $Co_xMn_{3-x}O_4$ is a highly active electrocatalyst for both ORR and OER processes owing to its high surface area and abundant defects [39]. First-principles calculation indicates that the surface of the cubic $Co_xMn_{3-x}O_4$ phase gives more stable molecular oxygen adducts than the corresponding tetragonal phase, leading to higher activity in the ORR but lower activity in the OER, which agrees with the experimental results.

A unique approach to form active ORR electrodes is to use conductive polymers. A poly(ethylenedioxythiophene) layer coated on a porous membrane exhibits stable ORR activity for more than 1,000 h [40].

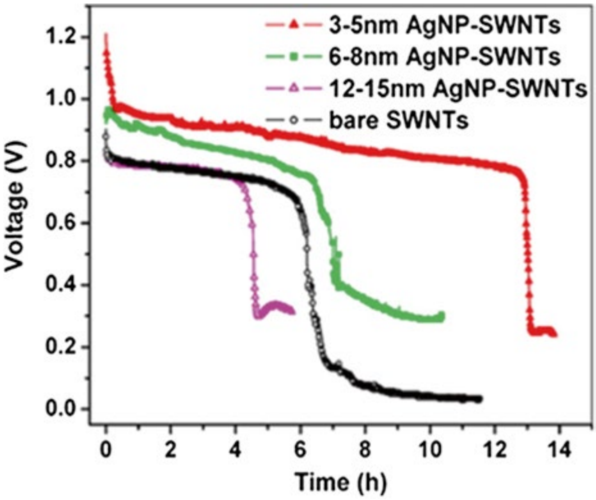

Fig. 14.13 Discharge with constant resistance of Zn–air batteries using gas diffusion electrodes based on AgNPs (silver nanoparticles)-SWNTs (single-walled carbon nanotubes) with AgNPs of various sizes (Reprinted from J. Power Sources 195, Wang T, Kaempgen M, Nopphawan P, Wee G, Mhaisalar S, Srinivasan M, Silver nanoparticle-decorated carbon nanotubes as bifunctional gas-diffusion electrodes for zinc-air batteries, p. 4354, Copyright (2010) with permission from Elsevier)

14.4 Nanotechnology Used in Nonaqueous Systems

Nonaqueous systems have been intensively examined since a report on a lithium system with a polymer electrolyte [41]. The handling of the electrolyte makes the nonaqueous system feasible only for electrical rechargeable batteries, and therefore a bifunctional air electrode is necessary. Nonaqueous electrolytes allow for the use of aluminum or magnesium as the negative electrode material, but for the time being only the lithium system has been studied and some rechargeability of the system has been demonstrated [42]. Nanotechnology studies on highly reactive metal elements are rare due to the difficulty in handling such elements. In this section, nanotechnology employed in the field of air electrodes is summarized.

14.4.1 Substrate

A problem associated with the nonaqueous type of metal–air battery is that the discharge product, $MO_{n/2}$ in reaction (14.3) or MO_n in reaction (14.9), is mostly

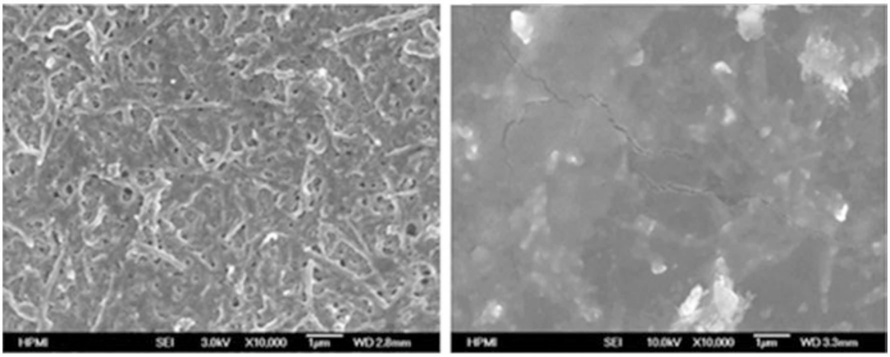

Fig. 14.14 Scanning electron microscopy images of air electrode surfaces at (*left*) separator and (*right*) air sides following discharge at 0.1 mA/cm^2 [43] (Reproduced with permission from *J. Electrochem. Soc.*, **157**, A955 (2010). Copyright 2010, The Electrochemical Society)

insoluble in electrolyte solution and deposits in the air electrode to fill the air inlet, leading to the termination of discharging. Single-walled CNTs or carbon nanofibers prepared as freestanding buckypaper (sheet made from aggregate CNTs) without using binders show good discharge performance without any loaded catalysts, but the pores on the air side of the electrodes are gradually filled with the discharge products, as shown in Fig. 14.14 [43]. An electrode with larger pores near the air side would exhibit a longer discharging period than a uniformly porous electrode.

14.4.2 Catalyst

Highly active nano-sized catalysts have also been developed in nonaqueous systems. Nano-sized γ-MnOOH obtained by $KMnO_4$ reduction with sucrose and $MnSO_4$ exhibits ORR activity as an air electrode catalyst when incorporated into lithium–air batteries [44]. MnO_x particles (20 to 50 nm in diameter) loaded on a carbon substrate exhibit a larger capacity than the commercialized electrolytic manganese dioxide, but the cyclability is insufficient, as shown in Fig. 14.15, due to the formation of solid Li_2O_2 filling the electrode pores [45]. Nano-sized platinum/gold particles loaded on a carbon substrate exhibit a high charge–discharge efficiency of 77 % at a rate of 50 mA g^{-1} (carbon) [46]. It has been demonstrated that platinum and gold respectively function as catalysts for OER and ORR processes, and therefore the mixture offers a highly active bifunctional electrocatalyst in lithium–air batteries.

14.5 Nanotechnology Used in Aqueous Lithium Systems

The behavior of bifunctional air electrodes in nonaqueous media is currently under intense investigation, as described in Sect. 14.4. Nevertheless, it seems that the difficulty in achieving high activity and durability is even harder than in aqueous

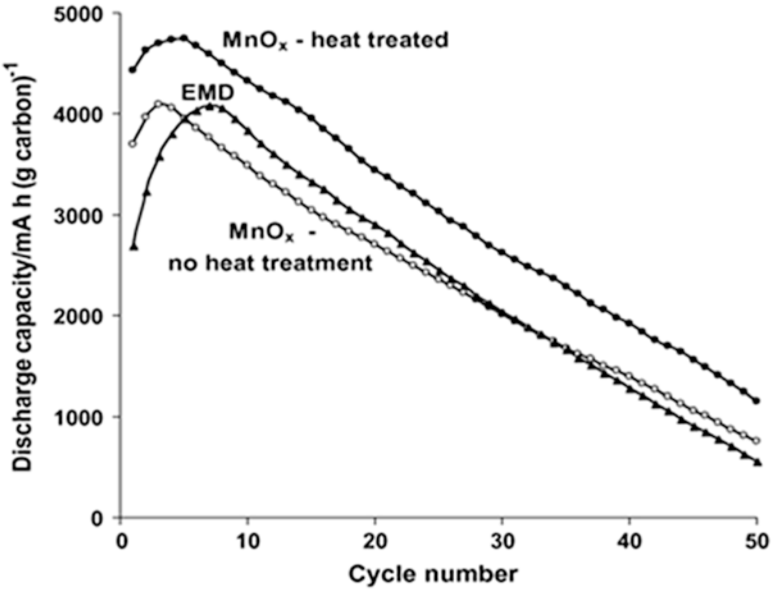

Fig. 14.15 Relationship between specific capacity and cycle number for Li–air batteries with carbon-supported manganese oxide (heat-treated or untreated) or electrolytic manganese dioxide (EMD) oxygen electrodes (Reprinted from J. Power Sources 195, Cheng G, Scott K, Carbon-supported manganese oxide nanocatalysts for rechargeable lithium-air batteries, p. 1372, Copyright (2010) with permission from Elsevier)

media. On this basis, trials are being conducted to use the established air electrode technology in aqueous media while utilizing the attractive features of metallic lithium negative electrodes. That is, air electrodes in aqueous media and lithium negative electrodes in nonaqueous media are separated by a lithium-conductive solid electrolyte to form lithium–air batteries, as shown in Fig. 14.1c. The main issue is to develop solidly constructed waterproof electrolytes between the aqueous and nonaqueous sections. A combination of a polymer membrane and a solid electrolyte is often used for this purpose. Nanotechnology can be used to decrease interfacial resistance as follows.

The interfacial resistance of poly(ethylene oxide) with a $LiN(SO_2CF_3)_2$ salt is reduced when $BaTiO_3$ nano-sized fillers are introduced into the polymer matrix [47]. Then a water-stable lithium electrode can be fabricated by setting this polymer membrane as a buffer layer in between a metallic lithium and lithium-ion conductive glass ceramics. Thus fabricated water-stable lithium electrode shows good rechargeability, as demonstrated in Fig. 14.16, when a LiCl aqueous solution and Pt black are respectively used as the electrolyte and the air electrode.

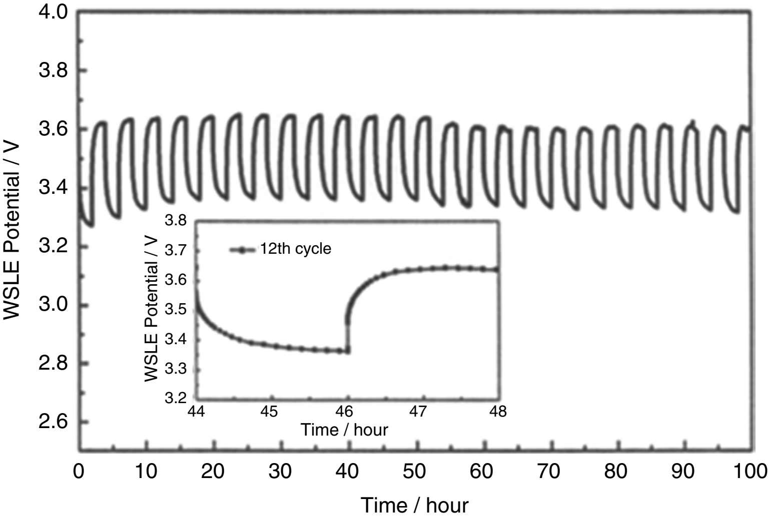

Fig. 14.16 Lithium electrode potentials for lithium dissolution/deposition in water-stable lithium electrode/1 M LiCl +0.002 M LiOH/Pt black, air cell at 0.3 mA cm^{-2} and at 60 °C (Reproduced with permission from *Electrochemistry*, **78**, 361(2010). Copyright 2010, The Electrochemical Society of Japan)

References

1. R.P. Hamlen, Metal/air batteries, in *Handbook of Batteries*, ed. by D. Linden, 2nd edn. (McGraw-Hill, New York, 1996)
2. H. Arai, M. Hayashi, Secondary batteries – metal-air systems, overview (Secondary and prmary), in *Encyclopedia of Electrochemical Power Sources*, ed. by J. Garche, C. Dyer, P. Moseley, Z. Ogumi, D. Rand, B. Scrosati, vol. 4 (Elsevier, Amsterdam, 2009)
3. H. Arai, S. Müller, O. Haas, AC impedance analysis of bifunctional air electrodes for metal-air batteries. J. Electrochem. Soc. **147**, 3584–3591 (2000)
4. T. Sakai, T. Iwaki, Z. Ye, D. Noréus, O. Lindström, Air-metal hydride battery construction and evaluation. J. Electrochem. Soc. **142**, 4040–4045 (1995)
5. R. Jain, T.C. Adler, F.R. McLarnon, E.J. Cairns, Development of long-lived high-performance zinc-calcium/nickel oxide cells. J. Appl. Electrochem. **22**, 1039–1048 (1992)
6. T.C. Adler, F.R. McLarnon, E.J. Cairns, Low-zinc-solubility electrolyte for use in zinc/nickel oxide cells. J. Electrochem. Soc. **140**, 289–294 (1993)
7. S. Müller, F. Holzer, O. Haas, Optimized zinc electrode for the rechargeable zinc-air battery. J. Appl. Electrochem. **28**, 895–898 (1998)
8. J.Z. Wu, J.P. Tu, Y.F. Yuan, X.L. Wang, L. Zhang, R.L. Li, J. Zhang, Ag-modification improving the electrochemical performance of ZnO anode for Ni/Zn secondary batteries. J. Alloys Compd. **479**, 624–628 (2009)
9. C.C. Yang, W.C. Chien, P.W. Chen, C.Y. Wu, Synthesis and characterization of nano-sized calcium zincate powder and its application to Ni-Zn batteries. J. Appl. Electrochem. **39**, 39–44 (2009)
10. M. Ma, J.P. Tu, Y.F. Yuan, X.L. Wang, K.F. Li, M.F., Z.Y. Zeng, Electrochemical performance of ZnO nanoplates as anode materials for Ni/Zn secondary batteries. J. Power Sources **179**, 395–400 (2008)

11. S. Martirosyan, Zinc electrode with reduced dendritic propagation. J. Power Sources **172**, 984–987 (2007)
12. K. Vijayamohanan, T.S. Balasubramanian, A.K. Shukla, Rechargeable alkaline iron electrodes. J. Power Sources **34**, 269–285 (1991)
13. L. Öjefors, Self-discharge of the alkaline iron electrode. Electrochim. Acta **21**, 263–266 (1974)
14. R.S. Schrebler Guzmán, J.R. Vilche, A.J. Arvía, The potentiodynamic behaviour of iron in alkaline solutions. Electrochim. Acta **24**, 395–403 (1979)
15. M. Pourbaix, *Atlas of Electrochemical Equilibria in Aqueous Solutions* (Pergamon Press, London, 1966)
16. R.D. Armstrong, I. Baurhoo, Solution soluble species in the operation of the iron electrode in alkaline solution. J. Electroanal. Chem. Interfacial Electrochem. **34**, 41–46 (1972)
17. B.T. Hang, M. Egashira, I. Watanabe, S. Okada, J. Yamaki, S.H. Yoon, I. Mochida, The effect of carbon species on the properties of Fe/C composite for metal–air battery anode. J. Power Sources **143**, 256–264 (2005)
18. B.T. Hang, H. Hayashi, S.H. Yoon, S. Okada, J. Yamaki, Fe_2O_3-filled carbon nanotubes as a negative electrode for an Fe–air battery. J. Power Sources **178**, 393–401 (2008)
19. C. Li, W. Ji, J. Chen, Z. Tao, Metallic aluminum nanorods: synthesis via vapor-deposition and applications in Al/air batteries. Chem. Mater. **19**, 5812–5814 (2007)
20. W. Li, C. Li, C. Zhou, H. Ma, J. Chen, Metallic magnesium nano/mesoscale structures: their shape-controlled preparation and Mg/air battery applications. Angew. Chem. Int. Ed. **45**, 6009–6012 (2006)
21. P.N. Ross, M. Sattler, The corrosion of carbon black anodes in alkaline electrolyte. J. Electrochem. Soc. **135**, 1464–1470 (1988)
22. L. Swette, N. Kackley, S.A. McCatty, Oxygen electrodes for rechargeable alkaline fuel cells. J. Power Sources **36**, 323–339 (1991)
23. J. Prakash, D.A. Tryk, E.B. Yeager, Kinetic investigations of oxygen reduction and evolution reactions on lead ruthenate catalysts. J. Electrochem. Soc. **146**, 4145–4151 (1999)
24. G.Q. Zhang, X.G. Zhang, Y.G. Wang, A new air electrode based on carbon nanotubes and Ag-MnO_2 for metal air electrochemical cells. Carbon **42**(15), 3097–3102 (2004)
25. K. Gong, P. Yu, L. Su, S. Xiong, L. Mao, Polymer-assisted synthesis of manganese dioxide/carbon nanotube nanocomposite with excellent electrocatalytic activity toward reduction of oxygen. J. Phys. Chem. C **111**(5), 1882–1887 (2007)
26. Y. Qian, S. Lu, F. Gao, Synthesis of manganese dioxide/reduced graphene oxide composites with excellent electrocatalytic activity toward reduction of oxygen. Mater. Lett. **65**(1), 56–58 (2011)
27. A. Weidenkaff, S.G. Ebbinghaus, T. Lippert, $Ln_{1-x}A_xCoO_3$ (Ln = Er, La; A = Ca, Sr)/carbon nanotube composite materials applied for rechargeable Zn/air batteries. Chem. Mater. **14**(4), 1797–1805 (2002)
28. D. Thiele, E.L. Colmenarejo, B. Grobety, A. Zuettel, Synthesis of carbon nanotubes on $La_{0.6}Sr_{0.4}CoO_3$ as substrate. Diam. Relat. Mater. **18**(1), 34–38 (2009)
29. M. Yuasa, M. Nishida, T. Kida, N. Yamazoe, K. Shimanoe, Bi-functional oxygen electrodes using $LaMnO_3$/$LaNiO_3$ for rechargeable metal-air batteries. J. Electrochem. Soc. **158**(5), A605–610 (2011)
30. Y. Shimizu, K. Uemura, H. Matsuda, N. Miura, N. Yamazoe, Bi-functional oxygen electrode using large surface area $Li1\text{-}_xCa_xCoO_3$ for rechargeable metal-air battery. J. Electrochem. Soc. **137**, 3430–3433 (1990)
31. M. Hayashi, H. Uemura, K. Shimanoe, N. Miura, N. Yamazoe, Enhanced electrocatalytic activity for oxygen reduction over carbon-supported $LaMnO_3$ prepared by reverse micelle method. Electrochem. Solid State Lett. **1**(6), 268–270 (1998)
32. M. Yuasa, K. Shimanoe, Y. Teraoka, N. Yamazoe, High-performance oxygen reduction catalyst using carbon-supported La-Mn-based perovskite-type oxide. Electrochem. SolidState Lett. **14**(5), A67–69 (2011)
33. S. Imaizumi, K. Shaimanoe, Y. Teraoka, N. Miura, N. Yamazoe, Preparation of carbon-supported Perovskite-type oxides $LaMn_{1-y}Fe_yO_{3+}\delta$ based on reverse homogeneous precipitation method. J. Electrochem. Soc. **151**(10), A1559–1564 (2004)

34. G. Zhang, J. Chen, Synthesis and application of $La_{0.59}Ca_{0.41}CoO_3$ nanotubes. J. Electrochem. Soc. **152**, A2069–A2073 (2005)
35. J. Yang, J.J. Xu, Nanoporous amorphous manganese oxide as electrocatalyst for ORR in alkaline solutions. Electrochem. Commun. **5**(4), 306–311 (2003)
36. G.Q. Zhang, X.G. Zhang, MnO_2/MCMB electrocatalyst for all solid-state alkaline zinc-air cells. Electrochim. Acta **49**(6), 873–877 (2004)
37. J.J. Han, N. Li, T.Y. Zhang, Ag/C nanoparticles as an cathode catalyst for a zinc-air battery with a flowing alkaline electrolyte. J. Power Sources **193**(2), 885–889 (2009)
38. T. Wang, M. Kaempgen, P. Nopphawan, G. Wee, S. Mhaisalar, M. Srinivasan, Silver nanoparticle-decorated carbon nanotubes as bifunctional gas-diffusion electrodes for zinc-air batteries. J. Power Sources **195**(13), 4350–4355 (2010)
39. F. Cheng, J. Shen, B. Peng, Y. Pan, Z. Tao, J. Chen, Rapid room-temperature synthesis of nanocrystalline spinels as oxygen reduction and evolution electrocatalysts. Nature Chem. **3**, 79–84 (2011)
40. B. Winther-Jensen, O. Winter-Jensen, M. Forsyth, D. Macfarlane, High rates of oxygen reduction over a vapor phase-polymerized PEDOT electrode. Science **321**(5889), 671–674 (2008)
41. K.M. Abraham, Z. Jiang, A polymer electrolyte-based rechargeable lithium/oxygen battery. J. Electrochem. Soc. **143**, 1–5 (1996)
42. T. Ogasawara, A. Débart, M. Holzapfel, P. Novák, P.G. Bruce, Rechargeable Li_2O_2 electrode for lithium batteries. J. Am. Chem. Soc. **128**, 1390–1393 (2006)
43. G.Q. Zhang, J.P. Zheng, R. Liang, C. Zhang, B. Wang, M. Hendrickson, E.J. Plichta, Lithium-air batteries using SWNT/CNF buckypapers as air electrodes. J. Electrochem. Soc. **157**(8), A953–A956 (2010)
44. V.M.B. Crisostomo, J.K. Ngala, S. Alia, C.H. Chen, X. Shen, S.L. Suib, A. Dobley, C. Morein, New synthetic route, characterization, and electrocatalytic activity of Nanosized manganite. Chem. Mater. **19**(7), 1832–1839 (2007)
45. G. Cheng, K. Scott, Carbon-supported manganese oxide nanocatalysts for rechargeable lithium-air batteries. J. Power Sources **195**(5), 1370–1374 (2010)
46. Y.C. Lu, Z. Xu, H.A. Gasteiger, S. Chen, K. Hamad-Schiferli, Y. Shao-Horn, Platinum-gold nanoparticles: a highly active bifunctional electrocatalyst for rechargeable lithium-air batteries. J. Am. Chem. Soc. **132**(35), 12170–12171 (2010)
47. T. Zhang, S. Liu, N. Imanishi, A. Hirano, Y. Takeda, O. Yamamoto, Water-stable lithium electrode and its application in aqueous lithium/air secondary batteries. Electrochemistry **78**(5), 360–362 (2010)

Chapter 15
Lithium–Air Batteries

Tao Zhang and Nobuyuki Imanishi

15.1 Aqueous Lithium–Air Batteries

The prerequisite for obtaining a practical aqueous lithium–air secondary battery is the development of a water-stable lithium electrode (WSLE) that can survive lithium stripping/deposition for a long lifespan in an aqueous electrolyte. This type of electrode was preliminarily addressed using the concept of a composite lithium anode with a three-layer construction as proposed by Visco et al. in 2004 [7]. This electrode concept adopts a water-stable NASICON-type lithium-conducting solid glass ceramic as a protective layer that covers and isolates the lithium metal from direct contact with the aqueous electrolyte. Conductivity and stability are key properties of glass ceramics.

15.1.1 Conductivity and Stability of Lithium-Conducting Glass Ceramics

At present, most research on WSLEs has utilized the $Li_{1+x+y}Ti_{2-x}Al_xP_{3-y}Si_yO_{12}$ (LTAP) glass ceramic provided by Ohara in Japan [9]. A typical LTAP plate has a thickness of around 260 μm and an ionic conductivity of 3.5×10^{-4} S cm^{-1} at 25 °C and 1.4×10^{-3} S cm^{-1} at 60 °C, as shown in Fig. 15.1. The stability of WSLEs in aqueous electrolytes is dependent on the sealing technology and the tolerance of LTAP to the aqueous electrolyte. The stability of the LTAP plate in acidic and alkaline aqueous electrolytes has been studied in detail. Figure 15.2 shows scanning electron microscopy (SEM) images of a LTAP plate that was immersed in aqueous solutions of various pH at 50 °C for 3 weeks. Conductivity measurements revealed

---

T. Zhang • N. Imanishi (✉)
Mie University, Tsu, Japan
e-mail: imanishi@chem.mie-u.ac.jp

T. Osaka and Z. Ogumi (eds.), *Nanoscale Technology for Advanced Lithium Batteries*,
Nanostructure Science and Technology 182, DOI 10.1007/978-1-4614-8675-6_15,

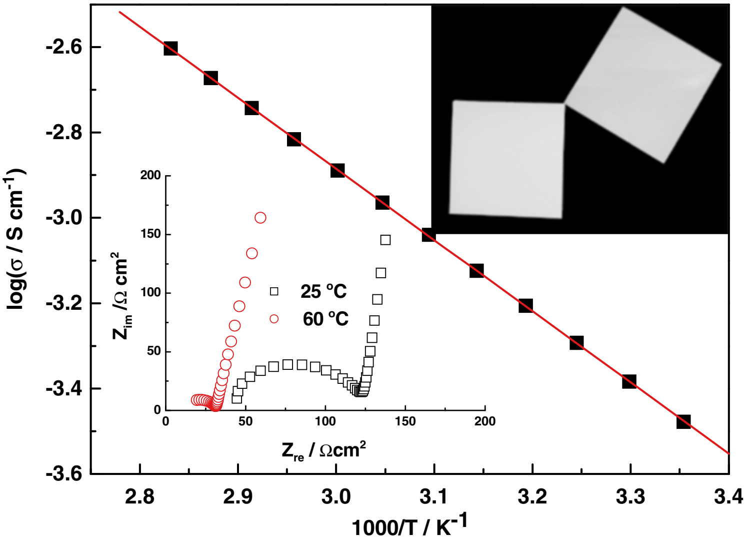

Fig. 15.1 Impedance spectra of Au/LTAP/Au and Arrhenius plots of conductivity of LTAP plate

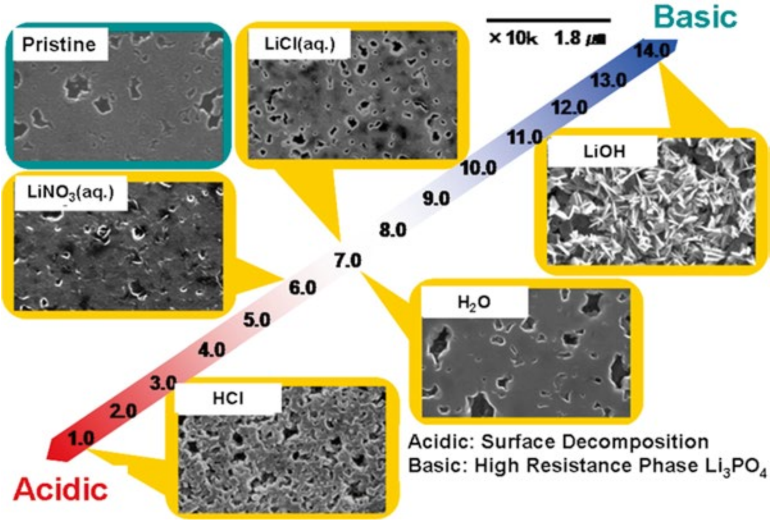

Fig. 15.2 SEM images of LTAP immersed in various aqueous solutions at 50 °C for 3 weeks

that the LTAP plate was unstable in acid and alkaline aqueous solution but more stable in lithium-ion-saturated solutions, such as LiCH$_3$COO-saturated CH$_3$COOH-H2O solution [10] and XXX-saturated LiOH solution [11]. Table 15.1 summarizes the electrical conductivity of LTAP plates immersed in various LiCl-LiOH-H$_2$O solutions at 50 °C for 3 weeks. The stability of LTAP in the XXX-saturated LiOH

Table 15.1 Electrical conductivity of LTAP plate immersed in various LiCl-LiOH-H_2O solutions at 50 °C for 3 weeks

LiOH (mol L^{-1})	LiCl (mol L^{-1})	pH	Conductivity at 25 °C ($\times 10^{-4}$ S cm^{-1})
0.57	0	–	0.27
0.057	0	12.78	0.58
0.0057	0	11.91	1.7
0.00057	0	10.91	2.0
3.6	8.1	9.53	2.51
5.0	11.8	8.25	2.61
2.3	10.4	7.64	2.55

aqueous solution suggests the possibility of developing an aqueous alkaline lithium–air battery with high energy density because the reaction product is LiOH and the electrolyte is saturated with LiOH at deep discharge.

Weppner and colleagues reported a new garnet-type lithium-ion-conducting solid electrolyte of $Li_7La_3Zr_2O_{12}$ that exhibited lithium stability with a high ionic conductivity of 2.4×10^{-4} S cm^{-1} at 25 °C [12]. $Li_{7-x}La_3Zr_2O_{12-1/2x}$ was also found to be stable in the XXX saturated aqueous solution [13]; the stability of this promising solid electrolyte with lithium metal should be further investigated because a high polarization for Li/$Li_7La_3Zr_2O_{12}$/Li was observed at a limited current density.

15.1.2 Water-Stable Lithium Electrodes

Selection of buffer layer: LTAP is unstable in direct contact with lithium metal, so a buffer layer must be used between the lithium metal and the LTAP plate. The buffer layer should have high lithium-ion conductivity and be stable in contact with lithium metal. Visco et al. proposed the deposition or evaporation of lithium-conducting solid conductive materials such as Li_3N or $Li_3(P,N)O_3$ onto the LTAP plate by a variety of techniques, including RF sputtering, e-beam evaporation, and thermal evaporation [14]. The electrical conductivity of Li_3N at room temperature is as high as 10^{-3} S cm^{-1}; however, these methods for the deposition of a protective layer are complicated and too expensive for scale-up at present.

Lithium-conducting polymer electrolytes are the other promising candidate for the buffer layer. A buffer layer based on an electrolyte consisting of polyethylene oxide (PEO) with the $Li(CF_3SO_2)N$ (LiTFSI) (O/Li = 18/1) lithium salt has been proposed due to its chemical compatibility with Li and LTAP [15]. A typical WSLE construction with a PEO-based electrolyte as the buffer layer is shown in Fig. 15.3. The ionic conductivity of PEO_{18}LiTFSI is 5×10^{-4} S cm^{-1} at 60 °C. The bulk conductivity of PEO can be increased by the addition of nano-sized ceramic fillers such as Al_2O_3, SiO_2, and $BaTiO_3$ [16] or room-temperature ionic liquids such as *N-methyl-N*-propylpiperidinium TFSI (PP13TFSI) [17].

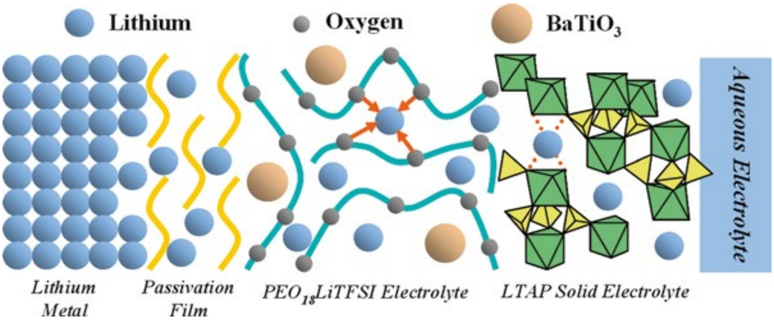

Fig. 15.3 Schematic diagram of proposed WSLE with $PEO_{18}LiTFSI$-$BaTiO_3$ buffer layer and LTAP

Interfacial resistance and dendrite formation: the interfacial resistance of WSLEs is somewhat complicated. Typical impedance spectra of Li/$PEO_{18}LiTFSI$-10 wt%$BaTiO_3$/LTAP/aqueous LiCl solution/Pt show a small semicircle at high frequency and a large semicircle at low frequency [16]. Analysis of the impedance profiles indicates that the small semicircle corresponds to a polymer electrolyte and LTAP grain boundary resistances and the large semicircle represents the resistance of a passivation film, the interfacial resistance between the polymer electrolyte and LTAP, and the charge-transfer resistance. Comparison of the impedance of Li/$PEO_{18}LiTFSI$/LTAP/Li/$PEO_{18}LiTFSI$/Li and Li/$PEO_{18}LiTFSI$/Li symmetrical cells indicates that the interfacial resistance calculated for $PEO_{18}LiTFSI$/LTAP is around 40 % that of the Li/$PEO_{18}LiTFSI$ interface. The high interface resistance between lithium and polymer electrolytes has been known to be reduced by the addition of oxide fillers [16]. The addition of PP13TFSI to $PEO_{18}LiTFSI$ has also been shown to decrease the interfacial resistance. It was suggested that the addition of nanofillers significantly reduces the growth rate of the lithium passivation layer, probably due to the trapping of residual impurities that promote the formation of compact thin passivation layers on the Li–polymer interface [18].

Lithium dendrite formation has been observed for WSLEs during repeated discharge–charge processes. In the early stage of lithium battery research, lithium metal was mostly used as an anode material. There have been many reports regarding severe lithium dendrite formation experienced with conventional organic electrolytes [19]; therefore, such organic electrolytes may not be suitable for the protective layer between lithium and LTAP. Lithium dendrite formation can be suppressed using a polymer electrolyte. The mechanism of dendrite growth in Li/polymer electrolyte/Li has been extensively studied by Brissot et al. [20] with the aid of a direct in situ observation technique and simultaneous cell potential evaluation. Recently, a visualization cell was employed that indicated acid-modified nano-SiO_2 and PP13TFSI [17] additives to the $PEO_{18}LiTFSI$ buffer layer were very effective at suppressing lithium dendrite formation. Table 15.2 shows the results for dendrite formation at the interface of lithium and various electrolytes. The capacity of a cell

Table 15.2 Dendrite formation onset time and capacity of lithium electrode with 10-µm-thick copper current collector

Electrolyte	Temperature (°C)	Current density (mA cm^{-2})	Onset time (h)	Capacity (mAh g^{-1})
PEO$_{18}$LiTFSI	60	0.5	15	688
		0.1	125	1,025
PEO$_{18}$LiTFSI-1.44PP13TFSI	60	1.0	17	1,270
		0.5	35	1,300
EC-DMC-EMC-LiPF$_6$	15	1.0	0.2	22
PAN-PC-EC-LiPF$_6$	Room temperature	1.0	1	100

with a liquid electrolyte, calculated according to the weight of a 10-µm-thick copper current collector and the weight of lithium deposited up to the onset time of dendrite formation, was much lower than that of a cell using a polymer electrolyte. The onset time of lithium dendrite formation was increased from 15 to 35 h at 0.5 mA cm^{-2} by the addition of PP13TFSI to PEO$_{18}$LiTFSI up to 1.44 mol, which corresponds to a specific capacity of 1,300 mAh g^{-1}. This capacity is acceptable for lithium–air batteries.

15.1.3 Polarization Behavior of WSLEs in Aqueous Electrolytes

Figure 15.4 shows the change in the lithium electrode potential over time at various current densities [16]. The open-circuit voltage (OCV) for the cell was 3.80 V at 60 °C, which is comparable to that calculated from the following cell reaction:

$$2\mathrm{Li} + 1/2\mathrm{O}_2 + \mathrm{H}_2\mathrm{O} = 2\mathrm{LiOH} \quad (15.1)$$

The multilayer Li anode showed a stable OCV for a period of 3 months and low charge and discharge polarization. At a current density of 0.1 mA cm^{-2}, the discharge anode potential was 3.75 V and the charge potential was 3.82 V, which indicates that the polarization for lithium oxidation and reduction is low. The polarization behavior for discharge and charge at 0.5 mA cm^{-2} was only slightly higher than at 0.1 mA cm^{-2}.

The high potential of lithium–air batteries at 3.8 V means that there is some concern regarding the stability of aqueous lithium–air batteries. It may simply be regarded that water will decompose at such a high cell voltage. However, the Li/PEO$_{18}$LiTFSI/LTAP/1M LiCl aqueous solution/Pt cell exhibited a stable cell voltage of 3.80 V for a long period over 3 months and good charge–discharge performance. The electrochemical window of aqueous electrolytes can be analyzed by the Pourbaix diagram shown in Fig. 15.5. The potential between the aqueous

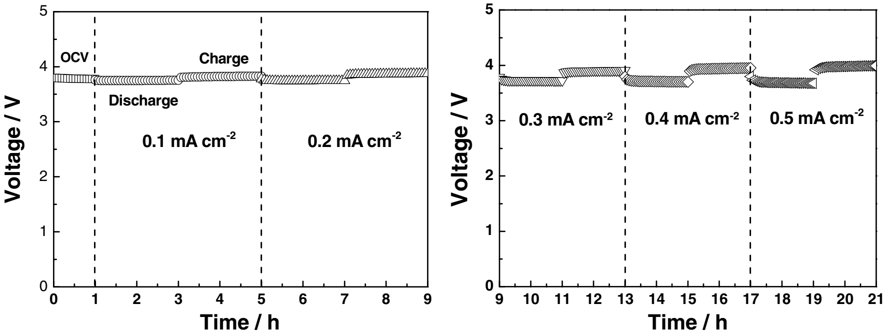

Fig. 15.4 Lithium electrode potential change with time for Li/PEO$_{18}$LiTFSI-10 wt% BaTiO$_3$/LTAP/aqueous 1M LiCl/Pt, air cell at 60 °C and at various current densities

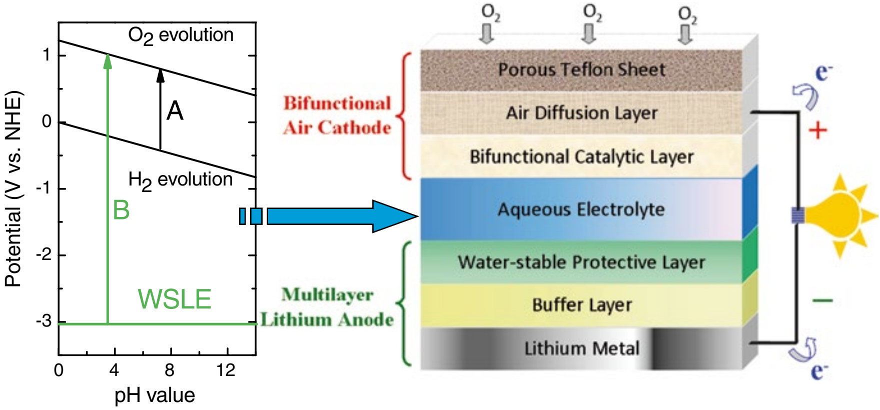

Fig. 15.5 Pourbaix diagram and schematic view of aqueous lithium–air battery

electrolyte and air electrode is estimated to be less than 1.22 V because the potential between the lithium metal and polymer electrolyte is 3.04 V. Detailed information and further illustration of the change in the cell potential of the WSLE/LiCl aqueous solution/Pt air cell are given in the literature [21]. Zhou and colleagues also obtained reversible discharge–charge curves using a Li/organic electrolyte/LTAP/aqueous electrolyte/graphene cathode air cell for 50 cycles, which suggests the stability of aqueous electrolytes [22].

15.1.4 A Prototype Aqueous Lithium–Air Cell

A schematic diagram of a prototype aqueous rechargeable lithium–air battery is presented in Fig. 15.6 [23]. The air cathode utilizes porous carbon including

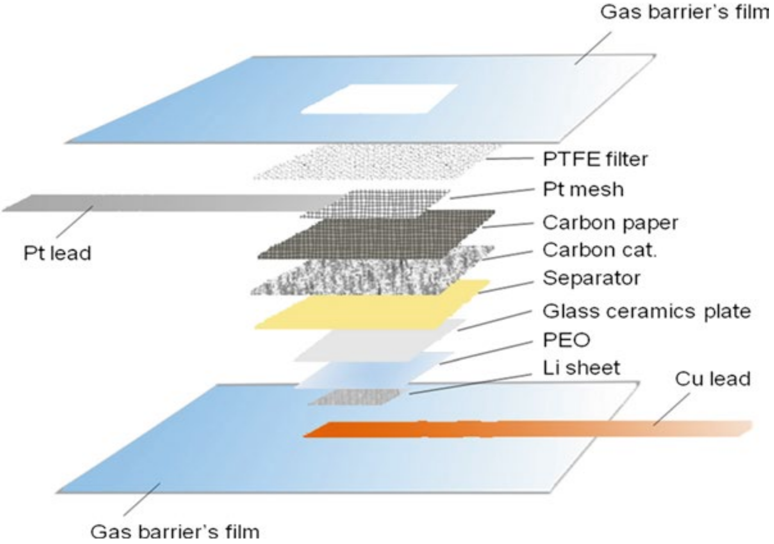

Fig. 15.6 Schematic diagram of prototype acidic lithium–air cell

superfine Pt particles (1–4 nm for acid electrolyte) or oxides (alkaline solution) as catalyst. Flat discharge and charge potentials at current densities up to 1.0 mA cm^{-2} were obtained for the acid cell with HAc-H_2O-LiAc. A discharge capacity of 225 mAh g^{-1} was obtained for 56 % HAc utilization. The estimated energy density from the weight of the lithium anode and HAc was as high as 779 Wh kg^{-1}, which is twice that of the conventional graphite/$LiCoO_2$ cell. This prototype lithium–air cell can retain a discharge–charge capacity of 250 mAh g^{-1} within 15 cycles, as shown in Fig. 15.7, and the cell voltage difference in the discharge and charge at 0.5 mA cm^{-2} was around 0.75 V. The cell reaction for this Li/HOAc/air system can be expressed as

$$2\mathrm{Li} + 1/2\mathrm{O_2} + 2\mathrm{CH_3COOH} = 2\mathrm{CH_3COOLi} + \mathrm{H_2O} \tag{15.2}$$

Compared with Eq. 15.1, high molecular weight acetic acid is involved in reaction (15.2); thus, the energy density was calculated to be 1,319 Wh kg^{-1} (including oxygen) with a measured cell OCV of 3.69 V, which is approximately 60 % lower than that of a nonaqueous system but approximately three times higher than that of lithium-ion batteries.

As shown in the previous section, the water-stable lithium-ion-conducting solid electrolyte LTAP is stable in XXX-saturated aqueous solution, which has a low pH of 8.25. Therefore, saturated XXX aqueous solution could be used as the electrolyte. The lithium–air cell reaction in alkaline solution is

$$4\mathrm{Li} + \mathrm{O_2} + 6\mathrm{H_2O} = 4\mathrm{LiOH{\bullet}H_2O} \tag{15.3}$$

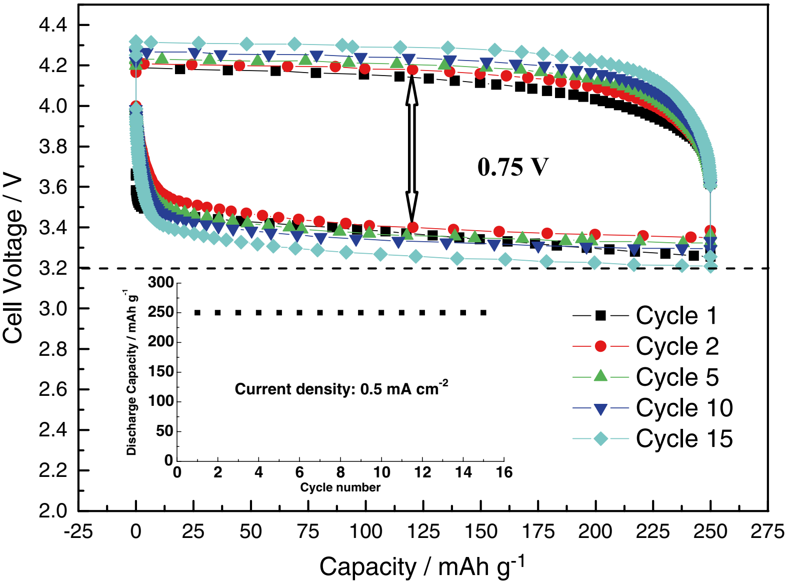

Fig. 15.7 Charge–discharge performance of prototype acidic lithium–air cell

LiOH in the electrolyte is saturated at approximately 10 % discharge depth. The cell voltage is dependent on the air electrode catalyst. The OCV in LiCl- and XXX-saturated aqueous solutions was around 3.0 V. The calculated energy density from Eq. 15.3 is 2,370 Wh kg^{-1} for the discharged state (excluding O_2) and 1,916 Wh kg^{-1} for the charged state (including O_2). These energy densities are decreased by the addition of LiCl to 1,866 and 1,573 Wh kg^{-1}, respectively. The calculated energy densities are four times higher than that of the conventional lithium-ion battery. A preliminary result for the charge–discharge performance of the Li/PEO_{18}LiTFSI/LTAP/XXX-saturated aqueous solution/Pt black cell at 60 °C is shown in Fig. 15.8. The performance of the saturated XXX aqueous lithium–air cell is similar to that of the acid solution lithium–air cell. Less noble metals and oxides could be used as catalysts for oxygen reduction/evolution reactions in alkaline solutions.

15.1.5 Bifunctional Air Electrodes for Aqueous Lithium–Air Cell

Bifunctional oxygen/air electrodes for the oxygen reduction reaction (ORR) and oxygen evolution reaction (OER) have been developed for zinc–air rechargeable batteries. Research on rechargeable zinc–air batteries with alkaline solutions started in the mid-1960s. Bifunctional oxygen electrodes consume oxygen during the discharge process, whereas oxygen is evolved during the charge process. Research on

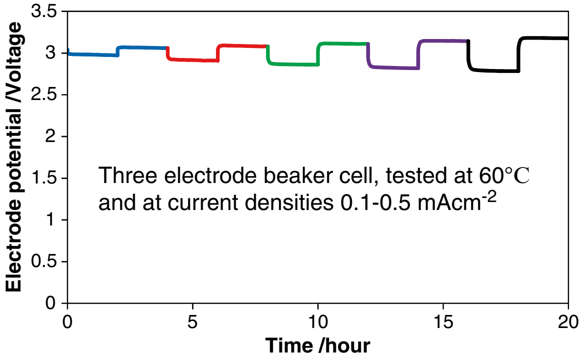

Fig. 15.8 Discharge–charge curves of Li/PEO$_{18}$LiTFSI-10 wt% BaTiO$_3$/LTAP/aqueous 15 M LiCl + 5 M LiOH/Pt, air cell

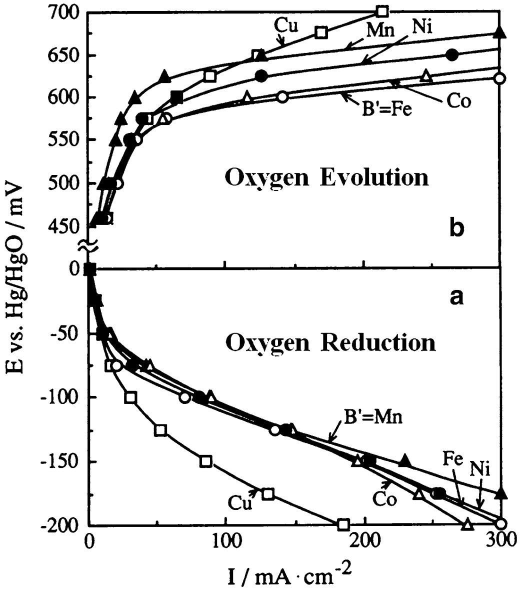

Fig. 15.9 Polarization curves showing (**a**) ORR and (**b**) OER for bifunctional air cathodes using PTFE bonded carbon loaded with 25 % La$_{0.6}$Ca$_{0.4}$Co$_{0.8}$B'$_{0.2}$O$_3$ (B' = Mn, Fe, Co, Ni, Cu) in 7 M KOH at 25 °C [24]

bifunctional catalysts has, until now, been focused mainly on perovskite, spinel, and pyrochlore oxides. Figure 15.9 shows polarization curves for bifunctional air cathodes of the perovskite-type oxide, La$_{1-x}$A$_x$B$_{1-y}$B$_y$'O$_3$, in 7 M KOH aqueous solution [24]. The current densities for the ORR were as large as approximately 200 mA cm^{-2} at −150 mV vs. Hg/HgO for all bifunctional catalysts except for that of B' = Cu, which had an exceptionally small surface area. Compared with the ORR, the OER activity was more dependent on the B′ cations, resulting in the following order of activity at +600 mV: Fe>Co>Ni>Mn. The OER current density with B′ = Fe reached 300 mA cm^{-2} at 620 mV. Unfortunately, the Co-based catalysts were found to be unstable in alkaline solutions. Thus, the Co-free perovskites of $La_{1-x}A'_xFe_{1-y}Mn_yO_3$ (A′ = La, Ca, Sr, Ba), which exhibited both chemical stability and bifunctional activity, were studied further. The OER activity was strongly dependent on the A′ cations, resulting in the order Sr>Ca>>Ba>>La. The HO_2^- decomposition reaction was found to be the rate-determining step for $La_{1-x}Ca_xFe_{0.8}Mn_{0.2}O_3$ in both the ORR and OER processes.

Ruthenium-based pyrochlores are also quite effective catalysts for the ORR and OER due to their metallic conductivity and high surface area. Lead- and iridium-substituted $Pb_2Pb_xRu_{1-x}O_{6.5}$ and $Pb_2Ru_xIr_{1-x}O_{6.5}$ pyrochlores exhibit better catalytic activity for the ORR and OER and significantly higher stability during the OER than their unsubstituted counterparts [25]. The spinel oxides, especially cobaltites such as MCo_2O_4 [M = Co(II), Ni(II)] and $CuCo_{3-x}O_4$ were also shown to have activity for the ORR and OER in alkaline solutions, which was strongly dependent on the preparation procedure and the nature of the initial precursors. Undoped and Li^+-doped $Co_{3-x}O_4$ spinel films prepared by a low-temperature sol–gel route had large surface areas and remarkable OER performance in 1 M KOH. In general, ion-site substitution, which has been widely studied, and size or surface nanocrystallization, which has been applied in some noble-metal bifunctional catalysts such as Pt and Ag [26], can be considered promising solutions to obtain applicable ORR and OER bifunctional catalysts.

15.2 Lithium–Air Batteries with Organic Electrolytes

In organic electrolytes, lithium metal contacts with the electrolyte directly and forms a solid electrolyte interface (SEI), which protects the metal from further reaction with the electrolyte. The SEI is an ionic conductor and an electronic insulator. The SEI allows H_2O molecules to form LiOH on the surface of lithium metal and, hence, lead to rapid capacity fade. This is evidence that the moisture in air will penetrate into the cell to contaminate the organic electrolyte. Adopting aprotic electrolytes and hydrophobic membranes may suppress but still cannot rule out this problem because moisture-penetration-free membranes have yet to be developed.

The fundamental cathode discharge reactions are considered to be

$$2\mathrm{Li} + \mathrm{O}_2 \rightarrow \mathrm{Li}_2\mathrm{O}_2; \mathrm{U} = 2.959\,\mathrm{V}, \tag{15.4}$$

and possibly

$$2\mathrm{Li} + (1/2)\mathrm{O}_2 \rightarrow \mathrm{Li}_2\mathrm{O}; \mathrm{U} = 2.913\,\mathrm{V}. \tag{15.5}$$

Single-cell Li–air battery tests followed by ex situ Raman spectroscopy have revealed Li_2O_2 as the major discharge product [3]. Gravimetric analysis and in situ mass spectrometry [5] demonstrated that the Li_2O_2 formed upon discharge was decomposed into Li and O_2 during the charge cycle, both with and without a catalyst. Oxygen adsorption measurements during discharge suggested a mixture of Li_2O_2 and Li_2O formation whose ratio was affected by the discharge rate and electrolyte formulation [4]. For instance, low oxygen concentration in the electrolyte would favor the formation of Li_2O over Li_2O_2. Therefore, the reaction mechanism for the ORR and OER in organic electrolytes still requires more evidential elucidation through further research. Although both Li_2O_2 and Li_2O are insoluble in organic electrolytes, it seems that reaction (15.4) is reversible, whereas reaction (15.5) is irreversible. Thus, the energy density is calculated as 3,456 Wh kg^{-1} (including oxygen) using reaction (15.4), controlling the resultant product as Li_2O_2, which is approximately 80 % higher than that for the aqueous system (including oxygen).

The research on nonaqueous systems has been emphasized mainly with three aspects: (1) investigation of electrolytes with low volatility and low moisture absorption, such as polyacrylonitrile-based plasticized polymers [3]; (2) evaluation and optimization of the electrolyte and air cathode formulation, such as improvement of the oxygen transport properties in electrolytes with appropriate viscosity and O_2 solubility [6], reduction of wetting and flooding of the carbon-based air electrode by increasing electrolyte polarity [27], and selection of air cathodes with suitable physical properties, e.g., thickness, porosity, and volume fraction of carbon [4]; and (3) searching for efficient catalysts to decrease the polarization potential during discharge–charge processes, i.e., the round-trip efficiency. The catalysts for ORR and OER are the main topics for nonaqueous systems. For instance, electrolytic manganese oxide or α-MnO_2 nanowires were utilized to improve the reversibility of cathode reactions, eventually achieving a high capacity of 600 mAh g^{-1} after 50 cycles [28]. In addition, Lu and coworkers found that Au/C had very high ORR activity, while Pt/C exhibited extraordinarily high OER activity in a 1 M $LiClO_4$ propylene carbonate (PC)/dimethyl carbonate (DMC) electrolyte [29]. A mixture of PtAu nanoparticles exhibited bifunctional catalytic activity, increasing the discharge voltage to above 2.7 V and lowering the charge voltage below 3.5 V at 50 mA $g^{-1}{}_{carbon}$ [30]. Ishihara et al. prepared a Pd-β-MnO_2 (mesoporous) catalyst using a SiO_2 template that also resulted in a significant reduction of the discharge and charge overpotential [31].

Organic-carbonate-based electrolytes (e.g., $LiPF_6$ in propylene carbonate) have been the most widely used in nonaqueous systems to date. However, it was recently reported that such electrolytes decompose in Li-O_2 cells upon discharge rather than form Li_2O_2 [8, 32]. Therefore, the most important research subject at the moment is to find an acceptable nonaqueous electrolyte.

15.3 Lithium–Air Batteries with Ionic Liquid Electrolytes

The ionic liquid referred to here is defined as a molten salt $[A^+][X^-]$ with a melting point below room temperature that serves as a solvent to dissolve some amount of lithium salts $[Li^+][X^-]$ to form a new ionic liquid $[Li^+]_m[A^+]_n[X^-]_{(m+n)}$ (ionic liquid

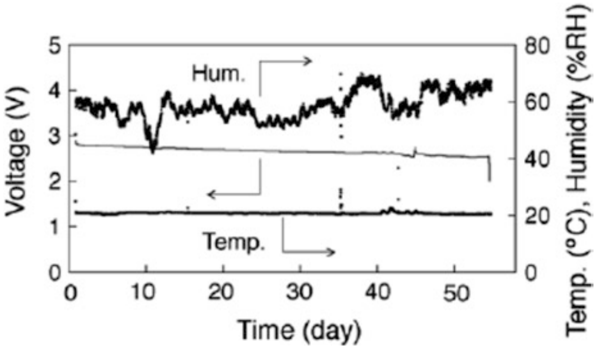

Fig. 15.10 Discharge curve and effect of humidity on discharge profile for 0.5 M LiTFSI-EMITFSI electrolyte at 0.01 mA cm^{-2} in air [34]

electrolytes). This neoteric electrolyte consists of only two cations and one anion, providing an all-ionic environment when coordinating with lithium metal, which is an essential difference from the aqueous and organic electrolytes. Compared with the conventional molecular solvent-type electrolytes, ionic liquids are characterized by low and even negligible vapor pressure that primarily satisfies the requirement of lithium–air batteries for the stability of the electrolyte in an ambient-open system. It is well known, and has also been noted in our research, that the evaporation of organic solvent or water gain/loss can cause a lithium–air battery to fail before delivering full capacity and can thus critically limit the energy output. Therefore, nonvolatility occupies a central position in the application of ionic liquids to lithium–air batteries.

Nonflammability is another fundamental property of ionic liquids that has significant advantages with respect to safety concerns. In addition, different series of ionic liquids possess other special physical or electrochemical performance appropriate for lithium–air battery applications. Quaternary ammonium (QA) cation-imide combinations exhibit high electrochemical stability, especially for the reduction reaction [33]. Among them, certain QA ionic liquids, for example 1-ethyl-3-methylimidazolium bis(trifluoromethylsulfonyl)amide (EMITFSI), are almost immiscible in water. Kuboki et al. reported an extremely high discharge capacity of 5,360 mAh g^{-1} for a primary lithium–air battery using the hydrophobic EMITFSI + 0.5 M LiTFSI at a current density of 0.01 mA cm^{-2}. The cell was operated for 56 days in air; the discharge curve is shown in Fig. 15.10 [34]. The QA ionic liquid of N-methyl-N-propylpiperidinium (PP13)TFSI has been demonstrated to be electrochemically stable against O_2 radicals. Mizuno and Iba studied the discharge–charge products of a carbon/MnO_2 cathode in PP13TFSI electrolyte and reported Li_2O_2 deposition and O_2 evolution [35]. It has been speculated that PP13TFSI favors the two-electron reduction path of oxygen to peroxide and then forms the reversible Li_2O_2 product, which is beneficial for the charge process.

At present, the novelty of ionic liquids and the very recent revival of high-energy-density lithium–air batteries means that there are few reports on ionic liquids as electrolytes for lithium–air batteries and the research results are extremely limited. Research issues that would be noticed in the future include, at least, the following three aspects: (1) the process of SEI formation and lithium dissolution/deposition in ionic liquids, (2) the electrochemical oxygen reduction/evolution reactions and the oxygen dissolution and physical transport behavior in ionic liquids, and (3) the effect of the high viscosity of ionic liquids on lithium transport and methods to synthesize new or optimize present ionic liquids.

15.4 All-Solid-State Lithium–Air Batteries

All-solid-state lithium-ion batteries have attracted much interest with respect to their safety advantages. In addition, with respect to lithium–air batteries, such consideration has also been anticipated in regard to the more important evaporation and contaminant problems of liquid electrolytes. Recently, Kumar and colleagues reported a totally solid-state, rechargeable lithium–air battery [36]. The cell is generally a five-layer laminate construction: Li anode/polymer-ceramic (Li_2O)/ high Li-ion-conducting glass ceramic/polymer-ceramic (boron nitride)/air diffusion cathode. The key component of the solid-state lithium–air battery is the high Li-ion-conducting glass ceramic, which corresponds to the $18.5Li_2O$:$6.07Al_2O_3$:37.05GeO_2:37.05P_2O_5 (LAGP) molar composition. It serves not only as the solid-state electrolyte of the lithium–air battery, but also as a component of the air cathode for the internal lithium ion pathway. The two polymer-ceramic membranes are electrochemically coupled to the lithium anode and air cathode with a solid-state electrolyte, which reduces the impedance of the cell and enhances the charge transfer ($Li^0 \rightarrow Li^+ + e^-$) at the anode. The cell exhibited excellent thermal stability and rechargeability in a range of 30–105 °C. The charge–discharge current densities ranged from 0.05 to 0.25 mA cm^{-2} over 40 cycles. The reversible charge–discharge voltage profiles and the equilibrium OCV of 3.1 V suggest that the electrochemical reaction in all probability proceeds according to Eq. 15.6, with Li_2O_2 as the reaction product:

$$2Li + O_2 \leftrightarrow Li_2O_2 \tag{15.6}$$

The authors have reported that the presently measured energy density is approximately 750 Wh kg^{-1} based on the weight of the cell, including an allowance for packaging, and they anticipate that a specific energy of over 1,000 Wh kg^{-1} could be realized when the Li–air cell is fully developed.

All-solid-state lithium–air batteries are attractive with respect to safety issues and the anticipation of long operation time, although some important problems remain. Changes at the solid/solid boundary during discharge/charge, especially at the lithium–solid electrolyte interface in a deep discharge state, remain to be detected. The mechanism of ORR/OER at the cathode also remains unclear, and the current density is limited by the low reactive kinetics at the solid–solid boundary.

References

1. H.F. Bauman, G.B. Adams, Lithium-water-air battery automotive propulsion. Technical Report, Lockheed Palo Alto Research Labs., (1976)
2. S.R. Younesi, K. Ciosek, K. Edstrom, Lithium oxygen batteries; challenges and possibilities. The 214th Electrochemical Society Meeting, Abstract 0465. (Honolulu, 2008)
3. K.M. Abraham, Z. Jiang, A polymer electrolyte-based rechargeable lithium/oxygen battery. J. Electrochem. Soc. **143**, 1–5 (1996)
4. J. Read, Characterization of the lithium/oxygen organic electrolyte battery. J. Electrochem. Soc. **149**, A1190–A1195 (2002)
5. T. Ogasawara, A. Débart, M. Holzapfel, P. Novák, P.G. Bruce, Rechargeable Li_2O_2 electrode for lithium batteries. J. Am. Chem. Soc. **128**, 1390–1393 (2006)
6. J. Read, K. Mutolo, M. Ervin, W. Behl, J. Wolfenstine, A. Driedger, D. Foster, Oxygen transport properties of organic electrolytes and performance of lithium/oxygen battery. J. Electrochem. Soc. **150**, A1351–A1356 (2003)
7. S.J. Visco, E. Nimon, B. Katz, L.C.D. Jonghe, M.Y. Chu, Lithium metal aqueous batteries. The 12th International Meeting on Lithium Batteries, Abstract 53. (Nara, 2004)
8. S.A. Freunberger, Y.H. Chen, Z.Q. Peng, J.M. Griffin, L.J. Hardwick, F. Bardé, P. Novák, P.G. Bruce, Reactions in the rechargeable lithium-O2 battery with alkyl carbonate electrolytes. J. Am. Chem. Soc. **133**, 8040–8047 (2011)
9. J. Fu, Lithium ion conductive glass ceramics. U.S. Patent 5,702,995, 1997
10. Y. Shimonishi, T. Zhang, N. Imanishi, D.M. Im, D.J. Lee, A. Hirano, Y. Takeda, O. Yamamoto, N. Sammes, A study on lithium/air secondary batteries-stability of the NASICON-type lithium ion conducing solid electrolyte in alkaline aqueous solutions. J. Power Sources **196**, 5128–5132 (2011)
11. Y. Shimonishi, T. Zhang, P. Johnson, N. Imanishi, A. Hirano, O. Yamamoto, N. Sammes, A study on lithium/air secondary batteries-stability of NASICON-type glass ceramics in acid solutions. J. Power Sources **195**, 6187–6191 (2010)
12. R. Murugan, V. Thangadurai, W. Weppner, Fast lithium ion conduction in garnet-type $Li_7La_3Zr_2O_{12}$. Angew. Chem. Int. Ed. **46**, 7778–7781 (2007)
13. Y. Shimonishi, A. Toda, T. Zhang, A. Hirano, N. Imanishi, O. Yamamoto, Y. Takeda, Synthesis of garnet-type $Li_{7-x}La_3Zr_2O_{12-1/2x}$ and its stability in aqueous solutions. Solid State Ion. **183**, 48–53 (2011)
14. S.J. Visco, Y.S. Nimon, B.D. Katz, Ionically conductive composites for protection of active metal anodes. U.S. Patent 728,229,6B2, 2007
15. T. Zhang, N. Imanishi, S. Hasegawa, A. Hirano, J. Xie, Y. Takeda, O. Yamamoto, N. Sammes, Li/polymer electrolyte/water stable lithium-conducting glass ceramics composite for lithium-air secondary batteries with an aqueous electrolyte. J. Electrochem. Soc. **155**, A965–A969 (2008)
16. T. Zhang, N. Imanishi, S. Hasegawa, A. Hirano, J. Xie, Y. Takeda, O. Yamamoto, N. Sammes, Water-stable lithium anode with the three-layer construction for aqueous lithium-air secondary batteries. Electrochem. Solid State Lett. **12**, A132–A135 (2009)
17. S. Liu, N. Imanishi, T. Zhang, A. Hirano, Y. Takeda, O. Yamamoto, J. Yang, J. Electrochem. Soc. **157**, A1092–A1098 (2010)
18. F. Croce, G.B. Appetecchi, L. Persi, B. Scrosati, Nanocomposite polymer electrolytes for lithium batteries. Nature **394**, 456–458 (1998)
19. H.E. Park, C.H. Hong, W.Y. Yoon, The effect of internal resistance on dendritic growth on lithium metal electrodes in the lithium secondary batteries. J. Power Sources **178**, 765–768 (2008)
20. C. Brissot, M. Rosso, J.N. Chazalviel, P. Baudry, S. Lascaud, In situ study of dendritic growth in Li/PEO-salt/Li cells. Electrochim. Acta **43**, 1569–1574 (1998)
21. T. Zhang, N. Imanishi, Y. Takeda, O. Yamamoto, Aqueous lithium/air rechargeable batteries. Chem Lett. **40**, 668–673 (2011)
22. E.J. Yoo, H.S. Zhou, Li-air rechargeable battery based on metal-free grapheme nanosheet catalysts. ACS Nano **5**, 3020–3026 (2011)

23. T. Zhang, N. Imanishi, Y. Shimonishi, A. Hirano, Y. Takeda, O. Yamamoto, N. Sammes, A novel high energy density rechargeable lithium/air battery. Chem. Commun. **46**, 1661–1663 (2010)
24. Y. Shimizu, H. Matsuda, N. Miura, N. Yamazoe, Bi-functional oxygen electrode using large surface area perovskite-type oxide catalyst for rechargeable metal-air batteries. Chem. Lett. **21**, 1033–1036 (1992)
25. L. Jörissen, Bifunctional oxygen/air electrodes. J. Power Sources **155**, 23–32 (2006)
26. T. Wang, M. Kaempgen, P. Nopphawan, G. Wee, S. Mhaisalkar, M. Srinivasan, Silver nanoparticle-decorated carbon nanotubes as bifunctional gas-diffusion electrodes for zinc-air batteries. J. Power Sources **195**, 4350–4355 (2010)
27. W. Xu, J. Xiao, J. Zhang, D. Wang, J.G. Zhang, Optimization of nonaqueous electrolytes for primary lithium/air batteries operated in ambient environment. J. Electrochem. Soc. **156**, A773–A779 (2009)
28. A. Débart, A.J. Paterson, J.L. Bao, P.G. Bruce, Alpha-MnO_2 nanowires: a catalyst for the O_2 electrode in rechargeable lithium/air batteries. Angew. Chem. Int. Ed. **47**, 4521–4524 (2008)
29. Y.C. Lu, H.A. Gasteiger, M.C. Parent, V. Chiloyan, S.H. Yang, The influence of catalysts on discharge and charge voltages of rechargeable Li-oxygen batteries. Electrochem. Solid State Lett. **13**, A69–A72 (2010)
30. Y.C. Lu, Z.C. Xu, H.A. Gasteiger, S. Chen, H.S. Kimberly, S.H. Yang, Platinum-gold nanoparticles: a highly active bifunctional electrocatalyst for rechargeable lithium-air batteries. J. Am. Chem. Soc. **132**, 12170–12171 (2010)
31. T. Ishihara, A.K. Thapa, Y. Hidaka, S. Ida, Preparation of porous MnO_2 and repeat property for Li-air rechargeable battery. in *The 51st Battery Symposium in Japan,* Abstract No. 3B02, Nagoya, 2010
32. F. Mizuno, S. Nakanishi, Y. Kotani, S. Yokoishi, H. Iba, Rechargeable Li-air batteries with carbonate-based liquid electrolytes. Electrochemistry **78**, 403–405 (2010)
33. H. Matsumoto, M. Yanagida, K. Tanimoto, M. Nobura, Y. Kitagawa, Y. Miyazaki, Highly room temperature molten salts based on small trimethylalkylammonium cations and bis(trifluoromethylsulfonyl)imide. Chem. Lett. **29**, 922–923 (2000)
34. T. Kuboki, T. Okuyama, T. Ohsaki, N. Takami, Lithium-air batteries using hydrophobic room temperature ionic liquid electrolyte. J. Power Sources **146**, 766–769 (2005)
35. F. Mizuno, H. Iba, Reaction control of rechargeable lithium-oxygen battery. in *The 51st Battery Symposium in Japan*, Abstract No. 3B06, Nagoya 2010
36. B. Kumar, J. Kumar, R. Leese, J.P. Fellner, S.J. Rodrigues, K.M. Abraham, A solid-state, rechargeable, long cycle life lithium-air battery. J. Electrochem. Soc. **157**, A50–A54 (2010)

Chapter 16
Nano Aspects of Lithium/Sulfur Batteries

Ho-Suk Ryu, Hyo-Jun Ahn, Ki-Won Kim, and Jou-Hyeon Ahn

16.1 Lithium/Sulfur Batteries

Rechargeable lithium batteries have been developed as power sources for mobile applications such as portable electronic devices and electric vehicles. The practical capacities of current systems such as $LiC_6/LiCoO_2$, $Li/LiMn_2O_4$, and Li/V_6O_{13} are normally in the range of 100–150 Wh kg^{-1} (theoretical specific energies are in the range of 425–890 Wh kg^{-1}). The battery capacity of a lithium-ion system is mainly determined by the capacities of its positive electrodes, which are typically in the range of 150–200 mAh g^{-1}, though this is limited by the extent of lithium intercalation into transition metal oxides [1–3].

In the pursuit of an inexpensive and safe energy storage material with high capacity (or energy) levels, elemental sulfur has garnered considerable interest. By combining lithium metal and elemental sulfur at the theoretical specific capacities of 3,830 and 1,675 mAh g^{-1}, respectively, as electrode materials in a battery, a theoretical specific energy of 2,600 Wh kg^{-1} can be generated, assuming a complete reaction to give the product Li_2S [4–7].

The theoretical energy provided by Li/S cells exceeds that provided by lithium-ion batteries, which are *widely used as the power source in electronic devices*, by a significant margin in terms of both the specific and volumetric energy densities, as shown in Fig. 16.1.

However, Li/S cells have serious problems like a low active material utilization and, thus, low efficiency and a poor cycle life. Sulfur is an insulating material, which means its cathodes need higher amounts of conducting materials like carbon, decreasing the sulfur content in the cathode, which in turn results in a decrease in the energy density per cell.

H.-S. Ryu • H.-J. Ahn (✉) • K.-W. Kim • J.-H. Ahn
WCU and PRC of Gyeongsang National University,
900 Gajwa-dong, Jinju 660-701, South Korea
e-mail: ahj@nongae.gsnu.ac.kr

T. Osaka and Z. Ogumi (eds.), *Nanoscale Technology for Advanced Lithium Batteries*,
Nanostructure Science and Technology 182, DOI 10.1007/978-1-4614-8675-6_16,

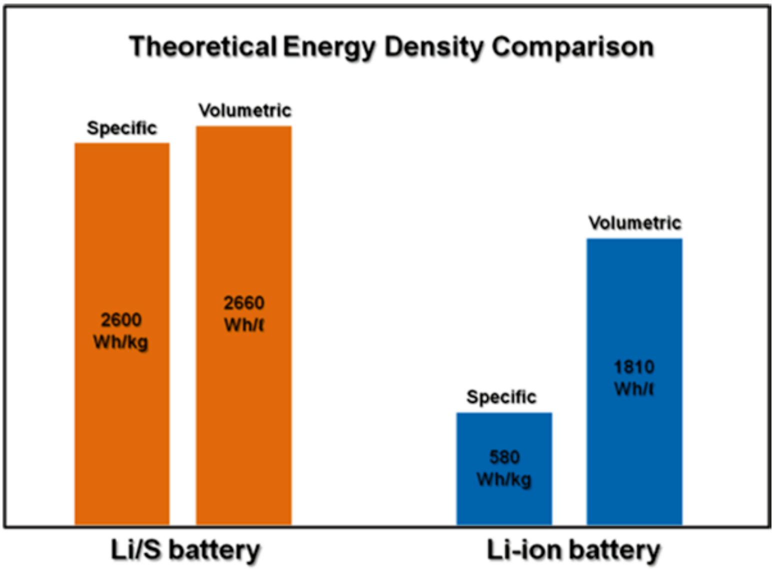

Fig. 16.1 Comparison of specific and volumetric energy densities of Li/S battery and Li-ion batteries

Soluble lithium polysulfides are produced by the discharge reaction of sulfur and can be dissolved in the electrolytes used, resulting in many problems. They cannot return to the cathode for further discharge reactions and can travel to lithium anodes and react with lithium, which ultimately results in a low material utilization of sulfur.

The low active material utilization upon cycling is associated with leads in the form of soluble polysulfides as a reaction product in electrolyte [8–14]. During the discharging of a Li/S battery, a dense and nonuniform Li_2S solid film covers the carbon matrix of the sulfur cathode. The Li_2S passivation layer affects the charge–discharge efficiency and the rate capability of Li/S batteries. The oxidization of reduced polysulfide to elemental sulfur rarely occurs, and a part of the Li_2S is left in the carbon matrix of the sulfur cathode, even in a fully charged state. The remaining Li_2S can be regarded as an irreversible loss of active material. This irreversible Li_2S develops in the carbon matrix and increases as the cyclability increases, resulting in capacity fading in Li/S batteries [7, 10, 15–18].

16.2 Principles of a Lithium/Sulfur Cell

The reduction–oxidation reaction mechanism of Li/S batteries is different from the intercalation–deintercalation mechanism of commercial secondary lithium-ion batteries [9]. Lithium metal is oxidized to give lithium ions, and sulfur reacts with lithium ions during the subsequent discharge; the reverse process occurs during the charging process.

Negative electrode:

$$2\text{Li} \rightarrow 2\text{Li}^+ + 2\text{e}^- \left(\text{anodic reaction during discharge}\right) \tag{16.1}$$

Positive electrode:

$$\text{S} + 2\text{e}^- \rightarrow \text{S}^{2-} \left(\text{cathodic reaction during discharge}\right) \tag{16.2}$$

Overall discharge reaction (formation of Li_2S):

$$2\text{Li} + \text{S} \rightarrow \text{Li}_2\text{S}\left(\text{full reaction}\right) \tag{16.3}$$

The high capacity and rechargeability of sulfur can be achieved from the electrochemical cleavage and reformation of a sulfur-sulfur bond in the cathode.

Previous studies indicated that the discharge process of a cathode consists of two main steps. First, elemental sulfur (S_8: cyclooctasulfur), which is the most stable form among sulfur allotropes [13], changes into various higher-order (long-chain) soluble lithium polysulfides [Li_2S_n, $n \geq 4$, Eq. 16.4], after which the polysulfides transform into lower-order (short-chain) lithium polysulfides (Li_2S_n, $n < 4$) and, finally, lithium sulfide [Li_2S, Eq. 16.5] [10, 12, 16, 19–26]:

$$2\text{Li} + n\text{S} \rightarrow \text{Li}_2\text{S}_n \left(n \geq 4\right) \tag{16.4}$$

$$\text{Li}_2\text{S}_n + \left(2n - 2\right)\text{Li} \rightarrow n\text{Li}_2\text{S} \tag{16.5}$$

Li_2S changes back into polysulfide while charging via the reverse reaction of Eq. 16.5. However, the formation of sulfur by the reverse reaction of Eq. 16.4 does not usually occur [12]. During charging, the current flow is reversed and the oxidation takes place at the positive electrode while the reduction occurs at the negative electrode. In short, the S-S bonds of sulfur-based compounds in the cathode break down to produce a series of polysulfides and sulfide during the discharging process. The S-S bonds are then reformed during the charging process [10, 12, 16, 19–26].

Based on the preceding reactions, the charge–discharge processes are schematically represented in Fig. 16.2.

16.3 History of Lithium/Sulfur Batteries

In the early 1970s, the possibility of a Li/S cell was revealed by researchers in a number of research papers. In the early stages, researchers concentrated on using sulfur in the liquid state with polysulfides as cathode materials (catholyte type). However, very poor discharge efficiencies were obtained due to the irreversibility of the polysulfides and contamination of the electrode by polysulfides [13, 27–30]. The development of a rechargeable Li/S cell was hindered by several problems,

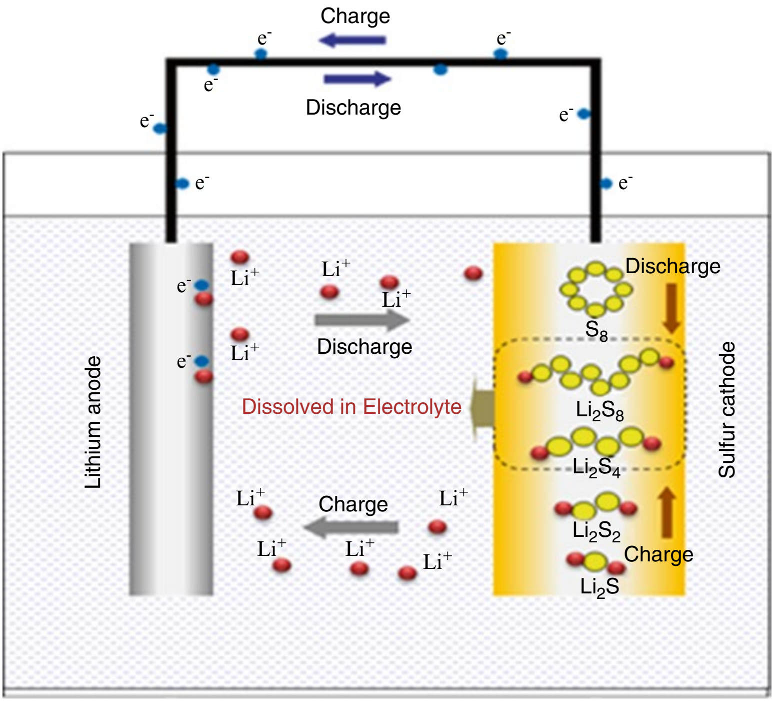

Fig. 16.2 Schematic diagram of charge–discharge process in Li/S battery

such as the insulating nature of sulfur and Li_2S, the solubility of the discharge products in electrolytes, and poor cyclability in a technologically demanding phase.

In the mid-1990s, Li/S batteries were considered commercially viable after a few patents were filed [31], after which Li/S batteries were investigated in an effort to enhance various electrochemical properties, such as the discharge capacity, cycle life, low-temperature performance, and self-discharge, and to solve problems such as the loss of the active material and the pollution of Li anodes by polysulfides dissolved in the electrolyte [8–26, 32–69]. As part of this progress, novel advances in materials design were achieved, such as protective films and improvement of the materials (active material, conducting material, binder, and additive) of sulfur cathodes and lithium anodes. In particular, nanomaterials and nanotechnologies were used, for example, in the enhancement of conductivity and in the absorption/adsorption of polysulfides and high conducting areas. Recently, a new type of Li/S cell was reported that has inspired studies showing high capacity and good cyclability. One type of Li/S battery uses sulfur embedded into nanostructured conducting materials [14, 61–68]. Other types include Li-ion batteries with a nanostructured anode as a substituent of lithium metal and another type with the cathode in “charged” state [69–71]. Research has revealed the tremendous potential of lithium/sulfur batteries.

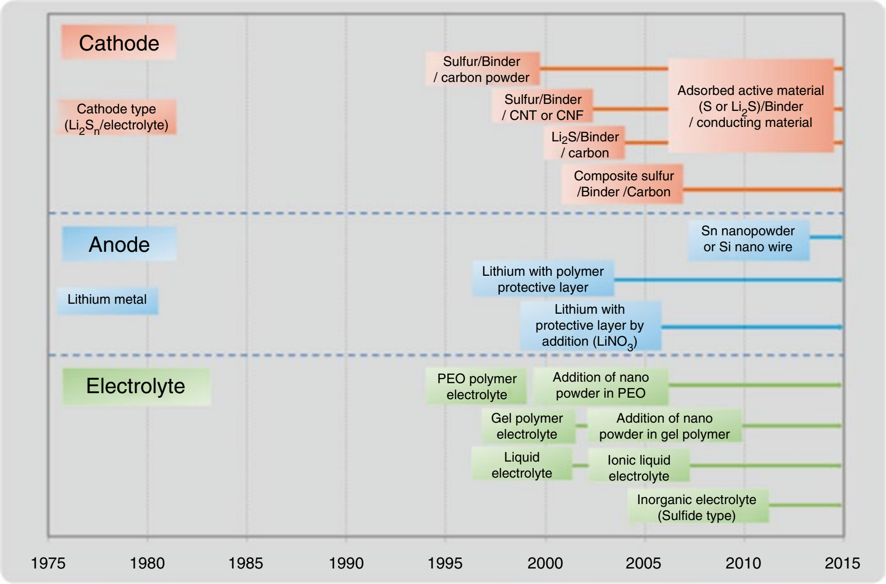

Fig. 16.3 Chart of technical transition showing papers and patents related to Li/S batteries

With the many papers and patents related to it, the technical transition of the Li/S battery is shown in Fig. 16.3.

The following section discusses how the problems of Li/S batteries were resolved by nanomaterials and nanotechnologies.

16.4 Nanomaterials in Sulfur Electrodes

A sulfur electrode is usually prepared by mixing the active material, binder, and conducting agent into an organic solvent, coating the homogeneous slurry onto a current collector, and then drying the film. Figure 16.4 shows a schematic diagram and SEM photographs of a sulfur electrode.

The initial electrochemical properties of a Li/S cell depend on a number of factors, such as the particle size and proportion of the constituents of the cathode, the homogeneity of the cathode film, and the thickness and porosity of the cathode. Specifically, one of the most important factors is the homogeneous mixing of the sulfur, binder, and conducting material, which depends on the mixing process and composition [31].

Conducting materials such as carbon powder and an appropriate binder material are necessary to provide structural integrity for a high electrical conductivity of a sulfur electrode because sulfur has very low electrical conductivity (5×10^{-30} S cm^{-1}

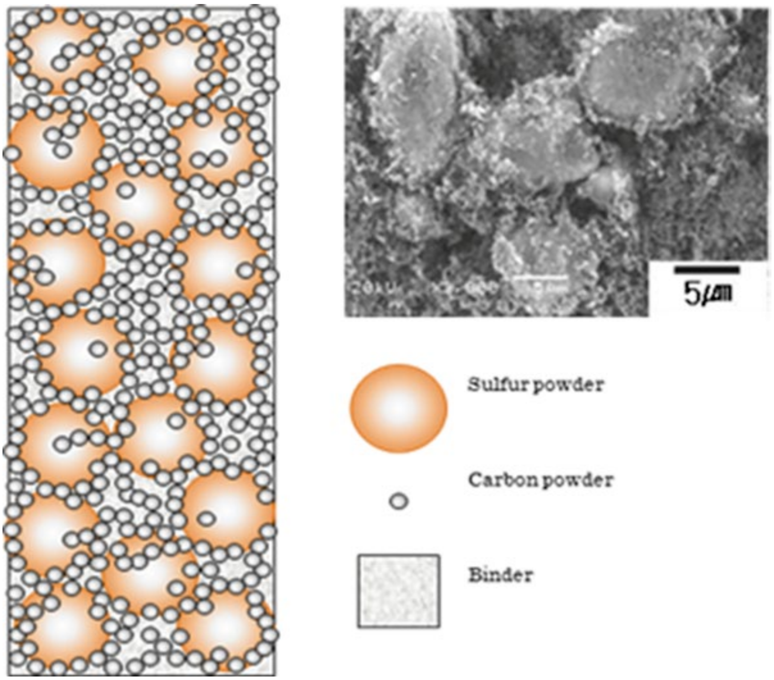

Fig. 16.4 Schematic diagram and SEM photographs of sulfur electrode

at 25 °C) as an insulating material [21, 72]. Moreover, the selection of the conducting materials is very important for producing better performance of Li/S batteries. A sulfur electrode usually contains 40–80 wt% of sulfur. Generally, higher sulfur contents lead to a decrease in the sulfur utilization and the discharge plateau potential due to the high resistance of the sulfur electrode. Carbon powder with a high surface area and good porosity is usually included in the cathode formulation as a conducting agent. Many researchers have reported the electrochemical properties of Li/S cells with various carbon ratios as cathode conducting materials [21, 22, 48, 73]. The carbon ratio for good electrochemical properties of a Li/S cell differs by type of carbon.

The initial properties of Li/S batteries are improved by the addition of nano carbon powder to the sulfur electrode. A model of the change in morphology of the cathode depending on the conducting material during cycling is given in Fig. 16.5. Although carbon powder as a type of acetylene black, Super P, or ketchen black can be added to the cathode, Li/S batteries continue to have poor cyclability. Discharge capacity can decrease during the cycling process owing to the low electric contact between sulfur and carbon caused by the aggregation of individual each carbon powder and sulfur during the cycling process [9].

To suppress aggregation, many conducting materials have been used in sulfur cathodes. One of the better conducting agents is carbon nanotube (CNT) material in the form of single-walled carbon nanotubes (SWNTs) and multiwalled carbon

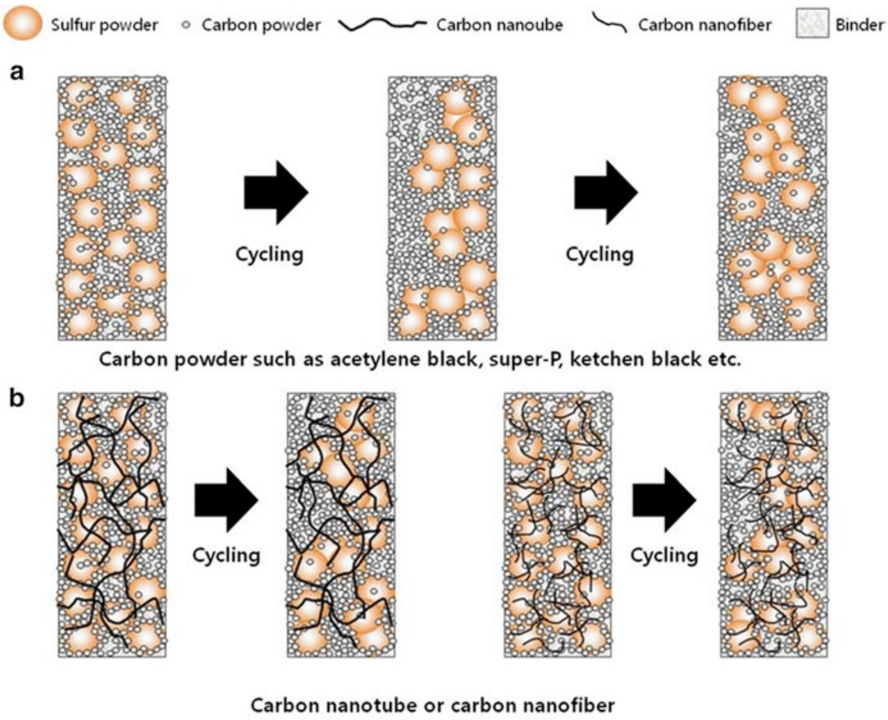

Fig. 16.5 Model of change in morphology of sulfur cathode with conductive material during cycling

nanotubes (MWNTs) with a long electronic-connection chain. CNTs are very effective conducting agents that can improve cycle life and sulfur utilization. However, homogeneous mixing between CNTs and sulfur is difficult in the preparation of the cathode. Another good conducting agent is carbon nanofiber (CNF) as vapor-grown carbon fiber (VGCF) with a medium electronic-connection chain length with a large surface area. One advantage of CNF is that it is easier to handle than CNTs during the process of homogeneous mixing. CNF is also an effective conducting agent that can improve cycle life and sulfur utilization.

Some researchers have investigated attractive sulfur composites in which the cathode material is prepared by heating a mixture of polyacrylonitrile (PAN) powder and sublimed sulfur at high temperatures (>300 °C). This approach yielded new levels of performance compared to an elemental sulfur cathode. The composite cathode materials were prepared as follows: sulfur dehydrogenated PAN was used to form a conductive main chain at a high temperature, and highly polar –CN groups then cyclize to form a thermally stable heterocyclic compound in which sulfur is intercalated [37, 38]. Other researchers have studied the core–shell structure of a carbon/sulfur composite in which the composite was prepared via a simple and fast deposition reaction, showing excellent electrochemical performance in terms of the capacity, rate performance, and cyclability due to the improved conductivity caused by a uniform coating of carbon onto sulfur [65].

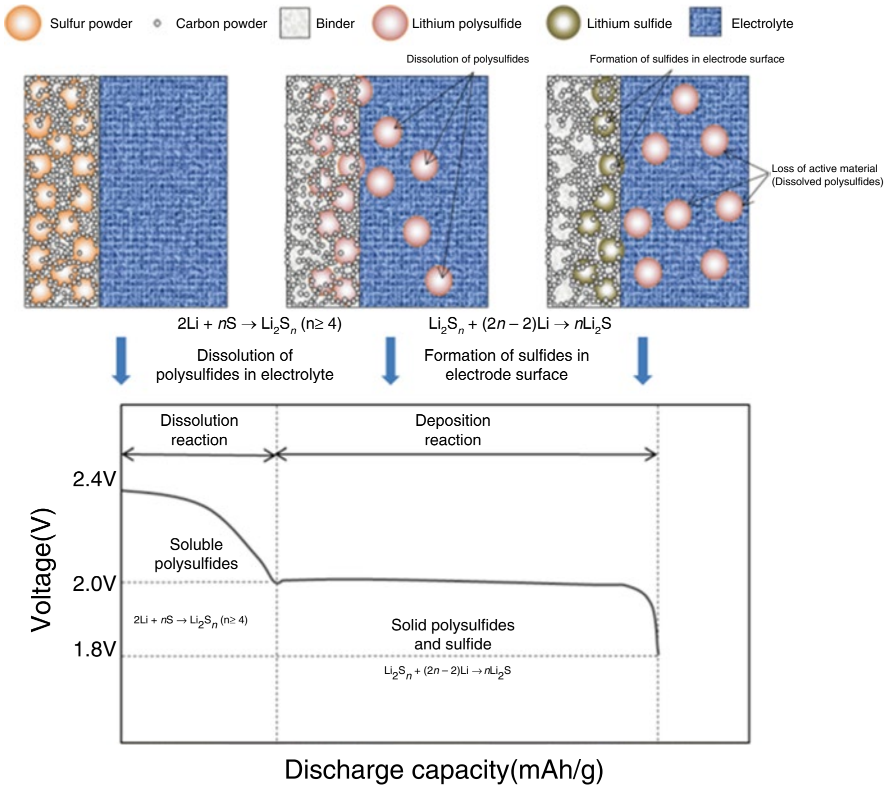

Fig. 16.6 Schematic diagram of active mass loss by dissolution in electrolyte during cycling

In cathodes, another problem was the loss of active materials. The loss of active materials, resulting in the degradation of the capacity during the cycling of the cell, is mainly due to the high solubility of the polysulfide anions that form as reaction intermediates during the cycling processes in the solvent used as electrolyte. Electrolytes are used as a charge transport medium and as an ionic conduction path within cathodes. During cycling, polysulfide anions can migrate through the electrolyte to the Li negative electrode, whereupon they are reduced to solid precipitates (Li_2S_2 or Li_2S), causing a loss of the active materials. In addition, the solid product that precipitates extensively on the surface of the positive electrode during the discharge process becomes electrochemically irreversible, which also contributes to the loss of the active mass. Figure 16.6 illustrates the active mass loss caused by dissolution in electrolyte during cycling via a schematic diagram.

In response to these considerable challenges, novel advances in materials design have been made, such as the mixing of electrolytes, the addition of filler in cathodes, and the use of protective films for lithium anodes. Combinations of solvent modification to control polysulfide dissolution in the electrolyte, the addition of nano-adsorption materials in the cathode, and the use of a protective layer material have led to some promising results. The dissolution of polysulfides in electrolyte is

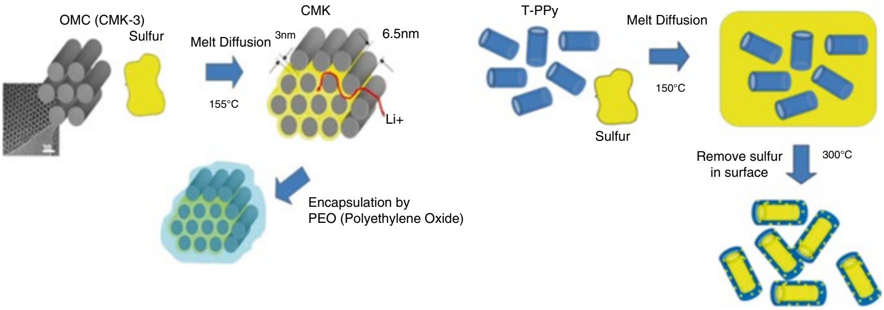

Fig. 16.7 Schematic diagrams illustrating preparation of sulfur composite electrode using mesoporous carbon and T-PPy

connected to the increase in the viscosity and the loss of active materials during cycling. Viscosity through the modified electrolyte showed only a slight increase during the cycling process [7, 21, 46, 50, 53, 55]. The reaction between lithium as an anode and the migrated polysulfide anions by dissolution in the electrolyte can be blocked by a protective layer consisting of a polymer coating [35] onto lithium metal or the addition of $LiNO_3$ in electrolyte [58, 74].

For the sulfur cathode, an adsorption material can be added. The adsorption material should have a small particle size and a large surface area so as to improve the efficiency and thus adsorb lithium polysulfides. An enhanced discharge capacity can arise due to the low electrolyte viscosity originating from the decrease in the dissolution of lithium polysulfides. Nanoceramic particles such as MgNiO, La_2O_3, and γ-Al_2O_3 have been used as adsorption materials in a sulfur cathode to prevent polysulfide dissolution in electrolyte [23, 51, 52]. A Li/S battery using an elemental sulfur cathode with nano-sized ceramic filler led to the improvement of not only the discharge capacity but also the cyclability. However, the amount of the filler added as nanoceramics (MgNiO, La_2O_3, and γ-Al_2O_3) to the cathode is restricted in this case due to the insulating nature of oxide fillers.

It is very challenging to use nano-adsorption materials with high electrical conducting characteristics in a sulfur cathode. These materials are carbon systems or conducting polymer systems. In a sulfur electrode, active carbon, CNT, mesocarbon microbeads (MCMBs), and mesoporous carbon as carbon types, along with tubular polypyrrole (T-PPy) as a conducting polymer, have been applied to nano-adsorption materials with high levels of electrical conductivity [61, 67, 70].

Recently, the sulfur or sulfide before cycling was replaced by the adsorption area of the ordered mesoporous carbon [61, 70] or T-PPy [67]. Because the insulating sulfur and sulfides existed within the mesoporous carbon or T-PPy framework as nanoscale-dimension conducting material, the framework not only acts as an electronic conductor for the active mass and as a sulfur or polysulfide reservoir, but also serves as a mini electrochemical reaction chamber. Liang et al. [67] reported that cycling stability was improved by coating a polymer on the external surface of ordered mesoporous carbon with active material because the entrapment of the active material ensured a more complete redox process. Figure 16.7 shows a schematic diagram of a sulfur electrode using mesoporous carbon and T-PPy.

16.5 Nano-Aspect Material in Electrolytes

The primary function of the electrolyte in a Li/S cell, as in any other electrochemical cell, is to transport ions effectively between electrodes. Thus, the electrolyte should have high ionic conductivity at the rated operating temperature of the cell. It should also have good electrochemical stability, chemical stability toward lithium, and feasible safety levels. The electrolytes used in Li/S batteries are widely identified as liquids or solids. Liquid electrolytes are organic liquid electrolytes and ionic liquid electrolytes. The initial studies of Li/S cells utilized liquid electrolytes (catholytes) as active material media and as ionic conductors [4, 5, 19]. Most early studies reported a very poor performance of the cells. For enhancement of the electrochemical properties of Li/S, various liquid electrolytes have been studied, including tetrahydrofuran (THF), tetra(ethylene glycol) dimethyl ether (TEGDME), 1,2-dimethoxyethane (DME), 1,3-dioxolane (DIOX), ethylene carbonate (EC), dimethyl carbonate (DMC), ethyl methyl carbonate (EMC), propylene carbonate (PC), and poly(ethylene glycol) dimethyl ether (PEGDME). Lithium salts such as lithium bis(trifluoromethanesulfonyl)imide (LiTFSI), lithium trifluoromethanesulfonate ($LiCF_3SO_3$), lithium hexafluorophosphate ($LiPF_6$), lithium tetrafluoroborate ($LiBF_4$), and lithium perchlorate ($LiClO_4$) have been used. The solvents in liquid electrolytes are used either alone or as binary/ternary mixtures. Mixing solvents with a properly controlled proportion as an electrolyte in a Li/S battery with proper sulfur solubility, viscosity, and the correct dielectric constant has been shown to improve the initial capacity and lead to increased cycle life. In recent years, room-temperature ionic liquids have been increasingly used as Li/S battery electrolytes [55].

Solid electrolytes include solid polymers and gel polymers as well as inorganic electrolytes. Inorganic solid electrolytes [41, 56], such as amorphous $60Li_2S{\bullet}40SiS_2$ (mol%) and $80Li_2S{\bullet}20P_2S_5$, are nonflammable, cause no leakage, and do not dissolve polysulfides that are produced during the discharge of a sulfur cathode. Hence, they are promising for application in Li/S batteries. Polymer electrolytes are advantageous compared to their liquid counterparts because they make batteries lightweight, flexible, and safer. In the mid-1990s, solid-state Li/S cells using a poly(ethylene oxide)-based electrolyte that operated at temperatures exceeding 60 °C were investigated [31]. Solid polymer electrolyte (SPE) based on the PEO–lithium salt complex is most desirable. However, the problems associated with PEO electrolyte for solid-state Li/S cells at high temperatures are as follows: (1) poor mechanical properties, (2) low ionic conductivity at low temperatures, and (3) reactivity with a lithium metal anode. Shin et al. [32] studied the mechanical stability of electrolytes and the effect of ceramic filler on the ionic conductivity and transference number using TiO_2 powder. Nanocomposite solid polymer electrolytes such as PEO + metal oxide ($LiAlO_2$, SiO_2) have a very stable lithium electrode interface and enhanced conductivity at low temperatures with good mechanical properties [32, 38, 45, 52]. In their results, Shin et al. [32] described PEO-based Li/S cells with approximately 95 % sulfur utilization at 90 °C. However, the cycling properties were not up to the desired level. Overall, it has been observed that SPE materials with low ionic conductivity are not suitable for Li/S cell operation at room temperature because they lead to poor cycling properties, even at moderate temperatures.

However, unlike PEO electrolytes at high temperatures, gel polymer electrolytes prepared by activating polymer membranes with liquid electrolytes possess higher ionic conductivity and, hence, can perform better than PEO electrolyte at room temperature. The ionic conductivity of gel polymer electrolyte depends on the amount of liquid electrolyte used as plasticizer. However, the physical strength in gel polymer electrolyte decreases as the plasticizer content increases. The addition of inorganic fillers such as silica (SiO2), alumina (Al_2O_3), or titania (TiO2) nanoparticles to the polymer electrolyte results in the enhancement of the physical strength and an increase in the absorption level of the electrolyte solution [33, 36, 37, 42, 44]. Microporous-membrane-based gel polymer electrolytes have been demonstrated to be suitable for room-temperature Li/S cells because they provide a high initial discharge capacity of approximately 80 % sulfur utilization.

16.6 Nano-Aspect Material in Anodes

The anode of a Li/S battery is mostly lithium metal. Although Li/S batteries with sulfur/mesoporous carbon nanocomposites have a high discharge capacity and a moderate cycle life, the use of lithium metal as an anode in these types of batteries continues to pose major problems related to safety due to the formation of dendrites and to the pollution caused by the dissolved polysulfide in the electrolyte. Although a considerable amount of research has been dedicated to solving these problems using a protective layer such as polymer, glass, or the addition of aprotic organic solvents, the lithium anode has yet to be commercialized for use in secondary batteries with a liquid electrolyte.

Presently, the challenge in solving this problem is the creation of a Li-ion type battery as a lithium-metal-free battery using the chemistry of Li/S batteries [69–71]. Researchers have reported batteries coupled with Sn nanopowder or Si nanowire as an anode and a lithium sulfide (Li_2S) composite electrode in the “charged” state as the cathode. The results were effective in controlling most of the sulfur-based lithium technology issues. This novel battery system avoids the intrinsic safety issues associated with the use of lithium metal. It also has a higher first specific discharge energy than commercial systems such as the $LiCoO_2$/graphite cell. Figure 16.8 presents a sketch of a new version of a lithium-metal-free/lithium–sulfide battery.

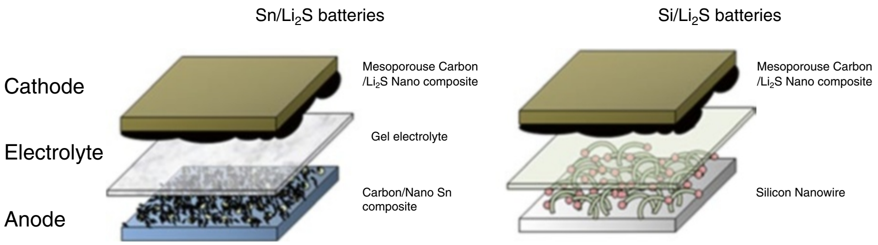

Fig. 16.8 Sketch of new version of lithium-metal-free/lithium–sulfide battery

16.7 Concluding Remarks

This article gives an overview of the science and technology of Li/S cells using nano-aspect materials and nanotechnology. Li/S battery technology has evolved over the years through a multilateral effect to solving problems related to the insulating nature of sulfur and Li_2S, the solubility of the discharge products in electrolytes, and, lately, the reaction rate, all in an effort to increase the capacity and the cycle life. Nanomaterials and nanotechnologies were used to solve the problems. The energy density and cycle life of Li/S cells have been enhanced dramatically over the past few years. Nanomaterials were applied to electrodes as active materials, conducting materials, and adsorption materials in the cathode and were used in polymer electrolytes to increase the ionic conductivity. A great deal of Li/S battery research is still being conducted in an effort to enhance the performance levels due to the potential for great applications in hybrid and purely electric vehicles and electrical storage systems for green energy. Having recently entered the commercial market also by providing more power relative to its weight, a low cost, and a long cycle life compared to its competitors, the Li/S battery is poised to become the most commendable achievement in battery technology in the immediate future. However, the road to a practical Li/S battery is still long. Many research activities are presently being conducted at universities and in institutional and industry settings for the further development of Li/S technology to meet the ever-growing amount of application demands.

References

1. M.S. Whittingham, Lithium batteries and cathode materials. Chem. Rev. **104**(10), 4271–4301 (2004)
2. M.S. Whittingham et al., The hydrothermal synthesis of new oxide materials. Solid State Ion. **75**, 257–268 (1995)
3. Y.K. Sun et al., High energy cathode material for long-life and safe lithium batteries. Nat. Mater. **8**(4), 320–324 (2009)
4. H. Yamin, E. Peled, Electrochemistry of a nonaqueous lithium/sulfur cell. J. Power Sources **9**, 281–287 (1983)
5. H. Yamin et al., Lithium sulfur battery; oxidation/reduction mechanisms of polysulfides in THF sSolutions. J. Electrochem. Soc. **135**(5), 1045–1048 (1988)
6. D. Marmorstein et al., Electrochemical performance of lithiumr/sulfur cells with three different polymer electrolytes. J. Power Sources **89**, 219–226 (2000)
7. D.-R. Chang, S.-H. Lee, S.-W. Kim, H.-T. Kim, Binary electrolyte based on tetra(ethylene glycol) dimethyl ether and 1,3-dioxolane for lithium–sulfur battery. J. Power Sources **112**, 452–460 (2002)
8. S.E. Cheon et al., Structural factors of sulfur cathodes with poly ethylene oxide-binder for performance of rechargeable lithium sulfur batteries. J. Electrochem.Soc. **49**(11), A1437–A1441 (2002)
9. B.H. Jeon, J.H. Yeon, K.M. Kim, I.J. Chung, Preparation and electrochemical properties of lithium-sulfur polymer batteries. J. Power Sources **109**, 89–97 (2002)

10. S.E. Cheon et al., Rechargeable lithium sulfur battery; I. Structural change of sulfur cathode during discharge and charge. J. Electrochem. Soc. **150**(6), 796–799 (2003)
11. Y.S. Choi et al., Effect of cathode component on the energy density of lithium–sulfur battery. Electrochim. Acta **50**, 833–835 (2004)
12. H.S. Ryu et al., Discharge process of Li/PVdF/S cells at room temperature. J. Power Sources **153**, 360–364 (2006)
13. V.S. Kolosnitsyn, E.V. Karaseva, Lithium–sulfur batteries: problems and solutions. Russ. J. Electrochem. **44**(5), 506–509 (2008)
14. J.-j. Chen et al., The preparation of nano-sulfur/MWCNTs and its electrochemical performance. Electrochim. Acta **55**, 8062–8066 (2010)
15. S.C. Han et al., Effect of multiwalled carbon nanotubes on electrochemical properties of lithium/sulfur rechargeable batteries. J. Electrochem. Soc. **150**(7), 889–893 (2003)
16. S.E. Cheon et al., Rechargeable Lithium Sulfur Battery; II. Rate Capability and Cycle Characteristics. J. Electrochem. Soc. **150**(6), 800–805 (2003)
17. H.S. Ryu et al., Self-discharge of lithium–sulfur cells using stainless-steel current-collectors. J. Power Sources **140**, 365–369 (2005)
18. S.-S. Jeong, Y.-J. Choi, K.-W. Kim, Effects of multiwalled carbon nanotubes on the cycle performance of sulfur electrode for Li/S secondary battery. Mater. Sci. Forum **510–511**, 1106–1109 (2006)
19. H. Yamin et al., The electrochemical behavior of polysulfides in THF. J. Power Sources **4**, 129–134 (1985)
20. J. Paris, V. Plichon, Electrochemical reduction of sulphur in dimethylacetamide. Electrochim. Acta **26**(12), 1823–1829 (1981)
21. J. Shim, K.A. Striebel, E.J. Cairns, The lithium/sulfur rechargeable cell: effects of electrode composition and solvent on cell performance. J. Electrochem. Soc. **149**(10), 1321–1325 (2002)
22. N.I. Kim et al., A study on the characteristics of PTFE as a binder for the cathode of lithium sulfur battery using liquid electrolyte. J. Korea Ind. Eng. Chem. **14**(8), 1138–1142 (2003)
23. M.S. Song et al., Effects of nanosized adsorbing material on electrochemical properties of sulfur cathodes for Li/S secondary batteries. J. Electrochem. Soc. **151**(6), 791–795 (2004)
24. S.E. Cheon et al., Capacity fading mechanisms on cycling a high-capacity secondary sulfur cathode. J. Electrochem. Soc. **151**(12), 2067–2073 (2004)
25. J.R. Akridge, Y.V. Mikhaylik, N. White, Li/S fundamental chemistry and application to high-performance rechargeable batteries. Solid State Ion. **175**, 243–245 (2004)
26. H.S. Ryu et al., Investigation of discharge reaction mechanism of lithium/liquid electrolyte/sulfur battery. J. Power Sources **189**, 1179–1183 (2009)
27. P.T. Cunningham, S.A. Johnson, E.J. Cairns, Phase equilibria in lithium-chalcogen systems; II. lithium-Sulfur. J. Electrochem. Soc. **119**(11), 1448–1450 (1972)
28. R.A. Sharma, Equilibrium phases in the lithium-sulfur system. J. Electrochem. Soc. **119**(11), 1439–1443 (1972)
29. R.D. Rauh et al., A Lithium/dissolved sulfur battery with an organic electrolyte. J. Electrochem. Soc. **126**(4), 523–527 (1979)
30. E. Peled et al., Lithium-sulfur battery: evaluation of dioxolane-based electrolytes. J. Electrochem. Soc. **136**(6), 1621–1625 (1989)
31. M.Y. Chu, U.S. Patent 5,814,420, Sept 1998
32. J.H. Shin et al., Electrochemical properties and interfacial stability of $(PEO)_{10}LiCF3_{S}O_{3}$/ $Ti_{n}O_{2n\text{-}1}$ composite polymer electrolytes for lithium/sulfur battery. Mater. Sci. Eng. **B95**, 48–156 (2002)
33. J.L. Wang et al., Sulfur–carbon nano-composite as cathode for rechargeable lithium battery based on gel electrolyte. Electrochem. Commun. **4**, 499–502 (2002)
34. Y.V. Mikhaylik, J.R. Akridge, Low temperature performance of Li/S batteries. J. Electrochem. Soc. **150**(3), 306–311 (2003)
35. Y.M. Lee et al., Electrochemical performance of lithium/sulfur batteries with protected Li anodes. J. Power Sources **119–121**, 964–972 (2003)

36. J. Wang et al., Polymer lithium cells with sulfur composites as cathode materials. Electrochim. Acta **48**, 1861–1867 (2003)
37. J. Wang et al., Sulfur composite cathode materials for rechargeable lithium batteries. Adv. Funct. Mater. **13**(6), 487–492 (2003)
38. X. Yu et al., All solid-state rechargeable lithium cells based on nano-sulfur composite cathodes. J. Power Sources **132**, 181–186 (2004)
39. S. Kim, Y. Jung, H.S. Lim, The effect of solvent component on the discharge performance of lithium–sulfur cell containing various organic electrolytes. Electrochim. Acta **50**, 889–892 (2004)
40. C.W. Park et al., Effect of sulfur electrode composition on the electrochemical property of lithium/PEO/sulfur battery. Met. Mater. Int. **10**(4), 375–379 (2004)
41. A. Hayashi et al., Rechargeable lithium batteries, using sulfur-based cathode materials and Li_2S–P_2S_5 glass-ceramic electrolytes. Electrochim. Acta **50**, 893–897 (2004)
42. J. Wang et al., Electrochemical characteristics of sulfur composite cathode materials in rechargeable lithium batteries. J. Power Sources **138**, 271–273 (2004)
43. N. Machida, T. Shigematsu, An All-solid-state lithium battery with sulfur as positive electrode materials. Chem. Lett. **33**(4), 376–377 (2004)
44. X. He et al., In situ composite of nano SiO_2–P(VDF-HFP) porous polymer electrolytes for Li-ion batteries. Electrochim. Acta **51**, 1069–1075 (2005)
45. X. Zhu et al., Electrochemical characterization and performance improvement of lithium/sulfur polymer batteries. J. Power Sources **139**, 269–273 (2005)
46. H.-S. Ryu et al., Discharge behavior of lithium/sulfur cell with TEGDME based electrolyte at low temperature. J. Power Sources **163**, 201–206 (2006)
47. H.S. Ryu et al., Self-discharge characteristics of lithium/sulfur batteries using TEGDME liquid electrolyte. Electrochim. Acta **52**, 1563–1566 (2006)
48. Y.-J. Choi et al., Effects on the carbon matrix as conductor in sulfur electrode for lithium/sulfur battery. Mater. Sci. Forum **510–511**, 1082–1085 (2006)
49. J. Wang et al., Sulphur-polypyrrole composite positive electrode materials for rechargeable lithium batteries. Electrochim. Acta **51**, 4634–4638 (2006)
50. S. Kim, Y. Jung, S.-J. Park, Effect of imidazolium cation on cycle life characteristics of secondary lithium–sulfur cells using liquid electrolytes. Electrochim. Acta **52**, 2116–2122 (2006)
51. W. Zheng et al., Novel nanosized adsorbing sulfur composite cathode materials for the advanced secondary lithium batteries. Electrochim. Acta **51**, 1330–1335 (2006)
52. Y.J. Choi et al., Electrochemical properties of sulfur electrode containing nano Al_2O_3 for lithium/sulfur cell. Phys. Scr. **129**, 62–65 (2007)
53. J.-W. Choi et al., Rechargeable lithium/sulfur battery with suitable mixed liquid electrolytes. Electrochim. Acta **52**, 2075–2082 (2007)
54. Y.-J. Choi et al., Effects of carbon coating on the electrochemical properties of sulfur cathode for lithium/sulfur cell. J. Power Sources **184**, 548–552 (2008)
55. J. Wang et al., Sulfur–meso-porous carbon composites in conjunction with a novel ionic liquid electrolyte for lithium rechargeable batteries. Carbon **46**, 229–235 (2008)
56. T. Kobayashi et al., All solid-state battery with sulfur electrode and thio-LISICON electrolyte. J. Power Sources **182**, 621–625 (2008)
57. B. Zhang, C. Lai, Z. Zhou, X.P. Gao, Preparation and electrochemical properties of sulfur–acetylene black composites as cathode materials. Electrochim. Acta **54**, 3708–3713 (2009)
58. D. Aurbach et al., On the surface chemical aspects of very high energy density, rechargeable Li-sulfur batteries. J. Electrochem. Soc. **8**, A694–A702 (2009)
59. V.S. Kolosnitsyn et al., The changes to lithium-sulphur cell component properties by cycling. ECS Trans. **16**(29), 173–180 (2009)
60. Y. Zhang et al., Effect of nanosized $Mg_{0.8}Cu_{0.2}O$ on electrochemical properties of Li/S rechargeable batteries. Int. J. Hydrogen Energy **34**, 1556–1559 (2009)
61. X. Ji, K.T. Lee, L.F. Nazar, A highly ordered nanostructured carbon–sulphur cathode for lithium–sulphur batteries. Nature Mater. **8**, 500–506 (2009)
62. C. Lai et al., Synthesis and electrochemical performance of sulfur/highly porous carbon composites. J. Phys. Chem. **C113**, 4712–4716 (2009)

63. L. Yuan et al., Improvement of cycle property of sulfur-coated multi-walled carbon nanotubes composite cathode for lithium/sulfur batteries. J. Power Sources **189**, 1141–1146 (2009)
64. C. Wang et al., Preparation and performance of a core–shell carbon/sulfur material for lithium/sulfur battery. Electrochim. Acta **55**, 7010–7015 (2010)
65. F. Wu et al., Sulfur–polythiophene composite cathode materials for rechargeable lithium batteries. Electrochem. Solid State Lett. **13**(4), 29–31 (2010)
66. L. Qiu et al., Preparation and enhanced electrochemical properties of nano-sulfur/poly(pyrrole-co-aniline) cathode material for lithium/sulfur batteries. Electrochim. Acta **55**, 4632–4636 (2010)
67. X. Liang, et al., A nano-structured and highly ordered polypyrrole-sulfur cathode for lithium–sulfur batteries. J. Power Sources, Article in Press (2010)
68. Jia-Zjao Wang et al., Sulfur-graphene composite for rechargeable lithium batteries. J. Power Sources, Article in Press (2010)
69. J. Hassoun, B. Scrosati, A high-performance polymer tin sulfur lithium ion battery. Angew. Chem. Int. Ed. **49**, 2371–2374 (2010)
70. Y. Yang et al., New nanostructured Li_2S/silicon rechargeable battery with high specific energy. Nano Lett. **10**(4), 1486–1491 (2010)
71. J. Hassoun, Y.-K. Sun, B. Scrosati, Rechargeable lithium sulfide electrode for a polymer tin/sulfur lithium-ion battery. J. Power Sources **196**, 343–348 (2011)
72. John A. Dean (ed.), *Lange's Handbook of Chemistry*, 3rd edn. (McGraw-Hill, New York, 1985) pp. 3–5
73. K.Y. Kang et al., Effect of carbon content of sulfur electrode on the electrochemical properties of lithium/sulfur battery using PEO electrolyte. Trans. Korean Hydrogen New Energy Soc. **17**(3), 317–323 (2006)
74. Y.V. Mikhaylik, U.S. Patent 7,352,680, 2008

Chapter 17
Possibility and Prospect for Future Energy Storages

Tetsuya Osaka and Hiroki Nara

17.1 Introduction

As mentioned in previous chapters, various efforts have been devoted to improving electric energy storage. Currently, lithium-ion batteries (LIBs), which are composed of a carbon anode and a transition metal oxide cathode, have been used in various applications such as mobile electronic devices [1], vehicles [2], and energy networks [3, 4]. Small LIBs have become widespread thanks to the development of mobile electronic devices, and now, large LIBs for hybrid electric vehicles (HEVs) and battery electric vehicles (BEVs) are becoming widespread. Consequently, the popularization of HEVs and BEVs will trigger the popularization of large LIBs for energy networks, so-called smart grids [4].

Electric energy storage systems have been widely investigated; they include alloy anode systems [5–8], sulfur cathodes [9], sodium anodes [10, 11], polyvalent ion batteries [12–18], sodium-sulfur batteries [19], metal–air batteries [9], organic batteries [20, 21], redox flow batteries [22], and lithium-ion capacitors [23]. Thus, energy storage comes in various forms. Most of these energy storage systems will be put to practical use in appropriate applications. Nevertheless, LIBs will be used for decades to come, as will lead-acid batteries. As a matter of course, LIBs will be upgraded through improvements to anodes, cathodes, electrolytes, and containers. First of all, capacity increases in anodes will be achieved by the development of alloy anode systems; however, the total energy density of LIBs depends on the balance of all their components. This chapter will discuss this issue and the possibility of enhancing the total energy density of LIBs for the combination of materials on anodes and cathodes. Finally, we will discuss prospects for future energy storage.

T. Osaka • H. Nara (✉)
Faculty of Science and Engineering, Waseda University,
3-4-1, Okubo, Shinjuku-ku, Tokyo 169-8555, Japan
e-mail: osakatets@waseda.jp; h-nara@aoni.waseda.jp

T. Osaka and Z. Ogumi (eds.), *Nanoscale Technology for Advanced Lithium Batteries*,
Nanostructure Science and Technology 182, DOI 10.1007/978-1-4614-8675-6_17,

17.2 Silicon Alloy Anodes

Capacity increases of LIBs will be achieved by the development of silicon alloy anodes because of their high theoretical capacity of 4,200 mAh g^{-1}, which is higher than that of conventional graphite anodes (372 mAh g^{-1}). Silicon alloy anodes, in combination with a graphite base material in LIBs, have been put to practical use by some manufacturers. However, the increase in the capacity has been limited so far: the capacity of Si-based anodes is around 120 % of that of a conventional graphite anode. Therefore, research and development of silicon alloy anodes has been going on for over 10 years. Various methods for synthesizing silicon materials exist; these include dry processes, such as chemical vapor deposition [24] and sputtering [25], and wet processes, such as electrodeposition developed by our group [5, 6] and electroless deposition. Of these, electro deposition might find application in industry because electrodeposition is an established process that is easy and cheap.

To cite one case, a Si-O-C composite anode for LIBs with outstanding cycle durability has been developed by means of an electrodeposition process [5, 6]. The electrodeposition method was introduced based on the assumption that, to form a Si-containing anode from an organic solution, a composite of Si with an organic/inorganic compound must be able to withstand stress during anode operation. Organic/inorganic compounds formed by a reduction of the organic solvent, as in the formation of a resultant solid electrolyte interphase (SEI) layer on anodes in LIBs, are widely known to exhibit permeability to Li^+ ions and chemical/electrochemical stability [26–28]. The Si-O-C composite anode delivered a discharge capacity of 1,045 mAh g^{-1} of Si at the 2,000th cycle and 842 mAh g^{-1} of Si even at the 7,200th cycle, as indicated in Fig. 17.1. The coulombic efficiency in the charge–discharge cycling was found to be higher than 98 %, except for a few initial cycles.

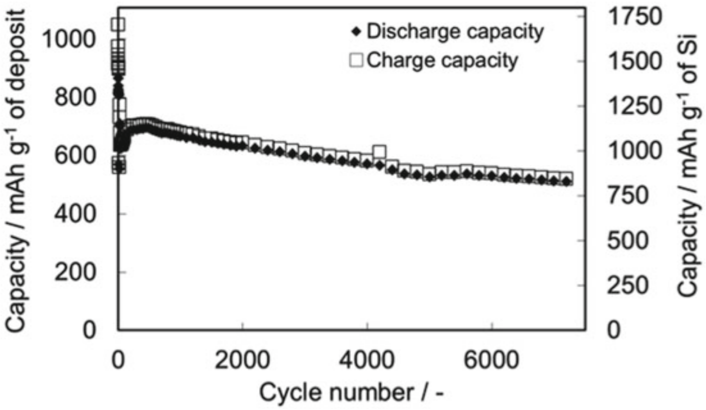

Fig. 17.1 Charge–discharge capacity vs. number of cycles. The capacity values were normalized with respect to the weight of the initial deposit or the calculated amount of Si in the deposit. The applied current density was 250 μA cm^{-2} (1.0 C-rate). (Reproduced by permission of The Royal Society of Chemistry)

17.3 Estimation on Capacity Increase of Lithium Batteries

As mentioned earlier, an alloy anode system will be developed in the near future that will lead to increases in the capacity of LIBs. The effect of a capacity increase of electrode materials on the capacity increase of LIBs is estimated on the basis of existing cells. In this estimation, the cell volume was set at existing cell values, and the components, except for active anode and cathode materials, were assumed not to be further developed. Table 17.1 and Fig. 17.2 indicate the estimation of capacity and energy density and the component volume ratio, respectively, in the case of an 18650-type cell, and Table 17.2 and Fig. 17.3 indicate those in the case of a LIB with a volume of 850 mL.

In the case of an 18650-type cell, the substitution of silicon-based anode, which delivers a capacity of 1000 mAh^{-1}, for the carbon-based anode used in currently

Table 17.1 Estimation of capacity and energy density in a LIB with volume of 17.7 mL, which is an 18650-type cell, by capacity increase of electrode materials. Values in *parentheses* indicate capacity of active materials in mAh g^{-1}

	Capacity (Ah)	Energy density (Wh L^{-1})	Energy density (Wh kg^{-1})
Existent	3.05	574	230
Si (1,000)/LNCAO (200)	4.50	812	299
Si (1,000)/Li_2S (600)	4.92	513	273
Si (4,200)/Li_2S (1120)	11.0	1165	632

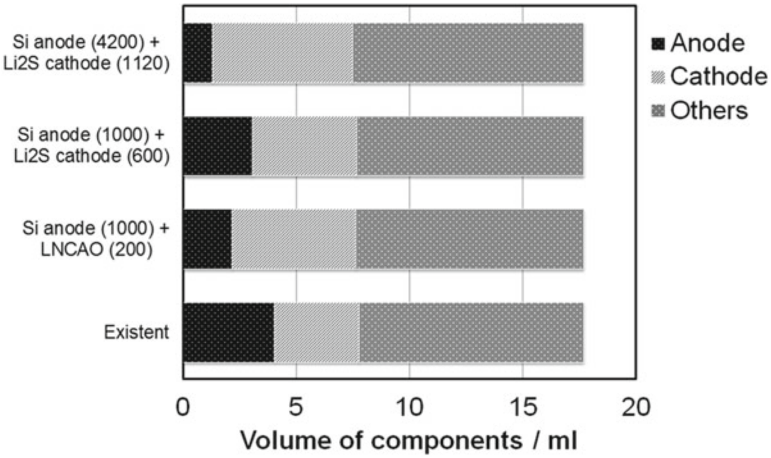

Fig. 17.2 Estimation of component volume ratio in LIB with volume of 17.7 mL, which is an 18650-type cell, by capacity increase of electrode materials

Table 17.2 Estimation of capacity and energy density in LIB with volume of 850 mL by capacity increase of electrode materials. Values in *parentheses* indicate capacity of active materials in mAh g^{-1}

	Capacity (Ah)	Energy density (Wh L^{-1})	Energy density (Wh kg^{-1})
Existent	50.5	218	109
Si (1,000)/LMO (110)	63.9	243	116
Si (1,000)/Li_2S (600)	111	236	142
Si (4,200)/Li_2S (1,120)	244	534	326

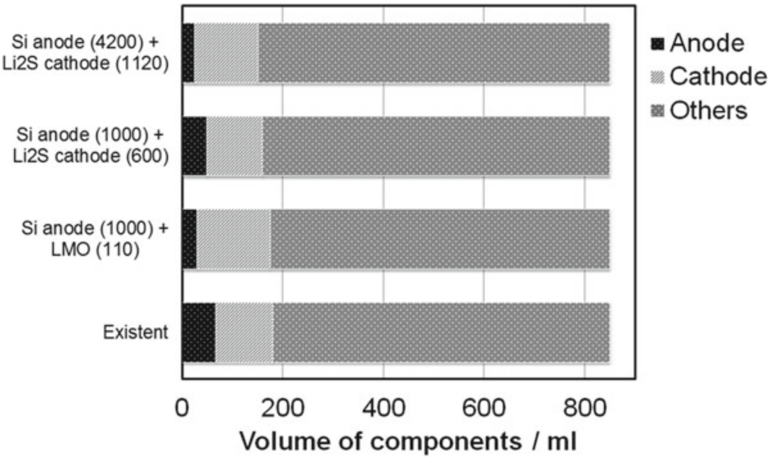

Fig. 17.3 Estimation of component volume ratio in LIB with volume of 850 mL by capacity increase of electrode materials

existing cells affects the capacity increase; the capacity of 3.05 Ah of currently existing cells will increase to a capacity of 4.50 Ah in Si (1,000 mAh g^{-1})/ $LiNi_xCo_yAl_zO_2$(LNCAO) (200 mAh g^{-1}) cells. On the other hand, in the case of a LIB with a volume of 850 mL, the substitution of silicon-based anode, which delivers a capacity of 1000 mAh^{-1}, for the carbon-based anode in currently existing cell will have less of an effect on capacity increases; a capacity of 50.5 Ah in currently existing cells will increase to 63.9 Ah in Si-based (1,000 mAh g^{-1})/ $LiMn_2O_4$(LMO) (110 mAh g^{-1}) cells. The difference in the capacity increase is attributable to the difference in the component ratios, as shown in Figs. 17.2 and 17.3. The 18650-type cells for portable devices have been around for a long time. However, because a large cell with a volume of 850 mL must be safe, the components related to safety, such as the container and compensating circuit, should occupy more space in the cell than an 18650-type cell. Thus, when the space for active materials is limited, capacity increases achieved simply by the replacement of the anode material will be limited. Therefore, a balance between the capacity of the anode and the cathode is important; cathode materials with a higher capacity must be developed. For example, if a lithium sulfide (Li_2S) cathode that delivers a capacity of 600 mAh g^{-1}, which is equal to a capacity of 857 mAh g^{-1} normalized by the weight of the sulfur, is achieved, the capacity of LIBs will drastically increase, especially on large cells, as indicated in Tables 17.1 and 17.2. In this estimation, the cathode material was assumed to be lithium sulfide (Li_2S), which in some cases would lead to a decrease in the volumetric energy density because of the low density and low redox potential of lithium sulfide (Li_2S). As a reference, the case where the capacity of both the silicon anode and the sulfur cathode attained the theoretical capacity is indicated in the tables and figures.

Thus the balanced development of anodes and cathodes is very important. At the same time, there is still room for improvement in other components, such as current collectors, separators, and containers; even on 18650-type cells, the other components occupy around 60 % of LIBs in this estimation. A decrease in the volume or weight of the other components might jeopardize the safety of batteries.

17.4 Safety of Lithium Batteries

To increase the energy density of LIBs, the capacity of the active materials must be increased and at the same time the volume or weight of the other components decreased. However, a decrease in the volume or weight of the other components might be incompatible with safety, especially in large LIBs. Therefore, a safer LIB system is required for large LIBs. Recently, separators with high thermal stability and retentivity of organic solvents have been developed by hybridization of inorganic materials with porous polymer membranes [29, 30] and used in practical applications. In addition, module design for radiation performance [31, 32] and impact resistance is important in large LIBs. There are several types of LIB. Cylinder-type cells, as typified by 18650-type cells, are superior with respect to cost because the cells are produced in large volume but inferior with respect to tap density. Square-type cells are superior in terms of tap density but inferior with regard to cost, weight, and heat management. Laminate-type cells are superior regarding tap density, cost, and heat management but inferior in terms of impact resistance because the cells are packed in a film; therefore, laminate-type cells must have some sort of protection. These LIBs will find uses in various applications.

17.5 Summary

The possibilities of future energy storage in batteries was demonstrated and discussed. Higher-energy-density batteries based on LIBs will be developed using new materials on the anodes and cathodes. Even when next generation batteries are developed, all the different electrodes in future batteries will have to be developed in capacity balance with one another.

References

1. J.M. Tarascon, M. Armand, Nature **414**, 359–367 (2001)
2. V. Etacheri, R. Marom, R. Elazari, G. Salitra, D. Aurbach, Energy Environ. Sci. **4**, 3243–3262 (2011)
3. B. Dunn, H. Kamath, J.M. Tarascon, Science **334**, 928–935 (2011)
4. Z.G. Yang, J.L. Zhang, M.C.W. Kintner-Meyer, X.C. Lu, D.W. Choi, J.P. Lemmon, J. Liu, Chem. Rev. **111**, 3577–3613 (2011)
5. H. Nara, T. Yokoshima, T. Momma, T. Osaka, Energy Environ Sci. **5**, 6500–6505 (2012)
6. T. Momma, S. Aoki, H. Nara, T. Yokoshima, T. Osaka, Electrochem. Commun. **13**, 969–972 (2011)
7. H. Nara, Y. Fukuhara, A. Takai, M. Komatsu, H. Mukaibo, Y. Yamauchi, T. Momma, K. Kuroda, T. Osaka, Chem. Lett. **37**, 142–143 (2008)
8. M. Winter, J.O. Besenhard, Electrochim. Acta **45**, 31–50 (1999)
9. P.G. Bruce, S.A. Freunberger, L.J. Hardwick, J.M. Tarascon, Nat. Mater. **11**, 19–29 (2012)
10. D.A. Stevens, J.R. Dahn, J. Electrochem. Soc. **147**, 1271–1273 (2000)
11. S. Komaba, W. Murata, T. Ishikawa, N. Yabuuchi, T. Ozeki, T. Nakayama, A. Ogata, K. Gotoh, K. Fujiwara, Adv. Funct. Mater. **21**, 3859–3867 (2011)
12. G.G. Amatucci, F. Badway, A. Singhal, B. Beaudoin, G. Skandan, T. Bowmer, I. Plitz, N. Pereira, T. Chapman, R. Jaworski, J. Electrochem. Soc. **148**, A940–A950 (2001)
13. T.D. Gregory, R.J. Hoffman, R.C. Winterton, J. Electrochem. Soc. **137**, 775–780 (1990)
14. D.B. Le, S. Passerini, F. Coustier, J. Guo, T. Soderstrom, B.B. Owens, W.H. Smyrl, Chem. Mater. **10**, 682–684 (1998)
15. K. Makino, Y. Katayama, T. Miura, T. Kishi, J. Power Sources **99**, 66–69 (2001)
16. P. Novák, W. Scheifele, O. Haas, J. Power Sources **54**, 479–482 (1995)
17. T. Tsuchida, M. Nakanishi, H. Takayanagi and K. Yamamoto, *Proceedings of the 2nd Battery Material Symposium*, 1985, 417–430.
18. D. Aurbach, Z. Lu, A. Schechter, Y. Gofer, H. Gizbar, R. Turgeman, Y. Cohen, M. Moshkovich, E. Levi, Nature **407**, 724–727 (2000)
19. T. Oshima, M. Kajita, A. Okuno, Int. J.Appl. Ceram. Technol. **1**, 269–276 (2004)
20. H. Nishide, S. Iwasa, Y.J. Pu, T. Suga, K. Nakahara, M. Satoh, Electrochim. Acta **50**, 827–831 (2004)
21. T. Suga, H. Ohshiro, S. Sugita, K. Oyaizu, H. Nishide, Adv. Mater. **21**, 1627–1630 (2009)
22. C. Fabjan, J. Garche, B. Harrer, L. Jorissen, C. Kolbeck, F. Philippi, G. Tomazic, F. Wagner, Electrochim. Acta **47**, 825–831 (2001)
23. G.G. Amatucci, F. Badway, A. Du Pasquier, T. Zheng, J. Electrochem. Soc. **148**, A930–A939 (2001)
24. S. Bourderau, T. Brousse, D.M. Schleich, J. Power Sources **81**, 233–236 (1999)
25. J.P. Maranchi, A.F. Hepp, P.N. Kumta, Electrochem. Solid State Lett. **6**, A198–A201 (2003)
26. J.R. Szczech, S. Jin, Energy Environ. Sci. **4**, 56–72 (2011)
27. P. Verma, P. Maire, P. Novak, Electrochim. Acta **55**, 6332–6341 (2010)
28. M. Winter, W.K. Appel, B. Evers, T. Hodal, K.C. Moller, I. Schneider, M. Wachtler, M.R. Wagner, G.H. Wrodnigg, J.O. Besenhard, Monatsh. Chem. **132**, 473–486 (2001)
29. H. Yoneda, Y. Nishimura, Y. Doi, M. Fukuda, M. Kohno, Polym. J. **42**, 425–437 (2010)
30. S.S. Zhang, J. Power Sources **164**, 351–364 (2007)
31. K. Smith, G.H. Kim, E. Darcy, A. Pesaran, Int. J. Energy Res. **34**, 204–215 (2010)
32. S.C. Chen, C.C. Wan, Y.Y. Wang, J. Power Sources **140**, 111–124 (2005)

Index

T. Osaka and Z. Ogumi (eds.), *Nanoscale Technology for Advanced Lithium Batteries*, Nanostructure Science and Technology 182, DOI 10.1007/978-1-4614-8675-6,